

Study of relaxation processes in simple glass formers by means of ^2H NMR spectroscopy

Der Universität Bayreuth
zur Erlangung des Grades eines
Doktors der Naturwissenschaften (Dr. rer. nat.)
vorgelegte Abhandlung

von

Sorin A. Lusceac

geboren am 23 Februar 1978 in Vatra Dornei

1. Gutachter: Prof. Dr. E. A. Rößler
2. Gutachter: Prof. Dr. F. Fujara

When you have eliminated the impossible, that which remains, however improbable, must be the truth.

Sir Arthur Conan Doyle

Contents

1. Introduction	1
1.1. Supercooled liquids and glasses	1
1.1.1. General aspects	1
1.1.2. The α -process	3
1.1.3. The β -process	4
1.1.4. The excess wing	6
1.2. Scope and structure of the present work	7
2. ^2H NMR - a Tool for Investigating Order and Dynamics	9
2.1. The main ^2H NMR interactions and their Hamiltonian	9
2.1.1. Hamiltonians	9
2.1.2. Orientation dependence of \hat{H}_Q	10
2.2. Density operator	11
2.2.1. Thermal equilibrium	12
2.2.2. Time evolution	12
2.2.3. Rotating frame	13
2.2.4. The effect of radio frequency pulses	14
2.3. Main pulse sequences and related measured functions	14
2.3.1. Solid echo	14
2.3.2. Stimulated echo	18
2.4. Relaxation phenomena	21
3. Cyanoadamantane - Study of the Supercooled Plastically Cristalline Phase	25
3.1. Introduction	25
3.1.1. Molecular shape and possible phases	26
3.1.2. Dielectric loss spectra and characteristic time constants	27
3.1.3. Uniaxial rotation of the molecule and the solid echo spectra in the glassy phase	27
3.2. Experimental details	29
3.2.1. Preparation of the deuterated sample	29
3.2.2. Measurement parameters	30
3.3. Experimental results, simulations and discussion	30

3.3.1.	Spin-lattice relaxation	30
3.3.2.	Solid echo spectra	33
3.3.3.	2D spectrum and stimulated echoes	35
3.3.4.	Analysis of the solid echo spectra	39
3.4.	Summary and conclusions	44
4.	NMR Study of the Glass Formers ortho-Terphenyl and Toluene in Confined Geometry	45
4.1.	Introduction	45
4.1.1.	ortho-Terphenyl	45
4.1.2.	Toluene	46
4.1.3.	Confining medium: SBA-15	47
4.1.4.	Properties of the glass formers in the confining medium	47
4.2.	Measurements details	48
4.3.	Results and discussion	49
4.3.1.	ortho-terphenyl confined in SBA-15	49
4.3.2.	Toluene confined in SBA-15	54
4.4.	Summary and conclusion	58
5.	Relaxation Processes in Polybutadiene and a Mixture of Benzene in Polybutadiene	59
5.1.	Introduction	59
5.2.	Some physical properties of polybutadiene	59
5.3.	Experimental details	60
5.3.1.	Samples used in the NMR measurements	60
5.3.2.	Samples used in the dielectric spectroscopy measurements	60
5.3.3.	Measurements parameters	61
5.4.	Neat polybutadiene: NMR results and discussion	62
5.4.1.	Solid echo spectra measured with a short interpulse delay	62
5.4.2.	Solid echo spectra for different interpulse delays	62
5.4.3.	The apparent spectral width	65
5.4.4.	Spin-lattice and spin-spin relaxation	66
5.5.	Benzene as a guest in polybutadiene: NMR results and discussion	68
5.5.1.	Solid echo spectra measured with a short interpulse delay	68
5.5.2.	Solid echo spectra for different interpulse delays	70
5.5.3.	The apparent spectral width	72
5.5.4.	Spin-lattice and spin-spin relaxation	72
5.6.	Dielectric spectroscopy results and discussion	74
5.7.	Summary and conclusions	77

6. Random walk simulations related to the β-process	81
6.1. Introduction	81
6.2. Results and discussion	82
6.2.1. Random motion on the edge of a cone (RO)	83
6.2.2. Multi-step motion on a cone (MO)	89
6.2.3. Random motion within a cone (RW)	93
6.2.4. Random motion on the edge of a cone with a distribution of jump correlation times (RO-D)	96
6.3. Further discussion and conclusions	98
6.3.1. Concluding the simulations	98
6.3.2. Applications	100
7. NMR study of meta-Fluoroaniline	107
7.1. Introduction	107
7.1.1. General properties	107
7.1.2. Dielectric spectroscopy results	108
7.2. Experimental details	110
7.2.1. The deuterated sample	110
7.2.2. Measurement parameters	110
7.3. Results	111
7.3.1. Spin-lattice and spin-spin relaxation	111
7.3.2. Solid echo spectra measured with a short interpulse delay . . .	113
7.3.3. Solid echo spectra measured with various interpulse delays . . .	116
7.3.4. Stimulated echo experiments	118
7.4. The β -process in m-FAN: discussion and conclusions	122
8. Summary	129
Appendix.	131
A. Matrix representation of important spin operators	131
B. Features of $\min(T_1)$ for a Cole-Davidson spectral density	132
C. Simulation details	134
C.1. Solid echo spectra	134
C.2. The 2D spectrum and F_{∞}^{sin} for cyanoadamantane	135
D. Additional data: polybutadiene	137
E. Additional data: ortho-terphenyl	139
F. Tables with the phase cycles for the used pulse sequences	144
List of Publications	147
Acknowledgments	149

Contents

Bibliography	151
Zusammenfassung	159
Erklärung	161

1. Introduction

Supercooled liquids and glasses display a large variety of features different from those of crystalline matter and they show molecular motion on virtually all time scales spanning from picoseconds to seconds. Although widely used in everyday life, still there is no theory that fully describes their physical properties in a large temperature range. All these facts contributed to the involvement of new researchers into the field of glass science in the last years.

This PhD thesis focuses on molecular glasses and plastic crystals, studying their relaxation properties by multidimensional ^2H NMR spectroscopy. Several different topics will be addressed, with special consideration given to the features of secondary relaxational processes which dominate the response of a glass, i. e. below the glass transition temperature. In addition, random walk simulations were performed in order to better understand the experimental results.

In the following we will try to present several of the main features of glass forming liquids and some of the typical results obtained while investigating such systems. Numerous reviews and books on the subject can be found (for example, [11, 28, 41, 46, 90] and references therein) therefore we will be as brief as possible. In the course of introducing the actual knowledge in the glass field, it will become clear what are the main topics dwelt on in this thesis.

1.1. Supercooled liquids and glasses

1.1.1. General aspects

The viscosity of a liquid, that is a macroscopic measure of its resistance to flow, continuously increases with decreasing temperature (cf. Fig. 1.1). If crystallization is avoided while cooling, rigidity of a solid is finally reached and the glassy state is obtained. This continuous transition from a liquid to a glass is called the glass transition, and it is not a first order phase transition from a thermodynamic point of view. Note that the change in viscosity amounts to about fourteen orders of magnitude! What is the cause of the slow dynamics at low temperatures and how can we understand this continuous slowing down of molecular dynamics starting from the melt till the solid body? These questions are still not completely answered.

The glass transition temperature T_g can be defined in many distinct ways, with results that are negligible different. For example, T_g may be taken as the temperature

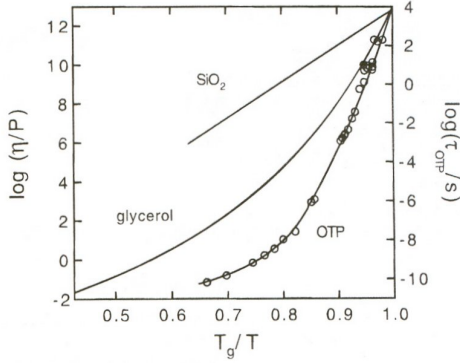


Figure 1.1. Solid lines: viscosity as a function of inverse reduced temperature for three liquids: SiO_2 , glycerol and o-terphenyl. Circles: reorientation correlation times for o-terphenyl. (Figure from Ediger et al. [46].)

at which the viscosity reaches a value of $\eta = 10^{13} P = 10^{12} Pa s$ (cf. Fig. 1.1). A liquid at a temperature between its melting temperature T_m and T_g is called supercooled liquid. The supercooled liquid state is a metastable state but it can be regarded as being in internal equilibrium as long as no crystal nuclei are present. On the other hand, the glassy state ($T < T_g$) is an unstable one but the time scale of the main relaxation process is usually several orders of magnitude larger than any realistic observation time, so for practical applications it can be regarded as a stable state.

One often finds in the scientific literature a distinction made between glass formers based on the different temperature dependence of the viscosity. That is, the glass formers that show a behavior close to an Arrhenius one (i.e. a straight line in the representation of Fig. 1.1) are called ‘strong’ glass formers while those departing from this behavior are called ‘fragile’. A quantitative description of ‘fragility’ can be done by calculating the fragility index [27]:

$$m = \left. \frac{d[\log_{10}(\tau_\alpha)]}{d(T_g/T)} \right|_{T=T_g}. \quad (1.1)$$

Along with transport properties (like viscosity), microscopic time constants display a continuous increase over many orders of magnitude with lowering the temperature, too. For example, the rotational correlation time of the primary relaxation process for the molecular glass former o-terphenyl shows the same temperature dependence as viscosity (cf. Fig. 1.1). Nevertheless, while a wide range of observables related to relaxation phenomena show a diverging tendency, they might be decoupled one from the other. That is, even at temperatures higher than T_g (but lower than some crossover temperature T_x) one mode of transport can occur on a somewhat different time scale from others. For example, in o-terphenyl and toluene diffusivity slows down less rapidly than viscosity therefore the two observables do not scale in an Arrhenius representation

[11].

1.1.2. The α -process

In a simple liquid, the main relaxation process that characterizes the structural relaxation and determines the long time behavior of any correlation function is called the α -process. One of the most employed technique in the research field of glasses is di-

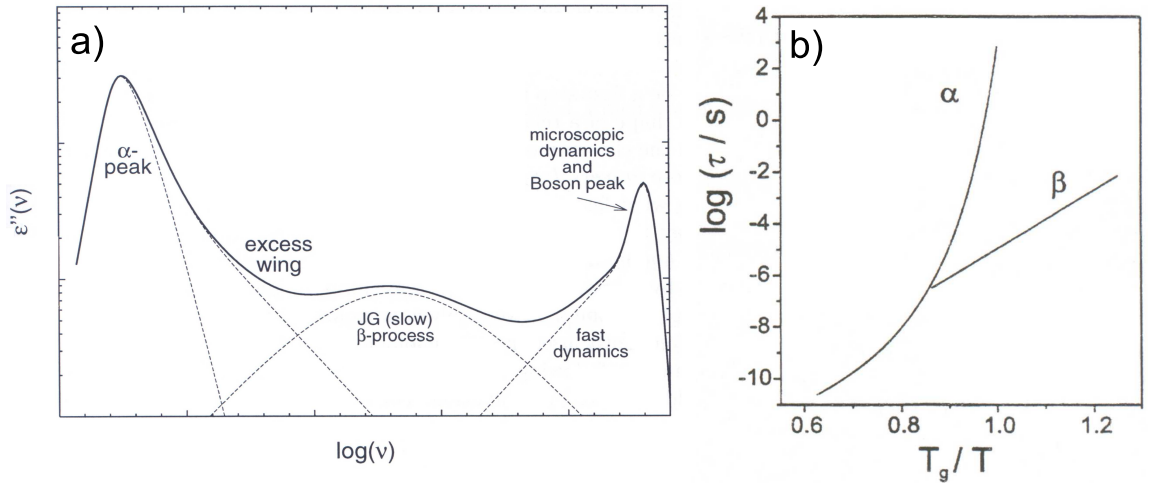


Figure 1.2. a) Sketch of the dielectric spectrum of a typical glass-former (figure from Blochowicz [20]); depending on material, the excess wing or/and the JG β -process might be absent. b) Sketch of the temperature dependence for the time constants of the α and β -process (figure from Vogel [129]).

electric spectroscopy due to the large frequency range accessible. The typical dielectric response of a molecular glass former is shown in the simple sketch in Fig. 1.2 (a) and one can see that the main relaxation process gives rise to a peak at the lowest frequencies. For organic liquids, the time constant of the α -process (τ_α) has a non-Arrhenius temperature dependence (cf. Fig. 1.2 (b)) that can be phenomenologically described to some extent by the Vogel-Fulcher-Tammann (VFT) equation [11]:

$$\tau = \tau_0 \exp \left(\frac{DT_0}{T - T_0} \right). \quad (1.2)$$

Analyzing τ_α in a large temperature range one observes that a single VFT function does not fit perfectly the experimental points over the entire temperature range and instead it is better to use three functions, in the most general case: an Arrhenius expression at high temperatures with a crossover to a VFT expression at a temperature T_A and another crossover to a second VFT at a lower temperature T_B [41, 90]. While at

high temperatures $T > T_A$, the rotational autocorrelation function of the α -process is believed to be exponential in a fair approximation, at lower temperatures it becomes stretched, being well described by the Kohlrausch-Wiliams-Watts (KWW) expression [90]:

$$f(t) = \exp \left[- \left(\frac{t}{\tau} \right)^{\beta_{KWW}} \right]. \quad (1.3)$$

The temperature T_B is often found to be close to the critical temperature T_c of the mode coupling theory [41, 54, 90].

One of the main characteristics of the α -process is the cooperativity of molecular motion, with typical correlation lengths that are not longer than a few nanometers [41, 124]. Moreover, ^2H NMR experiments at temperatures close to but above T_g proved that the rotational motion of the molecules is not diffusion-like but it is described by a bimodal angular distribution, as the simplest approach [28, 29, 52, 57] (the corresponding simulated trajectory for one molecule can be seen in Fig. 1.3).

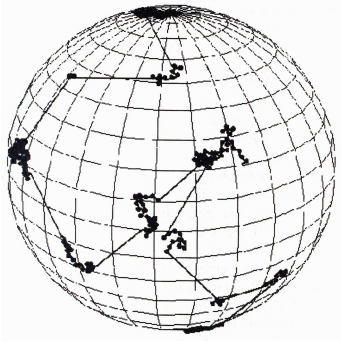


Figure 1.3. Simulated rotational jump process involving a bimodal jump angle distribution dominated by small angles (2°) with only a 2% fraction of 30° angles added. The trace on the sphere corresponds to an orientational trajectory of a single molecule (figure from Böhmer et al. [28]).

The distribution contains a large percent K_{small} of small angles, typically about $2^\circ - 3^\circ$ and a percent K_{large} of large angles in the range $30^\circ - 50^\circ$ [28]. The ratio K_{large}/K_{small} differs between glass formers, and it was argued that it is smaller when hydrogen bondings or other association effects are present [28]. Thus ^2H NMR techniques allowed to give a detailed portrait of the molecular motion involved in the α -process.

1.1.3. The β -process

While the α -process is the most discussed relaxation phenomenon when one refers to the physics of the glass transition, secondary processes captured the attention of many researchers in the last years (for example, [41, 74, 92] and references therein). Concerning these we will mention two of them, namely the β -process and the ‘excess

wing’, the former one being the subject of investigation for a large part of the research presented in this PhD work.

A β -process can be observed as a peak in the dielectric spectrum of most of the simple glass formers at frequencies higher than those of the α -process (cf. Fig. 1.2 (a)). For molecules that have internal degrees of freedom that are dielectrically active one would expect such a secondary peak. Still, as first pointed out by Johari and Goldstein, there are completely rigid molecules that display a β -process [63, 64, 66]. To honor their discovery this secondary relaxation process is called Johari-Goldstein (JG) β -processes. It was pointed out by many, including Johari, that the ‘molecular mobility seen as β -relaxation is intrinsic to the glassy state’ [65] and it is a feature that evolves from the liquid or supercooled liquid state. Nevertheless, there are several glass formers that do not exhibit a β -peak in their dielectric spectrum and they were called by Kudlik et al. [74] ‘type A’ glass formers in order to distinguish them from the so called ‘type B’ glass formers that do display a β -peak.

The general properties of the β -process are: it displays a symmetric DS peak and it is thermally activated, with an activation energy that is proportional with T_g and the rule $E_\beta \simeq 24T_g$ holds (with some exceptions) [24, 74, 91]. For several substances it is reported that above T_g the temperature dependence of the time constants for the β -process may depart from the sub- T_g Arrhenius behavior [24, 92, 93, 95]. Above T_g the dielectric relaxation strength of the β -process strongly decreases with cooling but stays essentially constant below T_g [13, 17, 74].

In order to explain the molecular origin of the secondary process Johari and Goldstein introduced the idea of ‘islands of mobility’ which are believed to survive in the glassy state and which contain a certain amount of molecules with a mobility considerably higher than that of the surrounding [64]. On the other hand, a different approach was introduced by Williams and Watts who assumed that all molecules participate in the β -process leading to a partial loss of dielectric correlation function at short times; at longer times, the α -process would lead to a complete loss of correlation [142, 143]. Solvation [137] and NMR experiments [30, 129, 132, 134, 135, 136] clearly demonstrated that all the molecules participate in the β -process therefore denying the existence of ‘islands of mobility’.

Applying multidimensional techniques in the case of toluene, ^2H NMR showed that for most of the molecules the amplitude of reorientation is close to 4° and, in addition, for 10 – 20% of the molecules it is in the range 10° to 90° . The main difference with respect to the α -process is that in the case of the latter, at low temperatures, a vector fixed on a molecule can explore the entire unit sphere although in steps of relative small angles; on the other hand, for the β -process the molecular motion is restricted, only a small part of the unit sphere is explored [129, 134, 135, 136]. In the case of toluene, a cone model was proposed in order to account for the experimental findings: a $C-^2\text{H}$ bond can move on the edge of a cone described by a full angle χ that displays a distribution $V(\chi)$ (cf. Fig. 1.4 (a)). In addition, it was demonstrated that the β -process

is characterized by a multi-step motion in the sense that the full circumference of the cone base is covered in a complex step-like manner (as suggested by Fig. 1.4 (b)) [129, 134, 135, 136]. Hence ^2H NMR was able to extract very thorough information on the nature of the β -process although it is highly restricted in angular amplitude.

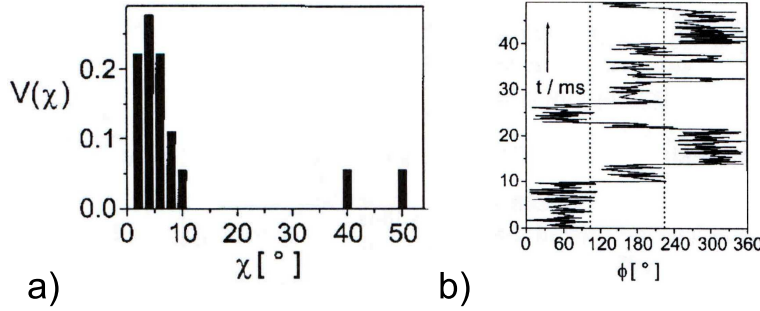


Figure 1.4. a) Distribution characterizing the full opening angles of the cone and b) example of a trajectory $\phi(t)$ on the edge of the cone showing the multi-step character of the molecular motion. (The angle ϕ defines the position of a unit vector describing the orientation of the molecule on the circumference of the cone.) Both figures are from Vogel [135] and refer to the specific model used in the simulations that accounted for the experimental findings in toluene- d_5 . Be advised that along this PhD thesis we used the notation χ in a different manner, as being the semiangle of the cone.

Recently, Ngai and Paluch proposed a classification of the β -processes claiming that different physical origin is responsible for them in distinct glass formers [92]. Their assertion was based on the fact that there is a group of β -processes that display very similar features and numerous ones that are somewhat different. It is still not very clear what criteria should one use to classify them but nevertheless Ngai and Paluch suggested that the term JG β -process should not be used for all β -processes. The question whether β -processes in diverse materials are different in nature or not can be addressed by ^2H NMR techniques, and it is one of the driving force in a part of the research presented in this PhD (for example, cf. Chapter 7).

1.1.4. The excess wing

At high temperatures the α -peak observed in the dielectric spectrum can be well interpolated by a Cole-Davidson function that predicts a single power law behavior on the right-hand flank of the peak [20, 73, 74]. With lowering the temperature, for some glass formers, one can observe on the high frequency flank of the α -peak an extra contribution to the expected single power law behavior (cf. Fig. 1.2 (a), see also

[20, 73, 74]). This feature is called ‘excess wing’ and its molecular origin is still debated [2, 24, 92, 116]. Dixon et al. [40], among others [77, 79], demonstrated that by an appropriate scaling of both ε'' and ν axes it is possible to collapse the $\varepsilon''(\nu)$ curves, including α -process and excess wing for different temperatures and different materials onto one master curve. Therefore they concluded that the excess wing and the α -peak are inseparable features of the same main relaxation process. Succeeding the above mentioned work, it was showed that the dielectric data of many glass formers cannot be scaled to a master curve by the procedure proposed by Dixon et al. [75, 76, 78]. In addition, some authors believe that the excess wing is nothing else but a Johari-Goldstein (JG) peak that is obscured because its maximum is well under the more intense α -peak [56, 92, 116]. Still, the debate is not over, with authors pointing out that there are differences between the physical properties of an JG β -process and those of the excess wing (for example, [2, 20] and references therein). Moreover, there are materials that display both an excess wing and a β -peak in their DS spectrum further stirring the controversy.

The high frequency features (fast dynamics) in Fig. 1.2 (a) are by no means completely understood in the eyes of the glass physics nowadays but we will not refer to them at all because the ^2H NMR experiments cannot access that frequency range.

1.2. Scope and structure of the present work

The main subject of this work is the β -process and its properties in simple molecular liquids composed of rigid molecules studied by means of ^2H NMR spectroscopy. The research was started with the purpose to continue previous NMR work done in Bayreuth (for example, [71, 103, 115, 129, 133]) and to develop methods of analyzing the experimental data as well as performing new simulations to gain an indepth view on the molecular mechanism involved in the β -process. As the β -processes are highly restricted in space the NMR experiments have to be pushed to new frontiers. Systems were investigated, trying to answer the question whether the classification of glass formers in type A and type B can be justified or not from a ^2H NMR point of view. More precisely, o-terphenyl (OTP, type A) and toluene (type B) were confined in materials with pores with a diameter of several nanometers in order to find out how their relaxational phenomena are modified. Is there a difference between the nature of β -processes in various compounds? Meta-fluoroaniline (m-FAN) is a molecular glass former that displays a β -process with a very small amplitude in the DS spectra and it is believed by some to be not intrinsic to the glass transition [92]. By investigating, in particular, m-FAN and comparing the obtained results with those from toluene we can make a statement regarding the above inquiry. From former dielectric experiments it was known that polybutadiene, a polymer without side groups, displays a β -process that is very similar to the one in toluene which was throughly investigated by means

of ^2H NMR [129, 134, 135, 136]. We studied polybutadiene, extending the investigated temperature range towards low temperatures in order to compare the ^2H NMR results with those available for toluene and in order to estimate the amplitude of the molecular motion involved in the β -process. A faster relaxation process was discovered and this result triggered further dielectric spectroscopy experiments done in our group by Gainaru [50, 81].

In addition to the study of the β -process, we also investigated the α -process in the plastic crystal (PC) cyanoadamantane (CNADM). Glass transition phenomena are displayed by PC in which due to translational order the molecules are lacking some of the degrees of freedom found in liquids. Therefore it is believed that the glass transition in PCs might be easier to understand than in molecular glasses, prompting experiments on this class of substances.

Besides the case of CNADM, α -process was briefly characterized for OTP and toluene in confining conditions and also for m-FAN as these systems were never studied by ^2H NMR.

The PhD thesis is structured as follows: the next chapter shows a short part of the ^2H NMR theory and defines the functions used in the experimental chapters. Starting from the Chapter 3 (Cyanoadamantane - Study of the Supercooled Plastically Crystalline Phase), the experimental findings are displayed and each chapter is organized as a more or less stand-alone piece of presentation. It means that every one of them was written with the intention to be understood without the need to refer often to the other ones. As a matter of fact, the findings presented in the first three experimental chapters were published as scientific papers in a format somewhat close to the one in here.

2. ^2H NMR - a Tool for Investigating Order and Dynamics

There are numerous books and papers on NMR that give an indepth view of the vast knowledge in the field today (for example, [1, 28, 80, 112] and references therein). Therefore the scope of this chapter is to present only a *minimum minimorum* on the NMR theory with application in ^2H NMR and to give some definitions that will be useful for understanding the chapters that present the experimental findings. The following parts are more or less a compilation from the book of Schmidt-Rohr and Spiess, so where references are missing it should stand [112].

2.1. The main ^2H NMR interactions and their Hamiltonian

2.1.1. Hamiltonians

In a normal NMR experiment, the constant external magnetic field B_0 is high (on the order of several Tesla) and thus, for the systems of our interest, the main interaction of the spins is the Zeeman interaction. For an isolated nucleus it is described by the Zeeman Hamiltonian:

$$\hat{H}_Z = -\gamma\hbar\hat{I}_zB_0, \quad (2.1)$$

where γ is the gyromagnetic ratio, \hbar is the Plank constant divided by 2π and \hat{I}_z is the quantum operator describing the z component of the nuclear spin angular momentum (the axis Oz of the laboratory-frame is parallel with the magnetic field \vec{B}_0). Some textbooks prefer to write the Hamiltonians in frequency units, substituting \hat{H}/\hbar by \hat{H} and in this notation Eq. 2.1 becomes:

$$\hat{H}_Z = -\gamma\hat{I}_zB_0 = \omega_0\hat{I}_z, \quad (2.2)$$

where ω_0 is the Larmor frequency. Other contributions to the total Hamiltonian which are local fields lead to small energy shifts that can be calculated in terms of first-order perturbation theory.

Nuclei with a nuclear spin quantum number $I \geq 1$ possess a quadrupolar moment Q which interacts with the electric field gradient $\overline{\overline{V}}$ found at their site. $\overline{\overline{V}}$ is a tensor

defined from the second spatial derivatives of the electrical potential Φ :

$$V_{\alpha\beta} = \frac{\partial^2 \Phi}{\partial r_\alpha \partial r_\beta} \quad (\alpha, \beta = x, y, z). \quad (2.3)$$

The corresponding Hamiltonian for a single spin is:

$$\hat{H}_Q = \frac{eQ}{2I(2I-1)\hbar} \hat{I} \bar{\bar{V}} \hat{I}, \quad (2.4)$$

where e is the elementary charge and \hat{I} is the quantum operator describing the nuclear spin angular momentum. For the treatment in the first-order perturbation theory only the parts of \hat{H}_Q that commute¹ with \hat{H}_z have to be retained (secular approximation). It follows that the quadrupolar Hamiltonian is:

$$\hat{H}_Q = \frac{eQ}{2I(2I-1)\hbar} V_{zz,l} \frac{1}{2} (3\hat{I}_z \hat{I}_z - \hat{I}^2) \quad (2.5)$$

and $V_{zz,l}$ stands for the zz element of the $\bar{\bar{V}}$ matrix in the laboratory-frame (l).

In the case of deuterons, the above described interactions are the most important for the experiments discussed in this work but still, there are several ones that play a less significant role. Their corresponding terms are the dipole-dipole \hat{H}_{DD} and chemical shift \hat{H}_{CS} Hamiltonians. As the name suggests, \hat{H}_{DD} describes the interaction between the magnetic dipole moment of spins and \hat{H}_{CS} describes the fact that the same spin in different chemical environments experiences a slightly different local magnetic field due to the different electronic distributions.

2.1.2. Orientation dependence of \hat{H}_Q

The expression of the quadrupolar Hamiltonian can be further developed if $V_{zz,l}$ is expressed in its principal axis system (pas):

$$V_{zz,l} = V_{zz,pas} \frac{1}{2} [3 \cos^2(\theta) - 1 - \eta \sin^2(\theta) \cos(2\phi)], \quad (2.6)$$

where θ and ϕ are the polar coordinates of \vec{B}_0 in the pas ; η is called the asymmetry parameter and is given by:

$$\eta = \frac{V_{yy,pas} - V_{xx,pas}}{V_{zz,pas}}. \quad (2.7)$$

Then, Eq. 2.5 becomes:

$$\hat{H}_Q = \frac{eQeq}{2I(2I-1)\hbar} \frac{1}{2} [3 \cos^2(\theta) - 1 - \eta \sin^2(\theta) \cos(2\phi)] \frac{1}{2} [3\hat{I}_z^2 - I(I+1)] \quad (2.8)$$

¹The commutator of two operators is: $[\hat{A}, \hat{B}] = \hat{A}\hat{B} - \hat{B}\hat{A}$. It is said that two operators commute if $[\hat{A}, \hat{B}] = [\hat{B}, \hat{A}]$.

and $eq = V_{zz,pas}$ is the customary expression for the principal value of the field-gradient tensor. From the above equation the quadrupolar frequency is defined in a manner formal similar with Eq. 2.2:

$$\omega_Q = \delta \frac{1}{2} [3 \cos^2(\theta) - 1 - \eta \sin^2(\theta) \cos(2\phi)] \quad (2.9)$$

in which δ is the anisotropy parameter:

$$\delta = \frac{3}{4} \frac{eQeq}{\hbar}. \quad (2.10)$$

Some publications use the quadrupolar coupling constant QCC instead of δ :

$$QCC = \frac{4}{3} \delta. \quad (2.11)$$

Most of the compounds interesting for us contain $C-^2H$ bonds and this type of bond is relevant for the charge density distribution and the resulting field gradient tensor at the 2H nucleus site. The asymmetry η for such bonds is usually negligible due to the approximate axial symmetry of the charge density. This cylindrical symmetry also causes the z axis of the *pas* of the electric field gradient tensor to coincide with the $C-^2H$ bond direction. Because of all the above facts and because of the relative simple angular dependence of the quadrupolar frequency (cf. Eq. 2.9) 2H NMR allows to extract direct information about the order and dynamics of molecular segments.

2.2. Density operator

For an ensemble of spins in a magnetic field, instead of considering each spin, it is more convenient to describe the system in terms of the density operator $\hat{\rho}$. The physical observables $\langle \hat{A} \rangle$ are obtained from the density operator as:

$$\langle \hat{A} \rangle = Tr(\boldsymbol{\rho} \mathbf{A}), \quad (2.12)$$

where Tr stands for $Trace^2$ and $\boldsymbol{\rho}$ and \mathbf{A} are the matrix representation of the corresponding operators.

²In the matrix representation *Trace* is the sum of the diagonal elements of the matrix.

2.2.1. Thermal equilibrium

A system in thermal equilibrium, at temperature T and with the Hamiltonian \hat{H} has its density operator defined as an exponential operator:³

$$\hat{\rho}_{eq} = \frac{1}{Z} e^{-\hat{H}/kT} \quad Z = \text{Tr}(e^{-\hat{H}/kT}). \quad (2.13)$$

Here k is the Boltzmann constant. In the fields currently used the dominant contribution to the Hamiltonian is the Zeeman contribution and at temperatures higher than 1 K all terms of higher order in Eq. 2.13 are negligible compared with the linear term (high temperature approximation), therefore:

$$\hat{\rho}_{eq} \propto \left(\hat{1} + \frac{\hbar\gamma B_0}{kT} \hat{I}_z \right). \quad (2.14)$$

The operator $\hat{1}$ commutes with all operators and it is irrelevant in most cases.

2.2.2. Time evolution

The evolution in time of $\hat{\rho}$ is described by the von Neumann equation:

$$\frac{d}{dt}\hat{\rho} = -i[\hat{H}, \hat{\rho}], \quad (2.15)$$

in which $[\cdot, \cdot]$ denotes the commutator. For a time independent Hamiltonian ($\partial\hat{H}/\partial t = 0$) a formal solution of the above equation is:

$$\hat{\rho}(t) = e^{-i\hat{H}t} \hat{\rho}(0) e^{i\hat{H}t}. \quad (2.16)$$

The operator:

$$\hat{U}(t) = e^{-i\hat{H}t}, \quad (2.17)$$

encountered in the calculation of $\hat{\rho}(t)$ is called propagator.

In matrix representation the same equation holds:

$$\boldsymbol{\rho}(t) = e^{-i\mathbf{H}t} \boldsymbol{\rho}(0) e^{i\mathbf{H}t}. \quad (2.18)$$

A simple application of Eq. 2.18 is to consider a system with $I = 1/2$ under the influence of the Zeeman interaction $\mathbf{H} = \omega_0 \mathbf{I}_z$ and the initial magnetization having

³The definition of the exponential operator is:

$$e^{\hat{A}} = \sum_{n=0}^{\infty} \frac{\hat{A}^n}{n!}$$

only an x component $\boldsymbol{\rho}(0) = \mathbf{I}_x$. Then, using the Pauli spin matrixes (see Appendix A) the time evolution of the density matrix is:

$$\boldsymbol{\rho}(t) = \mathbf{I}_x \cos(\omega_0 t) + \mathbf{I}_y \sin(\omega_0 t) \quad (2.19)$$

that produces the precession of magnetization around the z axis, a result that can be obtained also in the semiclassical approach.

For a spin $I = 1$, under the action of a quadrupolar Hamiltonian \mathbf{H}_Q and the initial density $\boldsymbol{\rho}(0) = \mathbf{I}_x$, the time evolution of $\boldsymbol{\rho}$ is:

$$\boldsymbol{\rho}(t) = \mathbf{I}_x \cos(\omega_Q t) - i \frac{\mathbf{r}_1}{\omega_Q} \sin(\omega_Q t), \quad (2.20)$$

where the matrix \mathbf{r}_1 is written in Appendix A. Because $\text{Tr}(\mathbf{I}_\alpha \mathbf{r}_1) = 0$, ($\alpha = x, y, z$) the term \mathbf{r}_1 is not observable thus the observed signal oscillates with $\cos(\omega_Q t)$. It follows that the corresponding spectrum, after Fourier transform, consists of two lines at ω_Q and $-\omega_Q$ (relative to Larmor frequency when the Zeeman interaction is taken into account). As ω_Q depends on the angular position of a $C-^2H$ bond, the spectra have an important potential for studying orientation and dynamics of molecular segments.

2.2.3. Rotating frame

This section will introduce the concept of the rotating frame as most of the NMR results nowadays are expressed in this frame. For a magnetization $\hat{\rho}(0) = \hat{I}_\alpha$, ($\alpha = x, y, z$), in the case of the Zeeman interaction $\hat{H}_Z = \omega_0 \hat{I}_z$, the Eq. 2.16 becomes:

$$\hat{\rho}(t) = e^{-i\omega_0 t \hat{I}_z} \hat{I}_\alpha e^{i\omega_0 t \hat{I}_z} \quad (2.21)$$

that is a rotation of \hat{I}_α by an angle $\omega_0 t$ about the z axis. The effect of this precession can be eliminated by a transition to a frame that rotates with a frequency $\omega_r = \omega_0$. It is very common that the time evolution of the density operator is considered in such a rotating frame. The density operator in a frame rotating with ω_r is:

$$\hat{\rho}_r(t) = e^{i\omega_r t \hat{I}_z} \hat{\rho}(t) e^{-i\omega_r t \hat{I}_z} = e^{i(\omega_r - \omega_0) t \hat{I}_z} \hat{I}_\alpha e^{-i(\omega_r - \omega_0) t \hat{I}_z} \quad (2.22)$$

For a Hamiltonian $\hat{H} = \hat{H}_Z + \hat{H}_A$ the von Neumann equation in the frame rotating with ω_0 is:

$$\frac{d}{dt} \hat{\rho}_r = -i[\hat{H}_{A,r}, \hat{\rho}] \quad (2.23)$$

and the Zeeman Hamiltonian \hat{H}_Z does not appear anymore, its direct effect being transformed away. Still, \hat{H}_Z plays a role in the transformation of the other Hamiltonians:

$$\hat{H}_{A,r}(t) = e^{i\omega_0 t \hat{I}_z} \hat{H}_A(t) e^{-i\omega_0 t \hat{I}_z} = e^{i\hat{H}_Z t} \hat{H}_A(t) e^{-i\hat{H}_Z t} \quad (2.24)$$

As the Zeeman interaction is not an interesting one from the point of view of acquiring information about molecular orientation or dynamics, in the following we will mainly use the rotating frame representation ($\omega_r = \omega_0$) and when this is the case we will drop the subscript r .

2.2.4. The effect of radio frequency pulses

Radio-frequency (RF) fields are very important for modern NMR and the effect of RF pulses on the spin density operator is discussed below. The RF components relevant for NMR are those perpendicular to the \vec{B}_0 field (in the laboratory frame (1)):

$$B_{1,l}(t) = 2B_1 \cos(\omega_{RF}t + \phi_{RF}). \quad (2.25)$$

$B_{1,l}(t)$ can be decomposed in two rotating fields with the angular frequencies $+\omega_{RF}$ and $-\omega_{RF}$. Choosing $\omega_{RF} = \omega_0$, the rotating field with $-\omega_{RF}$ can be neglected for most practical purposes. In order to make the \vec{B}_1 field appear static is customary to transform to the rotating frame $\omega_r = \omega_{RF} = \omega_0$. The Hamiltonian describing the effect of the \vec{B}_1 field in the rotating frame for an x pulse is:

$$\hat{H}_{pulse,x} = -\gamma B_1 \hat{I}_x. \quad (2.26)$$

An x pulse rotates the magnetization by the angle $-\gamma B_1 t_{pulse}$ with respect to the x axis. The Hamiltonian for an $-x$ pulse is similar with the one in Eq. 2.26 with the sole difference that \hat{I}_x is replaced by $-\hat{I}_x$ (the similar expressions hold for y and $-y$ pulses). The effect of $\hat{H}_{pulse,x}$ on the density operator in the rotating frame is described by a propagator:

$$\hat{P}_x(t_{pulse}) = e^{-i\hat{H}_{pulse,x}t_{pulse}} = e^{i\gamma B_1 \hat{I}_x t_{pulse}}. \quad (2.27)$$

Knowing the propagator for pulses and the Hamiltonian of a spin system, one can calculate the effect of any pulse sequence on the system. As the product $\gamma B_1 t_{pulse}$ gives an angle and in most experiments the time t_{pulse} when the RF field B_1 is applied it is short compared with all other experimental times it is usual to replace $\gamma B_1 t_{pulse}$ by an angle value (e.g. $\frac{\pi}{2}$, π etc.). In NMR jargon a $(\frac{\pi}{2})_x$ pulse would mean that $\gamma B_1 t_{pulse} = \frac{\pi}{2}$ and the corresponding propagator is $\hat{P}_x(t_{pulse}) = e^{i\frac{\pi}{2}\hat{I}_x}$.

2.3. Main pulse sequences and related measured functions

2.3.1. Solid echo

In ^2H NMR the solid echo sequence (or 1D experiment) is widely employed to circumvent the dead time of the receiver. It consists of two $\pi/2$ pulses that have a 90° phase shift (for example an x pulse and a y pulse) separated in time by a period t_p ($(\frac{\pi}{2})_x - t_p - (\frac{\pi}{2})_y$). At a time $2t_p$ after the first pulse we have the propagator (in the rotating frame):

$$\hat{U}(2t_p) = \underbrace{e^{-i\omega_Q(3\hat{I}_z\hat{I}_z - \hat{I}\cdot\hat{I})t_p}}_{\text{free evolution}} \underbrace{e^{i\frac{\pi}{2}\hat{I}_y}}_{(\frac{\pi}{2})_y \text{ pulse}} \underbrace{e^{-i\omega_Q(3\hat{I}_z\hat{I}_z - \hat{I}\cdot\hat{I})t_p}}_{\text{free evolution}}. \quad (2.28)$$

The density operator in the rotating frame is:

$$\hat{\rho}(2t_p) = \hat{U}(2t_p)\hat{\rho}(0)\hat{U}^{-1}(2t_p). \quad (2.29)$$

For $\hat{\rho}(0) = \hat{I}_y$ created by an x pulse from z magnetization one finds that $\hat{\rho}(2t_p) = \hat{I}_y = \hat{\rho}(0)$, thus the same magnetization as after the first pulse appears at a time $2t_p$. Repeating the calculation for the second pulse being a $-y$ pulse, the result is identical therefore the solid echo is independent of the sign of the second pulse. This proves important in practice for constructing the phase cycling of an experiment.

If changes of ω_Q take place during the solid echo evolution, the refocusing of a spin system is incomplete and, after the Fourier transformation, the line shape of the spectrum contains information about the dynamics of molecular segments.

Solid echo spectrum

In an isotropic, rigid sample (in NMR jargon usually referred to as a powder) the shape of the spectrum can be easily calculated when $\eta = 0$: the spectral intensity $S(\omega_Q)$ and the angular distribution $\mathcal{P}(\theta)$ are related by the equation

$$S[\omega_Q(\theta)] |d\omega_Q| = \mathcal{P}(\theta) |d\theta|. \quad (2.30)$$

(For simplicity in the following we will write ω instead of ω_Q .) One can write:

$$S[\omega(\theta)] = \frac{\mathcal{P}(\theta)}{|\frac{d\omega}{d\theta}|} \quad (2.31)$$

and using Eq. 2.9, with the knowledge that for powders $\mathcal{P}(\theta)$ is determined solely by the size of surface elements ($\mathcal{P}(\theta) = \sin(\theta)$) the spectral intensity is:

$$S(\omega) = \begin{cases} \frac{1}{\sqrt{6\delta}} \frac{1}{\sqrt{\frac{1}{2}\delta + \omega}} & -\delta/2 < \omega \leq \delta \\ 0 & \text{in rest.} \end{cases} \quad (2.32)$$

A ^2H spin gives a signal at $+\omega$ and $-\omega$ (see page 13) therefore the complete powder spectrum is a sum of the upper equation with its symmetric part with respect to $\omega = 0$. This pattern was calculated for the first time by Pake thus it is often referred to as a Pake spectrum [94]:

$$S_{Pake}(\omega) = \begin{cases} \frac{1}{\sqrt{6\delta}} \frac{1}{\sqrt{\frac{1}{2}\delta - \omega}} & -\delta \leq \omega \leq -\delta/2 \\ \frac{1}{\sqrt{6\delta}} \left(\frac{1}{\sqrt{\frac{1}{2}\delta - \omega}} + \frac{1}{\sqrt{\frac{1}{2}\delta + \omega}} \right) & -\delta/2 < \omega < \delta/2 \\ \frac{1}{\sqrt{6\delta}} \frac{1}{\sqrt{\frac{1}{2}\delta + \omega}} & \delta/2 \leq \omega \leq \delta \\ 0 & \text{in rest.} \end{cases} \quad (2.33)$$

It is seen that the theoretical Pake spectrum has two singularities at $\omega = \pm\delta/2$; in real life due to line-broadening effects they transform into a maximum and the spectrum looks like the one in Fig. 2.1 (a). Note that the ‘distance’ between the two maxima is in a good approximation δ . Because of that one can call in a somewhat less academic manner δ as the spectral width. (In the following chapters, where experimental results are presented, δ is expressed in units of (kHz) instead of (rad./s).)

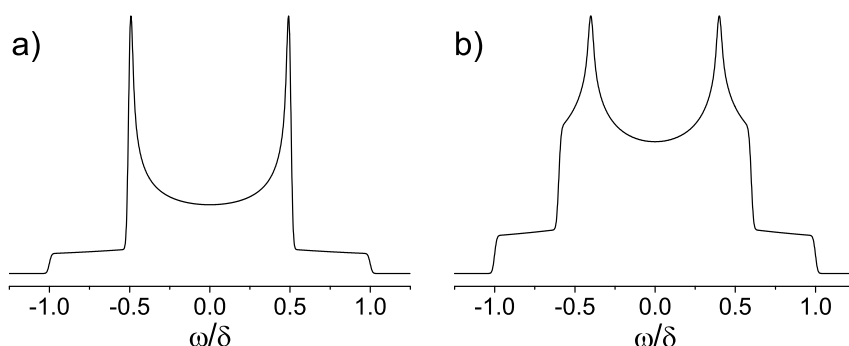


Figure 2.1. Numerically calculated powder spectra: a) Pake and b) spectrum with asymmetry parameter non-zero $\eta = 0.2$.

The calculations in the case of the powder spectrum for $\eta \neq 0$ are more involved implying evaluations of elliptical-integral functions (for example, see pp. 29-31 in [112] and references therein). Nevertheless, the spectra can be easily calculated numerically through Eq. 2.9, and such a spectrum for $\eta = 0.2$ it is shown in Fig. 2.1 (b). An increase in η will result in a translation of the two maxima in the direction $\omega = 0$ so that for $\eta = 1$ they coincide and lie at $\omega = 0$. The edges seen at $|\omega| > 0.5$ will translate towards $|\omega| = 1$ with increasing η , reaching that limit for $\eta = 1$. For the compounds investigated here $\eta = 0$ or $\eta < 0.1$, and the spectra look almost like a Pake spectrum so we will consider in the following only the case $\eta = 0$.

When the molecules experience motion on the time scale $\tau = 1/\delta$ or faster the spectral shape is changed; in the extreme case of an isotropic fast motion ($\tau \ll 1/\delta$) the spectrum is a narrow central line. There are two special cases of fast motion models that will prove useful in discussing the β -process. The first one is: a motion of the $C-^2\text{H}$ bond around a C_n axis ($n > 2$) with an angle χ (for a sketch, see Fig. 6.1 or

6.8); in this case Eq. 2.9 has to be rewritten as:

$$\omega = \bar{\delta} \frac{1}{2} [3 \cos^2(\alpha) - 1], \quad (2.34)$$

where α is the angle between the axis of rotation and the direction of the external magnetic field and

$$\bar{\delta} = \delta \frac{1}{2} [3 \cos^2(\chi) - 1]. \quad (2.35)$$

The second interesting model is the one comprising a random motion of the $C-H$ bond within a cone of semiangle χ (see Fig. 6.13). Eq. 2.34 still holds, with α now being the angle between the cone axis and the direction of the external magnetic field but $\bar{\delta}$ becomes [15]:

$$\bar{\delta} = \delta \frac{1}{2} \cos(\chi) [1 + \cos(\chi)]. \quad (2.36)$$

In the previous models, when the C_n axis or the cone axis is rigid, the obtained spectra have the Pake shape with the only difference that their spectral width is decreased according to the value of the averaged anisotropy parameter $\bar{\delta}$. Note that in order to obtain the same $\bar{\delta}$ in both cases one has to chose a higher angle χ for the second model.

C and R - two parameters that quantify the spectral shape

For the quantitative analysis of the temperature dependence of the solid echo spectra we define two phenomenological observables: the apparent spectral width C and the relative spectral intensity at zero frequency R . In real life it happens that the measured spectra are somewhat asymmetric with respect to the axis that passes trough $\nu = 0$. Therefore the averaged height $H = (h_1 + h_2)/2$ has to be considered for our definitions (cf. Fig. 2.2). C is defined as the spectral width measured at 80% of the averaged height H (cf. Fig. 2.2). It is obvious that $C \propto \delta$ or, in the case of molecular motion, $C \propto \bar{\delta}$, the exact identity being hindered by experimental artifacts and line broadening effects. Therefore, by measuring C in a wide temperature range, so that the slow motion limit $C_{slow} \propto \delta$ and the fast motion limit $C_{fast} \propto \bar{\delta}$ are reached, one can estimate, trough Eq. 2.35 or Eq. 2.36 the angular amplitude of the molecular motion. Using the apparent spectral width C in order to estimate the temperature dependence of $\bar{\delta}$ has advantages over doing a fit of the spectrum. That is because in order to obtain a good fit it is necessary to use several fit parameters and consequently the relative error in determining $\bar{\delta}$ becomes higher than in the case of measuring C . This is an important fact since, as it will be seen in the chapters presenting the experimental results, the temperature dependence of C is very subtle, with changes on the order of 1%.

The relative spectral intensity at zero frequency R is defined as:

$$R = \frac{S(0)}{H}, \quad (2.37)$$

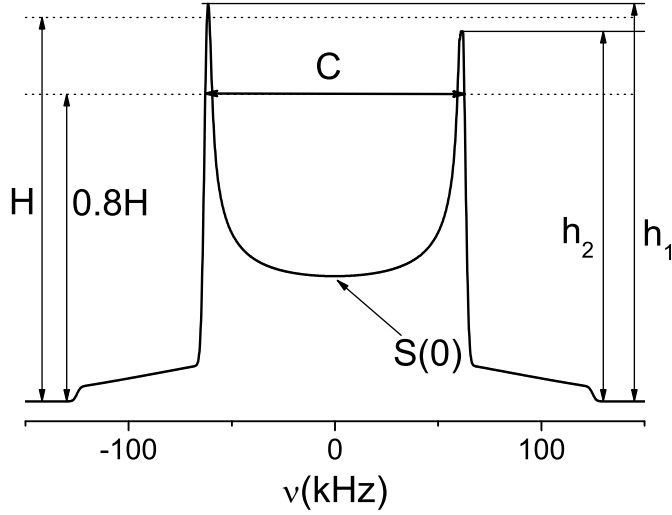


Figure 2.2. Numerically calculated powder spectrum; different from the one in Fig. 2.1 (a) we simulated a distortion regarding the maximum values and a pulse correction was also taken into account (cf. Eq. C.2, $\Delta_p = 2.5 \mu\text{s}$). A value $\delta = 125 \text{ kHz}$ was employed, as typical for $\text{C}-^2\text{H}$ bonds.

$S(0)$ being the spectral intensity in the ‘centrum’ of the spectrum. Measuring R proves valuable in quantifying the differences between spectra measured with different inter-pulse delays t_p at a certain temperature. This manner of analyzing the t_p evolution of the solid echo spectral shape is relatively new, being nowhere else reported to our knowledge (except in the work from our group [71, 81, 115]).

2.3.2. Stimulated echo

Two three-pulse sequences are of great importance for ^2H NMR: the Zeeman and the spin alignment pulse sequences.

The Zeeman pulse sequence contains three pulses as follows: $(\frac{\pi}{2})_x - t_1 - (\frac{\pi}{2})_{-x} - t_m - (\frac{\pi}{2})_x - t_2$ in which t_1 is called evolution time, t_m mixing time and t_2 detection time. It can be proved that the signal obtained after the detection time (in the rotating frame) is proportional to:

$$\cos(\omega_1 t_1) \cos(\omega_2 t_2), \quad (2.38)$$

where ω_1 is the frequency associated with a spin at the end of the time period t_1 and correspondingly for ω_2 and t_2 . In the most general case, with arbitrary pulses $(\vartheta_1)_x$, $(\vartheta_2)_{-x}$, $(\vartheta_3)_x$ the detected signal is proportional to:

$$\sin(\vartheta_1) \sin(\vartheta_2) \sin(\vartheta_3) \cos(\omega_1 t_1) \cos(\omega_2 t_2). \quad (2.39)$$

A similar signal with the cosine functions replaced by sine can be detected using the spin alignment pulse sequence in which the two first pulses have to be 90° out of

phase. In the general case, one obtains a signal proportional with:

$$\frac{3}{4} \sin(\vartheta_1) \sin(2\vartheta_2) \sin(2\vartheta_3) \sin(\omega_1 t_1) \sin(\omega_2 t_2). \quad (2.40)$$

In practice, to overcome dead time problems, a fourth $\pi/2$ pulse is used at the end of the three pulse sequence, after a time period Δ . This pulse has to be 90° out of phase with the one before it. The fourth pulse assures that the desired signal is refocused at a time longer than Δ (for example, for the Zeeman experiment: $(\frac{\pi}{2})_x - t_1 - (\frac{\pi}{2})_{-x} - t_m - (\frac{\pi}{2})_x - \Delta - (\frac{\pi}{2})_y - \Delta - t_2$).

In the case that the molecules or, better said, the segments of molecules are not changing their orientation during the experiment then $\omega_1 = \omega_2$ and the obtained information using the stimulated echo experiments is not richer than in a 1D experiment. But, when molecular motion is present it follows that $\omega_1 \neq \omega_2$ and the 2D experiments prove a precious tool for investigating molecular dynamics.

The stimulated echo techniques are widely used in ^2H NMR and specific applications and details can be found, for example, in [28, 29, 49, 53, 57, 69, 110, 139, 140].

Sin-sin and cos-cos correlation functions

As said above, for the spin alignment experiment, the measured signal is proportional to the product of a two sine functions so that one can define the normalized sin-sin correlation function:

$$\mathcal{F}^{\text{sin}}(t_1, t_m, t_2) = \frac{\langle \sin(\omega_1 t_1) \sin(\omega_2 t_2) \rangle}{\langle \sin(\omega_1 t_1) \sin(\omega_1 t_1) \rangle}, \quad (2.41)$$

where the brackets $\langle \rangle$ stand for ensemble average. For the time domain analysis of such experiments one usually is interested in the amplitude of the measured echo which is obtained at a detection time equal with the evolution time $t_2 = t_1$. Therefore, for a fixed t_1 , the mixing time is changed in a systematic way that the decay curve $\mathcal{F}^{\text{sin}}(t_1, t_m, t_2 = t_1) = \mathcal{F}^{\text{sin}}(t_1, t_m)$ is obtained. In real life a two-step decay function is measured which can be described by:

$$F^{\text{sin}}(t_1, t_m) = \{ [1 - F_\infty^{\text{sin}}(t_1)] \phi(t_1, t_m) + F_\infty^{\text{sin}}(t_1) \} e^{-\frac{t_m}{T_{1Q}}} \quad (2.42)$$

where the first one is due to the sin-sin correlation decay with $\phi(t_1, t_m)$ carrying the correlation loss from the molecular motion, and $\exp(-\frac{t_m}{T_{1Q}})$ is due to the decay of the spin alignment state [118]. (In the most simple case $1/T_{1Q} \propto J(\omega_0)$.) Usually $\phi(t_1, t_m)$ is described by a Kohlrausch-Wiliams-Watts (KWW) function which came out to be appropriate for disordered systems [28],

$$\phi(t_1, t_m) = \exp \left\{ - \left[\frac{t_m}{\tau(t_1)} \right]^{\beta_{\text{KWW}}(t_1)} \right\} \quad (2.43)$$

with the correlation time τ_{KWW} given by:

$$\tau_{KWW}(t_1) = \frac{\tau(t_1)}{\beta_{KWW}(t_1)} \Gamma\left[\frac{1}{\beta_{KWW}(t_1)}\right], \quad (2.44)$$

where Γ is the gamma function.

The final state of the sin-sin correlation function $F_\infty^{\sin}(t_1)$ gives information about the geometry of the molecular motion [49]. In special cases, when distinct positions are allowed for the $C-^2H$ bond (n -site jump model) and if the jump model has cubic point symmetry [49]:

$$F_\infty^{\sin}(t_1 \rightarrow 0) = 0. \quad (2.45)$$

Note that the above equation holds also for isotropic diffusion ($n \rightarrow \infty$). Considering the limit $t_1 \rightarrow \infty$ one obtains [49]:

$$F_\infty^{\sin}(t_1 \rightarrow \infty) = \frac{1}{n}, \quad (2.46)$$

and in the case when the point group of the model contains the inversion operation the above equation becomes [49]:

$$F_\infty^{\sin}(t_1 \rightarrow \infty) = \frac{2}{n}. \quad (2.47)$$

By setting t_1 to a small value, one measures the autocorrelation function of the second Legendre polynomial $P_2\{\cos[\theta(t)]\}$ (cf. Eqs. 2.56 and 2.41):

$$F^{\sin}(t_1 \rightarrow 0, t_m) = f_2, \quad (2.48)$$

(for the definition of f_2 , see Eq. 2.56)

Using the Zeeman experiment, one can measure in a similar manner the cos-cos correlation functions (cf. Eq. 2.41 where the sines are replaced by cosines) and the obtained decay is described by:

$$F^{\cos}(t_1, t_m) = \Phi^{\cos}(t_1, t_m)\psi(t_m), \quad (2.49)$$

where $\psi(t_m)$ is the normalized spin-lattice relaxation function (cf. Eq. 2.63). $\Phi^{\cos}(t_1, t_m)$ has different equations determined by the temperature range where the Zeeman experiment is employed. For example, at temperatures above T_g , when the α -process is investigated it might be expressed in terms of a KWW function, as the first decay in Eq. 2.41 ([57]). At temperatures below T_g , when the β -process is investigated $\Phi^{\cos}(t_1, t_m)$ shows itself a two step decay, the long one being a result of spin diffusion [129, 134, 135]. Hence, the following equation is used:

$$\Phi^{\cos}(t_1, t_m) = \{[1 - S^{\cos}(t_1)] \phi_{fast}(t_1, t_m) + S^{\cos}(t_1)\} \phi_{slow}(t_1, t_m), \quad (2.50)$$

where $\phi_{fast}(t_1, t_m)$ and $\phi_{slow}(t_1, t_m)$ are two KWW functions.

2D spectrum

The stimulated echo signal from both spin alignment and Zeeman experiment can be formulated as [120]:

$$\mathcal{F}(t_1, t_m, t_2) = \langle e^{-i\omega_1 t_1} e^{i\omega_2 t_2} \rangle, \quad (2.51)$$

where $\langle \rangle$ stands for ensemble average. It is seen that both the sine and cosine contributions are included in the complex exponential function.

The average in Eq. 2.51 above can be rewritten in terms of integrals as:

$$\mathcal{F}(t_1, t_m, t_2) = \int_{-\infty}^{+\infty} \int_{-\infty}^{+\infty} \mathcal{W}(\omega_1, \omega_2, t_m) e^{-i\omega_1 t_1} e^{i\omega_2 t_2} d\omega_1 d\omega_2, \quad (2.52)$$

where

$$\mathcal{W}(\omega_1, \omega_2, t_m) = \mathcal{W}(\omega_1) \mathcal{W}(\omega_1 | \omega_2, t_m) \quad (2.53)$$

is the joint probability density related with the probability density $\mathcal{W}(\omega_1)$ to find a spin with the frequency ω_1 , and $\mathcal{W}(\omega_1 | \omega_2, t_m)$ that is the conditional probability density that the frequency is ω_2 at a time t_m if it was ω_1 at a time $t = 0$ [120].

A two dimensional (2D) spectrum is obtained if $\mathcal{F}(t_1, t_m, t_2)$ is Fourier transformed with respect to t_1 and t_2 . Because the frequencies are related to the orientations of the $C-^2H$ bonds, the 2D spectra are a direct visualization of the motional process of the molecules and their shape can be easily calculated in the case of simple motional models [112].

When $\omega_1 = \omega_2$, $\mathcal{W}(\omega_1 | \omega_2, t_m)$ is a delta function and the 2D spectrum has only a diagonal component [87, 131]. In the case of a powder sample $\mathcal{W}(\omega_1)$ is described by a Pake spectrum $\mathcal{W}_{Pake}(\omega_1)$ and the 2D spectrum can be written as [87, 131]:

$$S_{2D}(\omega_1, \omega_2) = S_{2D}^{dia}(\omega_1, \omega_2) \propto \mathcal{W}_{Pake}(\omega_1) \delta(\omega_2 - \omega_1). \quad (2.54)$$

For an isotropic molecular motion with a time constant $1/\delta \ll \tau \ll t_m$ the frequency ω_2 is statistically independent of ω_1 and one obtains a spectrum [87, 131]:

$$S_{2D}(\omega_1, \omega_2) = S_{2D}^{iso}(\omega_1, \omega_2) \propto \mathcal{W}_{Pake}(\omega_1) \mathcal{W}_{Pake}(\omega_2). \quad (2.55)$$

2.4. Relaxation phenomena

In real systems there are weak interactions between spins that have to be taken into account. They all can be summarized in a stochastically fluctuating local field at the site of a spin and they are responsible for the relaxation of different components of the magnetization.

The phenomenon through which the magnetization parallel to the external magnetic field attains its equilibrium value is called spin-lattice relaxation. Correspondingly, the

phenomenon through which the magnetization perpendicular to the external magnetic field attains its equilibrium value is called spin-spin relaxation. The spin-lattice relaxation implies an exchange of energy between the spin system and the lattice while the spin-spin relaxation consists only of a loss of correlation between different spins without energy transfer to the lattice.

In order to describe the effect of the molecular local fields one has to define a normalized rotational autocorrelation function f_2 :

$$f_2(t) = \frac{\langle P_2\{\cos[\theta(0)]\}P_2\{\cos[\theta(t)]\} \rangle}{\langle P_2\{\cos[\theta(0)]\}P_2\{\cos[\theta(0)]\} \rangle} = \frac{\langle \{3\cos^2[\theta(0)] - 1\}\{3\cos^2[\theta(t)] - 1\} \rangle}{\langle \{3\cos^2[\theta(0)] - 1\}^2 \rangle}, \quad (2.56)$$

where P_2 is the second order Legendre polynomial and $\cos(\theta)$ is the direction of a fixed molecular vector with respect to the laboratory frame ($\langle \rangle$ stands for ensemble average). The corresponding spectral density is:

$$J_2(\omega) = 2\text{Re}\left[\int_0^\infty f_2(t)e^{i\omega t}dt\right], \quad (2.57)$$

where Re stands for the real part.⁴ Then, the spin-lattice and spin-spin relaxation rates for an isotropic molecular motion can be derived as [23, 28, 38, 123]:

$$\frac{1}{T_1} = \frac{3}{8} \left(\frac{eQeq}{\hbar} \right)^2 [J_2(\omega_0) + 4J_2(2\omega_0)] = \frac{2}{3} \delta^2 [J_2(\omega_0) + 4J_2(2\omega_0)], \quad (2.58)$$

$$\frac{1}{T_2} = \frac{1}{2} \delta^2 [3J_2(0) + 5J_2(\omega_0) + 2J_2(2\omega_0)]. \quad (2.59)$$

In the most simple case when $f_2(t) = e^{-t/\tau}$, the spectral density is:

$$J_2(\omega) = \frac{\tau}{1 + (\omega\tau)^2} \quad (2.60)$$

and there are two extreme limits with respect to ω_0 :

- slow motion $\omega_0\tau \gg 1$:

$$\frac{1}{T_1} \propto \frac{1}{\tau}, \quad \frac{1}{T_2} \propto \tau \quad (2.61)$$

⁴Note: in dielectric spectroscopy (DS) the dipole autocorrelation function $f_1(t)$ is measured provided that cross-correlation effects can be neglected [32]. For the imaginary part of the permittivity $\varepsilon''(\omega)$ the relation:

$$\frac{\varepsilon''(\omega)}{\Delta\varepsilon} = \omega J_1(\omega),$$

holds, where $\Delta\varepsilon$ is the relaxation strength. Because of these relations DS results can be compared with ^2H NMR. J_1 is defined in a similar manner to J_2 using Eq. 2.56 and Eq. 2.57 with the difference that P_2 is replaced by P_1 , the first order Legendre polynomial.

- fast motion $\omega_0\tau \ll 1$:

$$\frac{1}{T_1} = \frac{1}{T_2} \propto \tau. \quad (2.62)$$

Although Eqs. 2.58 and 2.59 hold for a normal liquid they are not longer valid for an anisotropic motion of the molecules [123]. In addition, in a deeply supercooled liquid or a glassy system, there are subensembles with different relaxation rates so that one has to consider a mean relaxation rate $\langle 1/T_1 \rangle$. While $\langle 1/T_1 \rangle \propto [J_2(\omega_0) + 4J_2(2\omega_0)]$ still holds it is a complicated task to correctly estimate $J_2(\omega)$ and reproduce the measured mean relaxation time constants and their temperature dependence (see, for example, [23]). For type B glass formers at temperatures close to and below T_g the spectral density is strongly influenced by the β -process and how this is reflected in T_1 it is still a matter of research (see, for example, [59, 60, 82]).

Notes on spin-lattice relaxation measurements

In order to estimate the spin-lattice relaxation time one has to measure the spin-lattice relaxation function:

$$\psi(t) = \frac{M_0 - M_z(t)}{M_0}, \quad (2.63)$$

where M_z is the magnetization in the z direction and M_0 its equilibrium value. At temperatures below T_g this function is not exponential and it is parameterized by a KWW function, and a mean spin-lattice relaxation time $\langle T_1 \rangle$ can be calculated via Eq. 2.44. Because in glassy systems spin diffusion may influence the long time shape of the spin-lattice relaxation function [60] some authors prefer to discuss the average rate $\langle 1/T_1 \rangle$ that is obtained at short times:

$$\left\langle \frac{1}{T_1} \right\rangle = -\lim_{t \rightarrow 0} \left[\frac{d}{dt} \psi(t) \right]. \quad (2.64)$$

The rate can be estimated by a linear fit of the initial part of the spin-lattice relaxation function and, in the glassy state, $\langle 1/T_1 \rangle \neq 1/\langle T_1 \rangle$ (see, for example, [59]).

Since the magnetization of a single deuteron decays exponentially in time independent of the form of the molecular correlation functions if the dipolar interactions among deuterons are neglected, one can write in the most general form [58]:

$$\psi(t) = \int_0^\infty g(T_1) e^{-t/T_1} dt, \quad (2.65)$$

where $g(T_1)$ is the distribution function of the spin-lattice relaxation times. We made use of this approach in Chapter 4 to compare the distributions $g(T_1)$ in different systems.

3. Cyanoadamantane - Study of the Supercooled Plastically Crystalline Phase

3.1. Introduction

The nature of the glass transition is still a matter of debate thus numerous experiments on glass forming systems are performed. Usually one uses liquids made of molecules structurally as simple as possible in order to have the minimum degrees of freedom in the studied systems. Still, there are even simpler systems that present a glass transition phenomenon, the so called plastic crystals. The molecules of these substances have their center of mass located on a well defined lattice (therefore the name crystals) but they are orientationally disordered. Certain plastic crystals exhibit, in addition to the calorimetric glass transition, features that resemble those observed in structural glass formers: the main relaxation is nonexponential and its time constant shows non-Arrhenius temperature dependence [33, 126]. Secondary relaxation processes as well as tunneling states have been observed, too [31, 100, 117].

While there are NMR works on plastic crystals [28] those applying multidimensional NMR techniques are still rare [144] and the latter in particular allow to unravel details of the molecular process involved in the glass transition.

Because it was studied by several other techniques [7, 8, 33, 48, 141] cyanoadamantane (CNADM) was chosen for our experiments in the hope that the NMR investigation will help to further understand the glass transition phenomenon in this plastic crystal. Several other reasons make CNADM an appealing candidate for research: the molecule is rigid with no internal degrees of freedom and can be easily deuterated. As it will be seen in the following the motion around its C_3 axis is an ‘intrinsic’ probe for the molecular disorder in the glassy state. Also, CNADM presents in the dielectric spectrum an α -peak (cf. Fig. 3.3) without an excess wing; consequently measuring it in tandem with a plastic crystal that displays an excess wing would enable one to pinpoint the properties of the molecular motion behind the excess wing.

In one of the previous studies of our group Roggatz, in his PhD work, used ^2H NMR spectroscopy to investigate CNADM in the glassy and orientationally ordered crystalline phase, showing that in the former state the molecular rotation around the C_3 axis displays a broad distribution of correlation times, signature of diverse environments

[103]. Still he did not succeed in preparing the supercooled plastically cristalline phase although in the literature there were indications that the phase can be obtained [8, 33, 96]. Therefore the scope of this work was to prepare and study the supercooled phase.

3.1.1. Molecular shape and possible phases

In the following part of the introduction several properties of CNADM will be presented. The chemical formula of CNADM (also known as 1-cyanoadamantane or adamantane carbonitrile or 1-cyano(3,3,1,1)decane [7]) is $C_{10}H_{15}CN$. Its molecule is globular in shape, presenting a C_3 symmetry axis (see Fig.3.1).

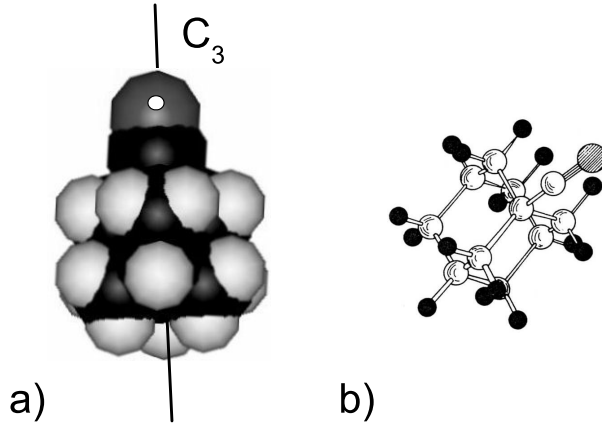
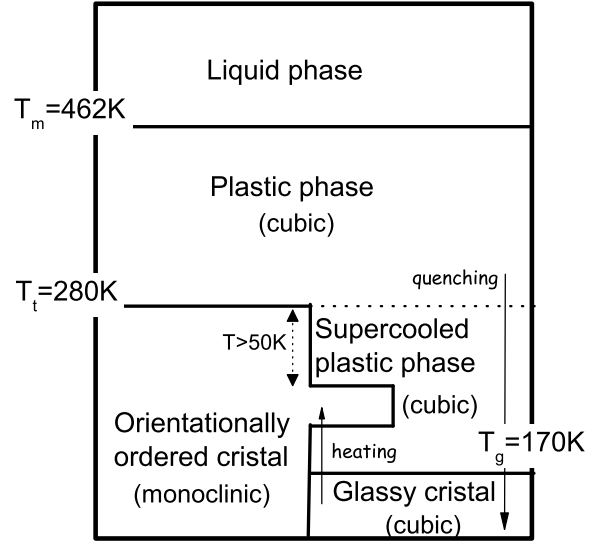


Figure 3.1. The CNADM molecule: a) Spheres representation, the grey spheres are hydrogen atoms, the black ones carbon atoms and the one with a white circle is the nitrogen atom; the C_3 axis is also sketched. b) Balls and sticks representation, the black balls are hydrogens, the white ones are carbons and the grey one is the nitrogen atom (from Amoureux et al. [8]).

In Fig. 3.2 we present an illustration of possible phases and phase transitions. The melting temperature is $T_m = 462\text{ K}$ [8], below the sample is in the plastically cristalline phase and the centers of mass of molecules are placed on a cubic lattice (Fm3m [8]). As said before, this phase displays translational but no orientational order. The transition temperature T_t from the orientationally disordered crystalline state (plastically crystalline, PC) to the orientationally ordered crystalline state (OOC) is around $T_t = 280\text{ K}$ (slightly different values are reported in Ref. [48, 127, 141]); note that at T_t there is a solid-solid phase transition [8]. The transition temperature may depend on thermal history and if the sample is slowly cooled the transition may be avoided, obtaining a supercooled plastically cristalline phase (supercooled PC), that is metastable. Previous experiments showed that there is a high tendency for the supercooled PC phase to transform into the OOC phase at temperatures lower than T_t by roughly 50 K . Nevertheless, when the PC phase is quenched down to low temperatures from a temperature above T_t the transition from the supercooled PC phase to the OOC phase may be avoided and a calorimetric glass transition is observed at $T_g = 170\text{ K}$ [8].

Figure 3.2. Sketch of the phases in CNADM (after Amoureux et al. [8]).



3.1.2. Dielectric loss spectra and characteristic time constants

Fig. 3.3 (a) shows the dielectric spectra of CNADM for several temperatures. As no secondary relaxation peak is observed one may conclude that CNADM is a type A glass former [74]. The observed α -peak is shifting towards lower frequencies with lowering the temperature, being well described by a Cole-Davidson (CD) function with a $\beta_{CD} = 0.80 - 0.85$ [33]. The characteristic time constants associated with the reorientation motion of the C_3 axis are displayed in Fig. 3.3 (b) and one observes that they show deviations from an Arrhenius temperature dependence.

3.1.3. Uniaxial rotation of the molecule and the solid echo spectra in the glassy phase

Before presenting the results of our investigation, we show a finding from the PhD thesis of Roggatz [103] that helps to understand the shape of the spectrum at temperatures close to T_g . In the supercooled PC phase and in the glassy state at temperatures not far below T_g the molecule is rotating around its C_3 axis with a time constant which is fast with respect to the NMR solid echo time scale, thus one expects an averaged spectral width (cf. Eq. 2.35) [7, 8, 16, 103]. The effect of the uniaxial motion on the solid echo spectrum can be seen in Fig. 3.4 for a measurement performed at 159.6 K (that is roughly 10 K below T_g): the spectrum looks as it is composed of two Pake spectra with different spectral widths, fact revealed by the presence of two pairs of ‘singularities’ (one around $\pm 20\text{ kHz}$ and one around $\pm 60\text{ kHz}$), each belonging to a certain Pake spectrum. This spectral shape can be well understood if one correlates the uniaxial molecular

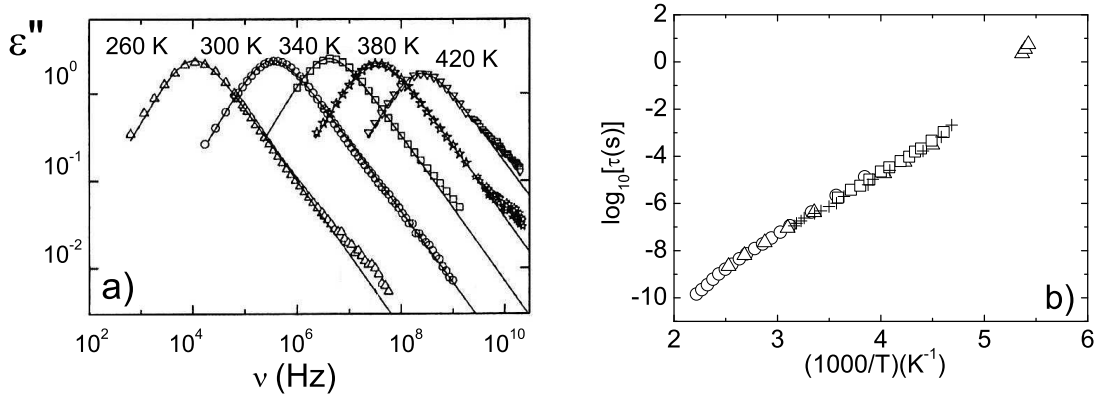
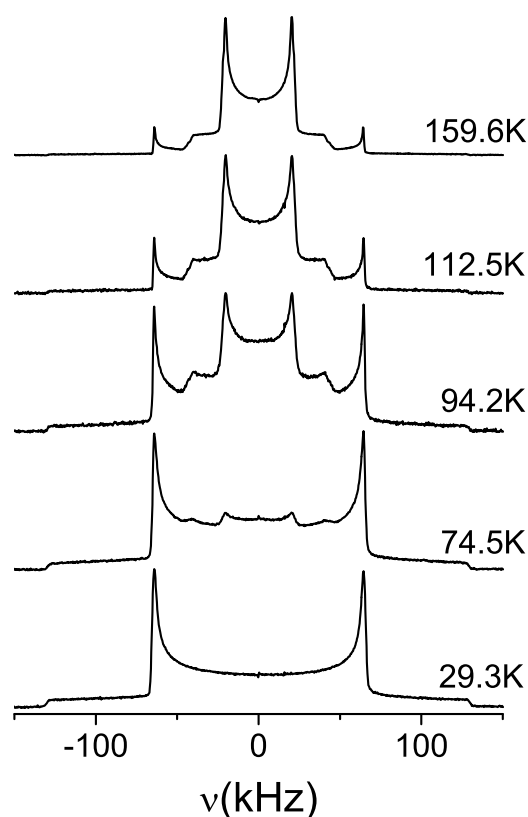


Figure 3.3. a) Imaginary part of the complex permittivity ϵ'' for CNADM. The lines are fits with the Cole-Davidson function (from Brand et al. [33]). b) Correlation times for the motion of the C_3 axis; circles: Brand et al. [33], squares: Pathmanathan and Johari [96], plus signs: Tyagi and Murthy [127], triangles: Amoureux et al. [9].

motion with the structure of the CNADM molecule. The central spectrum presents an averaged spectral width as a consequence of the fast rotation of the corresponding $C-^2H$ bonds around the C_3 axis. Despite the fast rotation of the molecule, the outer Pake spectrum displays no averaged spectral width as a consequence of the fact that the corresponding $C-^2H$ bonds are parallel with the C_3 axis (cf. Eq. 2.35, $\chi_1 = 180^\circ$ and therefore $\bar{\delta} = \delta$). The intensities of the spectra are directly related to the number of bonds that are responsible for them, respectively 3 $C-^2H$ bonds are the source of the wide, non-averaged Pake spectrum and 12 bonds correspond to the central spectrum. Actually, the central part is given by two Pake spectra with almost identical averaged widths because the corresponding $C-^2H$ bonds are oriented at the angles $\chi_2 = 71.4^\circ$ (6 bonds) and $\chi_3 = 110.1^\circ$ (6 bonds) with respect to the C_3 axis (cf. Eq. 2.35). (Note: The small difference between χ_2 and $180^\circ - \chi_3$ is due to the slight deformation of the adamantane skeleton by the cyano group. In adamantane one finds the tetrahedral angles $\chi_{2a} = 70.5^\circ$, $\chi_{3a} = 109.5^\circ$ ($\chi_{2a} = 180^\circ - \chi_{3a}$)).

Fig. 3.4 reveals an important feature of the glassy phase of CNADM: at the lowest measured temperature the spectrum displays a broad Pake shape, proof that the rotation motion around the C_3 axis is slow with respect to the 2H NMR solid echo time scale (slow motion limit). With increasing the temperature, a complex spectrum is observed, a sum of the one in the slow motion limit and the one in the fast motion limit. These ‘two phase’ spectra are the fingerprint of a broad distribution of rotational correlation times reflecting the very different environments the molecules experience in the glassy state [103].

Figure 3.4. The solid spectra measured in the glassy state ($T_g = 170\text{ K}$) with the inter-pulse delay $t_p = 20\text{ }\mu\text{s}$ (adapted from Roggatz [103]).



3.2. Experimental details

3.2.1. Preparation of the deuterated sample

The deuterated sample cyanoadamantane- d_{15} was prepared in our chemistry laboratory by J. Gmeiner and the procedure is described elsewhere, too [83, 103]. That is: 1 g fully deuterated adamantane was dissolved in 20 ml of dry chloroform and 2 g aluminum chloride were added under stirring and heating the solution up to 60 °C. Then 1.35 g trimethyl silylcyanide dissolved in 2 ml of chloroform were added droplet-wise. After 3 hours at 60 °C the reaction was finished. The substance was isolated by precipitation with water and afterwards redissolved in chloroform for purification with column chromatography. Finally, sublimation yielded white crystals with a melting point of 193 – 194 °C.

3.2.2. Measurement parameters

For the NMR experiments a i.) Bruker CXP 300 spectrometer (operating at a magnetic field strength of 7.05 T corresponding to a ^2H Larmor frequency of 46.07 MHz) equipped with a TecMAG data acquisition system and a ii.) Bruker DSX 400 spectrometer (operating at a magnetic field strength of 9.4 T corresponding to a ^2H Larmor frequency of 61.4 MHz) were used. For spectrometer i.) the sample was placed in a home build low temperature probe inserted into an Oxford static cryostat CF1200. The temperature stability was better than 0.3 K . The experiments in spectrometer ii.) were done with a commercial probe (Bruker) and a heating device Bruker VT 2000. Here the temperature stability was better than 1 K .

The sin-sin and cos-cos functions compiled for the 2D spectrum as well as the dependence of the solid echo on the interpulse distance t_p (at 256 K) were measured on spectrometer ii.) while the 1D spectra and the spin-lattice relaxation functions experiments were done on i.). The 1D spectra were obtained with a solid echo sequence preceded by a saturation sequence (five $\pi/2$ pulses) with the delay time between the end of the saturation sequence and the beginning of the solid echo sequence $t_d = 1\text{ s}$. The pulse length of a $\pi/2$ pulse was around $2.9\text{ }\mu\text{s}$. For monitoring the spin-lattice relaxation the saturation recovery method was applied.

The stimulated echoes decay curves were measured with a four pulse sequence with a minimum phase cycling of 16 scans to cancel double-quantum coherences [109]. For compiling the 2D spectrum a five pulse sequence was chosen and the lengths of the pulses before and after the mixing time were set to a common length corresponding to the magic angle (54.7°); the minimum phase cycling was 32 scans [109]. For both spin-alignment and 2D spectrum measurements a saturation sequence with five pulses was preceding the measuring sequence, too.

3.3. Experimental results, simulations and discussion

The scope of this work was to prepare and study the supercooled PC phase of CNADM, i.e. the interesting range of interest is $T_g < T < T_t$. In order to avoid history effects, in all the following presented experiments, when not stated differently, the target temperature was reached with a low cooling rate, every time starting from 300 K (that is 20 K above T_t , in the stable PC phase).

3.3.1. Spin-lattice relaxation

The normalized spin-lattice relaxation function $\psi(t)$ (cf. Eq. 2.63) at different temperatures is presented in Fig. 3.5. At temperatures around T_t and above, the relaxation function is mono-exponential. Starting with 246 K , the relaxation curve is clearly bi-exponential. The weight of the second exponential (the one with longer relaxation

time) is increasing with decreasing temperature so that at 225 K the relaxation is almost mono-exponential again but significantly slower. The data are well fitted by the following function $\psi_{fit}(t)$:

$$\psi_{fit}(t) = f_{fast}e^{-\frac{t}{T_{1fast}}} + (1 - f_{fast})e^{-\frac{t}{T_{1slow}}}, \quad (3.1)$$

where f_{fast} and T_{1fast} are the fraction respectively the time constant for the fast decay while T_{1slow} is the time constant of the slow decay. This behavior of the relaxation

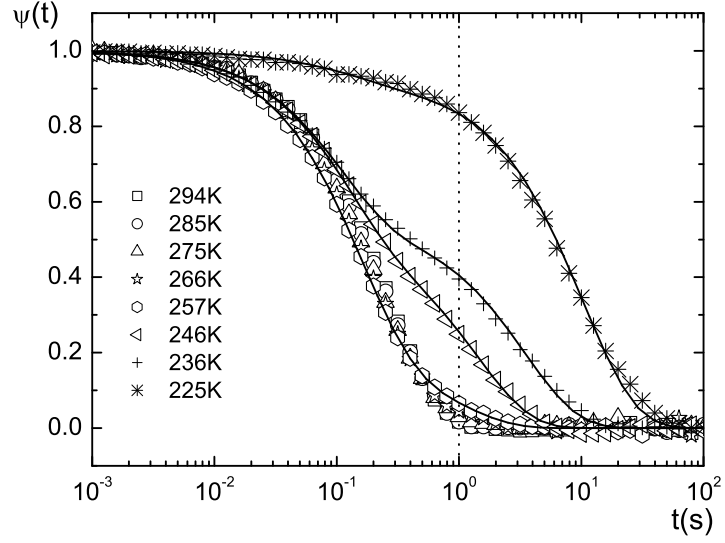


Figure 3.5. Spin-lattice relaxation function at different temperatures, lines are fits with a sum of two exponential functions; the dotted line marks $t_d = 1$ s, the delay applied after the saturation sequence for measuring the solid echo spectra presented in the following section.

function is interpreted as a consequence that both supercooled PC and OOC phase coexist in different proportions depending on temperature, i.e., partial formation of the ordered crystal was taking place. By cooling the sample below T_t a part of the supercooled PC phase transforms into the OOC phase and the lower the temperature the larger this amount is. To test this interpretation, a solid echo spectrum with a short saturation delay $t_d = 1$ s and with a long $t_d = 50$ s were measured at ~ 235 K in order to probe the spectra at different parts of the spin-lattice relaxation curve (the spectra shown in Fig. 3.6 (a), respectively (c) were obtained). The one measured at short t_d shows a shape similar to the one in Fig. 3.4 acquired at 159.6 K in the glassy phase thus it is characteristic of the supercooled PC phase (at temperatures close to T_g one expects to find similar spectra disregarding the fact that the sample is in the

supercooled or in the glassy phase). On the other hand, the spectrum for $t_d = 50$ s is more complex and in order to explain its shape we refer to a spectrum acquired in the neat OOC phase that is presented in Fig. 3.6 (b) (from Roggatz [103]). (The OOC phase was prepared by cooling the sample below T_g and slowly heating it up to the target temperature.) One can see that the spectrum in Fig. 3.6 (c), measured at a long t_d can be explained as a weighted sum of the two spectra in Fig. 3.6 (a) and (b), a further evidence of the coexistence of the two phases at ~ 235 K.

The conclusion agrees with the result of Pathmanathan and Johari [96] who suggested that the gradual transition from supercooled PC to OOC phase takes place in such a way that partially OOC domains are embedded in a PC matrix. In the measurements at a given temperature, the weighting factors for the two exponential lines in the spin-lattice relaxation functions were essentially not changing in time during data acquisition on a time scale of hours. Therefore we concluded that the fraction of the two phases was practically constant during the experiment.

The results obtained by fitting the normalized spin-lattice relaxation function $\psi(t)$ with Eq. 3.1 are displayed in Fig. 3.7. Note that by fitting $\psi(t)$ above T_t with a mono-

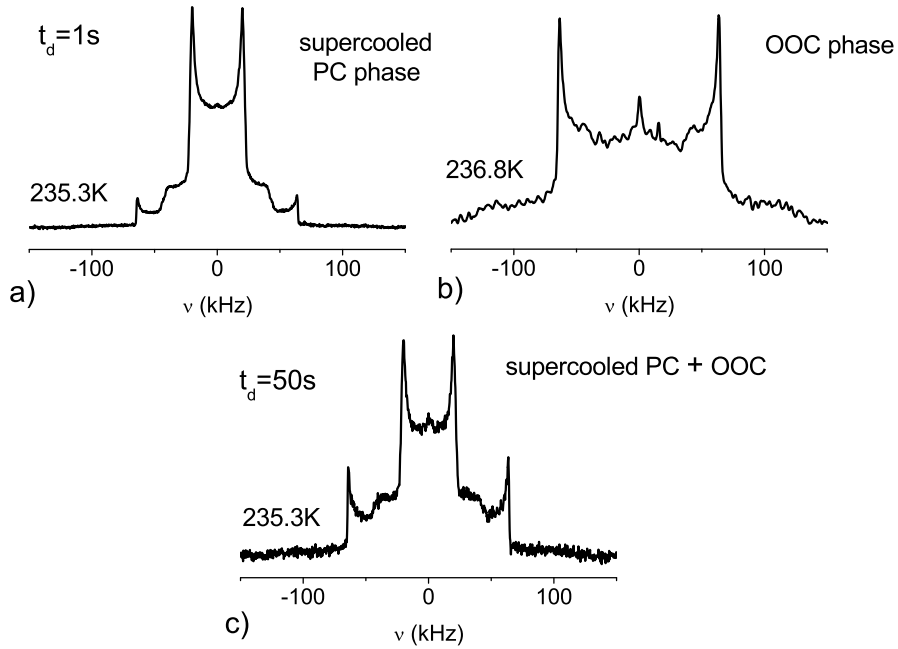


Figure 3.6. Spectra measured at 235.3 K with (a) $t_d = 1$ s and (c) $t_d = 50$ s; (b) spectrum measured at 236.8 K in the orientationally ordered crystal (OOC) phase (from Roggatz [103]).

exponential function, the obtained T_{1mono} values smoothly continue the temperature dependence of T_{1short} line without any discontinuity. This is an extra argument that indeed a certain fraction of the supercooled PC is obtained by lowering the temperature (cf. Fig. 3.7 (a)).

Although there are two phases coexisting, the fact that they exhibit different spin-lattice relaxation times can be exploited. Using a saturation sequence with a delay time of $t_d = 1$ s before the acquisition sequence, the magnetization originating from the supercooled PC phase was selected and the signal of this phase was measured without a considerable interference from the signal of OOC phase. The procedure was employed for all the experiments discussed in the following sections.

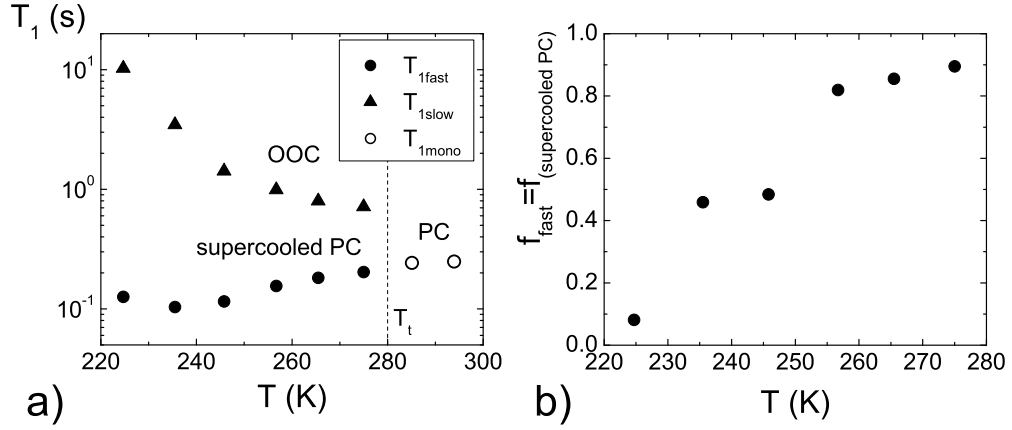


Figure 3.7. Fitting results obtained by using a biexponential function for the spin-lattice relaxation function (cf. Eq 3.1). a) T_{1fast} and T_{1slow} and b) the fraction f_{fast} that has a fast time constant. In a) we plotted T_{1mono} values obtained from using a single exponential fit.

3.3.2. Solid echo spectra

The solid echo spectra measured in the PC and supercooled PC phases are presented in Fig. 3.8 (a). A continuous broadening is observed, starting from a narrow central line at the highest temperature and ending with a broad shape at the lowest temperature.

Because there is a continuous evolution of the spectral shape with no abrupt changes at the transition temperature T_t , it means that it was possible to supercool and measure the fraction of sample in the supercooled PC phase as expected from the spin-lattice experiment.

Regarding high temperatures, the obtained narrow central line is a proof that the

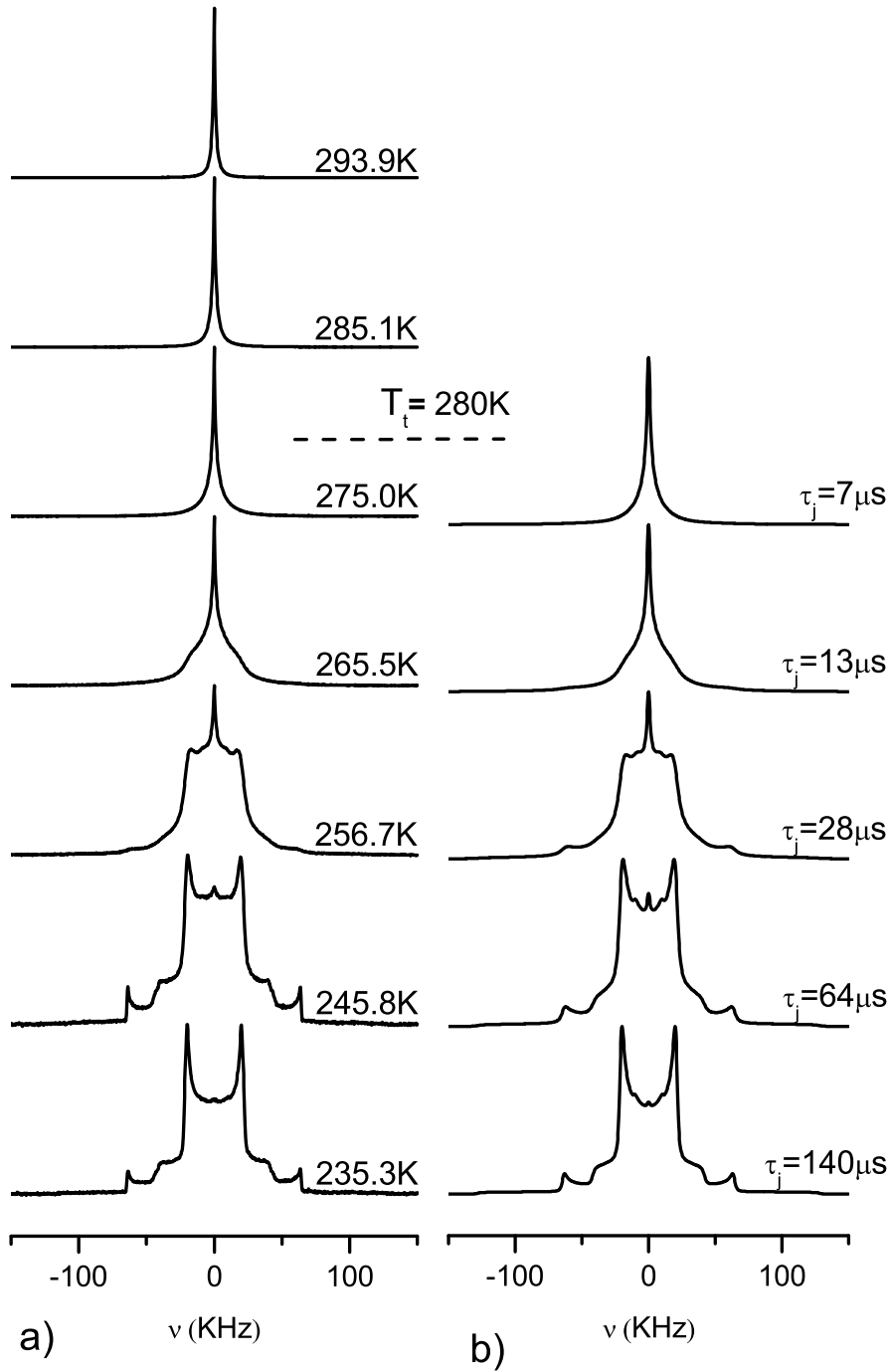


Figure 3.8. a) Dependence of the measured solid echo spectra on temperature (the temperature T_t of the phase transition from the PC phase to the OOC phase is marked); b) simulated spectra with the jump time constant τ_j .

C_3 axis of the molecule itself rotates fast with respect to the solid echo time scale providing an efficient average of the line shape.

The spectrum measured at $\sim 235\text{ K}$ is very similar to the one measured close to but below T_g (see Fig. 3.4), where the motion of the C_3 axis itself is too slow to have an influence on the spectral shape [103]. We interpret the changes in Fig. 3.8 (a) as being caused solely by the slowing down of the reorientation motion of the C_3 axis and this fact is supported by the findings presented in the following sections. The spectra were successfully simulated (Fig. 3.8 (b)) by using a proper motional model with properties set by further experiments (see next sections).

3.3.3. 2D spectrum and stimulated echoes

As the temperature dependence of the spectra does not provide enough information about the model to be applied for describing the molecular motion involved in the α -process, further 2D experiments were performed.

Because a 2D NMR spectrum gives a direct insight on the geometry of the motion (cf. page 21 in Chapter 2) we measured one at 245 K with mixing time $t_m = 3\text{ ms}$, shown in Fig. 3.9 (a) in an oblique presentation of the data. The spectrum is composed of two parts: one diagonal (for which $\nu_2 = \nu_1$) and one off-diagonal whose structure can be easier seen in the contour plot in Fig. 3.9 (b). The off-diagonal spectrum has a simple form, and having in mind previous calculations of 2D spectra for simple motions [112] it can be connected to a motion of the C_3 axis between a limited number of sites: when moving from one site to the other, the molecular axis reorients with an angle of 90° . It should be mentioned that 90° reorientation is the single case where the characteristic elliptic exchange pattern in the 2D spectrum collapses to a line. (Note: One expects an exchange pattern for the broad part of the spectrum as well and this 2D spectrum should lie in the frequency range $-150\text{ kHz} \leq \nu_1, \nu_2 \leq 150\text{ kHz}$. However, because it has a very low intensity with respect to the noise level, only the exchange pattern in the range $-80\text{ kHz} \leq \nu_1, \nu_2 \leq 80\text{ kHz}$ is clearly visible.)

In Fig. 3.9 (b) we also present a calculated 2D spectrum for such a motion (details of the calculations are given in Appendix C) which proves to be very similar to the experimental one. The slight differences between the measured and calculated spectra may arise from the fact that for the measured one, the assumption of no motion of the C_3 axis during the evolution and detection times t_1 and t_2 was not sufficiently well fulfilled. If it were the case that there is no motion in the before mentioned times, we would expect that the diagonal spectrum would look like a Pake spectrum which is not the case. Motion of the molecules during t_1 and t_2 gives rise to a small central line at $\nu_2 = \nu_1 = 0$ (visible as a peak in the center of the spectrum in Fig. 3.9 (a)) and broadens the lines. The analysis of the 2D experiment proves that the orientation of the C_3 axis of the molecule changes by 90° angles, with the number of available sites remaining to be revealed by stimulated echo experiments in the time domain.

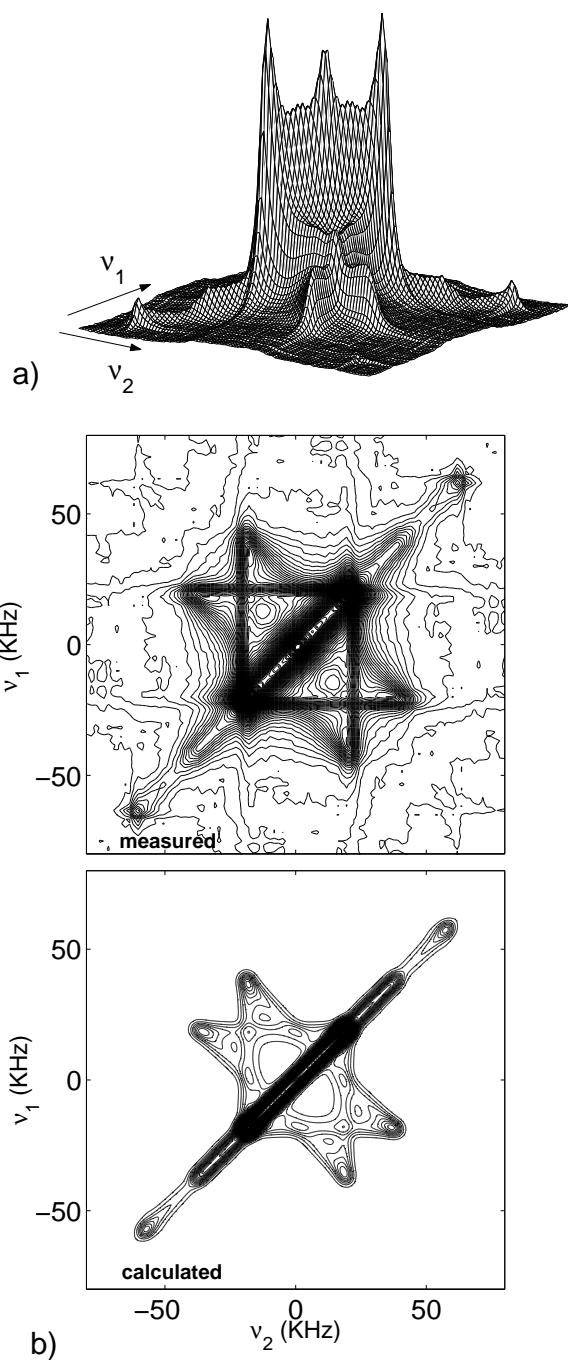
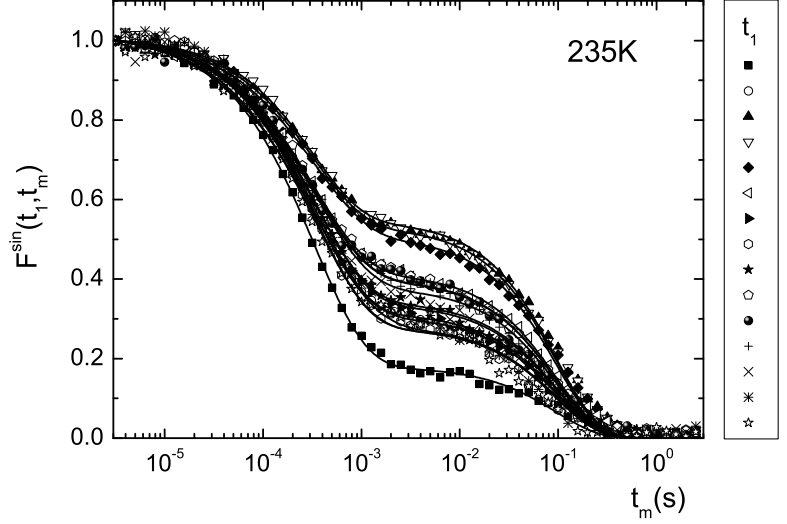


Figure 3.9. (a) 2D spectrum acquired at 245 K with a mixing time $t_m = 3 \text{ ms}$ - oblique representation and (b) contour plot of the measured and simulated spectrum.

Figure 3.10. Sin-sin correlation functions measured at 235 K for different evolution times t_1 . Solid line is fit with Eq. 2.42, symbols correspond to different values of t_1 , starting from the upper one in the legend with $t_1 = 3 \mu s$ and increasing with a step of $7 \mu s$.



As the sin-sin correlation function disclose more aspects of the molecular motion we measured them for several t_m values and the result for 235 K is plotted in Fig. 3.10. A two-step decay is observed, the first one is the actual sin-sin correlation function, the second one is caused by the relaxation of the spin-alignment state (cf. Eq. 2.42). With changing t_1 , the decay curve varies strongly. The data were fitted with Eq. 2.42 where $\phi(t_1, t_m)$ was the Kohlrausch-Wiliams-Watts (KWW) function which came out to be appropriate for disordered systems [28] with the correlation time τ_c given by Eq. 2.44. First a free fit for all sin-sin functions at a given temperature was performed, then the average value of T_{1Q} was kept fixed and a second fit was performed. The such obtained fits are included in Fig. 3.10.

As the resulting fit parameters for the sin-sin correlation functions vs. t_1 reveal information about the molecular motion we present them for two temperatures in Fig. 3.11. The correlation times $\tau_c(t_1)$ normalized by $\tau_2 = \tau_c(t_1 \rightarrow 0) \simeq \tau_c(t_1 = 3 \mu s)$ (cf. Eq. 2.48) are essentially independent of t_1 . In the limit $t_1 \rightarrow \infty$ one obtains $\tau_c(t_1) = \tau_j$, the later being the characteristic time constant of the distribution of waiting times between two consecutive jumps. It seen from our results that $\tau_2 \simeq \tau_j$ holds, meaning that the rotational correlation is lost after a single jump, as expected in the case of a large angle jump process. This behavior is different from the one found for molecular glass formers where the above mentioned ratio has a strong temperature dependence and $\tau_2 \neq \tau_j$ [29, 52, 57].

The stretching parameter β_{KWW} describes the deviation of the correlation function from exponentiality. Its large value around 0.82, which exhibits basically no dependence

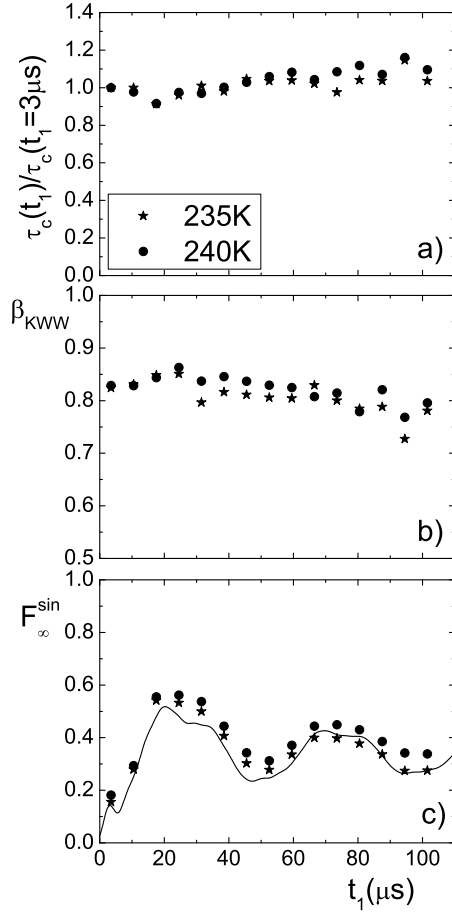


Figure 3.11. Parameters for the sin-sin correlation function at two temperatures: (a) normalized time constant, (b) stretching parameter β_{KWW} and (c) F_∞^{\sin} ; solid line: simulation (the time axis t_1 of the calculated line was shifted with $-3\mu s$ to account for the effects of finite pulses).

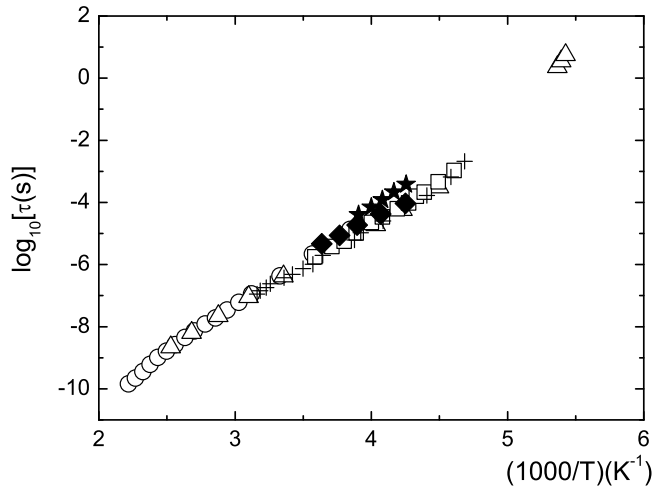
on t_1 , reflects only a small deviation from an exponential correlation function.

The values F_∞^{\sin} for the final state of the sin-sin correlation functions are plotted in Fig. 3.11 (c). It is observed that the points indicate a curve which is oscillating, reaching a maximum between 20 and 30 μs and a value close to 1/3 at long t_1 ; with lowering temperature, the experimental points for $F_\infty^{\sin}(t_1)$ are shifted towards somewhat smaller values. Thus the outcome of the experiment is still slightly sensitive to variations in temperature probably again because the mean correlation time of the reorientation motion of the C_3 axis is not much greater than the evolution time ($\tau \gtrsim t_1$). The information extracted from the experimental values of F_∞^{\sin} is: $F_\infty^{\sin}(t_1 \rightarrow \infty) \simeq 1/3$ and taking into account Eq. 2.47 and the cubic symmetry of the crystalline lattice [48, 96] we concluded that there are six sites for the C_3 axis to jump in between with the sites placed in the corners of a cube. $F_\infty^{\sin}(t_1)$ was calculated using this simple model (see Appendix C) and the result is presented in Fig. 3.11 (c) along with the experimental points. The calculated line reproduces well the measured data. As said, the slight

differences between the experimental data and the calculated ones might arise from the fact that, in the calculation of the F_{∞}^{\sin} line we assumed that $\tau \gg t_1$ and this condition is not completely fulfilled in the experiment.

The correlation time τ_2 obtained from the $F^{\sin}(t_1 = 3\mu s, t_m)$ function is displayed in Fig. 3.12 along with data available in literature (Ref. [33] and references therein). The points from the NMR experiments are closed to the reported data points and indicate the same activation energy. Since the molecule is heavier due to deuteration, the absolute values of τ_2 are expected to be somewhat longer.

Figure 3.12. Correlation times for the motion of the C_3 axis; full stars: τ_2 obtained from the fit of sin-sin correlation function, full diamonds: τ_j^* correlation times obtained from the jump correlation times used for the simulation of the 1D spectra, circles: Brand et al. [33], squares: Pathmanathan and Johari [96], plus signs: Tyagi and Murthy [127], triangles: Amoureux et al. [9].



3.3.4. Analysis of the solid echo spectra

By applying a six-fold jump model for the motion of the CNADM molecule, the results of the 2D experiments were reproduced and now it is possible to return to the analysis of the 1D spectra in Fig. 3.8 (a) and to simulate them by applying the same jump model.

The ingredients of the model are: in the entire temperature range of the measurements the molecule rotates fast around its C_3 axis. Beside this motion, the C_3 axis of the molecule is jumping between six sites performing 90° reorientations. The value of the frequency ω for a site which has the $C-^2H$ bond orientation θ is the same with one which has the $C-^2H$ bond orientation $180^\circ - \theta$ thus we have only three (3) non-equivalent sites to consider. For the motional model we choose the Ivanov model [62]: the jump from one site to another is instantaneous and the jump probability depends only on the actual position of the C_3 axis; between jumps, the orientation of the C_3

axis is fixed. Assuming Poisson distributed jump events, the distribution of the waiting time between two jumps is described by an exponential function with a characteristic jump correlation time τ_j [128]. The fast rotation of the molecule around the C_3 axis gives rise to an averaged spectral width, as already presented on page 27. For the sake of simplicity we disregarded the fact that there are two central spectra with only slightly different spectral width and proceeded in the simulation as if there was only one central spectrum with $\bar{\delta} = 42 \text{ kHz}$; for the broad spectrum a value $\delta = 128 \text{ kHz}$ was used. (More details on the simulation procedure can be found in Appendix C.)

In Fig. 3.8 (b) the simulated 1D spectra are showed and the evolution of the experimental line shape with temperature is well reproduced by properly choosing τ_j . The slowing down of the reorientation motion of the C_3 axis causes the evolution of the spectrum from a narrow line above T_t to a broad one close to T_g . For each temperature, a value for τ_j was obtained from which a rotational correlation time $\tau_j^* = \frac{2}{3}\tau_j$ was calculated according to Spiess [118] knowing that the motional model contains three distinguishable sites. The such obtained τ_j^* are plotted in Fig. 3.12 and they agree well with the rest of the data.

In order to cross-check the motional model a further experiment was performed: the inter-pulse distance t_p in the solid echo experiment was varied and the corresponding 1D spectra at a given temperature were recorded. As an example the line shapes measured at 256 K with different t_p are displayed in Fig. 3.13 (a) where the spectra were all normalized to their maximum value. With increasing t_p , there is an obvious change in the line shape and the model chosen to explain the temperature dependence of the line shape should reproduce this, too. First, in Fig. 3.13 (b) the line shape simulations for different t_p with a single jump correlation time τ_j are presented. The evolution of the line shape is well reproduced at short values of t_p but not at long values. In order to improve the agreement between simulation and experimental data a distribution of jump correlation times was considered, an approach usually taken for disordered systems. Note: the non-exponentiality of $F^{\text{sin}}(t_1 \rightarrow 0, t_m)$ is also an indicator for the presence of a distribution of correlation times. Thus a log-Gauss distribution for the jump correlation times $G[\lg(\tau_j)] = (\sqrt{\pi}\sigma)^{-1} e^{-\lg(\tau_j/\tau_m)/\sigma}$ was used as a starting point but it was not possible to reproduce *the temperature dependence* of the spectra as indicated in Fig. 3.15 (a). As a second approach an asymmetric distribution was chosen: the generalized gamma distribution $G_{GG}[\ln \tau_j]$ [25]:

$$G_{GG}[\ln(\tau_j)] = N(\alpha, \beta) e^{(-\beta/\alpha)(\tau_j/\tau_0)^\alpha} \left(\frac{\tau_j}{\tau_0} \right)^\beta, \quad (3.2)$$

where N is:

$$N(\alpha, \beta) = \left(\frac{\beta}{\alpha} \right)^{(-\beta/\alpha)} \frac{\alpha}{\Gamma(\beta/\alpha)}. \quad (3.3)$$

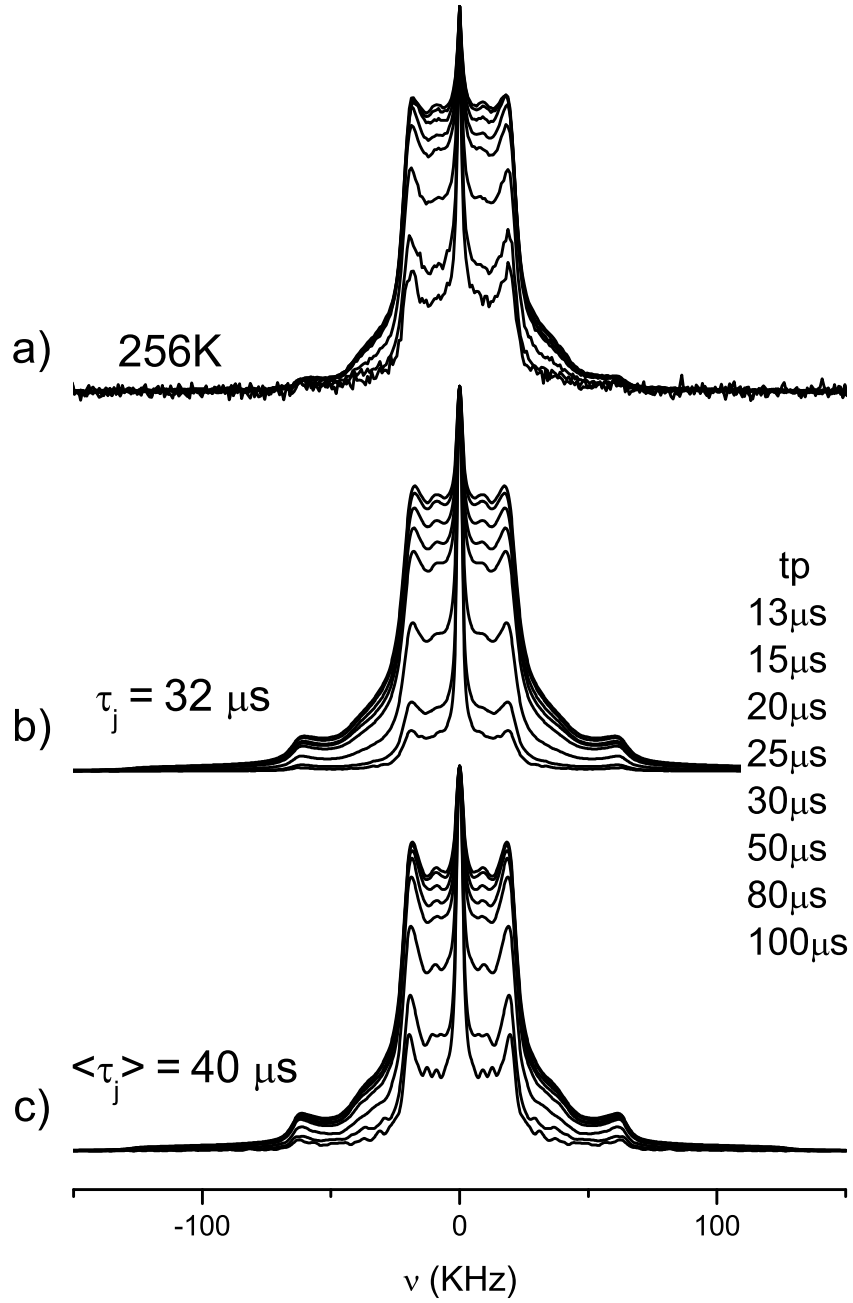


Figure 3.13. a) Measured solid echo spectra at 256 K with different inter-pulse distance t_p . b) The simulated spectra assuming one jump correlation time τ_j and c) assuming a generalized gamma distribution for the jump correlation times.

and the mean correlation time is given by:

$$\langle \tau_j \rangle = \tau_0 \left(\frac{\alpha}{\beta} \right) \frac{\Gamma\left(\frac{\beta+1}{\alpha}\right)}{\Gamma\left(\frac{\beta}{\alpha}\right)}, \quad (3.4)$$

where Γ is the gamma function. The advantage of this function is that it is flexible enough to be applied to the dielectric data [25] therefore the dielectric loss ε'' at 300 K taken from Brand et al. [33] was fitted and we obtained $\alpha = 20$ and $\beta = 2$. In Fig. 3.14 one sees that the distribution function with the obtained parameters is not a broad one. In order to minimize the number of the fit parameters, the values of α and β

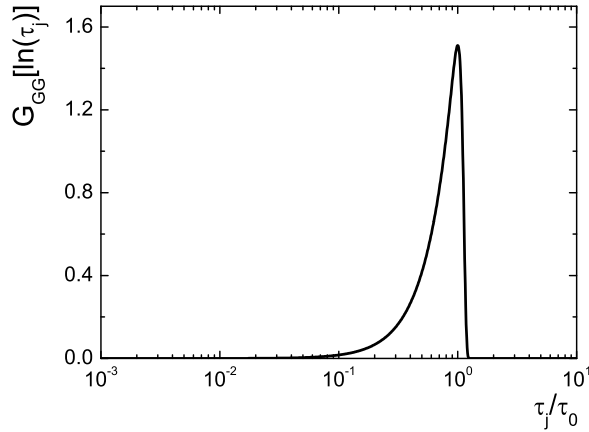


Figure 3.14. Generalized gamma function - the jump time distribution used to simulate the spectra in Fig. 3.13 c) and in Fig. 3.15 b) (for details see text).

from dielectric-spectroscopy data were fixed and only τ_0 was used as fit parameter to describe the dependence on temperature of the measured solid echo in Fig. 3.8 (a). As it can be seen in Fig. 3.15 (b) for a $t_p = 20 \mu s$ this function gives roughly the same result as in the simple case of no distribution meaning that it fits well *the temperature dependence* of the measured spectra. The averaged jump correlation times $\langle \tau_j \rangle$ is comparable with the jump correlation time τ_j for similar spectra simulated with the two models (cf. Fig. 3.15 (b) and Fig. 3.8 (b), $\langle \tau_j \rangle = 7.4; 29; 73 \mu s$ and $\tau_j = 7; 28; 64 \mu s$). Concerning *the t_p dependence*, the mean correlation time $\langle \tau_j \rangle = 40 \mu s$ was chosen in the simulation program to fit the spectra at 256 K. The result is displayed in Fig. 3.13 (c) and is better reproducing the experimental data than in the case of no distribution of jump correlation times.

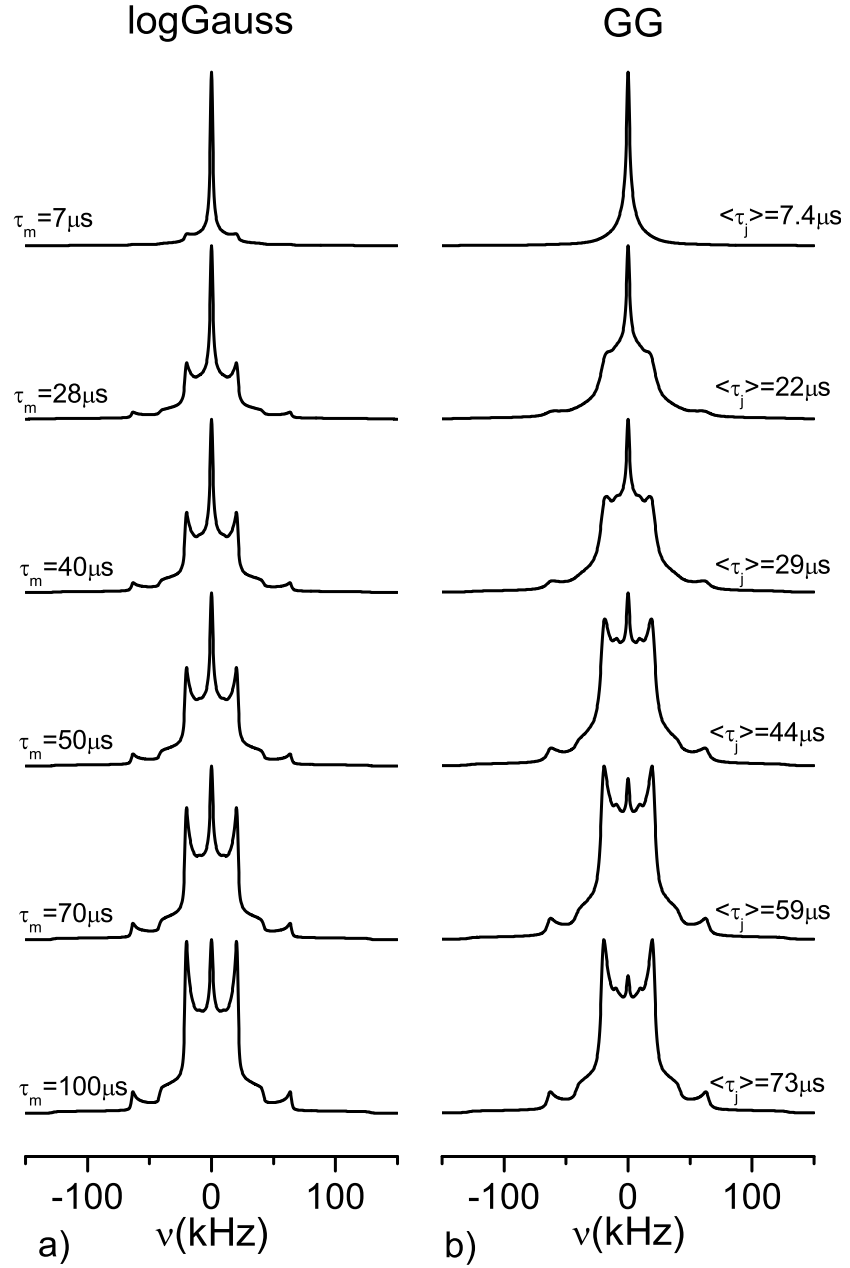


Figure 3.15. Simulations made in order to reproduce the temperature dependence of the solid echo spectra employing different distributions of jump correlation time: a) the log Gauss distribution function with $\sigma = 0.8$ and b) the generalized gamma distribution function G_{GG} . Compare with the temperature evolution of the spectra in Fig. 3.8 a) and note that the spectra generated with the log Gauss distribution do not fit the experimental data.

3.4. Summary and conclusions

Applying different ^2H NMR methods we analyzed the molecular motion in the supercooled plastically crystalline phase of CNADM, a paradigmatic case of a glassy crystal. Although the disordered phase was coexisting with the ordered one, NMR was able to single out the signal from the glassy crystal due to the significantly faster spin relaxation with respect to that of the ordered phase.

A simple jump mechanism reflecting the cubic symmetry of the crystalline lattice is consistently derived from the NMR data. In first approximation assuming a single jump correlation time it is sufficient to reproduce the salient features of the NMR experiments. Refining the analysis, a narrow distribution of the correlation times is introduced leading to a stretching parameter $\beta_{KWW} = 0.91$ which is in agreement with dielectric data where the relaxation peak is close to the Debye limit (a Cole-Davidson fit gives: $\beta_{CD} = 0.80 - 0.85$ [33]). No indication of small amplitude motion was found, a fact that is opposite to the finding in structural glass formers. This may correlate with the observation that in CNADM no excess wing on the high frequency side of the main relaxation peak is observed in the dielectric spectrum [33]. Similar results were observed by a NMR study of o-carborane where at low temperatures the molecule is performing jumps of 120° about its quasi- C_3 axis (though a small-angle tilting of the axis exists at high temperatures) [144]. All in all, the results are similar to what one finds in rotor phases where molecular motion is ruled by the symmetry of the molecule making up the crystal, for example in crystalline benzene. In other words, no signs of cooperativity are observed in the performed experiments. Indeed even the extent of non-Arrhenius behavior of the jump correlation time in CNADM is quite small and peculiar at high temperatures (cf. Fig. 3.12). On the other hand, the large-angle reorientation of the CNADM molecules which does not exhibit the symmetry of molecule but rather that of the lattice can only occur in the crystal via a cooperative process, i.e. several molecules have to move in a more or less coherent way to achieve this reorientational process.

4. NMR Study of the Glass Formers ortho-Terphenyl and Toluene in Confined Geometry

4.1. Introduction

When confined into pores with dimensions in the nanometers range the properties of a glass former differ considerably from those of the bulk. For example, in the case of molecular liquids, the phase transition temperatures, the transport coefficients and the distribution of time constants of specific molecular motions are strongly modified ([3] and references therein). By varying the pore dimensions in different experiments, information on the correlation length of the molecular motion associated with a certain process may be obtained. Many studies of supercooled liquids used this idea focusing on the α -process [3, 89] and therefore investigating the temperature range close to but above T_g . In contrast, the main purpose of this work is to explore whether new light might be shed onto the nature of secondary relaxational processes by extending the study of confined liquids to temperatures well below T_g . One of the most important question that we asked ourselves was whether the β -process has a different correlation length than the process responsible for the excess wing or not.

Toluene (rigid molecule) and ortho-terphenyl were chosen because they belong to the most studied glass forming liquids ([41] and references therein). The former one exhibits a β -process [74] while the last does not when the system is slowly cooled [138]. As a confining medium we used SBA-15, prepared in the group of C. Alba-Simionesco, Paris, Université de Paris-Sud. As a matter of fact, the entire project of investigating by ^2H NMR glass forming liquids in confined geometry is a close cooperation between our group and the one in Paris.

A short presentation of the main properties of the investigated samples is given in the following.

4.1.1. ortho-Terphenyl

Ortho-terphenyl (OTP) is one of the most well investigated fragile glass-forming liquids that present van der Waals interactions (e.g. [41, 122] and references therein). The molecule is composed of three phenyl rings as sketched in Fig. 4.1 and it presents

internal degrees of freedom, reorientations of the two outer rings being characterized by different techniques (e.g. [67] and references therein, also cf. Appendix E). We used as the glass transition temperature $T_g = 248\text{ K}$ as obtained from a measurement performed in the group of Alba-Simionesco [82].

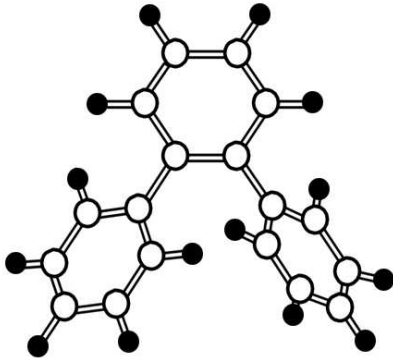


Figure 4.1. The OTP molecule in balls and sticks representation. White balls are carbon atoms, black ones are hydrogen atoms (after [114]).

Although in early experiments [66] a β -process was observed in OTP this was not confirmed in more recent work. Wagner and Richert [138] showed that a secondary process in OTP only occurs when the liquid is quenched into the glass, while the secondary relaxation peak disappears when the system is annealed and it is not observed when the system is slowly cooled therefore the system is a type A glass former [74].

The perdeuterated sample OTP- d_{14} was purchased from CDN Isotopes (98.2% atom D, product no. D-4165) and used as received (courtesy of C. Alba-Simionesco).

4.1.2. Toluene

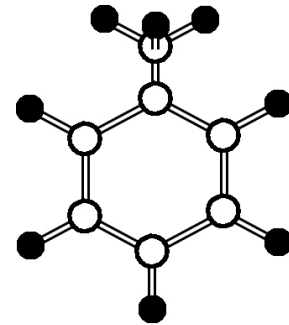
The molecular structure of toluene (methyl-benzene) is simple (cf. Fig. 4.2): a phenyl ring and a methyl group. Regarding only the phenyl ring, toluene is a rigid molecule and its dipole moment is not affected by methyl group rotations [20].

In the dielectric loss spectra a well pronounced β -process is observed leading to the classification of toluene as a type B glass former [74].

In our experiments we employed the ring deuterated sample toluene- d_5 purchased from Aldrich (98% atom D) and used as received. Because of the specific deuteration, the ^2H NMR measurements are insensitive to the methyl dynamics.

The glass transition temperature is $T_g = 117\text{ K}$ [89].

Figure 4.2. The toluene molecule in balls and sticks representation. White balls are carbon atoms, black ones are hydrogen atoms.



4.1.3. Confining medium: SBA-15

SBA-15 is a nanostructured porous silicate that was synthesized (according to the procedure reported in Ref. [145]) and characterized in the group of C. Alba-Simionesco. The structure consists of parallel cylindrical pores arranged in a honeycomb-type lattice with a narrow distribution of pore size. The length over diameter ratio is more than 1000, the structure being confirmed by small- and wide-angle neutron scattering experiments [6]. The pore diameter of the matrix was and 8.0 nm and post-synthesis silanization of the surface of a part from this sample was carried out in order to suppress large interactions with polar molecules, leading to a pore diameter of 7.1 nm . As a result two different matrices were available for the experiments.

4.1.4. Properties of the glass formers in the confining medium

The properties of a confined glass former are different from those in the bulk because of several effects. From these, an easily anticipated one is the *finite size effect*: when the typical pore size is comparable with the correlation length of the glass transition phenomenon in the confined liquid then the properties of the last one may be modified. Faster dynamics and lower values of T_g are systematically observed for large pore size, i.e., for d larger and decreasing to roughly 10σ whatever is the surface treatment or the shape of the pore [89] (σ describes the size of the molecule). This behavior was interpreted as a finite size effect. In addition to the size effect, a significant *surface effect* is induced by the large surface-to-volume ratio of porous systems. Its influence on the dynamical properties of the confined liquid depends on the nature of the fluid-wall interaction [6, 138]. Slower dynamics and higher values of T_g than in the bulk are observed for d smaller than roughly 10σ . However, in this case a post-synthesis surface treatment, like silanization, can play a major role. It can suppress strong interactions with glass former's polar molecules and, hence, lead to a lower rather than a higher

value of T_g .

The pore size dependence of the calorimetric glass transition temperature T_g is non-trivial, and depends on the interplay of the finite size effect and the surface effect (and possibly on density changes in confinement when compared to the bulk [89]). This complex situation was observed for both toluene [89] and OTP [3, 97].

We choosed to perform experiments on toluene-d₅ ($\sigma \simeq 5 \text{ \AA}$) confined in sylanized SBA-15 materials, i.e., in the limit $d/\sigma > 10$ (roughly 14), so that finite size effects are expected to dominate the overall dynamics of the liquid. Consistently, $T_{g,confined} \simeq 112 \text{ K}$ is found (as reported by C. Alba-Simionesco, Paris, Université de Paris-Sud), which is somewhat lower than the bulk value $T_g = 117 \text{ K}$. Furthermore, we studied OTP-d₁₄ ($\sigma \simeq 8 \text{ \AA}$) confined in a unsilanized SBA-15 matrix with some silanols groups at the surface. In this case, we were in the limit $d/\sigma < 10$ (roughly 8), where the surface plays the dominant role. For this sample $T_{g,confined} \simeq 265 \text{ K}$ was obtained, higher than the bulk value 248 K (as reported by C. Alba-Simionesco, Paris, Université de Paris-Sud).

4.2. Measurements details

The OTP sample was measured using a Bruker DSX 400 spectrometer (operating at a magnetic field strength of 9.4 T corresponding to a ^2H Larmor frequency of 61.4 MHz) while in the case of toluene a Bruker CXP 300 spectrometer (operating at a magnetic field strength of 7.05 T corresponding to a ^2H Larmor frequency of 46.07 MHz) equipped with a TecMAG data acquisition system was employed. The probes and temperature stability were similar with those reported in Section 3.2. For monitoring the spin-lattice relaxation the saturation recovery method was applied. The 1D spectra for OTP in SBA-15 were obtained with a solid-echo sequence preceded by a saturation sequence (five $\pi/2$ pulses) with a delay time between the end of the saturation sequence and the beginning of the solid-echo sequence long enough that more than 95% of the equilibrium magnetization was probed. The 1D spectrum for toluene in SBA-15 was obtained with a solid-echo sequence repeated with a triggering time of 1 s , the entire experiment lasting almost 18 h (this procedure was employed due to the low signal-to-noise ratio caused by the small amount of the deuterated sample). The pulse length of a $\pi/2$ pulse was around $3.5 \mu\text{s}$ for OTP in SBA-15 and $2.4 \mu\text{s}$ for toluene in SBA-15.

4.3. Results and discussion

4.3.1. ortho-terphenyl confined in SBA-15

Line shape analysis

Fig. 4.3 displays the ^2H NMR spectra of OTP-d₁₄ in SBA-15 as obtained by applying the solid echo technique. The spectra show a crossover from a motionally averaged spectrum at highest temperatures, typical of a liquid (central Lorentzian line), to a broad Pake spectrum at lowest temperatures, characteristic of slow motion.

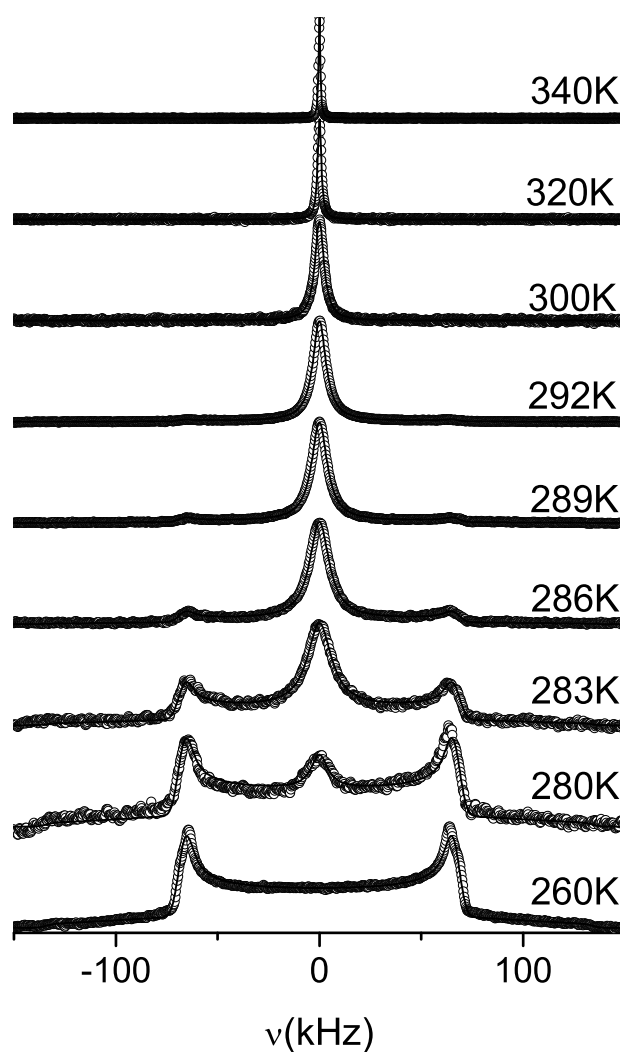


Figure 4.3. ^2H NMR spectra of OTP-d₁₄ confined in SBA-15; solid lines: fit of the ‘two-phase’ spectra by a sum of a Lorentzian and a Pake spectrum (and fit by only a Lorentzian for $T \geq 300\text{ K}$).

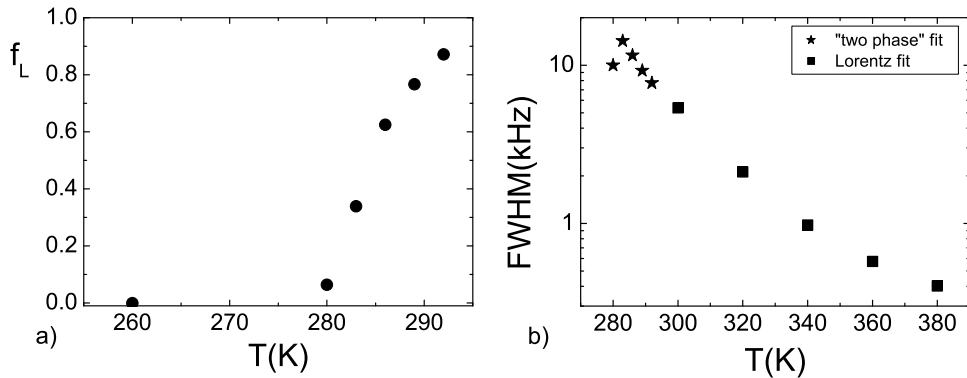


Figure 4.4. Results of the spectra's fit: a) f_L , relative weight of the Lorentz subspectrum vs. temperature; b) $FWHM$, full width at half maximum for the Lorentz subspectrum (or spectrum, at high temperatures).

The spectra at intermediate temperatures can be reproduced by a weighted superposition of a Lorentzian line and a Pake spectrum (cf. fits in Fig. 4.3). Note that the fraction of the corresponding subspectra continuously changes with temperature (cf. Fig. 4.4 (a)). Such 'two-phase' spectra composed of a superposition of a Lorentzian line and a Pake spectrum are the fingerprint of a broad distribution of correlation times $G[\ln(\tau_\alpha)]$; fast ($\tau_\alpha \ll 10 \mu s$) and slow molecules ($\tau_\alpha \gg 10 \mu s$) exist simultaneously [28]. Two-phase spectra are neither observed in bulk OTP nor in any other neat glass former where the spectra continuously broaden upon cooling. Usually, it is argued that the width of $G[\ln(\tau_\alpha)]$ in bulk glass formers is too small to provide two-phase spectra [28]. Clearly, this is no longer the case for OTP-d₁₄ under confining conditions. Similar two-phase spectra were measured for benzene in SBA-15 [51] and ethylene glycol in a zeolite [86]. In the latter case, structurally quite different from SBA-15, the 2D NMR experiments showed that no exchange between fast and slow molecules occurs on the *ms* time scale, confirming the presence of a heterogeneous distribution $G[\ln(\tau_\alpha)]$.

Fig. 4.4 (b) shows the full width at half maximum $FWHM$ of the Lorentzian line as a function of temperature. At low temperatures the spectra were fitted with a sum of a Pake spectrum and a Lorentz line while at high temperature there was no need for the Pake contribution therefore we employed only a Lorentzian line. When the spectral line is very narrow one expects that the shape of the spectrum is dominated by the effects due to the inhomogeneity of the applied external magnetic field. As even at the highest temperatures the $FWHM$ trace does not saturates we consider that the above mentioned effects are negligible for our experiments.

Spin-lattice and spin-spin relaxation

The temperature dependence of the mean spin-lattice relaxation time $\langle T_1 \rangle$ along with that of the spin-spin relaxation time $T_2 = 2/FWHM$ for OTP-d₁₄ confined in SBA-15 is displayed in Fig. 4.5 (a). For comparison, in the same figure the corresponding data for bulk OTP-d₁₄ [44] are plotted. At a first glance it is seen that both relaxation times

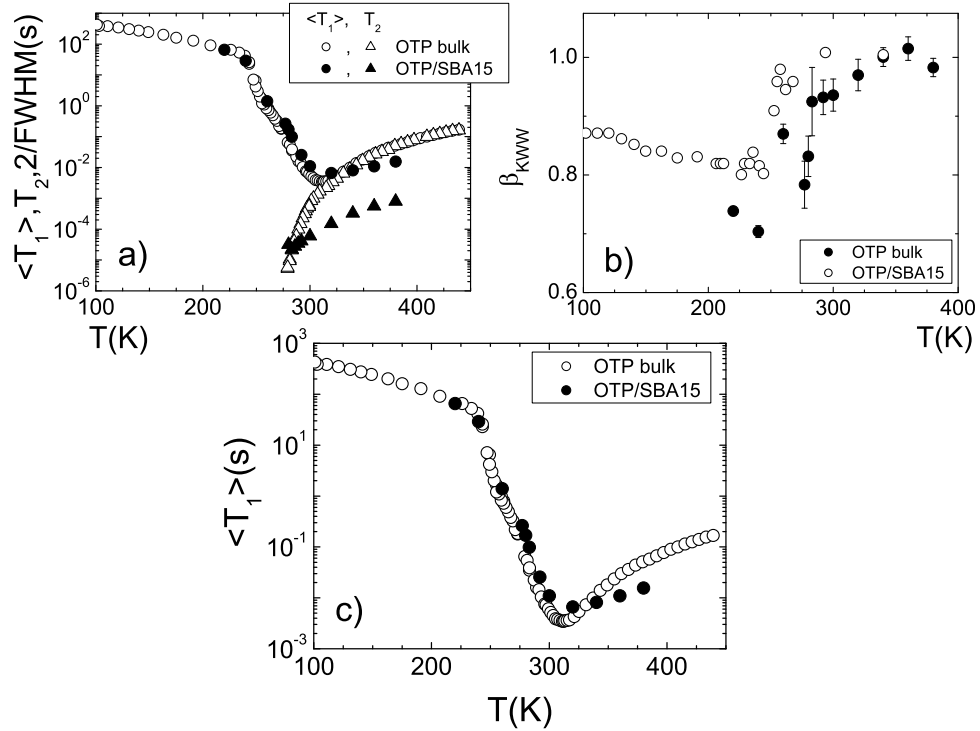


Figure 4.5. a) Spin-lattice $\langle T_1 \rangle$ and spin-spin T_2 relaxation times of bulk OTP ($\omega_L/2\pi = 55$ MHz, from [44]) compared with those of OTP confined in SBA-15 ($\omega_L/2\pi = 61$ MHz; for confinement T_2 was calculated from the width of the Lorentzian line $T_2 = 2/FWHM$). b) Stretching parameter β_{KWW} for the spin-lattice relaxation function for bulk OTP (from [114]) and in confinement. For clarity $\langle T_1 \rangle$ vs. T for bulk and confined OTP is once again displayed in c).

differ in the confinement from those in the bulk. Definitely the confinement changes the relaxation properties of OTP-d₁₄. Although the larger effect is seen in T_2 , these data for OTP-d₁₄ in SBA-15 should be considered with care because they are not actually measured T_2 but an estimate from line-shape analysis. In the case when the spectra show only a Lorentz line, the estimate of T_2 from the line-shape analysis is reliable. On

the other hand, when the spectra display two-phase features, the estimated T_2 refers to only a fraction of the molecules, the ones that are much faster than $1/\delta \simeq 10 \mu s$.

Concerning Fig. 4.5 (c), it is seen that $\langle T_1 \rangle$ data for bulk and confined OTP-d₁₄ have a minimum around the same temperature $T_{min} \simeq 310 K$. Note that in the confinement, the relaxation time is by a factor of two longer near the minimum as compared to the bulk (more precisely, $p = \min(\langle T_1 \rangle_{conf.}) / \min(\langle T_1 \rangle_{bulk}) = 1.9$). With lowering the temperature below T_{min} the difference between the $\langle T_1 \rangle$ values decreases so that below 250 K they are practically indistinguishable. On the other hand, at temperatures higher than T_{min} the values for the spin-lattice relaxation time are considerably different.

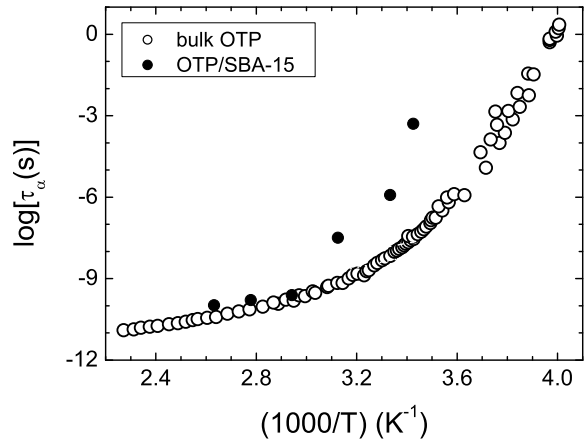
As it was demonstrated many times for bulk liquids [28, 44, 106, 114], the $\langle T_1 \rangle(T)$ curves around the minimum can be well described by assuming a Cole-Davidson (CD) spectral density in the Bloembergen-Pound-Purcell expression for the relaxation rate, in other words by introducing a distribution of correlation times $G[\ln(\tau_\alpha)]$. Making the same assumption for the confined glass former, from the minimum of $\langle T_1 \rangle(T)$ one can estimate the Cole-Davidson width parameter $\beta_{CDconf.} = 0.140 \pm 0.006$ (see Appendix B, we used $\delta = 135.5 kHz$ [114]). Since in the case of confined OTP-d₁₄ β_{CD} is by a factor of about four lower than in the bulk ($\beta_{CDbulk} = 0.519$ [114]), one can estimate that the distribution of the correlation time, $G[\ln(\tau_\alpha)]$, is by a factor of four broader than in bulk. The broad distribution in confinement was evidenced by line-shape analysis, too (see previous section).

We talk about heterogeneous dynamics when the molecules in the broad distribution $G[\ln(\tau_\alpha)]$ preserve their specific time constant at any observation time, in other words, dynamic exchange does not take place. Heterogeneous dynamics may show up in a non-exponential spin-lattice relaxation. Regarding the structural relaxation (or the α -process), above T_g , in the supercooled liquid dynamical exchange may take place on the time-scale of T_1 so that a exponential spin-lattice relaxation results. Inspecting the exponent β_{KWW} of the stretched exponential describing the spin-lattice relaxation function of OTP-d₁₄ in SBA-15 (cf. Fig. 4.5 (b)) we see that its value drops below 1 at about 340 K and finally reaches $\beta_{KWW} \simeq 0.7$ at 220 K. Compared to bulk OTP-d₁₄, the deviation from exponential relaxation starts at significantly higher temperatures. At such high temperatures where the spectra are given by a central line (cf. 4.3) the correlation times of the molecules are on the order of ns . The observation of a non-exponential spin-lattice relaxation at these temperatures leads to the conclusion that exchange processes among fast and slow molecules do not occur on the time scale $t \simeq \langle T_1 \rangle \simeq 10 ms$. In the SBA-15 confinement, the various sub-ensembles of OTP-d₁₄ molecules with different dynamical behaviors are isolated on that time scale. In contrast, this is not the case for bulk OTP-d₁₄ where the exchange rate is always on the order of the time constant, resulting in an exponential relaxation function at $T > T_g$ as it was demonstrated by several experiments [28] (cf. also Fig. 4.5 (b)). This result demonstrates that molecules in a given environment do not change their dynamic state, and the two-phase spectra displayed in Fig. 4.3 are thus a fingerprint

of a heterogeneous distribution. A similar conclusion was drawn by Medick et al. as a result of a 2D ^2H NMR experiment on ethylene glycol- d_4 embedded in a zeolite [86].

For temperatures around the minimum value of $\langle T_1 \rangle$ we may analyze the data in a manner analogous with the one Hinze and Sillescu employed in a former work [59]. The spin-lattice relaxation rate $1/T_1$ can be related to the spectral density of molecular reorientation $J(\omega_0)$ by Eq. 2.58 and assuming a Cole-Davidson distribution of correlation times, the spectral density is described by Eq. B.2. Therefore one can directly calculate the correlation time $\tau_c(T) = \langle \tau_\alpha \rangle(T)$ (cf. Eq. B.3) from the experimental data $\langle T_1 \rangle(T)$ for OTP- d_{14} in confinement, the result being presented in Fig. 4.6 (we used $\delta = 135.5 \text{ kHz}$ [114] and $\beta_{CDconf.} = 0.140$). The time constants estimated from T_1 for

Figure 4.6. Open circles: the time constants of the α -process τ_α in bulk OTP (from Ediger et al. [46]); circles: τ_α for OTP- d_{14} confined in SBA-15 estimated from $\langle T_1 \rangle$ data.



OTP in SBA-15 are longer than the corresponding ones for bulk OTP and show a diverging tendency at a smaller value of $1000/T$, hence a higher temperature. This finding correlates well with the higher glass transition temperature in confined OTP compared with bulk OTP (cf. page 48). A remark about the validity of the above approach worth to be mentioned: the assumption of isotropic rotational diffusion is essential and if it does not hold then the dependence of $1/T_1$ on the correlation time τ_α cannot anymore be described within the simple approach proposed here. From the present experiments we cannot make any statement about the isotropy or anisotropy of the molecular motion; we suggest performing future experiments with partially deuterated samples.

It was demonstrated by Blochowicz et al. [23] that for type A glass-formers the spin-lattice relaxation at low temperatures ($T \lesssim T_g$) is dictated by the contributions of the excess wing to the spectral density. Figure 4.5 (c) shows that $\langle T_1 \rangle$ is almost identical below T_{min} for bulk and confined OTP and this finding is interpreted as an indication that the excess wing properties are not modified under confinement in contrast to those

of the β -process (cf. next section). We would like to stress the relevance of the result: it proves that ^2H NMR provides a tool that can differentiate between the excess wing and the β -process, two relaxation features that are claimed by some researchers to be the same (for example, [92] and references therein).

4.3.2. Toluene confined in SBA-15

Figure 4.7 (a) presents the mean spin-lattice relaxation time $\langle T_1 \rangle$ of toluene- d_5 confined in silanized SBA-15. The data are compared with those obtained for bulk toluene- d_5 [106, 129]. As in the case of previously discussed OTP- d_{14} , the minimum of the function $\langle T_1 \rangle(T)$ lies at approximately the same temperature $T_{\min} \simeq 153 \text{ K}$ for both bulk and confined toluene. Around T_{\min} the relaxation time is by a factor of two longer (more precisely, $p = \min(\langle T_1 \rangle_{\text{conf.}}) / \min(\langle T_1 \rangle_{\text{bulk}}) = 1.6$) whereas it is considerably shorter at the highest temperatures, as compared to the bulk data. Repeating the same argument used for analyzing the OTP- d_{14} data around T_{\min} , one can conclude that in the case of confined toluene, the distribution of correlation times $G[\ln(\tau_\alpha)]$ is by a factor three broader than that in bulk toluene ($\beta_{CD\text{conf.}} = 0.125 \pm 0.005$, $\beta_{CD\text{bulk}} = 0.32$ [106]). The finding of a broad $G[\ln(\tau_\alpha)]$ is consistent with investigations using inelastic neutron scattering [3, 43, 97]. ‘Two phase’ spectra are also recorded in the case of confined toluene confirming the broad character of the distribution (cf. Fig. 4.8).

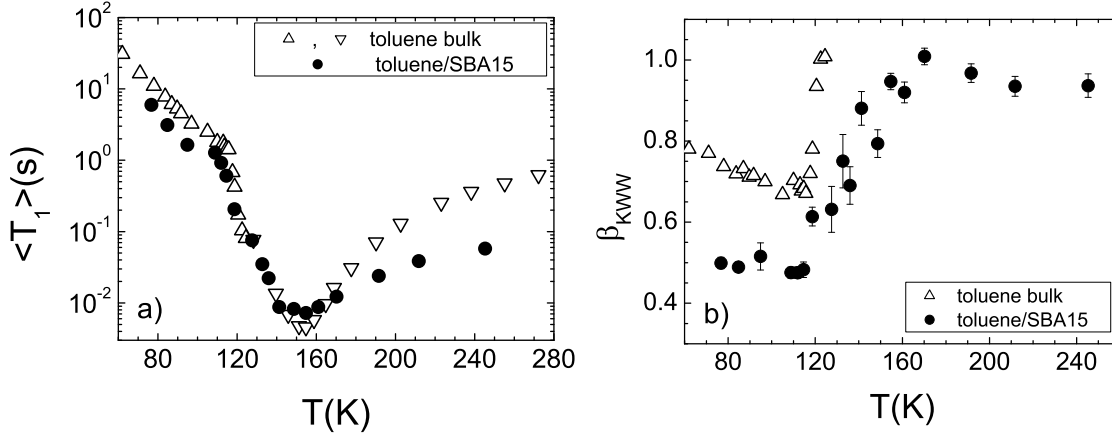
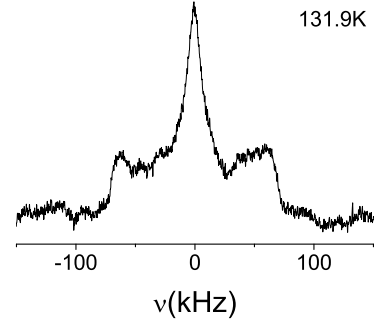


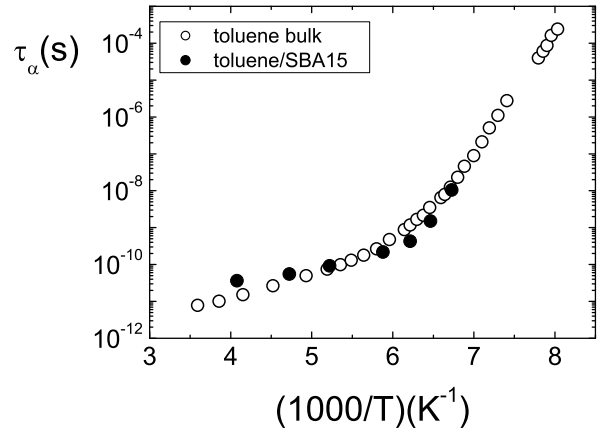
Figure 4.7. a) Spin-lattice relaxation time $\langle T_1 \rangle$ for bulk toluene- d_5 (triangles up: data from [129], $\omega_L/2\pi = 46 \text{ MHz}$; triangles down: data from [106], $\omega_L/2\pi = 55 \text{ MHz}$) and for toluene- d_5 in SBA-15 ($\omega_L/2\pi = 46 \text{ MHz}$). b) Stretching parameter β_{KWW} for the spin-lattice relaxation function for bulk toluene- d_5 (from [129]) and in confinement.

Figure 4.8. Solid echo spectrum for toluene-d₅ confined in SBA-15. Despite the fact that the signal to noise ratio is low, the ‘two phase’ structure is distinguishable (a fingerprint of broad distribution of correlation times $G[\ln(\tau_\alpha)]$).



For temperatures higher than T_{min} we analyzed the $\langle T_1 \rangle$ data of toluene-d₅ in a manner analogous with the one employed for OTP-d₁₄, assuming a Cole-Davidson distribution of correlation times. The so estimated correlation times for toluene in SBA-15 are depicted in Fig. 4.9. One can see that they are somewhat different from those corresponding to bulk toluene but the difference is not so large as in the case of bulk and confined OTP (cf. Fig. 4.6).

Figure 4.9. Correlation times calculated from ²H spin-lattice relaxation time $\langle T_1 \rangle$ for bulk toluene-d₅ (data from [59], $\omega_L/2\pi = 55.8 \text{ MHz}$) and for toluene-d₅ in confinement ($\omega_L/2\pi = 46 \text{ MHz}$).



Comparing the stretching parameters β_{KWW} for bulk and confined toluene-d₅ we see that the spin-lattice relaxation is more stretched in confinement (cf. Fig. 4.7 (b)). Regarding the α -process, although β_{KWW} for bulk toluene-d₅ is not measured at temperatures higher than roughly 120 K we may assume that it stays constant and close to a value of 1, typical of an exponential spin-lattice relaxation in a normal liquid. If this were the case then the confinement data would depart from an exponential relaxation

at temperatures much higher than those of the bulk toluene (similar to what we found for OTP-d₁₄).

Analysis of the β -process

The low temperature behavior of toluene-d₅ (i.e. for $T < T_{min}$) deserves special attention. While for temperatures down to, say, 120 K $\langle T_1 \rangle$ of toluene-d₅ in SBA-15 is similar to that of bulk toluene, for lower temperatures it becomes shorter so that the last measured points are significantly different from the bulk data (in contrast to OTP-d₁₄ where at low temperatures $\langle T_1 \rangle$ in bulk and confinement is similar). One expects that the spin-lattice relaxation features at temperatures $T < T_g$ are dictated by the β -process as the α -process has become too slow. Hence, we can conclude that not only the α -process but also the β -process is affected by confinement.

By inspecting the normalized spin-lattice relaxation curves at low temperatures (cf. Fig. 4.10 (a)) we see that those corresponding to the confined toluene are more stretched than the ones of bulk toluene. Thus, besides the mean spin-lattice relaxation time $\langle T_1 \rangle$ also the width of the distribution of spin-lattice relaxation times $g(T_1)$ determining the extend of non-exponential relaxation is altered under confining conditions. Nevertheless, the long time end of the relaxation curves looks similar in both systems. In order to explain this feature we refer to the work of Hinze et al. [58] which demonstrated, using reasonable assumptions, that the long time end of the spin-lattice relaxation traces is damped due to spin-diffusion. Therefore we tentatively conclude that time constant of the spin-diffusion is similar in bulk as well as confined toluene.

In the glassy state (i.e. $T < T_g$) no dynamical exchange is expected and the non-exponential spin-lattice relaxation reflects the heterogeneous dynamics of the β -process. The normalized spin-lattice relaxation function provides the average [28, 58]:

$$\psi(t) = \int g(T_1) e^{-t/T_1} dT_1 = \langle e^{-t/T_1} \rangle. \quad (4.1)$$

Convoluting an exponential decay with a log Gauss distribution $g(T_1)$ an estimate of $g(T_1)$ may be obtained. As illustrated in Fig. 4.10 (b), the distribution in the confinement appears significantly broadened towards faster times. However, a clear-cut conclusion concerning the change of distribution $G[\ln(\tau_\beta)]$ is not straightforward. In the glassy state, if one assumes that the structural relaxation (i.e. α -process) no longer contributes to the spin-lattice relaxation, then the following equation holds [22]:

$$\frac{1}{\langle T_1 \rangle} \propto \left\langle \frac{1}{T_1} \right\rangle \propto (1 - S) J_\beta(2\omega_L), \quad (4.2)$$

with ω_L being the Larmor frequency and $J_\beta(\omega)$ the spectral density of molecular re-orientation (for details on the equations describing the spin-lattice relaxation, see Section 2.4). In the equation above S is the fraction of correlation relaxed by the α -process.

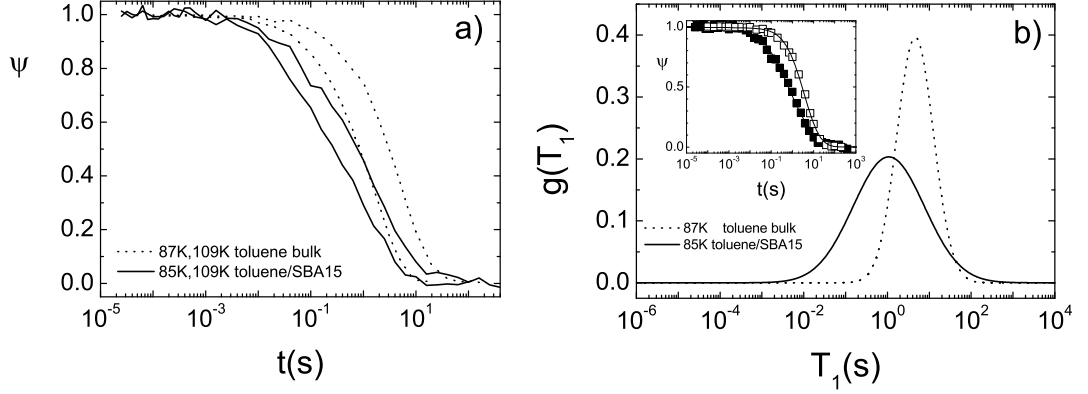


Figure 4.10. a) Comparison between spin-lattice relaxation functions of toluene bulk and toluene in SBA-15 at two similar temperatures. b) Distribution of relaxation times $g(T_1)$ (log Gauss) reflecting in first approximation the distribution $G[\ln(\tau_\beta)]$ of the β -process in toluene. Inset: relaxation curves fitted by a log Gauss; solid symbols: toluene in SBA-15 at $T = 85$ K, open symbols: bulk toluene at $T = 87$ K.

In a strict sense the above equation holds only for one site in the glass because the relaxation strength $(1 - S)$ may depend on the site. The β -process is slow with respect to the NMR time scale (i.e. $\omega_L \tau_\beta \gg 1$) hence, for a given site $1/T_{1,i} = \mathcal{K}(1 - S_i)/\tau_{\beta,i}$, (where \mathcal{K} is an ^2H NMR coupling constant) and we can rewrite Eq. 4.1:

$$\langle e^{-t/T_1} \rangle = \sum_i e^{-t/T_{1,i}} = \sum_i e^{-t\mathcal{K}(1-S_i)/\tau_{\beta,i}}, \quad (4.3)$$

where the sum is over all sites. Thus, regarding the difference observed between the relaxation functions in confinement and in bulk, one can not decide whether the distribution $G[\ln(\tau_\beta)]$ or the distribution of $(1 - S)$ or both have changed. Only in the case, where $(1 - S_i)$ and $\tau_{\beta,i}$ are independent of each other and the distribution of $(1 - S)$ is unaltered in the confinement, the change of the distribution $g(T_1)$ can be directly traced back to a change of the distribution $G[\ln(\tau_\beta)]$. Since the different $(1 - S_i)$ are not expected to change by an order of magnitude, one may argue that the large changes observed in $g(T_1)$ on a logarithmic scale are to large parts due to changes of $G[\ln(\tau_\beta)]$ (cf. Fig. 4.10 (b)). Thus the dynamics of the β -process are considerably influenced by the confining conditions.

4.4. Summary and conclusion

Presenting NMR results on type A and type B glass formers in confining geometry we found that the $G[\ln(\tau_\alpha)]$ is considerably broadened and it is heterogeneous. In addition, the mean time constant $\langle T_1 \rangle$ exhibits a different temperature dependence in the confinement as compared to the bulk. We emphasize that neither in the spectra nor in the spin-lattice relaxation we saw indications of immobilized molecules at $T > T_g$, but rather a continuous broad distribution $G[\ln(\tau_\alpha)]$ was observed. Thus, it may be possible that the dynamics gradually slows down, being faster in center of the pore and slower at the surface, a situation encountered by solvation dynamics experiments on confined methylpentane [102] and neutron spin echo measurements on confined OTP [43], and also by recent MD simulation of a Lennard-Jones binary liquid [111, 121]. Then, however, exchange among the different subensembles is slow with respect to the time scale of the reorientational dynamics.

Regarding the β -process its distribution $g(T_1)$ is also significantly broadened in confinement. In the presence of a heterogeneous distribution of correlation times it is not straightforward to conclude from a single averaged time constant whether the dynamics accelerates in the confinement. The full information can only be obtained by the corresponding distribution functions. For toluene, NMR allowed us to determine the distribution $g(T_1)$, which extends to shorter time constants in the confinement. The finding that the distributions are similar at the long time side may be an artifact since here spin-diffusion (magnetization exchange without mass transport) may average the relaxation. Thus, although the β -process is believed to be a ‘local’ process it is strongly changed in a 7 nm confinement. We are inclined to attribute the changes in the confinement to finite size effects since previous experiments have demonstrated that, in the case of toluene in SBA-15 close to the glass transition temperature finite size effects dominate the dynamics for pore diameter $d > 5\text{ nm}$ [89]. However, from the present experiments we cannot strictly decide whether the geometry (in terms of the angular amplitude of the spatially restricted motion) and/or the dynamics are modified. To disentangle both contributions is not an easy task. Maybe future line shape experiments can settle this point.

Concerning the excess wing in OTP the NMR results show that although the glass transition temperature is changed in confined OTP with respect to bulk, the $\langle T_1 \rangle$ values corresponding to the ‘region’ where they are governed by the excess wing are very similar in both systems at the same absolute temperature. This may be an indication that the excess wing is a very ‘local’ one, depending only on absolute temperature. However in the OTP in SBA-15 case, the presence of an attractive surface plays a major role, in addition to a possible decrease of the confined density when compared to the bulk. Under such conditions a change of the excess wing should not be expected and further experiments with larger pore sizes will shed light on the matter.

5. Relaxation Processes in Polybutadiene and a Mixture of Benzene in Polybutadiene

5.1. Introduction

It is well established that, in addition to the main relaxation (α -process), polymers exhibit secondary relaxation processes that determine the relaxation behavior in the glassy state, i.e. below the glass transition temperature T_g [32, 72, 84, 143]. Often these processes are attributed to motions of side groups or to conformational changes within the main chain. Secondary relaxation processes, however, are also observed in polymers without side groups, a prominent example being polybutadiene (PB) [13, 34, 37, 74, 55, 105]. A ^2H NMR study including line shape and stimulated echo analyses of PB was performed in our group by Vogel (e.g [129, 134, 136]) and his work focused on explaining the features of the β -process, investigating the temperature range close to T_g . The present work was started in order to extend the ^2H NMR line shape analysis at temperatures well below T_g . In addition high precision dielectric spectroscopy (DS) measurements were performed by Gainaru down to 4 K [50, 81] in order to test the conclusions of the NMR analysis. Finally, a mixture of benzene- d_6 in polybutadiene was investigated to obtain further information about the relaxation processes in PB. As it will be demonstrated a third relaxational process (in addition to α and β) will be identified and characterized by ^2H NMR and DS.

5.2. Some physical properties of polybutadiene

Polybutadiene (1,4-polybutadiene) is a polymer with a simple structure that made it a preferred subject of investigations for various techniques (cf. [39] and references therein). It may contain any of the three base units displayed in Fig. 5.1 and the percentage of *cis*, *trans* and *vinyl* in a specific sample depends on the chemical method used to prepare it [61, 108]. Regarding future comparison between NMR and DS results, it is worth mentioning that the *trans* group has no dipole moment [61]. The polymer can be prepared within a large range of molecular weights, starting from around 300 g/mol till more than 300000 g/mol (for example, samples provided by Polymer Standard

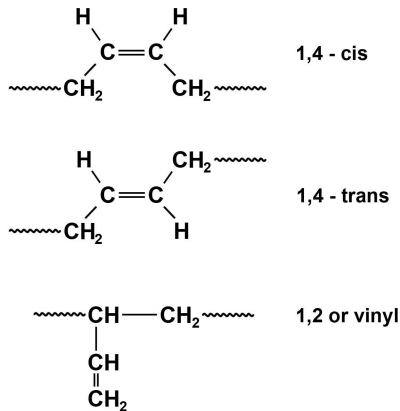


Figure 5.1. The possible units of 1,4-polybutadiene (from [61]).

Service). Among others, Hofmann et al. [61] proved that T_g of PB is strongly dependent on the content of *vinyl* units in polymers with similar molecular weight. That is, in a sample with 7% *vinyl*, T_g determined using dielectric spectroscopy is 171 K, while in sample with 95% *vinyl* $T_g = 268$ K. Therefore care should be taken when assuming the same T_g for samples with similar molecular masses.

5.3. Experimental details

5.3.1. Samples used in the NMR measurements

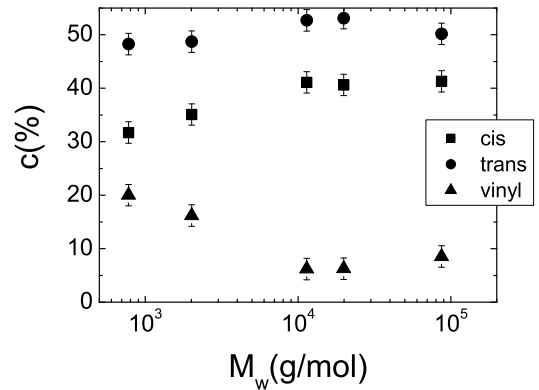
For the ^2H NMR experiments we used 1,4-polybutadiene- d_6 (PB- d_6 , $M_w = 80000$ g/mol, courtesy of D. Richter, Jülich) previously employed for studies done by Rössler et al. and Vogel et al. [107, 134, 136]. Also a mixture of 9.4% weight percent benzene- d_6 in 1,4 polybutadiene (bnz- d_6 +PB-777, $M_w = 777$ g/mol) was investigated. Benzene- d_6 was purchased from Sigma-Aldrich while PB-777 from Polymer Standard Service (Mainz, Germany) and both compounds were used without further purification. For the sample PB- d_6 we employed $T_g = 181$ K as reported in Ref.[107]. In the case of the mixture an DSC experiment was performed providing $T_G = 164$ K (for the definition of T_G see Appendix D).

5.3.2. Samples used in the dielectric spectroscopy measurements

In the dielectric experiments the following protonated samples were measured: 1,4 polybutadiene with $M_w = 577$ g/mol (PB-577), $M_w = 777$ g/mol (PB-777), $M_w = 1450$ g/mol (PB-1450), $M_w = 2010$ g/mol (PB-2010), $M_w = 11400$ g/mol (PB-11400), $M_w = 19900$ g/mol (PB-20000) and $M_w = 87000$ g/mol (PB-87000). All samples

were purchased from Polymer Standard Service and used as received. In order to find the concentration of *cis*, *trans* and *vinyl* units in the samples a ^{13}C high resolution study was performed on PB-777, PB-2010, PB-11400, PB-19900 and PB-87000 (details of measurements and one representative spectrum are presented in Appendix D). Fig. 5.2 shows the obtained results and one can see that the *trans* concentration is roughly constant disregarding molecular mass M_w ($\approx 50\%$). On the other hand, the *cis* concentration is slightly decreasing with decreasing M_w from around 40% till more than 30% at the lowest measured M_w . Correspondingly, the *vinyl* content is increasing with decreasing molecular mass from roughly 10% to 20%.

Figure 5.2. The concentration of repeating units in several employed polybutadiene samples.



Besides the ones already mentioned, a sample with $M_w = 25000 \text{ g/mol}$ (PB-25000) and 7% *vinyl* manufactured by Scientific Polymer Products Inc. (USA) was investigated (courtesy of A. P. Sokolov, University of Akron, Akron, USA) since a light scattering study was done on this polymer by Ding et al. [39].

A partially deuterated polybutadiene- d_{2,h_4} ($M_w = 18000 \text{ g/mol}$, PB-18000- d_2 , courtesy of D. Richter, Jülich) was included in the DS experiments, too.

5.3.3. Measurements parameters

NMR measurements

The NMR spectra were measured applying a solid echo pulse sequence preceded by a saturation sequence (five 90° pulses). We chose a time period t_d between the saturation and the solid echo sequences so that more than 95% of the equilibrium magnetization was probed. For the sample PB- d_6 a Bruker CXP 300 spectrometer equipped with a TecMAG data acquisition system was used and for the 9.4% benzene- d_6 in PB-777 sample a Bruker DSX 400 spectrometer. For both spectrometers, the same superconducting magnet was employed, with a magnetic field strength of 7.05 T correspond-

ing to a ^2H Larmor frequency of 46.07 MHz . The pulse length for the 90° pulse was about $2.3\text{ }\mu\text{s}$ for PB- d_6 and $2.7\text{ }\mu\text{s}$ for bnz- d_6 +PB-777. The spin-lattice relaxation time was measured by applying the saturation recovery sequence. The spin-spin relaxation time was obtained by measuring the echo height for different interpulse delays t_p in the solid echo sequence. The samples were placed in a home built low temperature probe inserted in an Oxford static cryostat CF 1200 providing a temperature stability better than 0.2 K .

Dielectric spectroscopy measurements

The dielectric measurements were performed by Gainaru [50, 81] employing an Andeen Hagerling AH 2700 A high precision capacitance bridge and the instrument covered a frequency range from 50 to 20000 Hz with a resolution $\tan(\delta) \geq 2 \times 10^{-6}$. Broad band dielectric measurements were additionally performed in several cases using a Schlumberger SI 1260 phase gain amplifier together with a BDC current to voltage converter from Novocontrol (the setup provided a frequency range from 10^{-3} to 10^7 Hz). A temperature stability better than 0.2 K was achieved by placing the samples in an Oxford CF 1200 dynamic cryostat. The design proposed by Wagner and Richert [138] was used in constructing the sample cell made of gold plated Invar steel to provide thermal invariance of the geometric capacitance ($C_0 \simeq 30\text{ pF}$).

5.4. Neat polybutadiene: NMR results and discussion

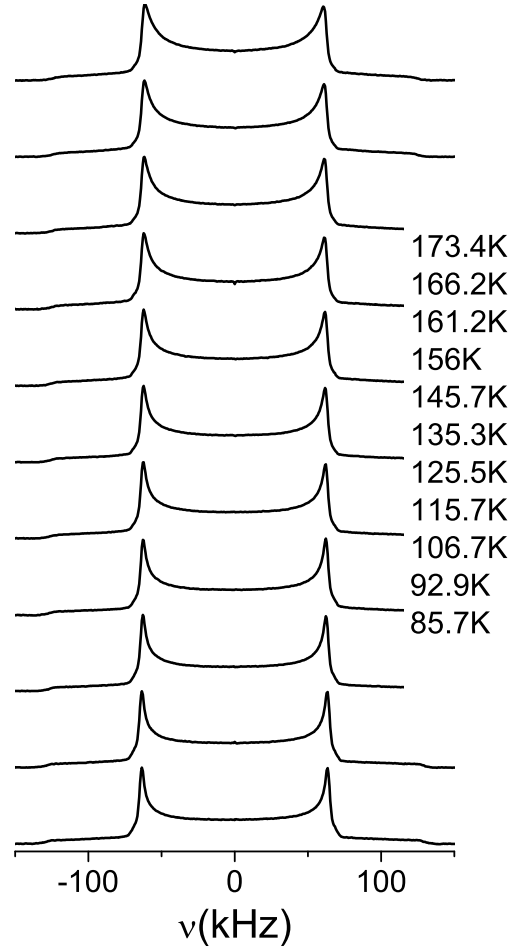
5.4.1. Solid echo spectra measured with a short interpulse delay

In Fig. 5.3 we display the spectra of polybutadiene- d_6 with the molecular weight $M_w = 80000\text{ g/mol}$ (PB- d_6) measured at temperatures below T_g , with an interpulse delay $t_p = 20\text{ }\mu\text{s}$. The spectra are almost identical and similar to a Pake spectrum. This is an indication that, if any molecular motion is present in the time window of the experiment, it has a very small angular amplitude [129, 133]. Because of the closer resemblance of the spectral shape one cannot obtain indepth information about the molecular motion below T_g therefore further experiments are required.

5.4.2. Solid echo spectra for different interpulse delays

As discussed in the theoretical section, the presence of secondary processes with highly restricted angular amplitude can be revealed by measuring t_p dependent solid echo ^2H NMR spectra [132, 134, 135, 136]. To demonstrate the capability of such experiments we first summarize previous ^2H NMR results for toluene, which exhibits a strong β -process as revealed by dielectric spectroscopy (DS) [74]. In Fig. 5.4 (a) we present solid echo spectra of toluene- d_5 measured below $T_g = 117\text{ K}$, where the spectra are

Figure 5.3. Solid echo spectra of polybutadiene-d₆ ($M_w = 80000 \text{ g/mol}$, PB-d₆) measured with the interpulse delay $t_p = 20 \mu\text{s}$ at temperatures below T_g .



normalized to their maximum value. At $T = 110 \text{ K}$ the spectrum for $t_p = 20 \mu\text{s}$ is essentially given by a Pake spectrum. However with increasing t_p the line shape changes: the central region of the spectrum decreases with respect to the height of the ‘singularities’. This line shape change is typical of small angle fluctuations which can be probed only for long t_p values [133, 136]. Upon cooling the line shape effects become smaller and finally at $T \simeq \frac{1}{2}T_g$ the spectra for different values of t_p are indistinguishable and described by a Pake spectrum. To account for these experimental findings one should keep in mind that the relaxation strength of the β -process is essentially constant below T_g , as proven by DS [74]. Then we can explain the temperature dependence of the solid echo spectra by the shift of the distribution $G[\ln(\tau_\beta)]$ through the experimental time window. While close to T_g the β -process lies right in the time window of the line shape analysis (microseconds time scale), it is too slow to be probed any longer by the

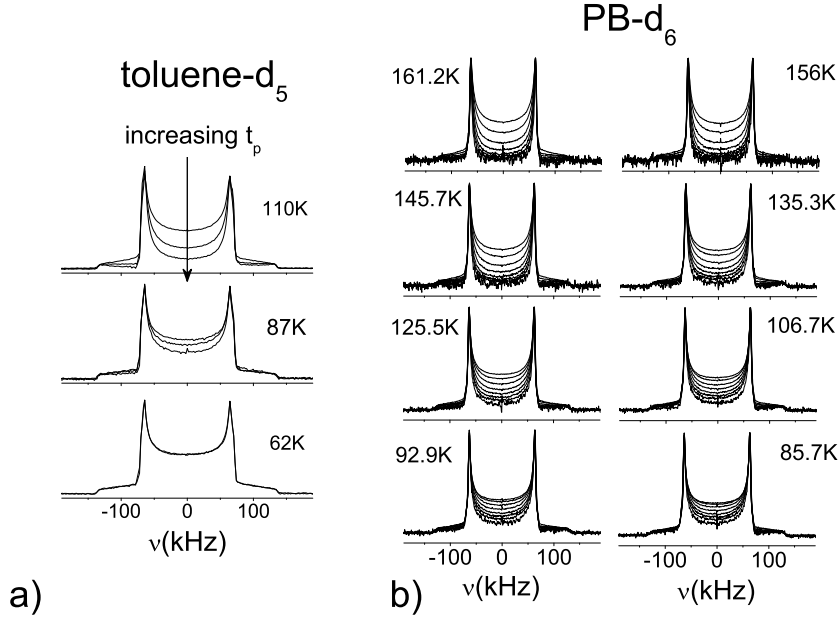


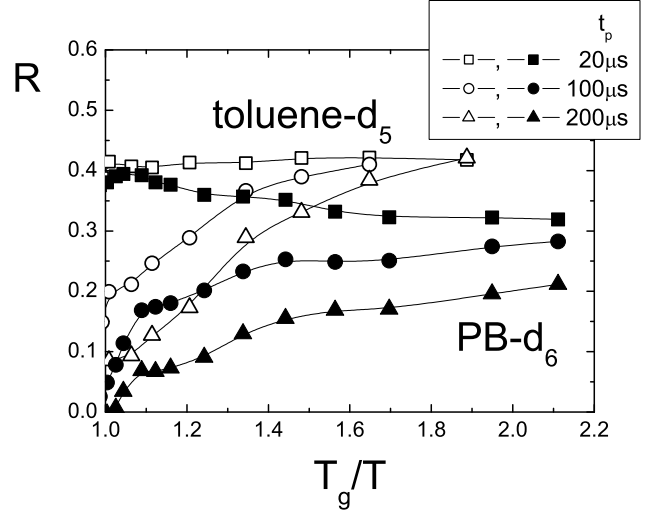
Figure 5.4. Normalized solid echo spectra as a function of solid echo pulse delay t_p at different temperatures for a) toluene- d_5 ; t_p values are 20, 100, 200 μs for the two highest temperatures and 20, 200 μs for 62 K (from Vogel [129]). b) Corresponding spectra for PB- d_6 , t_p values are 20, 50, 100, 150, 200, 250, 300, 400 μs . For both pictures, the larger is the area of the spectrum, the smaller t_p .

spectra at $T = \frac{1}{2}T_g$.

From DS experiments it is known that the β -process of PB and toluene show similar features [136], i.e. the same reduced activation energy E_a/T_g , a comparable exponential prefactor in the Arrhenius law and a similar relaxation strength with respect to that of the α -process are found. Therefore we performed the same t_p dependent measurements of the spectra for PB- d_6 and the results are shown in Fig. 5.4 (b). The spectra observed at $T = 161.2 K$ are similar to those for toluene- d_5 slightly below T_g indicating that they are typical of the β -process. However, unlike for toluene, the t_p dependence of the spectra does not change in a significant manner when lowering the temperature. At $T = 86 K$ ($T < \frac{1}{2}T_g$) the line shapes for various t_p values are still clearly different. Thus on the T/T_g scale, the PB- d_6 spectra show a different dependence than those of toluene. While the features of the solid echo spectra of PB- d_6 close to T_g can be explained as a consequence of the β -process, those at lower temperatures cannot since the β relaxation is already too slow to cause line shape changes, as shown by DS. Hence, the t_p dependence at, say, $T \leq \frac{1}{2}T_g$, can only be rationalized by the presence of

an additional motional process with a time constant much shorter than that of the β -process. We will call this relaxation process the γ -process.

Figure 5.5. Relative spectral intensity at zero frequency R (cf. Eq. 2.37) for toluene- d_5 and PB- d_6 , three solid echo pulse delays t_p are considered; lines are guides for the eye.



In order to quantify the changes in the solid echo spectra we present in Fig. 5.5 the quantity $R(t_p, T)$, measuring the relative spectral intensity at $\nu = 0$ (for further details on the definition, see page 17). At a given temperature, $R(t_p)$ is determined by the angular amplitude of the motion, the time constant of the rotational autocorrelation function τ_1 and by the width of $G[\ln(\tau_1)]$ function (for the definition of f_1 see Eq. 2.56 and the corresponding notes). Simulations have shown that $R(t_p)$ decays faster when the angle is larger, and, regarding the time τ_1 , the decay is the fastest when $\tau_1 = \frac{1}{\delta} \simeq 10^{-5} s$ (cf. Chap. 6). For toluene- d_5 near T_g there is a large difference between the values of $R(20 \mu s, 110 K)$ and $R(200 \mu s, 110 K)$ that results from the β -process. With lowering the temperature this difference decreases and reaches zero at $T \simeq \frac{1}{2}T_g$, indicating that the β -process exited the time window of the experiment. When inspecting the R values for PB- d_6 we see that the difference $R(20 \mu s, 161.2 K) - R(200 \mu s, 161.2 K)$ close to T_g is similar to that of toluene reflecting again the β -process. However, even at the lowest temperature, $R(20 \mu s, 85.7 K) \neq R(200 \mu s, 85.7 K)$, i.e. a strong t_p dependence of the line shape persists. This different behavior has to be attributed to the presence of the γ -process.

5.4.3. The apparent spectral width

NMR experiments can estimate the angular amplitude of molecular motion (cf. Eq. 2.9); given a motion faster than $1/\delta$, solid echo spectra should yield an averaged $\bar{\delta}$ (hence an averaged apparent spectral width C).

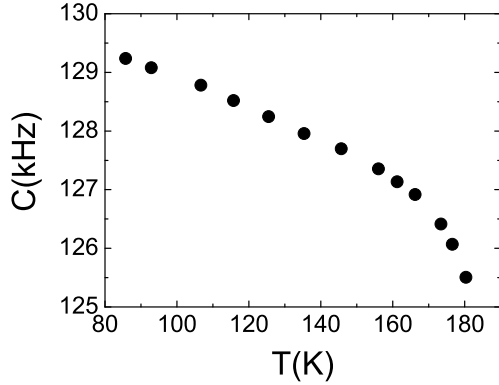


Figure 5.6. Apparent spectral width C vs. temperature T for PB-d₆ (spectrum measured with the solid echo pulse delay $t_p = 20 \mu s$).

In Fig. 5.6 we plotted the apparent spectral width C that is measured at 80% of the averaged singularity height (cf. page 17). As indicated in Fig. 5.6, C shows a significant dependence on temperature. The molecular weight of the sample used in the NMR experiments PB-d₆ ($M_w = 80000 \text{ g/mol}$) is close to that of a sample used in dielectric spectroscopy (DS) experiments PB-87000 ($M_w = 87000 \text{ g/mol}$). According to the DS results for the γ -process (cf. Section 5.6) at T_g $\tau_\gamma \simeq 10^{-9} \text{ s} \ll \frac{1}{\delta} \simeq 10^{-5} \text{ s}$ is found and thus a motionally averaged spectral width $\bar{\delta}$ is expected for the solid echo spectrum. Assuming that the change of the spectral width depicted in Fig. 5.6 (in the temperature range $80 - 180 \text{ K}$) is entirely caused by the γ -process we can estimate the upper bound of the angular amplitude of molecular motion within a simple cone model, by applying Eq. 2.35. More precisely, presuming that during the γ -process the $C-^2H$ bond of the PB molecule describes a cone, we found as an upper limit for the semiangle of the cone $\chi \simeq 8^\circ$. Hence, a highly restricted motional process is responsible for the γ -process, which is not easily associated with conformational changes of the polymer chain, which imply large angle motion. However, a behavior of $C(T)$ similar to that shown in Fig. 5.6 is found in many glass formers even when fast secondary relaxational processes are absent [28]. Thus the continuous change of C with temperature may be connected to vibrational phenomena or other fast processes. As a consequence the angular amplitude of the γ -process might be even smaller than 8° .

5.4.4. Spin-lattice and spin-spin relaxation

Spin-lattice relaxation times

Information about molecular motion can also be extracted from measurements of the spin-lattice relaxation [83, 112].

In Fig. 5.7 (a) we present the temperature dependence of the mean spin-lattice

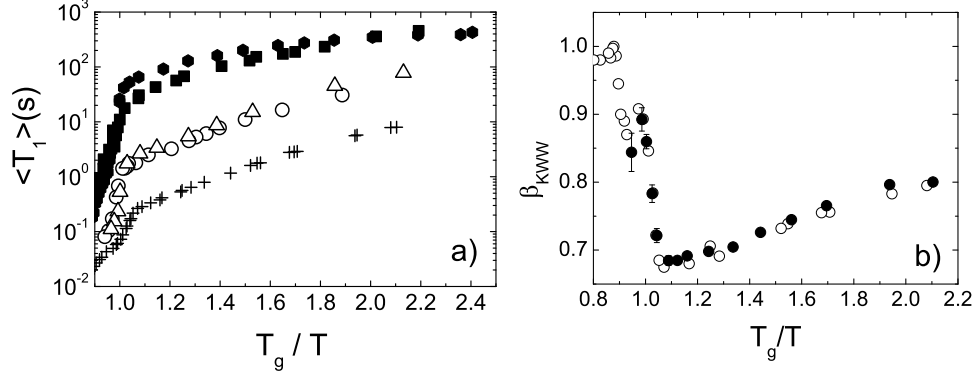


Figure 5.7. a) Mean spin-lattice relaxation times $\langle T_1 \rangle$ for some glass formers as a function of reduced reciprocal temperature T_g/T ; full squares: glycerol-d₅ ($\omega_L/2\pi = 55$ MHz, from [114]); full hexagons: o-terphenyl-d₁₄ ($\omega_L/2\pi = 55$ MHz, from [44]); open circles: toluene-d₅ ($\omega_L/2\pi = 46$ MHz, from [81, 129]); open triangles: 45% chlorobenzene-d₅ in decaline ($\omega_L/2\pi = 46$ MHz, from [71, 81]); plus signs: PB-d₆ ($\omega_L/2\pi = 46$ MHz, from [81, 129], including present work). b) The stretching parameter β_{KWW} for the normalized spin-lattice relaxation functions for PB-d₆, open circles: [129], full circles: present work.

relaxation time $\langle T_1 \rangle$ for several glass formers. Focusing on temperatures well below T_g we see that for glycerol-d₅ and o-terphenyl-d₁₄ (OTP-d₁₄), which do not exhibit a β peak but only the excess wing [74, 138], $\langle T_1 \rangle$ is significantly longer than for the other glasses. Regarding toluene-d₅ and 45% chlorobenzene-d₅ in decaline, which display a β -process [74, 136], $\langle T_1 \rangle$ is by more than an order of magnitude shorter than that of OTP-d₁₄, for example. The difference can be rationalized by Eq. 2.58 that connects T_1 and the spectral density $J_2(\omega_0)$: at $T < T_g$ the spectral density $J_2(\omega_0)$ is much larger in systems that exhibit a β -process than in those without one, hence a shorter $\langle T_1 \rangle$ is obtained. For PB-d₆ the $\langle T_1 \rangle$ values are even an order of magnitude shorter than those for toluene-d₅ and chlorobenzene-d₅ in decaline. This indicates an even larger spectral density, corroborating our conclusion that an additional process exists in PB.

The corresponding stretching parameter β_{KWW} of the normalized spin-lattice relaxation functions for PB-d₆ is displayed in Fig. 5.7 (b). It shows a typical behavior for a glass former: it is close to 1 at high temperatures, indicating an exponential relaxation. Then at temperatures slightly above T_g it strongly decreases till a minimum value at a temperature close to but lower than T_g . For even lower temperatures the value of β_{KWW} increases with a weak dependence on $\frac{T}{T_g}$ indicating that spin diffusion has now a large contribution to the spin-lattice relaxation function.

Spin-spin relaxation times

In Fig. 5.8 (a) we present the mean spin-spin relaxation time $\langle T_2 \rangle$ for PB-d₆. Below T_g $\langle T_2 \rangle$ is continuously increasing in contrast to its behavior for glass formers that do not display a β -process where it is very weakly temperature dependent. Moreover its slope is changing in a strong manner. Thus we tentatively assume that the dependence of $\langle T_2 \rangle$ on T_g/T is ‘dictated’ by the β -process close to but below T_g and by the γ -process at lower temperatures.

The stretching parameter β_{KWW} increases below T_g , reaching a plateau-like behavior between, say $1.4 < T_g/T < 1.8$ after which is increasing sharply. We interpret this finding as a further evidence that the γ -process affects the temperature dependence of $\langle T_2 \rangle$ at the lowest measured temperatures.

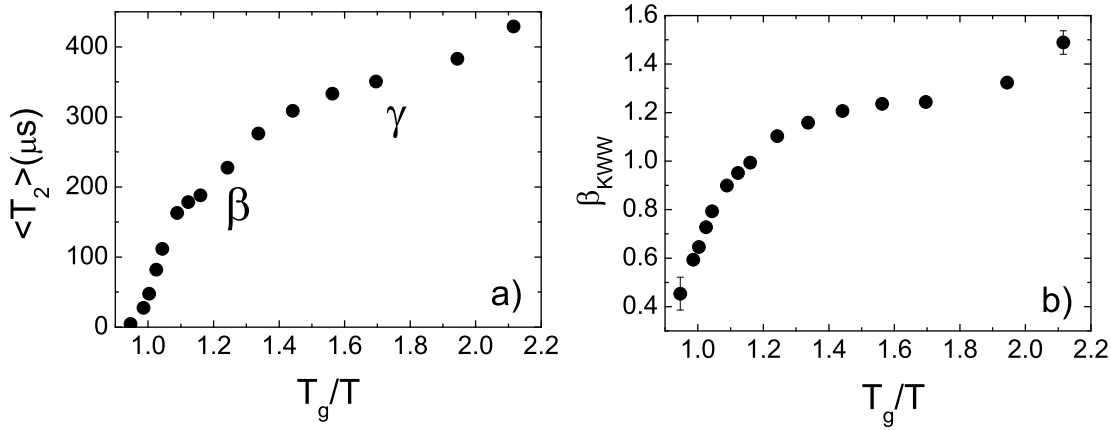


Figure 5.8. a) Mean spin-spin relaxation times $\langle T_2 \rangle$ for PB-d₆; we indicate the temperature range where the β and the γ -process are believed to influence the spin-spin relaxation. b) The corresponding stretching parameter β_{KWW} .

5.5. Benzene as a guest in polybutadiene: NMR results and discussion

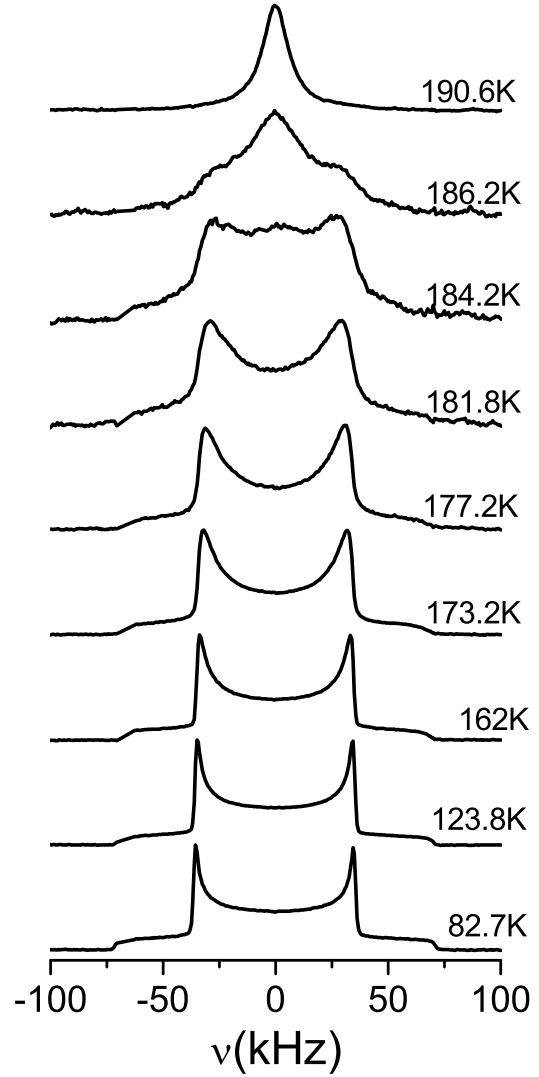
In order to further investigate the γ -process we studied by NMR a mixture of 9.4% benzene-d₆ in PB-777 (bnz-d₆+PB-777).

5.5.1. Solid echo spectra measured with a short interpulse delay

The ²H NMR spectra of bnz-d₆+PB-777 measured with an interpulse delay $t_p = 20 \mu s$ are displayed in Fig. 5.9. The spectra acquired at low temperatures have a reduced

spectral width because benzene- d_6 shows a rotation around its C_6 axis (see Eq. 2.35) [112]. The rotational motion is fast with respect to the ^2H NMR 1D time window in the investigated temperature range. Therefore, any change seen in the line shape is due to the reorientation motion of the C_6 axis. For temperatures below the glass transition temperature T_G the spectra are similar indicating that there is no large angular motion of the C_6 axis. Above T_G the line starts to collapse and finally, at $T = 190.6\text{ K}$ one sees an averaged spectrum, characteristic to an isotropic motion.

Figure 5.9. Solid echo spectra at different temperatures for 9.4% benzene- d_6 in 1,4-polybutadiene with $M_w = 777\text{ g/mol}$; the spectra are measured with a solid echo-pulse delay $t_p = 20\text{ }\mu\text{s}$.



The spectra for 184.2 and 186.2 K show features of a ‘two-phase’ spectrum indicating a distribution of correlation times $G[\ln(\tau_\alpha)]$ for the motion of the C_6 axis, feature not found in neat PB [130]. While generally a ‘two-phase’ spectrum is expected in binary mixtures (for example, [86]), the temperature range in which it manifests in our

experiment is rather small ($\Delta T < 6\text{ K}$) compared to previous reported results ($\Delta T > 20\text{ K}$ for benzene in oligostyrene [86]). Then, one can conclude that the width of $G[\ln(\tau_\alpha)]$ is significantly smaller in the present experiment. This might be caused by the fact that the glass transition temperature T_g for neat benzene- d_6 is close to T_G of the mixture $\text{bnz-}d_6 + \text{PB-777}$ ($T_g = 121\text{ K}$ as estimated from micro-emulsion experiments [45] and $T_G = 164\text{ K}$). On the other hand, when a large temperature range was observed for the ‘two-phase’ spectra of mixtures, the difference between the T_g of the observed compound and the T_G of the mixture was large (e.g. benzene in oligostyrene, where the mixture has $T_G = 240\text{ K}$ [86]).

5.5.2. Solid echo spectra for different interpulse delays

The solid echo spectra measured at temperatures below $T_G = 164\text{ K}$ for various interpulse delays t_p are displayed in Fig. 5.10. For all temperatures, the line shape strongly depends on t_p , indicating that molecular motion is present in the experimental time window. We remind the reader that the t_p dependence of the spectra in Fig 5.10 probes the reorientation of the C_6 axis and not that of the $C-^2H$ bonds.

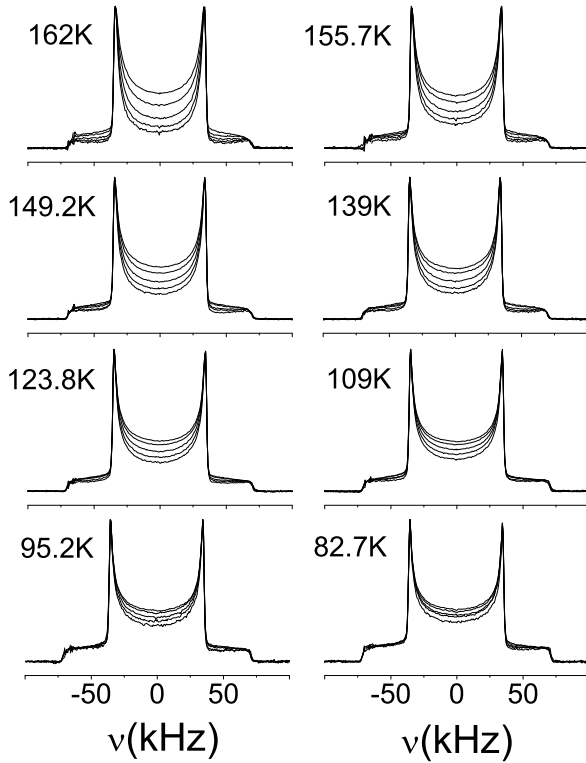


Figure 5.10. Normalized solid echo spectra for $\text{bnz-}d_6 + \text{PB-777}$ at temperatures smaller than T_G and various solid echo pulse delays t_p . The values of t_p are: 20, 50, 100, 150, 200 μs ; the smaller is t_p , the larger the area of the spectrum.

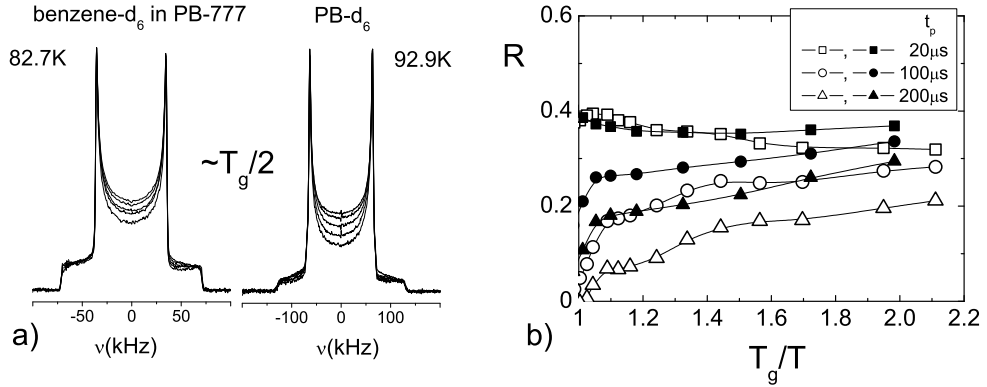


Figure 5.11. a) Comparison between $\text{bnz-d}_6 + \text{PB-777}$ and neat PB-d_6 at $T \simeq T_g/2$, t_p values are the same as in Fig. 5.10. b) R values, closed symbols: benzene-d₆+PB-777; open symbols: PB-d₆. Lines are guides for the eye.

In order to compare the findings in the mixture with those in neat PB, in Fig. 5.11 (a) a set of spectra for both $\text{bnz-d}_6 + \text{PB-777}$ and PB-d_6 are presented at the same reduced temperature $\sim T_g/2$ and $\sim T_g/2$. Clearly the spectra are similar. Although the line shape changes are a little more pronounced in neat PB-d_6 , the benzene-d₆ molecules show similar behavior as the neat polybutadiene; this is also seen when the R values are compared (see Fig. 5.11 (b)).

In the light of the results concerning the cone model simulations (cf. Chapter 6) a few details of Fig. 5.11 (b) worth a further discussion. For example, regarding the dependence of $R(t_p = 20 \mu\text{s})$ on T_g/T , one can see that for PB-d_6 the minimum value ($\min[R_{PB}(t_p = 20 \mu\text{s})] \approx 0.32$) is smaller than the one for benzene-d₆ ($\min[R_{bnz}(t_p = 20 \mu\text{s})] \approx 0.35$). Thus the average angular amplitude χ for the molecular motion in PB-d_6 is larger than in $\text{bnz-d}_6 + \text{PB-777}$ or the distribution of correlation times for $\text{bnz-d}_6 + \text{PB-777}$ is significantly broader than that for PB-d_6 . As the last possibility seems less probable (see the following results) we conclude that the C_6 axis of the benzene-d₆ molecules explores a somewhat smaller average angle than the $C-^2H$ bonds in PB-d_6 . Moreover, if one regards closely the lines for PB-d_6 it is seen that the R vs. T_g/T function presents two distinct regions: one that starts closely below T_g and lasts till $T_g/T = 1.5$ and a second one at higher values of T_g/T . They can be directly related to the manifestations of the β and γ -process, respectively.

We conclude that the motion of the benzene molecules reflects to some extent the motion of the PB segments involved in the β as well as in the γ -process.

5.5.3. The apparent spectral width

As a further analysis of the solid echo spectra we present in Fig. 5.12 the apparent spectral width C for bnz-d₆ in PB-777 as a function of temperature. It is observed that its values are around, say, 68 kHz as a consequence of the fast rotation around the C_6 axis. Nevertheless it shows basically the same temperature dependence as C for neat polybutadiene-d₆ (see inset in Fig. 5.6). At lower temperatures, when the C_6 rotation becomes slow one expects a further leading to a final value around 135 kHz or more.

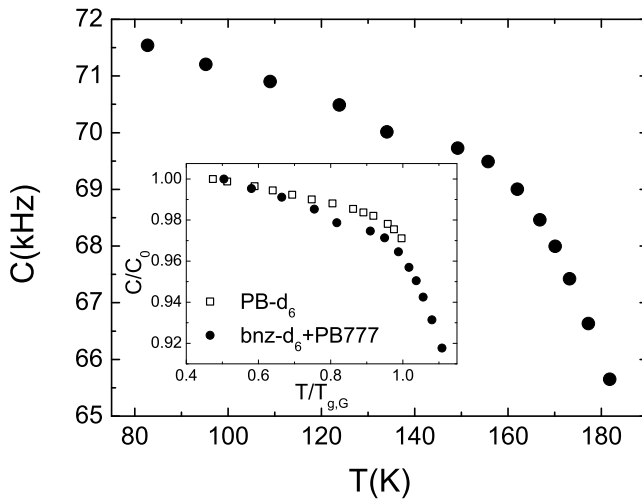


Figure 5.12. Apparent spectral width C vs. temperature T for bnz-d₆ in PB-777 (spectra measured with the solid echo pulse delay $t_p = 20 \mu s$). Inset shows a comparison of the normalized apparent spectral width vs. reduced temperature between the mixture and neat PB-d₆.

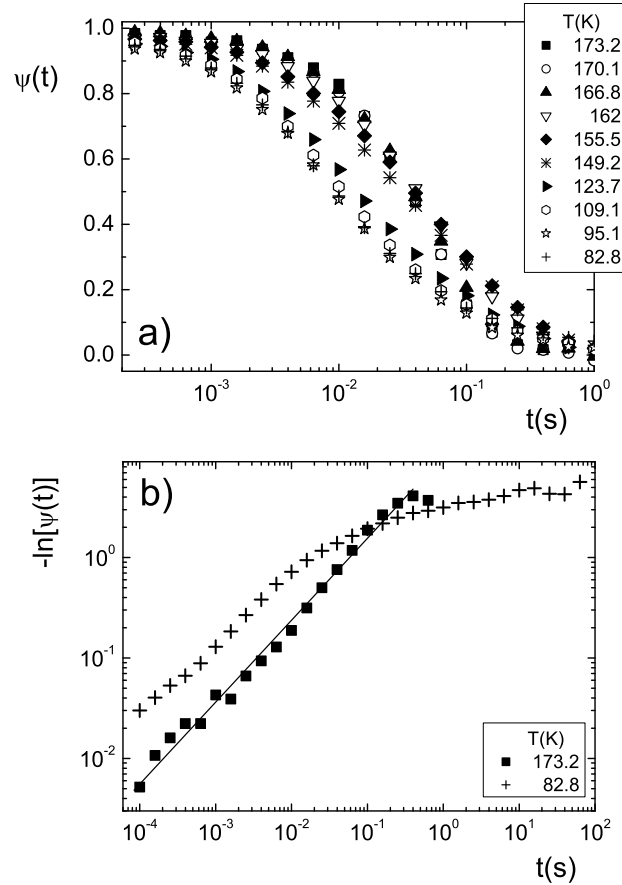
5.5.4. Spin-lattice and spin-spin relaxation

Spin-lattice relaxation

The spin-lattice relaxation function $\psi(t)$ for bnz-d₆+PB-777 in the temperature range investigated in this work is displayed in Fig. 5.13 (a). While above T_G the relaxation is almost exponential, at lower temperatures it becomes non-exponential, as expected for glasses. Still, there are several features that differ from a neat glass-forming liquid. First, the time scale of the decay for all $\psi(t)$ functions shows a weak temperature dependence. Second, $\psi(t)$ decays till zero relatively fast, in less than 1 s even for the lowest temperature ($\sim T_G/2$). That is faster than, for example, in case of polybutadiene that has $\langle T_1 \rangle(T_g/2) \simeq 7$ s or toluene $\langle T_1 \rangle(T_g/2) \simeq 30$ s. Third, although the spin lattice relaxation function is non-exponential at low temperatures, it cannot be interpolated by a KWW function (like, for example, in the case of neat PB) as can be more clearly

observed in the KWW representation in Fig. 5.13 (b). In this picture we plotted $-\ln[\psi(t)]$ for 173.2 K and it is seen that the experimental points can be interpolated by a straight line, proof that the KWW function can fit these data points. On the other hand, for 82.8 K the experimental points are not describing a straight line therefore they are not compatible with a KWW description.

Figure 5.13. Bnz-d₆+PB-777: a) The spin-lattice relaxation function $\psi(t)$ at different temperatures. (For the sake of clarity a narrow time scale is presented.) b) The spin-lattice relaxation functions for the lowest and highest measured temperature in Kohlrausch representation. Solid straight line is a guide for the eye.



The presented spin-lattice relaxation results are similar with the ones found by Roggatz et al. [104] for deuterated benzene in the glass former tricresyl phosphate. All these features can be attributed to the fact that the rotation motion around the C_6 axis is the main process that dictates the spin-lattice relaxation. In addition the spin diffusion that usually plays a role in neat glasses is too slow to have an influence in this case.

Spin-spin relaxation

In Fig. 5.14 (a) the spin-spin relaxation time $\langle T_2 \rangle$ is displayed as a function of reduced inverse temperature T_G/T . It reaches a minimum value around $T_G/T = 0.9$ and with further cooling is increasing till at a temperature somewhat below T_G it becomes temperature independent. The corresponding stretching parameter β_{KWW} (Fig. 5.14 (b)) has a similar behavior as function of T_G/T like $\langle T_2 \rangle$ with the difference that below T_G it still shows a weak dependence on temperature with its value around $\beta_{KWW} = 1.2$ reflecting a non exponential spin-spin relaxation function. We interpret this different behavior with respect to neat PB (cf. Fig. 5.8) as a proof that the spin-spin relaxation below T_G in bnz-d₆+PB-777 is dominated by effects due to the rotation motion of the benzene molecule around its C_6 axis.

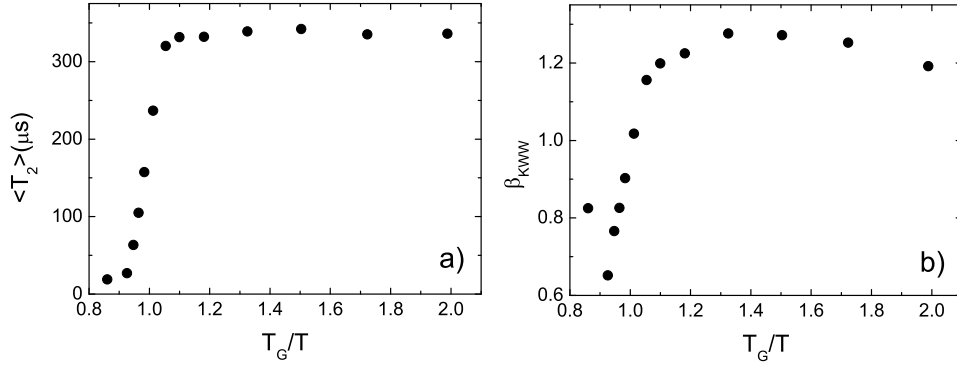


Figure 5.14. a) Mean spin-spin relaxation times $\langle T_2 \rangle$ for bnz-d₆ in PB-777 and b) the stretching parameter β_{KWW} .

5.6. Dielectric spectroscopy results and discussion

A straightforward way to study whether a third relaxation process exists in polybutadiene (PB) is to conduct a dielectric spectroscopy (DS) study. However, the small electric dipole moment of PB hampers such investigation for most experimental setups. Up to our knowledge no systematic low temperature PB dielectric study exists. We note that in a paper by Hansen and Richert [55] indications of a γ -process were presented but neither analyzed nor discussed. Therefore, initiated by the ²H NMR findings, Gainaru [50, 81] performed dielectric experiments in which the Andeen Hagerling high

precision bridge (cf. Section 5.3.3) was used in order to extend the accessible range of permittivity and to measure down to low temperatures.

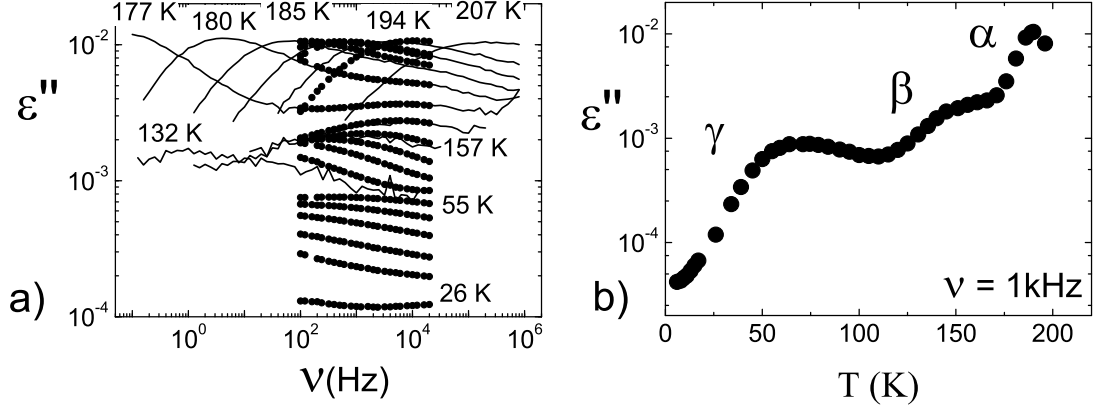


Figure 5.15. Imaginary part ε'' of the complex permittivity for 1,4-polybutadiene: a) as a function of frequency ν ; Lines are: broad band data from Kudlik et al. [74] ($M_w = 20000 \text{ g/mol}$); points: high precision bridge data ($M_w = 19900 \text{ g/mol}$) [50, 81]. b) The dependence of ε'' on temperature at fixed frequency $\nu = 1 \text{ kHz}$.

In Fig. 5.15 (a) the imaginary part ε'' of the complex permittivity is presented for two samples: PB with $M_w = 19900 \text{ g/mol}$ studied with the high precision bridge and PB with $M_w = 20000 \text{ g/mol}$ used in a former broad band experiments [74]. They have very similar molecular weights so that we will call them both PB-20000 in the following. Inspecting the broad band data, we see the main relaxation (α -peak) at high temperatures. With lowering temperature the peak shifts to lower frequency and a secondary peak (β -process) becomes visible. This β peak is the only feature observed at the lowest temperature (around $T = 130 \text{ K}$) in the broad band spectrum where the signal reaches the resolution limit of the setup ($\tan(\delta) \simeq 10^{-3}$). The spectral width covered by the high precision measurements is smaller than that of the former experiment but the improvement in ε'' resolution is obvious. Both data sets overlap at high temperatures. Around $T = 55 \text{ K}$ a new relaxation feature (a third peak) can be seen in the experimental frequency window. In Fig. 5.15 (b), where $\varepsilon''(\nu = 1 \text{ kHz})$ vs. T is displayed, this third relaxation peak is clearly recognized. The results prove that, in addition to the α and the β -process, a third process is present in PB-20000. Examining the temperatures as well as the time window in which the NMR line shape effects are observed we conclude that dielectric spectroscopy and NMR probe the same γ -process at low temperatures.

In the hope to improve our understanding of the nature of the γ -process PB samples with different molecular masses were investigated (see Section 5.3.2). In Fig. 5.16 we present $\varepsilon''(\nu = 1 \text{ kHz})$ normalized to its maximum value as a function of temperature for different polymers. The processes mentioned so far are recognized: the

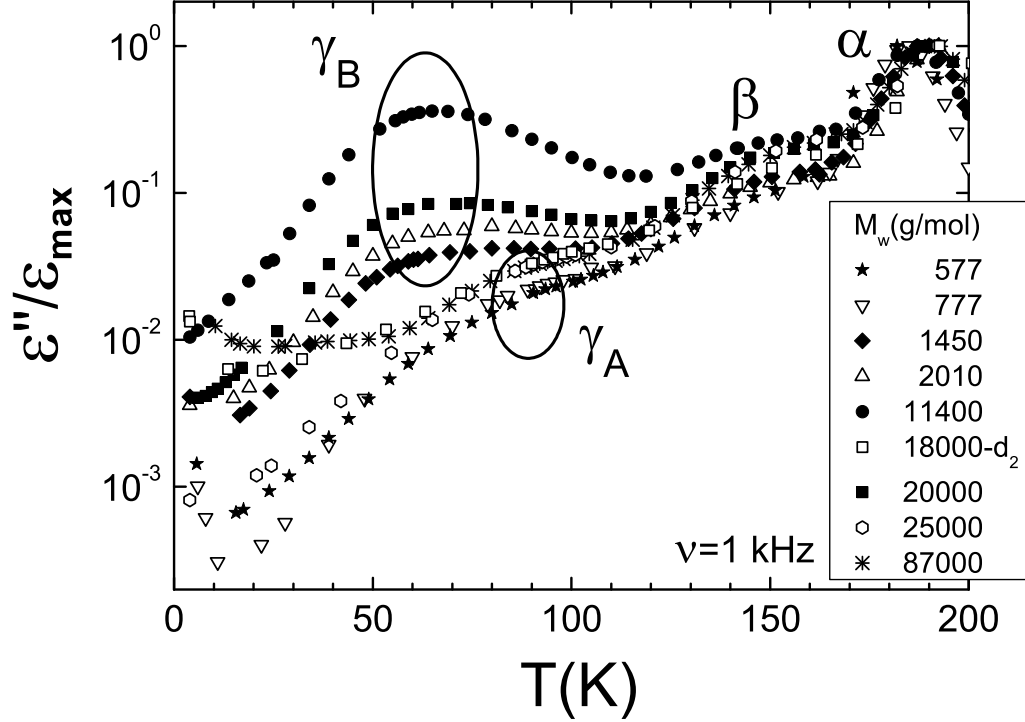


Figure 5.16. Normalized $\varepsilon''(1 \text{ kHz})$ vs. temperature T for PB samples with indicated molecular weight [50, 81].

α -process ($170 \text{ K} < T < 200 \text{ K}$), the β -process ($130 \text{ K} < T < 170 \text{ K}$) and the γ -process at temperatures lower than 130 K . We conclude that the γ -process is present in PB independent of the molecular weight. However, regarding the temperature dependence of the γ -process two groups can be distinguished: for PB-1450, PB-2010, PB-11400 and PB-20000 the peak lies around 60 K while for PB-577, PB-777, PB-18000- d_2 , PB-25000 and PB-87000 it is found roughly 20 K higher. For convenience we will denote the first group γ_B -PB and the second one γ_A -PB. Surprisingly, no systematic relation with the molecular weight or with the concentration of repeating units shows up (for the *cis*, *trans* and *vinyl* concentrations see Fig. 5.2).

While the relaxation strength of the β -process relative to that of the α -process is only slightly different, that of the γ -process strongly varies for the various polymers. For example, the value of $\varepsilon''(1 \text{ kHz})/\varepsilon''_{\max}(1 \text{ kHz})$ for the γ -process is roughly the same for all the γ_A -PB and it is by almost two orders of magnitude smaller than the value for

the α -process. In the group γ_B -PB, with augmenting molecular weight, the peak height is continuously increasing for PB-1450, PB-2010 and PB-20000. The sample PB-11400 is singular manifesting the strongest γ -process, with an amplitude of the peak of only a factor 3 smaller compared to that of the α -process. However, again no systematic dependence on molecular weight is found in both γ_A -PB and γ_B -PB groups. Generally we found the relation: $\Delta\varepsilon_{\gamma_B}/\Delta\varepsilon_\alpha > \Delta\varepsilon_{\gamma_A}/\Delta\varepsilon_\alpha$.

Spectra for which the γ -peak was clearly discernable were fitted with a log Gauss function $H[\ln(\nu)]$. From the frequency shift of the maximum ν_γ we estimated the time constant of the γ -process as $\tau_\gamma = 1/(2\pi\nu_\gamma)$. Due to the narrow frequency window of the high precision bridge a more advanced approach is not possible and for the low molecular weight samples (PB-577, PB-777) a quantitative analysis is hampered by a not well resolved γ -peak.

In Fig. 5.17 (a) we display the time constants obtained from DS as a function of the reciprocal temperature. For different molecular weights the curves τ_α vs. $1/T$ for the α -process have essentially the same temperature dependence, being slightly shifted because T_g is somewhat different. The time constants for the β -process show an Arrhenius temperature dependence with a somewhat different activation energies; note that $E_\beta/T_g \simeq \text{const.}$ is expected to hold [24, 74, 91]. Regarding the γ -process, one can see that it is well separated from both α and β -process and the two groups γ_A and γ_B are rediscovered. Among each group the time constants of the γ -process are very similar and they exhibit a thermally activated behavior. Inspecting the LS and DS data for the γ_A -PB class it is tempting to assume that the same process is probed though in quite different temperature ranges (as suggested by the straight line interpolation). Fits with an Arrhenius law on the DS time constants ($\tau_\gamma = \tau_0 \exp(E/RT)$) provide mean activation energies depicted in Fig. 5.18 (a). One can see that the activation energies are separated in two groups corresponding to the γ_A and γ_B -PB. The range for γ_B -PB reads: $11 < E_{\gamma_B} < 14 \text{ kJ/mol}$ and the one for γ_A -PB: $17 < E_{\gamma_A} < 22 \text{ kJ/mol}$. The prefactors τ_0 are in the range: $-13.5 < \log_{10}[\tau_0(s)] < -16.5$ (cf. Fig. 5.18 (b)).

5.7. Summary and conclusions

Both ^2H NMR and DS experiments on PB reveal that, in addition to the α and β -processes, a third process is present, which is called γ -process in this work. It shows the following features:

- i) The γ -process is significantly broader than a Debye process (see Fig. D.3 in the Appendix).
- ii) The time constants of the process exhibit an Arrhenius temperature dependence; two groups of polymers can be distinguished according the temperature dependence of their time constants. Within each group (γ_A -PB or γ_B -PB) a similar activation energy is found.

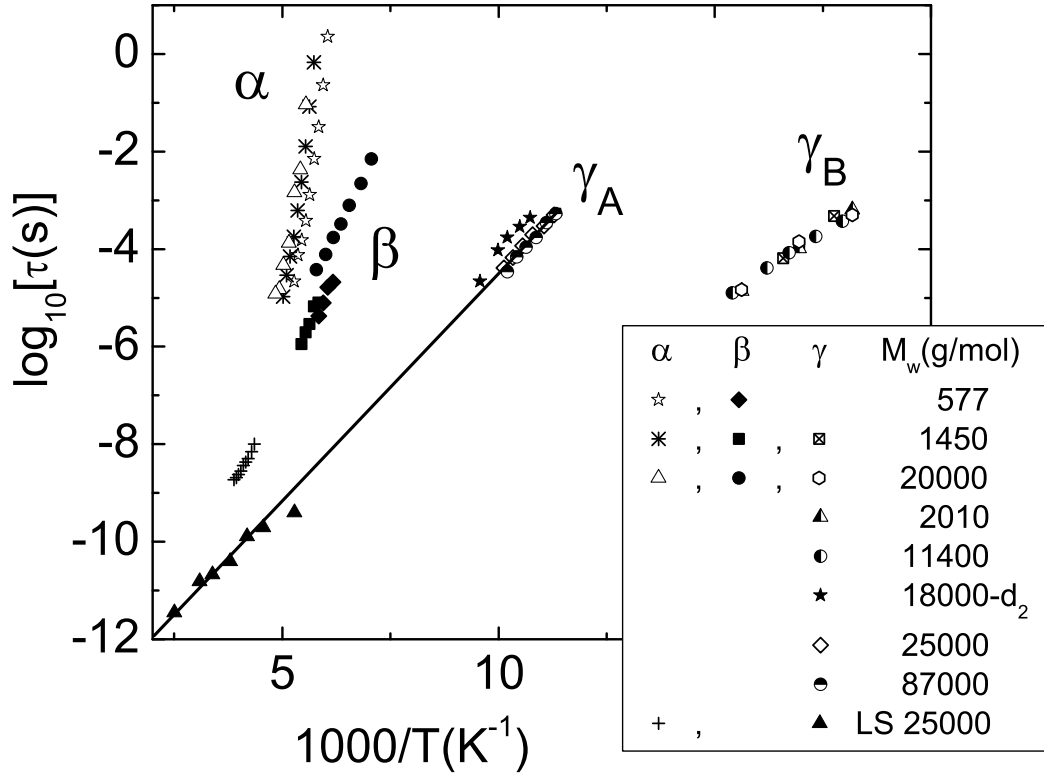


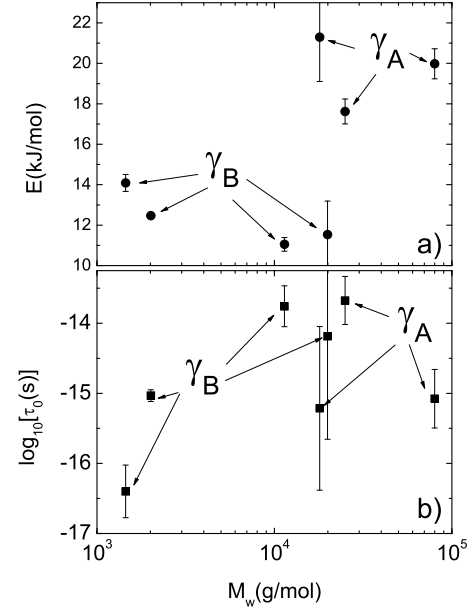
Figure 5.17. Time constants obtained from dielectric spectroscopy for the various processes in PB [50, 81]. Light scattering (LS) data from Ding et al. [39] are also included. Straight line is an Arrhenius interpolation.

- iii) The relaxation strength $\Delta\epsilon_\gamma$ varies strongly for the different polymers, no clear cut dependence on M_w or on the concentration of *cis*, *trans* and *vinyl* units is found. The relation $\Delta\epsilon_{\gamma_B}/\Delta\epsilon_\alpha > \Delta\epsilon_{\gamma_A}/\Delta\epsilon_\alpha$ is discovered.
- iv) Benzene as a guest molecule in PB participates in the γ -process.

Compiling the properties of the γ -process, we believe it is an intrinsic property of the PB polymers. We emphasize that we see no indication for both γ_A and γ_B being present simultaneously. Thus we assume tentatively that they have the same origin but different activation energies for reasons not yet understood.

There are several studies about processes other than α or β for PB, most of them focusing on the dynamics in the melt. For example Kanaya et al. [68], performing

Figure 5.18. a) Activation energies E vs. M_w obtained from an Arrhenius fit for the time constants of the γ -processes presented in Fig. 5.17. b) The corresponding prefactors τ_0 vs. M_w . [50, 81]



a neutron scattering study, report, in addition to the α -process, a process with an activation energy of $E \sim 10.5 \text{ kJ/mol}$. Aouadi et al. [12] applying Brillouin scattering, found an activation energy of $E = 20 \text{ kJ/mol}$. Finally, Brillouin and X-ray scattering by Fioretto et al. [47] reveal a process with $E = 7.2 \text{ kJ/mol}$. While the first two experiments were carried out above T_g the last one was done between 30 K and 330 K . The reported activation energies are within the range of the ones obtained in our study therefore we are inclined to believe that same γ -process is probed. Using light scattering (LS, GHz range, $T > T_g$), Ding et al. [39] investigated one of the polybutadiene samples studied here (PB-25000). They found a fast process in addition to the α -process, which cannot be identified as the β -process because the latter has already merged with the α -process in this temperature range. Its activation energy ($E = 15 \text{ kJ/mol}$ [39]) is close to the one we find ($E = 17.5 \text{ kJ/mol}$). A straight line interpolates well the time constants obtained from LS and DS (cf. Fig. 5.17) suggesting that their Arrhenius dependence on temperature is preserved from the glassy state to the melt.

Most of the authors ascribe the γ -process to conformational motions in the polymer chain. For example, Ding et al. [39] proposed that it originates from a rotation of the $-H_2C-CH=$ bond in the backbone of the polymer, explicitly: “fast counterrotation around the double bond allows the double bond to hop without disturbing other monomers along the chain”. Since in all cases the experiments were not directly probing a specific bond the statements concerning the provenance of the γ -process remained

somewhat speculative.

NMR experiments can estimate the angular amplitude of molecular motion (cf. Section 5.4.3) and applying a cone model the half opening angle χ is expected to have an upper bound of about 8° .

The angular amplitude of the γ -process can also be estimated from the DS spectra. As shown by Döss et al. [42], applying a cone model and making the approximation $\Delta\varepsilon_\gamma, \Delta\varepsilon_\beta \ll \Delta\varepsilon_\alpha$ one obtains for the cone semiangle χ : $\sin(\chi) \simeq (\Delta\varepsilon_\gamma/\Delta\varepsilon_\alpha)^{1/2}$. By using the amplitude of the relaxation peaks multiplied with its width as an estimate for $\Delta\varepsilon_\gamma$ and $\Delta\varepsilon_\alpha$ we get $\chi_{DS} \simeq 11^\circ$ for the sample PB-87000 (that has its M_w close to the one measured by NMR), which again reflects a small amplitude process. However, one should keep in mind that the DS relaxation strength of the investigated polymers varies strongly therefore also the estimated angular amplitude of the motion may be larger for some (an extreme case is PB-11400).

For the sample PB-25000 (measured by LS) we can conclude from the DS data that the angular amplitude of the molecular motion for the γ -process is very small, comparable to that of PB-87000. On the other hand, the LS data [39] from the melt suggest motion with a larger angular amplitude (as deduced from the intensity of the γ -peak compared to that of the α -peak). Then, in order to resolve this discrepancy it may be that the γ -process exhibits a similar property as the β -process: its relaxation strength increases above T_g but is small and essentially constant below as indicated by our NMR and DS experiments. In the case of the β -process this was concluded from NMR [134, 135], DS [74] and neutron scattering experiments [13]. Though, similar to the β -process, a small percent of molecules having a large angular amplitude cannot be ruled out. Again, it is not easy to explain such a behavior by a simple conformational change and it points into the direction that also the γ -process couples to structural relaxation (α -process). Moreover, the observation that a guest molecule (benzene) participates in the γ as well as in the β -process demonstrates that secondary processes in glasses cannot be described by single particle motion.

While the origin of the γ -process in PB remains to be unraveled, this work proves without doubt its presence and puts strong constraints on any model chosen to rationalize it. We emphasize once again that the strength of the γ -process varies strongly in the different polymers studied. However, there is no clear cut relationship between the manifestation of the γ -process and the molecular weight or concentration of the building units though two groups with essentially the same time constants are found. It is difficult to understand why the small amplitude motion (γ -process) varies strongly in the various polymers. Although the content of *cis*, *trans* and *vinyl* units is similar in the high molecular weights samples (see Section 5.3.2) it still may be possible that sequence distribution is different in a considerable way and this may change significantly the local microstructure in the glass ($T < T_g$) thus influencing the relaxation strength of the γ -process.

6. Random walk simulations related to the β -process

6.1. Introduction

The aim of the present study is to extract both time scale and geometry of the molecular motion involved in the β -process by performing random walk simulations (for technical details on simulations see Appendix C). Moreover, the goal is to find out if we can get these properties model independent and without using input parameters provided by other experimental techniques than ^2H NMR.

An extensive study on the β -process employing random walk simulations was carried out by Vogel who described simultaneously solid echo and stimulated echo data by using the same molecular motion model [129, 133, 135]). In that model, the distribution of correlation times $G[\ln(\tau_\beta)]$ was used as measured by dielectric spectroscopy (DS). The experimental data for toluene were satisfactory reproduced by the random walk simulations by properly choosing the geometric parameters of the model (cf. Fig. 1.4). Unlike Vogel, we tested if it is possible to obtain information not only on the geometry but also on the time scale and the distribution of $G[\ln(\tau_\beta)]$ from the ^2H NMR data solely. This work focuses only on solid echo simulations as they are a favorable starting point in terms of computing time and simplicity of line shape analyses. Therefore terms as apparent spectral width C and relative spectral intensity R , already encountered in the previous chapters, will be discussed in the following and several conclusions of this work were already used along the thesis. We remind the reader that the β -process has a very subtle influence on the line shape of the solid echo and in order to obtain detailed informations about it one records a series of solid echoes with different interpulse delay t_p . Hence, the same procedure was applied in the simulations, too.

Before starting we would like to present the frame-work of the simulations and define two correlation times that are important in order to understand the next part of the chapter. As translational motion cannot be directly detected by solid echo experiments, we will refer in the following only to rotational motion. Specific for random walk simulations, one uses the Ivanov model [62]: the jump from one site to another is instantaneous and the jump probability depends only on the actual position of the $C-^2\text{H}$ axis; between jumps, the orientation of the $C-^2\text{H}$ axis is fixed. Note that in the real life ^2H NMR experiments for the majority of the materials investigated in our group the molecules are rigid, thus the $C-^2\text{H}$ bonds are fixed in the molecule. Hence,

the rotational motion of a $C-^2H$ bond reflects the motion of the entire molecule and the results of the present simulations can be regarded in terms of molecular dynamics. Assuming Poisson distributed jump events, the waiting time t_w is randomly chosen from an exponential distribution of correlation times described by the jump correlation time τ_j [128]:

$$P(t_w) = \frac{1}{\tau_j} e^{-\frac{t_w}{\tau_j}}. \quad (6.1)$$

Therefore τ_j is the input parameter for the simulation. On the other hand, in a real life experiment a different correlation function is accessible through a measurement, namely the rotational autocorrelation function:

$$f_1(t) = \frac{\langle P_1\{\cos[\theta(0)]\} P_1\{\cos[\theta(t)]\} \rangle}{\langle P_1\{\cos[\theta(0)]\} P_1\{\cos[\theta(0)]\} \rangle} = \frac{\langle \cos[\theta(0)] \cos[\theta(t)] \rangle}{\langle \{\cos[\theta(0)]\}^2 \rangle}, \quad (6.2)$$

where P_1 is the first Legendre polynomial and $\cos(\theta)$ is the direction of a fixed molecular vector with respect to the laboratory frame ($\langle \rangle$ stands for ensemble average). Its corresponding correlation time τ_1 is the one usually reported in the literature (for example, from DS experiments). Performing spin-alignment experiments one can measure a similar function f_2 in which P_1 is replaced by P_2 (cf. Section 2.3.2). Because we were interested in comparing the time constants from line-shape analysis with those from DS, we did not simulated f_2 but f_1 .

For a random motion jump process one can say that the rotation correlation is lost after one jump and $\tau_1 = \tau_j$ holds. On the other hand, for a multi-step process in which the reorientation takes place step by step via several elementary jumps one after the other, the rotational correlation is lost after numerous jumps (e. g. rotational diffusion). Hence, in this case it is found that $\tau_1 \neq \tau_j$ [10, 129, 133, 135]. One of the important questions we would like to answer through this work is how this time constants, τ_1 and τ_j , are relevant for solid echo experiments.

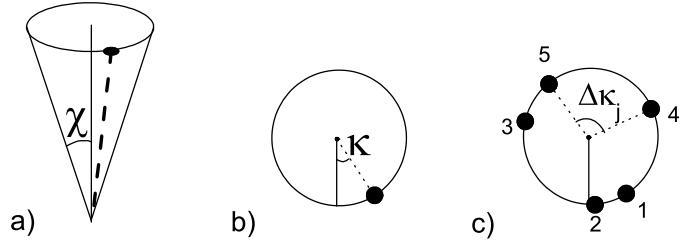
6.2. Results and discussion

It was proved that the effects of the β -process on the 2H NMR observables can be well understood by restricted motion models, the most successful being the so called cone models [133, 129, 135] from which several will be used in the following parts. Note: for all the following simulations $\delta = 125 \text{ kHz} = 1/(8 \mu s)$ was used.

6.2.1. Random motion on the edge of a cone (RO)

The most simple model to use in the attempt to describe the β -process is a **random motion on the edge of a cone model (RO)**. The $C-H$ bond can occupy any site solely on the circumference of the base circle as described in Fig. 6.1 (a) and (b). When jumping from one site to the other, any angle $0^\circ \leq \Delta\kappa_j < 360^\circ$ has the same probability.

Figure 6.1. Sketch of the random motion on the cone model (**RO**). a) The dashed line is the $C-H$ bond and the filled black circle illustrates the position of the bond on the circumference of the base circle. b) An upper view of the base circle, the position of the bond indicated by the filled black circle. c) Five possible consecutive sites for the bond are designated by numbers.



The rotational autocorrelation functions

The rotational autocorrelation function $f_1(t)$ (cf. Eq. 6.2) can be easily obtained in a random walk simulation by calculating a sum over the of the $C-H$ bonds:

$$f_1(t) = \frac{\sum_{i=1}^N \{ \cos[\theta_i(0)] \cos[\theta_i(t)] \}}{\sum_{i=1}^N \{ \cos[\theta_i(0)] \cos[\theta_i(0)] \}}, \quad (6.3)$$

where θ_i is the orientation of a bond and N is the number of bonds. We simulated the rotational autocorrelation functions for the **RO** model with two different cone angles χ ; selected results are shown in Fig. 6.2. It is seen that the functions for various jump correlation time τ_j decay to the same plateau value (that is solely dictated by χ). With increasing τ_j , the characteristic time of the decay τ_1 is also increasing. A fit was performed using the function $[(1 - F) \exp(-t/\tau_1) + F]$ in order to estimate the rotational correlation time τ_1 for each curve. The fits are included in the figure and it is seen that they interpolate well the data. Note that the correlation loss amounts to only about 4% that is generally difficult to probe in an real experiment (with the noticeable difference of DS experiments). For the **RO** model it is expected that $\tau_1 = \tau_j$ holds (see, for example, [129, 133, 135]). Fig. 6.3 shows the ratio τ_1/τ_j for different τ_j for the two employed angles χ and it is seen that $\tau_1/\tau_j = 1$ is reproduced in a good approximation by our simulation. As τ_1 is accessible experimentally, in the following parts of this chapter we will plot our results using it instead of τ_j , where possible.

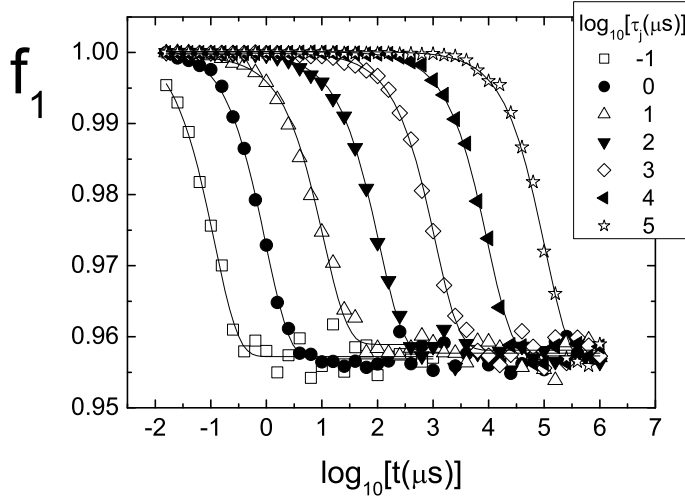


Figure 6.2. The simulated rotational autocorrelation functions for the **RO** model with $\chi = 12^\circ$. The lines are fits (see text).

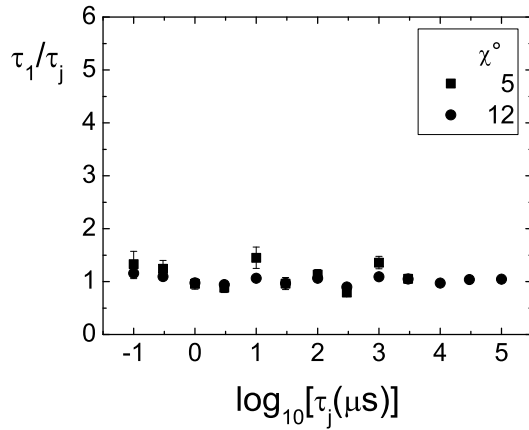
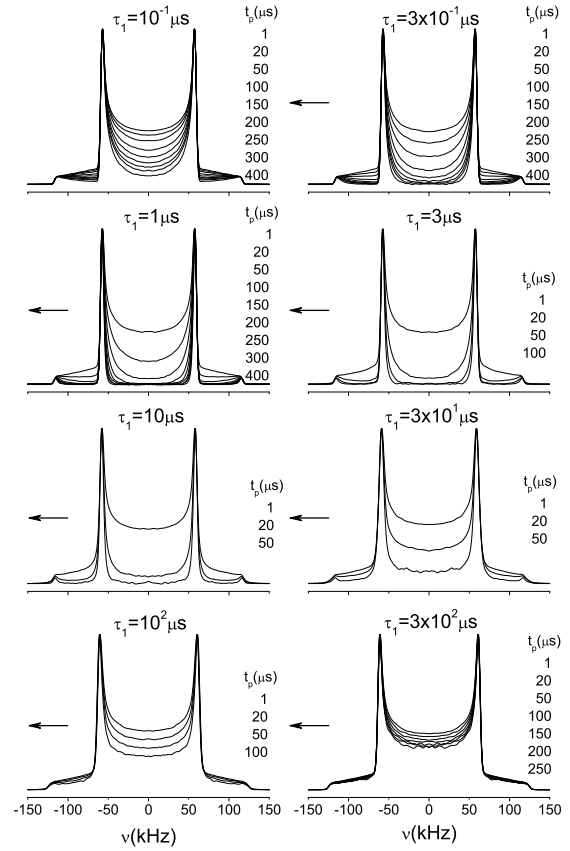


Figure 6.3. The ratio of rotational correlation time and jump correlation time τ_1/τ_j vs. the jump correlation time used for the **RO** model with two different cone angle χ .

Solid echo spectra

Figure 6.4 shows the simulated solid echo spectra for the **RO** model with $\chi = 12^\circ$; several τ_j (τ_1) were employed and also different interpulse delays t_p (for details on the pulse sequence and theoretical spectra, see Section 2.3.1). It is seen that for the spectra simulated with the longest rotational correlation time, $\tau_1 = 300 \mu s$, those with distinct t_p are very similar. That happens because τ_1 is close to the slow motion limit, $\tau_1 \gg 1/\delta$, when the molecular motion has no influence on the spectra any longer. With shortening τ_1 , the spectra at various t_p become more and more different till, say

Figure 6.4. Simulated normalized solid echo spectra for the **RO** model with the cone angle $\chi = 12^\circ$. For a certain rotational correlation time τ_1 several spectra with different interpulse delays t_p were simulated; the larger the area of the spectrum, the smaller is t_p . (The spectra were normalized to their maximum value.)



$\tau_1 = 10 \mu s$, when the difference is the greatest. With further shortening τ_1 , this t_p dependence becomes less important, with the smallest used τ_1 being close to the fast motion limit $\tau \ll 1/\delta$, when the line is not affected by molecular motion. Note that the spectra corresponding to the shortest t_p value look indistinguishable at a first glance.

This example of a simple model for the molecular motion behind the β -process offers a taste of the ^2H NMR real life findings when using solid echo experiments. That is, experimental spectra are very similar when they are acquired with a short interpulse delay t_p at different temperatures, in the range where only the β -process is relevant. Only using long t_p values the effect on the line shape of the highly hindered motion involved in the β -process becomes visible.

The effects of motion on the shape of the solid echo spectra can be quantitatively analyzed by investigating the relative spectral value at zero frequency $R(t_p, \tau_1)$ and the apparent spectral width $C(t_p, \tau_1)$ (for definitions of R and C see Section 2.3, page 17). The following part shows a more detailed analysis of the simulated spectra performed with the aim to precisely describe and rationalize the observed results.

a) R values

We present in Fig. 6.5 the R values normalized through the slow motion plateau value R_0 for the **RO** model with $\chi = 12^\circ$ (corresponding to the spectra displayed in Fig. 6.4). In an ^2H NMR experiment the absolute values of R may depend on the pulse length, on the electronical properties of the receiving and excitation units but the normalized R/R_0 values are believed to be not affected by the experimental conditions, therefore the R/R_0 representation is preferred. It is easily observed that at large correlation times τ_1 all the simulated data have practically the same value, a consequence of reaching the slow motion limit. At shorter τ_1 , the R/R_0 values are decreasing, except for the interpulse delay $t_p = 1 \mu\text{s}$. The curve corresponding to $t_p = 20 \mu\text{s}$ shows a minimum around $\tau_1 \simeq 1/\delta = 8 \mu\text{s}$. Starting with, say, $\tau_1 \simeq 3 \times 10^{-1} \mu\text{s}$ the R/R_0 values are increasing, approaching the fast motion limit, where the same plateau value as for the slow motion limit is expected. Shorter jump correlation times were not achievable due to the long computational time involved. (One has to consider that the simulated solid echo signal for one bond spans to roughly 1 ms ; for this time $1 \text{ ms}/\tau_j$ jumps have to be calculated. In order to get a good averaged signal and a reasonable signal to noise ratio we used $10^6 - 10^7$ bonds. It is seen that when $\tau_j \ll 1 \text{ ms}$ the number of required calculations is huge and it requires a long computational time. As an example, the time needed to simulate the spectra for $\tau_j = 10^{-1} \mu\text{s}$ was roughly 18 hours. If we targeted, say, a jump correlation time ten times shorter, then the computational time would have been about ten times longer.) In order to find out what influence the

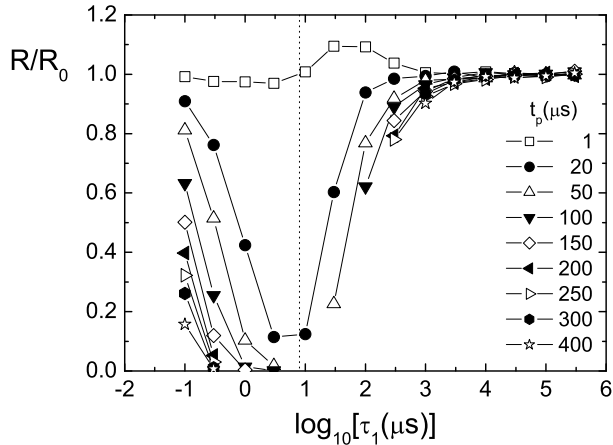
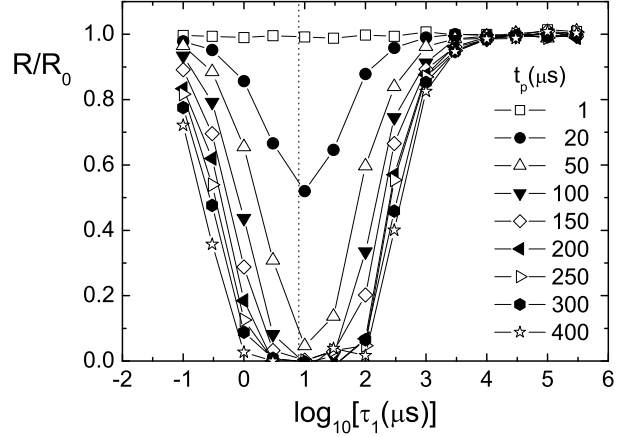


Figure 6.5. Normalized relative spectral value at zero frequency R/R_0 for the **RO** model with $\chi = 12^\circ$. The lines through the points are guides for the eye and the vertical dotted line marks $\tau_1 = 1/\delta = 8 \mu\text{s}$.

cone angle χ has on the spectral shape, we performed the same simulation like above, using the **RO** model but this time with $\chi = 5^\circ$. The corresponding R/R_0 values are shown in Fig. 6.6. It is observed that the same slow motion limit is reached in a similar

Figure 6.6. Normalized relative spectral intensity at zero frequency for the **RO** model with $\chi = 5^\circ$. The lines through the points are guides for the eye and the vertical dotted line marks $\tau_1 = 1/\delta = 8 \mu s$.



manner like for the simulations with $\chi = 12^\circ$. However, the level of the minimum for $R(t_p = 20 \mu s/R_0)$ is significantly higher than in the previous simulation. Also, for the shortest τ_1 , the R/R_0 values for various t_p extend across a smaller range than in the case of $\chi = 12^\circ$.

These results are easy to be understood: if the opening angle becomes extremely small $\chi \rightarrow 0$ then the base circle of the cone is reduced to a point and consequently the $C-^2H$ bond is not moving. Therefore the spectra at various t_p values are identical for different τ_1 and the R/R_0 values are all 1. If the angle χ is slightly different from zero it follows that a minimum in the $R(t_p = 20 \mu s/R_0)$ curve is expected to emerge around $1/\delta$ but its value will be very closed to 1. As χ is increasing, the minimum value is decreasing until it reaches 0.

b) Apparent spectral width

When the time constant of the molecular motion varies from the slow motion to the fast motion limit, a change in the apparent spectral width C is expected (for definition of C see Section 2.3, page 17). The normalized apparent spectral width C/C_0 for the **RO** model and two values of χ is shown in Fig. 6.7; one observes that in the case $\chi = 5^\circ$ both fast and slow motion limits are reached within the τ_1 used in the simulations, as proven by the constant values at short and long correlation times τ_1 . In between, the apparent spectral width displays a step-like behavior for short t_p . For long t_p an overshooting of the C_0 value is observed in the range $10^2 < \tau_1 < 10^3 \mu s$. The ratio between the slow motion and fast motion limit reproduces perfectly the expected value predicted by Eq. 2.35 ($C_{fast}/C_0 = 0.9886$). For the simulation with an angle ($\chi = 12^\circ$) the same features are observed (cf. Fig. 6.7 (b)), with the difference that the ratio

C_{fast}/C_0 is smaller, as expected from Eq. 2.35.

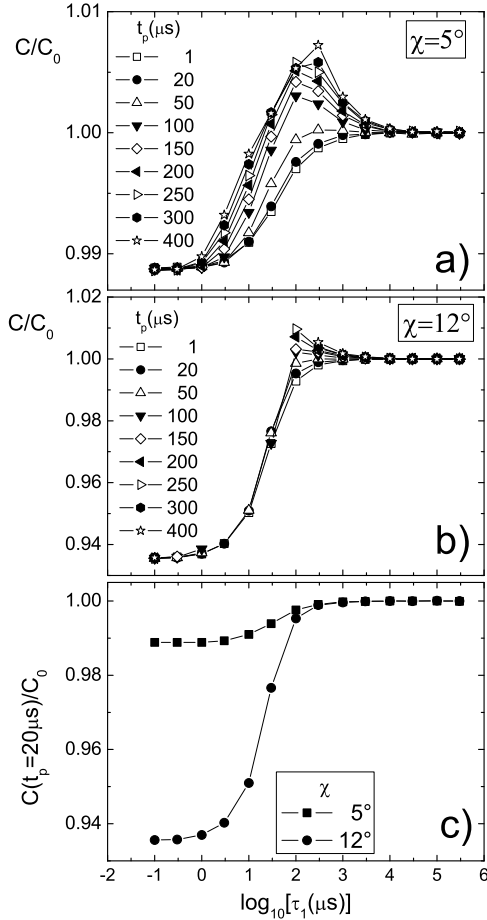


Figure 6.7. The normalized apparent spectral width C/C_0 versus the rotational correlation time τ_1 for the **RO** model. a) Cone angle $\chi = 5^\circ$; b) $\chi = 12^\circ$. c) Comparison between C/C_0 ($t_p = 20 \mu s$) for the two angles used in the simulations. Lines are guides for the eye.

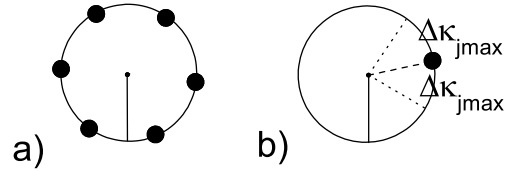
In a laboratory experiment the apparent spectral width is the most conveniently measured for t_p around $20 \mu s$; that is because at a shorter t_p the dead-time of the receiver distorts the spectrum while at a longer t_p the signal decays due to spin-spin relaxation and the signal to noise ratio becomes worst. For this reason we present in Fig. 6.7 (c) the values $C/C_0(t_p = 20 \mu s)$ for the two simulated models as to estimate the outcome of a real experiment if the $C-^2H$ bonds of the molecules were moving as described above. Note that for an angular amplitude of $\chi = 5^\circ$, a change of around 1% is to be expected in the apparent spectral width! That is close to the resolution limit of the experiment and measuring this effect constitutes a challenge for a 2H NMR spectroscopist.

6.2.2. Multi-step motion on a cone (MO)

The **RO** model previously presented can reproduce some experimental results for the β -process when a distribution of angles χ and jump time constants τ_j is introduced. Still, it failed to interpolate simultaneously, with the same set of parameters, both stimulated echo and solid echo experiments. The reason for this failure is the fact that the β -process is described by a multi-step motion instead of a random one as proven by the large difference between τ_j and τ_1 observed in ^2H NMR studies of Vogel [129, 133, 135] (also cf. Section 1.1.3).

Therefore, we consider different models that restrict the values $\Delta\kappa_j$ may take (in the **RO** model $0^\circ \leq \Delta\kappa_j < 360^\circ$, cf. Fig. 6.1.) These are: multi-step motion on a cone between 6 equidistant sites (**6 sites on the edge of the cone: 6SO**) and **multi-step motion on the edge of a cone** in which the maximum amplitude is limited to less than 360° (**MO**). Fig. 6.8 (a) shows the **6SO** model where $\Delta\kappa_j = \pm 60^\circ$. For the **MO** model

Figure 6.8. a) Multi-step motion on a cone between six equidistant sites: sketch of the allowed sites (**6SO**). b) Model of multi-step motion on a cone with limited maximum amplitude $\Delta\kappa_j$ (**MO**) (for details see text).



the bond can jump randomly in a restricted range so that $-\Delta\kappa_{jmax} \leq \Delta\kappa_j \leq \Delta\kappa_{jmax}$. After a jump, the same rule holds so that the bond can describe the whole base circle but this will be done in a larger number of jumps than in the case of **RO** model. In the extreme case when $\Delta\kappa_{jmax} \rightarrow 0$ the model describes a diffusive motion on the base circle of the cone.

The simulations presented in the following for the two restricted models were done for a cone angle $\chi = 12^\circ$.

The rotational autocorrelation functions

As said before, using a restricted model, the rotational correlation time τ_1 will be different from the jump correlation time τ_j [133, 129, 135]. Simulating and analyzing the rotational autocorrelation functions f_1 as described in the previous section, we indeed obtain this result. The ratio τ_1/τ_j for the **6SO** model and **MO** model with three values for $\Delta\kappa_{jmax} = 1, 10, 60^\circ$ is displayed in Fig. 6.9. It is observed that in all the cases $\tau_1/\tau_j \neq 1$. With decreasing the angle $\Delta\kappa_{jmax}$, the ratio τ_1/τ_j for the **MO** model changes more than four orders of magnitude. Thus the loss of orientational correlation takes place on much longer scale than the jump time in the case of a restricted random motion.

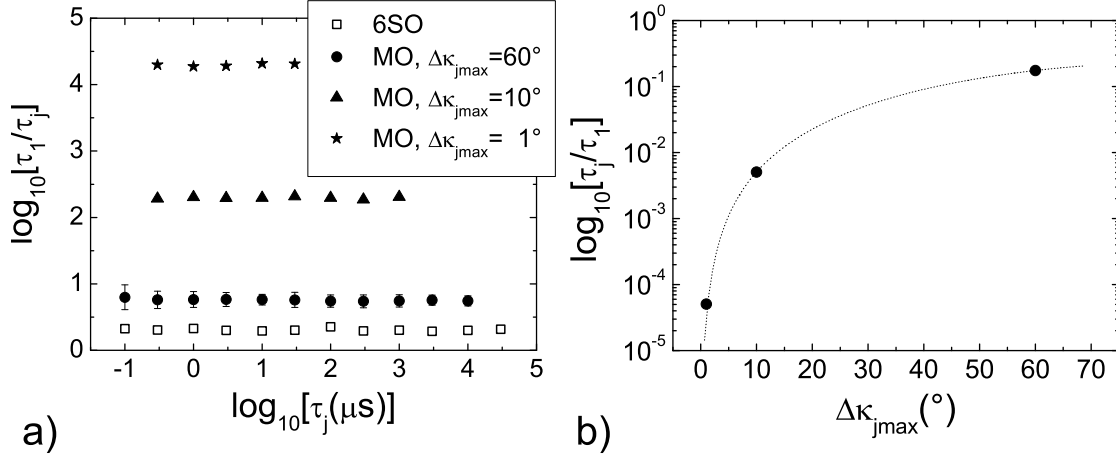


Figure 6.9. a) The ratio τ_1/τ_j for the models comprising restricted motion on a cone ($\chi = 12^\circ$). b) Mean τ_j/τ_1 versus $\kappa_{j\text{max}}$ for the **MO** model; dotted line is a fit with the function $\tau_j/\tau_1 = a \sin^b(\Delta\kappa_{j\text{max}})$ with $a = 0.240$ and $b = 2.20$.

An empirical relation for the **MO** model was found, namely: $\tau_j/\tau_1 = 0.24 \sin^{2.2}(\Delta\kappa_{j\text{max}})$. This dependence is somewhat similar with the one calculated by Anderson for his isotropic multi-step model for the α -process: $\tau_j/\tau_1 = 3/2 \sin^2(\Delta\Omega)$ [10]. In the above mentioned model $\Delta\Omega$ is a fixed angular value that describes the difference between two successive orientations of the molecule.

Solid echo line shape analysis

a) R values

Solid echo spectra were simulated for the multi-step models presented in this section and the resulting normalized relative spectral intensity at zero frequency R/R_0 are shown in Fig. 6.10. It is seen that in all the four cases, the R/R_0 values for different interpulse delays are similar $R/R_0 = 1$ at the longest correlation time τ_1 , a sign that the slow motion limit was reached. Moreover, all the data display a well contoured minimum for the interpulse delay $t_p = 20 \mu\text{s}$ except those for the **MO** model with $\Delta\kappa_{j\text{max}} = 1^\circ$, where simulations were not possible at shorter τ_1 due to a extremely long computation time. An important fact is that the minimum occurs at a rotational correlation time $\tau_1 \simeq 1/\delta$ as in the case of the **RO** model. One observes that the curves for the **6SO** and **MO** models with $\Delta\kappa_{j\text{max}} = 60^\circ$ look similar with those for the **RO** model simulated with the same χ (cf. Fig. 6.10 (a), (b) and Fig. 6.5 (b)). With further decreasing the constrained angle $\Delta\kappa_{j\text{max}}$ the R/R_0 values depart from 1 at a longer τ_1 , the extreme case takes place for $\Delta\kappa_{j\text{max}} = 1^\circ$ for which the deviation from 1 starts

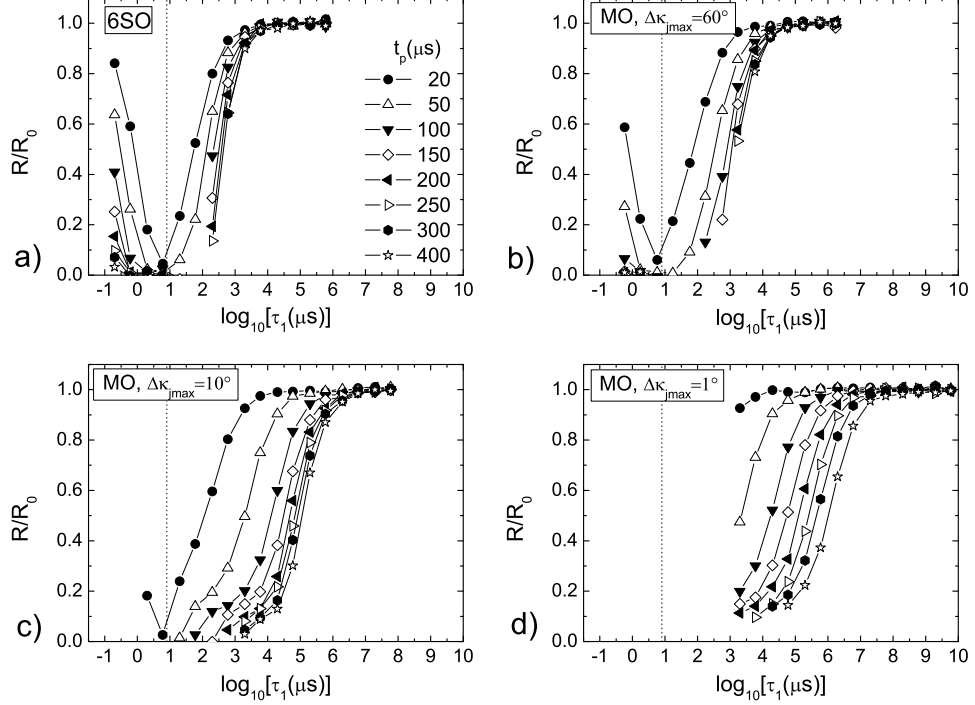


Figure 6.10. Normalized relative spectral intensity at zero frequency vs. the rotational correlation time τ_1 for the multi-step models ($\chi = 12^\circ$). For all figures the same symbols were used for t_p values; the lines are guides for the eye and the vertical dotted line marks $\tau_1 = 1/\delta = 8 \mu\text{s}$.

at times longer than $\tau_1 = 10^7 \mu\text{s} = 10\text{s}$. A remarkable conclusion can be drawn: in the case of a multi-step process with a small $\Delta\kappa_{j\text{max}}$ one can observe line shape effects due to the β -process in spectra measured with long t_p values at rotational correlation times $\tau_1 \gg 1/\delta$. In other words, the time window of the ^2H NMR line shape changes is greatly extended towards long times.

In Fig. 6.11 we display for clarity all the curves R/R_0 vs. τ_1 for an interpulse delay of $t_p = 20 \mu\text{s}$ obtained from the models presented so far and a minimum value is observed for all around $\tau_{1\text{min}} = 1/\delta = 8 \mu\text{s}$. With increasing the restriction angle the R/R_0 curve becomes broader and asymmetric with respect to the vertical line that crosses through the minimum. (The left side looks similar for all traces while the right side not.) Note that the minimum $\min(R/R_0)$ in Fig. 6.11 displays the same value for all the presented data. Thus, both $\min(R/R_0)$ and $\tau_{1\text{min}}$ do not depend on how the $\text{C}-^2\text{H}$ bond is moving on the circumference of the base circle but only on the cone angle χ .

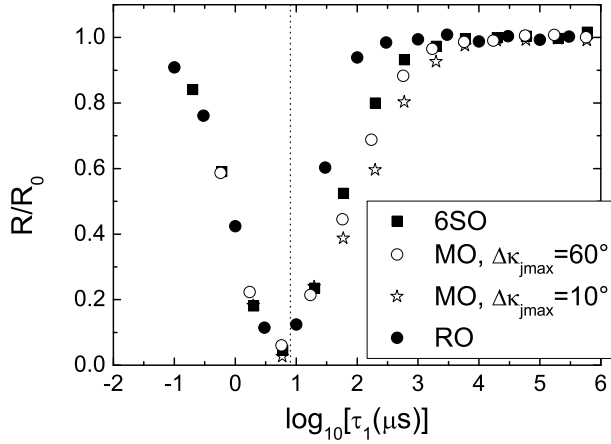


Figure 6.11. Normalized relative spectral intensity at zero frequency for indicated models and an interpulse delay $t_p = 20 \mu s$ ($\chi = 12^\circ$). The vertical dotted line marks $\tau_1 = 1/\delta = 8 \mu s$

This is an important finding which will be exploited to a great extend in the following.

b) The apparent spectral width

The apparent spectral width for the spectra simulated with the previously mentioned models is displayed in Fig. 6.12 and the observed step in C/C_0 looks very similar. In addition, the fast motion limit value does not depend on the employed model, as expected.

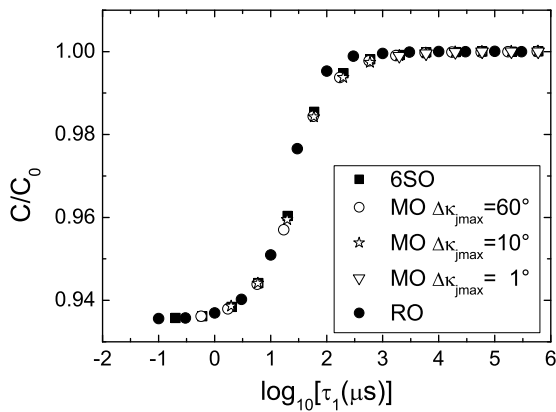


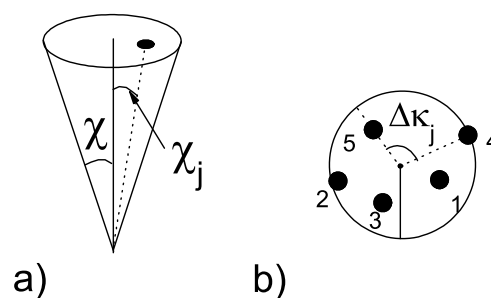
Figure 6.12. Normalized apparent spectral width C/C_0 vs. τ_1 for the indicated models and an interpulse delay $t_p = 20 \mu s$ ($\chi = 12^\circ$).

6.2.3. Random motion within a cone (RW)

For both the random motion on the cone (**RO**) and the multi-step motion on the cone (**MO**) models the $R(t_p = 20 \mu s)/R_0$ curve displays a minimum at the same rotational correlation time $\tau_1 \simeq 1/\delta$. Moreover, the value of the minimum $\min(R(t_p = 20 \mu s)/R_0)$ is very similar for the different parameters employed, being solely determined by the cone angle χ for the two models mentioned before. Therefore, as we intend to extract information regarding the β -process by analyzing the features of the R/R_0 minimum, it is not relevant whether the used model consists of a random or a multi-step motion. A simulation with a model comprising random motion is much faster than one with a multi-step model because in the latter case $\tau_1 > \tau_j$ and extremely short τ_j must be used in order to probe a rotational correlation time of say, $0.1 \mu s$. Therefore in order to save computational time, for all the following models we preferred a random motion instead of a multi-step one.

A simple extension of the **RO** model is the **r**andom motion **w**ithin a cone model (**RW**) and Fig. 6.13 shows a sketch of it. Like in the case of **RO** model, the angle $\Delta\kappa_j$ can take, with the same probability, any value between 0 and 360° . In addition, the $C-^2H$ bond can move within the cone, its position being described by an angle χ_j that is limited $0 \leq \chi_j \leq \chi$. Moreover, the angle χ_j is chosen with a probability proportional with $\sin(\chi_j)$ ensuring a homogeneous distribution of $C-^2H$ bond orientations. The **RW** model seems more ‘natural’ than the **RO** model for a restricted motion because it does not restrict the loci of the site of a certain bond to a circle. This model implies random jumps therefore it is expected that $\tau_1 = \tau_j$ holds. By simulating the solid echo spectra we intend to find out what are the main differences between the 2H NMR observables of the **RO** and **RW** models.

Figure 6.13. The **RW** model: a) a site position is described by the angle χ_j ; b) five consecutive numbered positions for the $C-^2H$ bond within the base circle of the cone.



Solid echo line shape analysis

a) R values

Using the **RW** model for three different angles $\chi = 5, 7, 12^\circ$ we simulated the solid echo spectra for various t_p and the corresponding R/R_0 values are displayed in Fig. 6.14. It is observed that the slow motion limit is reached in all cases around $\tau_1 = 10^4 \mu s$. Besides that, for $t_p = 20 \mu s$ each set of data show a minimum close to $\tau_1 \simeq 1/\delta = 8 \mu s$. The value of minimum for $R(t_p = 20 \mu s)/R_0$ depends on the angle χ , increasing with decreasing the angle. In addition, the minimum for a certain angle χ is noticeably higher for the **RW** model compared to the **RO** model (cf. Fig. 6.14 (a) and (c), Fig. 6.6 and Fig. 6.5 (b)). Still, by properly choosing the cone angles χ it is possible to obtain a very similar curve $R(t_p = 20 \mu s)/R_0$ for both models (cf. Fig. 6.14 (d)).

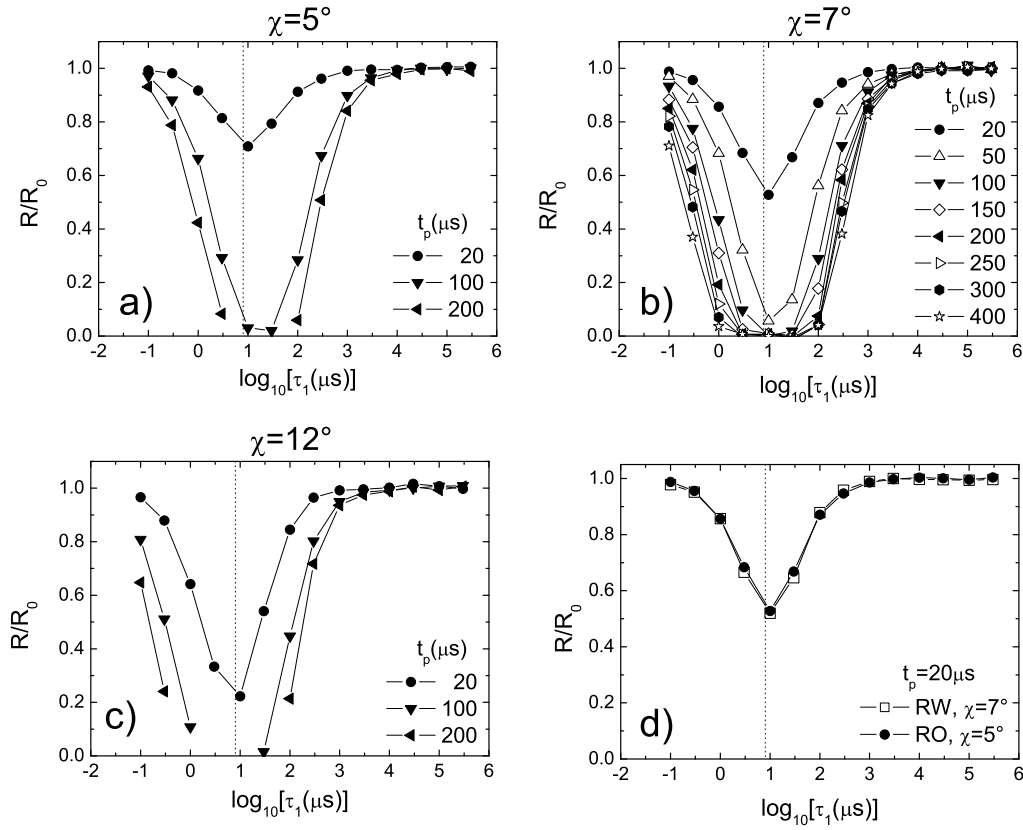


Figure 6.14. a), b), c) R/R_0 values for the **RW** model in the case of three different cone angles χ . d) Comparison between the R/R_0 values at $t_p = 20 \mu s$ for the **RW** model with $\chi = 7^\circ$ and **RO** model with $\chi = 5^\circ$. The lines through the points are guides for the eye and the vertical dotted line marks $\tau_1 = 1/\delta = 8 \mu s$.

b) The apparent spectral width

Figure 6.15 (a) shows the normalized apparent spectral width C/C_0 for the **RW** model along with data for **RO** model. It is seen that the spectral width reaches its fast motion limit, the value being higher when the angle is smaller. The fast motion limit value agrees well with the one predicted by Eq. 2.36. Note that in the **RW** model one should use an angle $\chi = 7^\circ$ to obtain the same effect in C/C_0 like in the case of the **RO** model with an angle $\chi = 5^\circ$. The use of these angles also ensures that the $R(t_p = 20 \mu s)/R_0$ curves are very similar (cf. 6.14 (d)). Therefore we may conclude that the same NMR effects can be obtained with both the **RO** and **RW** models with the only difference being a different cone angle χ . In Fig. 6.15 (b) one can see the dependence of the fast motion value C_{fast}/C_0 on the cone angle χ for the two random motion models. The dotted and the solid line mark the theoretical predictions for the above mentioned models and they can be regarded as determining the extreme values that can be estimated for the angular amplitude χ of the molecular motion from a certain value of C_{fast}/C_0 .

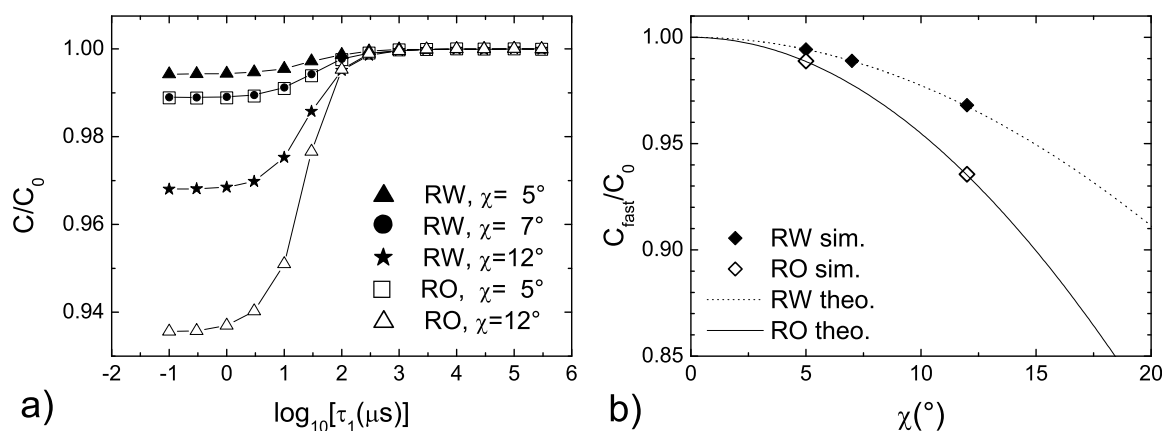


Figure 6.15. a) The normalized spectral width for the random motion models; lines are guides for the eye. b) The fast motion limit C_{fast}/C_0 vs. the cone angle χ for the two random motion models used so far. Points are obtained from simulations (the value of C/C_0 for $\tau_1 = 0.1 \mu s$ from the graph in a)), the lines are theoretical predictions: dotted line is given by Eq. 2.36 and solid line corresponds to Eq. 2.35.

6.2.4. Random motion on a the edge of a cone with a distribution of jump correlation times (RO-D)

As the two random motion models presented before (**RO** and **RW**) produce similar results if the cone angle χ is properly chosen, we proceed in our simulation by using only one of them. For the random motion on the cone model (**RO**) a smaller number of calculations is required for one jump therefore it is more economic in computational time being employed in the following.

It was proven, mainly by dielectric spectroscopy, that the β -process is characterized by a distribution of correlation times [28, 74, 129]; thus we take it into account in the model used for the simulations. A logarithmic Gaussian distribution for the jump correlation proves appropriate [20, 74]:

$$G[\ln(\tau_j)] = \frac{1}{\sigma\sqrt{2\pi}} \exp \left\{ - \frac{[\ln(\tau_j) - \ln(\tau_m)]^2}{2\sigma^2} \right\}, \quad (6.4)$$

where τ_m gives the position of the maximum and the decadic full width at half maximum is $\sigma_d(\text{decades}) = 1.02\sigma$ [112].

When using $G[\ln(\tau_j)]$ for a random motion model (in our case, **RO**), it is expected that it translates into the same distribution of rotational correlation times τ_1 therefore $\langle \ln(\tau_1) \rangle = \ln(\tau_m)$. The simulations presented in the following for the model **random motion on the edge of a cone with a distribution of jump correlation times (RO-D)** were done for a cone angle $\chi = 5^\circ$.

Solid echo line shape analysis

a) R values

Employing several widths ($\sigma = 0.5, 1, 2, 3, 3.5$) for the distribution of jump correlation times, we simulated the solid echo spectra for two interpulse delays ($t_p = 20, 100 \mu s$), the resulting R values being presented in Fig. 6.16. In the same figure are also plotted the corresponding data for the **RO** model (that comprises no distribution of jump correlation times). For both t_p and all σ values the R/R_0 curves display a minimum $\min(R(t_p)/R_0)$ with its value increasing with increasing σ . Concerning the shorter $t_p = 20 \mu s$, the minimum of the R/R_0 curve is situated at a time $\tau_m \simeq 1/\delta$.

The angle χ being determined, the minimum of $R(t_p = 20 \mu s)/R_0$ depends only on the width of the distribution function $G[\ln(\tau_j)]$. We tried to describe the data in Fig. 6.16 (a) by a simple function:

$$\left(\frac{R}{R_0} \right) [\log(\tau_m)] = 1 - A \frac{1}{W\sqrt{2\pi}} \exp \left\{ - \frac{[\log(\tau_m) - \log(x_0)]^2}{2W^2} \right\}, \quad (6.5)$$

that is an ‘upside-down’ log-Gauss. As it can be seen in Fig. 6.17 (a) the fits with the above equation work satisfactorily. The important result of the fitting procedure is the

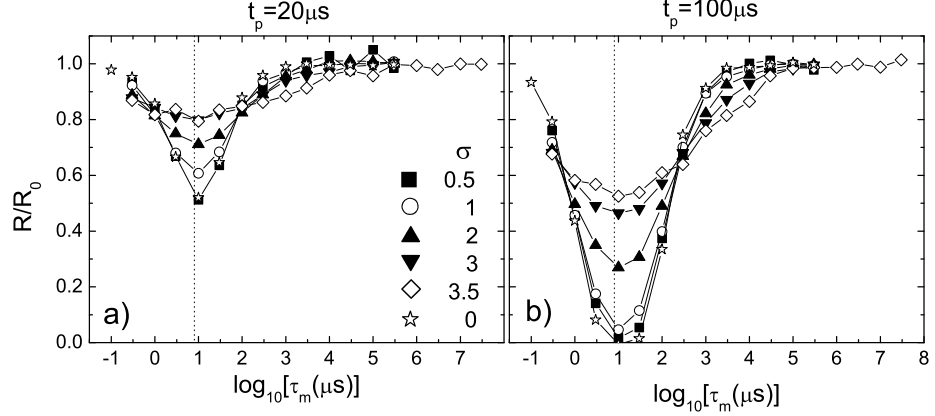


Figure 6.16. The normalized R values for the **RO-D** model with different widths σ ($\chi = 5^\circ$). Two interpulse delays were simulated, a) $t_p = 20 \mu s$ and b) $t_p = 100 \mu s$. We also plotted the data for the corresponding t_p in the **RO** model, designated with $\sigma = 0$. The symbols correspond to the same σ in both figures. The lines through the points are guides for the eye and the vertical dotted line marks $\tau_m = 1/\delta = 8 \mu s$.

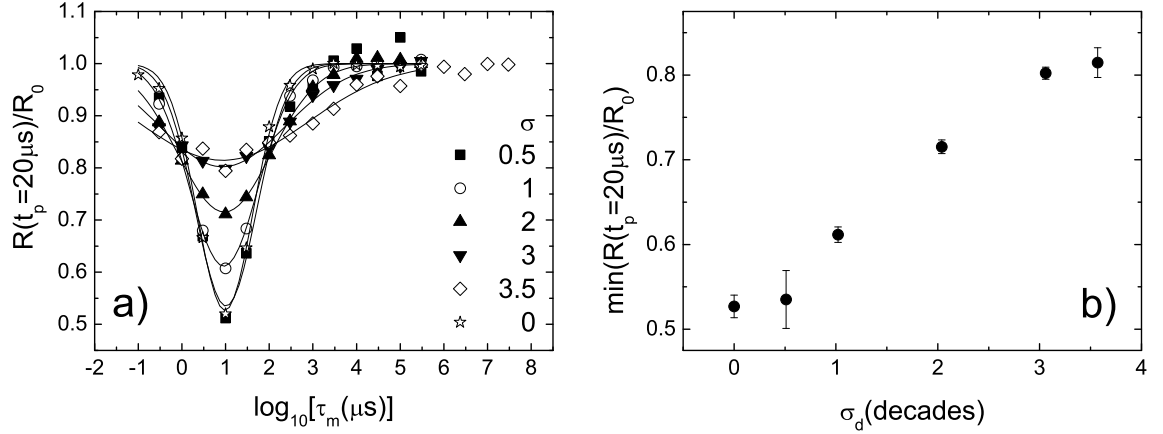


Figure 6.17. a) The normalized R values for the **RO-D** model ($\chi = 5^\circ$) for $t_p = 20 \mu s$ (shown also in Fig. 6.16 (a)). The lines are fits with Eq. 6.5. b) The minimum value of R/R_0 functions vs. the decadic width σ_d of the distribution function $G[\ln(\tau_j)]$.

dependence of the minimum of $R(t_p = 20 \mu s)/R_0$ on the width σ_d of the distribution $G[\ln(\tau_j)]$ displayed in Fig. 6.17 (b). From this dependence, measuring in a real life experiment the value of the R/R_0 at minimum, one can estimate the width of the distribution of correlation times for the β -process, given that $\chi = 5^\circ$.

b) The apparent spectral width

The step in the normalized apparent spectral width in the case of the **RO-D** model extends for a larger time range with increasing σ (cf. Fig. 6.18): one observes that

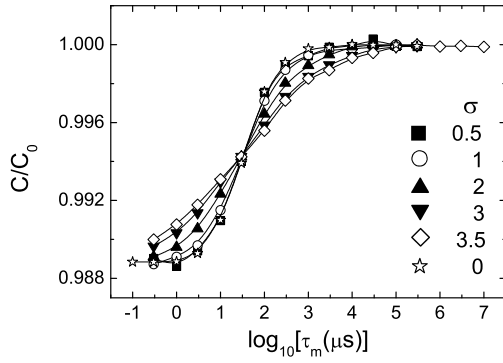


Figure 6.18. The normalized apparent spectral width for the **RO-D** model and indicated widths σ of the distribution $G[\ln(\tau_j)]$. The lines are guides for the eye; $t_p = 20 \mu s$.

C/C_0 for the smallest σ departs from 1 at roughly $10^3 \mu s$ while for $\sigma = 3.5$, C/C_0 trace departs from 1 at more than $10^{4.5} \mu s$. Translated into a real experiment, this observation is: the larger the width of the distribution times for the β -process the larger the temperature range in which C/C_0 curve is temperature dependent.

6.3. Further discussion and conclusions

6.3.1. Concluding the simulations

Performing random walk simulations several observations useful for the analyses of real solid echo data arose:

1. Model independent, the correlation time of the minimum of R/R_0 curve for $t_p = 20 \mu s$ is situated close to the value $\langle \ln(\tau_1) \rangle = 1/\delta$ (it holds also for the multi-step model). This conclusion is the rediscovery of a well known fact: the solid echo line shape is most affected when molecular motion takes place on a time scale of $1/\delta$ [1, 112, 119]. Thus an important fact is revealed: it is possible to estimate model-independently, a time constant for the β -process by using the solid echo experiment. To our knowledge, nobody reported time constants for the β -process estimated solely from 2H NMR experiments.
2. The value C_{fast}/C_0 provides direct information about the angular amplitude of the motion. C_{fast}/C_0 is directly related via Eq. 2.35 or Eq. 2.36 to the angular amplitude of the motion. It seems more reasonable that the $C-^2H$ bond moves

within the entire base circle of the cone rather than on its circumference. Therefore Eq. 2.36 should be favored when estimating angular amplitudes. The τ_1 range in which the step in the C/C_0 curve occurs is mostly influenced by the width of the distribution of correlation times.

3. From the value of the minimum $R(t_p = 20 \mu s)/R_0$, one can derive the width of the distribution of rotational correlation times if the angular amplitude of the motion is known. It was seen that the same value for the minimum of $R(t_p = 20 \mu s)/R_0$ curve can be obtained in both cases when the $C-^2H$ bond was moving on the cone (**RO** model) and within the cone (**RW**), if the angle of the cone was properly chosen (compare Fig. 6.6 and Fig. 6.14 (b)). Thus, when the angle χ is correctly estimated via Eq. 2.35 for the **RO** model or via Eq. 2.36 for the **RW** model, the minimum of $R(t_p = 20 \mu s)/R_0$ curve is given only by the width of the distribution of rotational correlation times. Therefore, measuring the value of this minimum offers a quasi model-independent way of estimating the width of $G[\ln(\tau_\beta)]$ at a certain temperature.
4. The trace R/R_0 departs from the slow motion limit value (that is 1) at a certain $\langle \ln(\tau_1) \rangle$ that depends both on the motional model and on the width of the distribution times. This observation is crucial in analyzing the experimental data when the correlation time for the β -process is far from $1/\delta$. If the β -process can be described by a random motion model then at long correlation time, say 1 s, the solid echo line shape should be independent of t_p . On the other hand, if the motion is characterized by a multi-step process it follows that, even at such a long correlation time the line shape changes with changing t_p (see p. 90 and the following one). The same line of thinking was followed by Vogel [129, 133, 135] in analyzing solid echo data in toluene and it was proved that a multi-step model is required to interpret the results.

As an output of the simulation work we gain knowledge how to determine model-independently by 2H NMR a rotational correlation time for the β -process. Moreover we show that, when the mean angular amplitude of molecular motion is estimated from the value of C_{fast}/C_0 , one can evaluate the width of the distribution of rotational correlation times for the β -process at least at one temperature.

In order to get a feeling of the results expected in a real measurement Fig. 6.19 shows the normalized apparent spectral width C/C_0 and relative spectral intensity at zero frequency R/R_0 for the random motion on cone with a distribution of jump correlation times model (**RO-D**) with $\sigma = 3$ and $\chi = 5^\circ$. The scale $(-\log_{10}[\tau_m(\mu s)])$ is meant to mimic the temperature scale to some extent. One can see that the step in the C/C_0 curve is correlated with the position of the minimum of R/R_0 curve and a similar picture is to be expected in a real measurement. Still, since the β -process is thermally activated, the width σ of the distribution of correlation functions decreases

with increasing the temperature. Therefore both traces in Fig. 6.19 would change more abrupt on their right hand side ('high temperatures') and probably will reach 1 on their left side hand in a smoother manner.

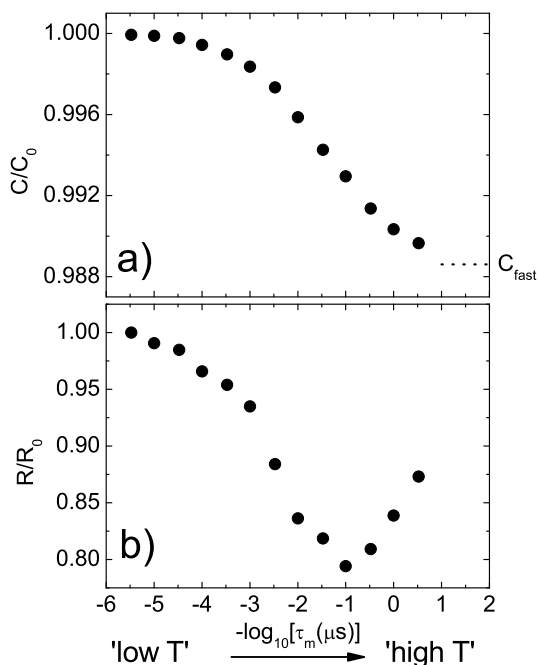


Figure 6.19. a) Normalized apparent spectral width and b) normalized relative spectral intensity at zero frequency for the **RO-D** model with $\sigma = 3$ and $\chi = 5^\circ$. The dotted line in a) is the calculated fast motion limit for C/C_0 .

As the expected difference in the apparent spectral width $\Delta C = (C_0 - C_{fast})$ is on the order of only several percents of C_0 , it is an experimental challenge to measure it. In addition, most of the glass formers investigated so far by ^2H NMR (toluene, polybutadiene [129, 133, 135], mixture of chlorobenzene in cis-decaline [71]) are not appropriate for the analysis proposed here, the reason being that the effect of fast motion limit on the solid echo for the β -process cannot be measured. This happens because the α -process influences considerably the line shape at temperatures where the β -process reaches its fast motion limit. Therefore only the so-called fast β -processes, that have a large time scale separation from the α -process, are well suited for the presented analysis. From those, m-fluoroaniline will be discussed in a next chapter (Chap. 7) and ethanol will be discussed in the following section.

6.3.2. Applications

Ethanol- d_1

Figure 6.20 demonstrates that ethanol displays a well pronounced β -process. As it will be seen, the properties of the β -process shown by ethanol are very convenient to put to

work the conclusions of the simulations because both slow and fast motion limit of the solid echo line shape are reached in the ^2H NMR experiments. The data of Schneider who investigated ethanol- d_1 and ethanol- d_2 in a wide temperature range by ^2H NMR [115] are analyzed in the light of the results of the simulations carried out in this PhD work.

Figure 6.20. Imaginary part of the complex permittivity ε'' for ethanol (from Benkhof [18]).

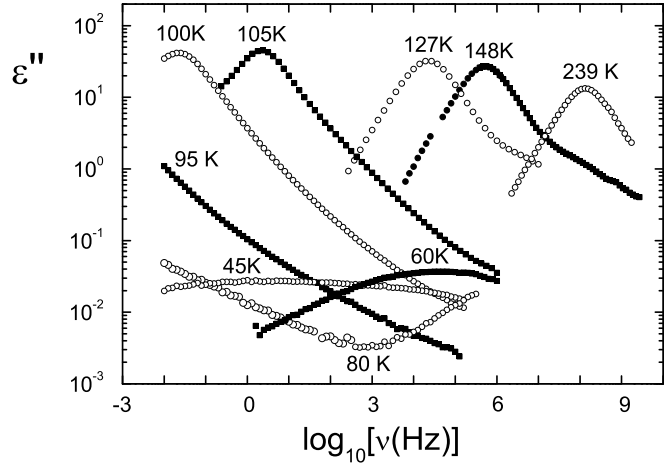


Fig. 6.21 (a) shows the normalized apparent spectral width C/C_0 as a function of temperature for the ethanol- d_1 ($\text{CH}_3\text{CH}_2\text{OD}$) sample. The plateau at low temperatures is interpreted as a consequence of the fact that the slow motion limit concerning C/C_0 was reached. With increasing the temperature, C/C_0 shows a constant decreasing till around 80 K where two points at different temperatures are almost equal. At higher temperatures the spectral width further decreases. We tentatively interpret the points around 80 K as being a proof of C/C_0 attaining the fast motion limit (marked by C_{fast} in the same figure). The decrease in C/C_0 at higher temperatures ($T > 90$ K) is attributed to the α -process (and/or the excess wing), that further reduces the spectral width. The ratio between the fast and the slow motion limit gives an angular amplitude of the motion: $\chi \simeq 5^\circ$ (**RO** model, Eq. 2.35) or $\chi \simeq 8^\circ$ (**RW** model, Eq. 2.36). Figure 6.21 (b) shows the corresponding normalized R values and one observes a similar result with that expected from simulations: for different t_p the R/R_0 values display a local minimum below T_g . The value of the minimum is the lower, the longer t_p is. At the lowest measured temperature it seems that still the points for different t_p are not equal although close. It means that the slow motion limit for R/R_0 is not yet reached. At temperatures around 80 K the values show a plateau though the plateau level is somewhat different for various t_p . At even higher temperatures the R/R_0 values drop

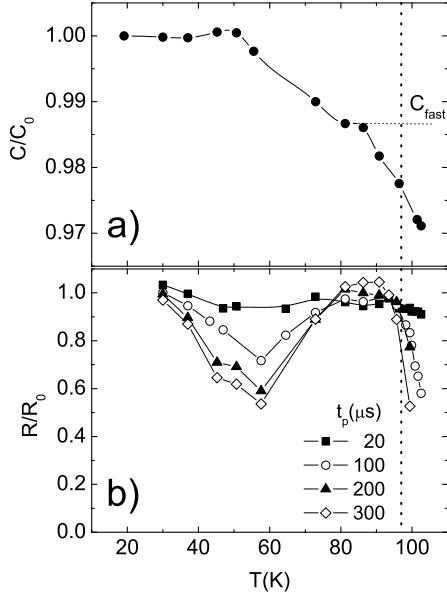


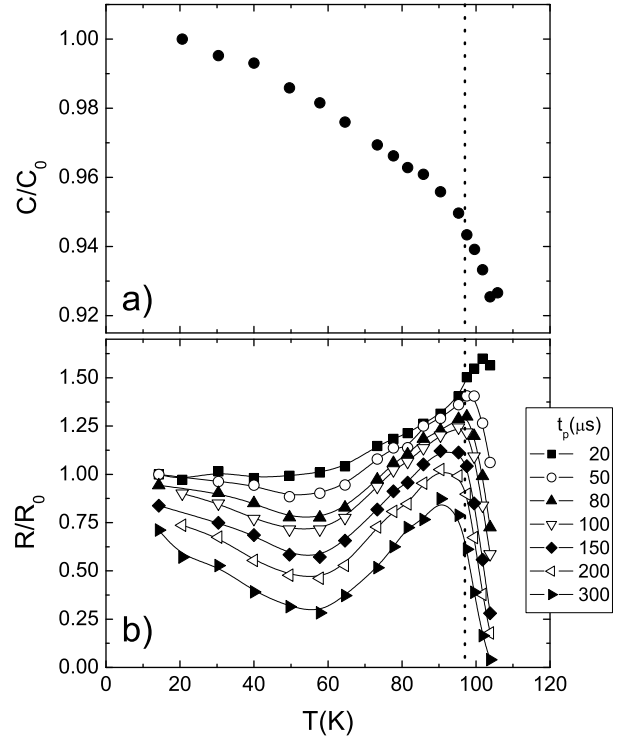
Figure 6.21. Ethanol-d₁ data: a) normalized apparent spectral width for the spectrum measured with $t_p = 20 \mu s$. b) normalized relative spectral intensity at zero frequency (normalized to the mean value at the lowest temperature). Solid lines are guides for the eye, vertical dotted line marks $T_g = 97$ K (data from Schneider [115]).

sharply, a fact that we interpret as the influence of the α -process. At the position of the minimum of $R(t_p = 20 \mu s)/R_0$ the temperature reads $T_{min} \simeq 57 \pm 7$ K and the corresponding the time constant of the β -process is $1/\delta$ (displayed along with the dielectric spectroscopy time constants in Fig. 6.24). From the minimum of (R/R_0) for $t_p = 20 \mu s$ one can make a rough estimate of the width of the distribution of correlation times $G[\ln(\tau_1)]$ and referring to the simulations results we can only say that it is larger than $\sigma_d = 3.5$ decades (cf. Fig. 6.17).

Ethanol-d₂

Fig. 6.22 (a) shows the normalized apparent spectral width C/C_0 for ethanol-d₂ (CH_3CD_2OH). In contrast to ethanol-d₁, no plateau is observed at low temperatures and neither at temperatures close to but below T_g , feature that still remains to be explained. In the R/R_0 curve, displayed in Fig. 6.22 (a), one observes a minimum around 50 – 60 K that decreases with increasing t_p . Because the $R(t_p = 20 \mu s)/R_0$ curve does not display a well contoured minimum, we focused on the $R(t_p = 50 \mu s)/R_0$ trace that does show a minimum at a temperature $T_{min} \simeq 49 \pm 7$ K. The corresponding average rotational correlation time of the β -process at this temperature is $1/\delta$, being displayed in Fig. 6.24. At the lowest temperature, the values for various t_p are considerably different, thus the slow motion limit concerning R/R_0 is not reached. Also at

Figure 6.22. Ethanol-d₂ data: a) normalized apparent spectral width for the spectrum measured with $t_p = 20 \mu s$ (normalized to the value measured at the lowest temperature). b) normalized relative spectral intensity at zero frequency (normalized at the value for $t_p = 20 \mu s$ and the lowest temperature). Solid lines are guides for the eye, vertical dotted line marks $T_g = 97 K$ (data from Schneider [115]).



temperatures close to T_g , R/R_0 for different t_p do not reach a common value or show a plateau. The sharp drop at temperatures somewhat higher than T_g is to be attributed to the α -process.

The different features of C/C_0 and R/R_0 curves in ethanol-d₂ with respect to ethanol-d₁ allow us to conclude that the molecular motion is anisotropic in the sense that different chemical bonds have distinct angular motion. Still, we may assume that the width of the distribution of rotational correlation times for ethanol-d₂ is similar with the one in ethanol-d₁. Then, from the fact that the value of $\min(R/R_0)$ at $t_p = 300 \mu s$ for ethanol-d₂ is much smaller than the corresponding one for ethanol-d₁ we may conclude that the angular motion for the $C-^2H$ bonds in ethanol-d₂ is larger than for the $O-^2H$ bond in ethanol-d₁. A further support for this conclusion is the direct comparison of C/C_0 values for the two different deuterated ethanol samples (cf. Fig. 6.23). It is seen that C/C_0 for ethanol-d₂ decreases to a much lower value close to T_g reflecting a larger angular amplitude.

The average time constants estimated from the R/R_0 traces are shown in Fig. 6.24. It is observed that the time constant obtained from 2H NMR for ethanol-d₁ agrees well with those obtained from dielectric spectroscopy (DS). On the other hand, τ_1

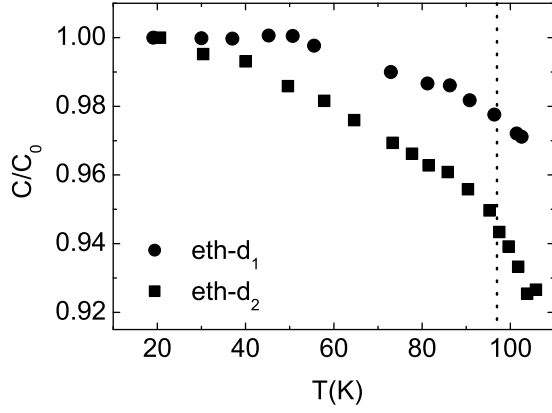


Figure 6.23. Normalized apparent spectral width C/C_0 for ethanol- d_1 and for ethanol- d_2 ; the dotted line marks T_g (data from Schneider [115]).

for ethanol- d_2 is slightly shorter than the values from DS. Therefore not only angular amplitude is different between the motion of the $C-^2H$ and $O-^2H$ bond in ethanol but also the corresponding time constants at the same temperature.

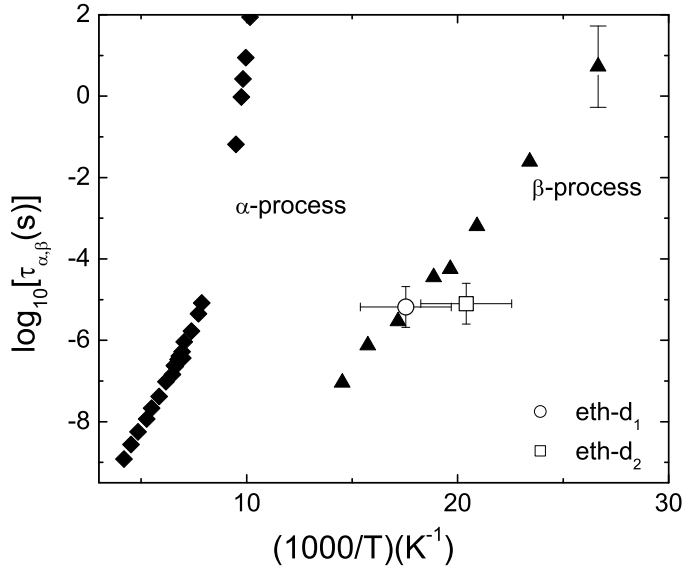


Figure 6.24. Time constants for ethanol. Full symbols: dielectric spectroscopy measurements (from Benkhof [18]), open symbols: line shape analysis. (We used $\delta = 152 \text{ kHz}$ for ethanol- d_1 and $\delta = 126 \text{ kHz}$ for ethanol- d_2 [115] and estimated half decade error in determining the time constant.)

In this section we successfully analyzed the ethanol data of Schneider [115] in the light of the simulations conclusions, showing that the study of C/C_0 values in connection with R/R_0 traces can reveal important information about the properties of fast

β -processes. (Fast in the sense that the fast motion limit with respect to the solid echo line shape is accessible by experiment and the line shape is not significantly influenced by the α -process.)

7. NMR study of meta-Fluoroaniline

7.1. Introduction

Since Johari and Goldstein (JG) [66] discovered that glasses made of molecules without internal degrees of freedom show secondary relaxational processes, the interest on such systems increased. Meta-fluoroaniline (m-FAN) is a simple, dielectrically rigid molecule that has been the subject of several studies (for example, [4, 19, 25, 36, 70, 74, 88] and references therein). Its dielectric spectrum shows an α -process, an excess wing and a β -process. The time constants of the β -process indicate a faster secondary process than in the case of common type B glass formers, like for example, toluene (cf. Fig. 7.3). Another interesting feature of this compound is that the dielectric strength of its β -process $(1-S) = \Delta\epsilon_\beta/\Delta\epsilon$ is by almost an order of magnitude smaller than in the case of toluene (cf. Fig. 7.4 (b)). We asked ourselves what is the cause of this behavior, is the molecular motion highly different in m-FAN in comparison with toluene? Can one probe by ^2H NMR such a process with a very small relaxation strength?

Morineau et al. [88], performing a neutron scattering study and molecular dynamics simulations, concluded that the m-FAN molecules form hydrogen-bond-induced-clusters. Recently, Reiser et al. [101] backed up the idea with the interpretation of their dielectric study under high pressure. Following these findings and giving some other arguments, Ngai and Paluch [92] argued that the β -process in m-FAN is fundamentally different than a ‘genuine’ JG β -process (like, for example in toluene). Considering these facts, it is interesting to see what we can conclude on the nature of the β -process and investigate whether ^2H NMR is sensitive to the distinction between a ‘genuine’ JG β -process and a non-‘genuine’ one.

7.1.1. General properties

Meta-fluoroaniline ($\text{FC}_6\text{H}_4\text{NH}_2$) is a substituted benzene ring compound; a sketch of the molecule can be seen in Fig. 7.1. In contrast to toluene, that is a van der Waals liquid, m-FAN exhibits a weak tendency to form intermolecular hydrogen bonds [4]. It is one of the most fragile low molecular weight glass formers, with a Vogel-Fulcher parameter $D = 3.0 \pm 0.4$ (cf. Eq. 1.2), estimated from the self diffusion coefficient measured in a NMR study [70]. A peculiar and convenient property of this glass former is that it is practically impossible to be crystallized at ambient pressure [4]. The glass transition temperature of m-FAN is $T_g = 173\text{ K}$ [4].

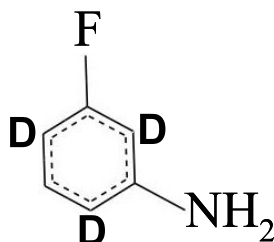


Figure 7.1. The chemical structure of m-fluoroaniline (m-FAN), with D are marked the deuterated sites for the compound used in the NMR experiment, m-FAN-d₃.

7.1.2. Dielectric spectroscopy results

This section features the main results of dielectric spectroscopy investigations of m-FAN; the measurements were done in our group initially by Benkhof [18] while later Blochowicz extended the accessible frequency range [20]. In the dielectric spectra of m-FAN displayed in Fig. 7.2 it is easy to observe a β -process present from high temperatures, say, 182 K till at the lowest one, 110 K. Note that also an excess wing is clearly recognized, for example, in the spectrum measured at 172 K.

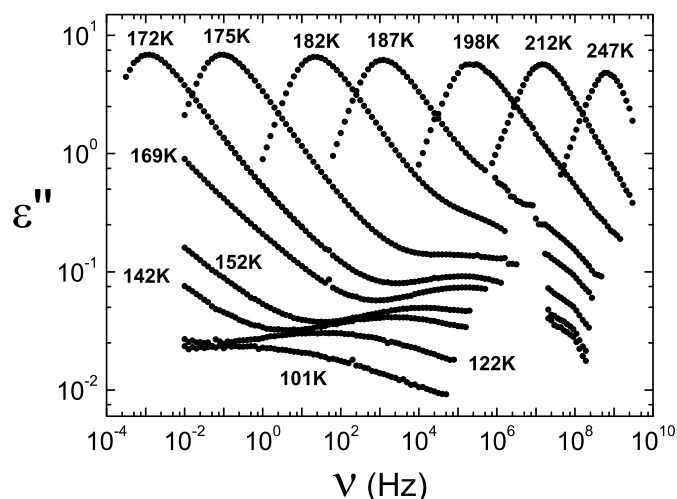


Figure 7.2. Imaginary part of complex permittivity ε'' for m-FAN (from Blochowicz [20]).

The time constants of the α - and β -process in m-FAN are presented in Fig. 7.3 along with those of several other type B glass formers. It is seen that τ_β is similar for toluene, 44% chlorobenzene in cis-decaline and polybutadiene. On the other hand τ_β

of m-FAN is shorter by more than a decade. Also the activation energy in the case of m-FAN ($E_a = 20.6 T_g$) is somewhat smaller than the $24 T_g$ value found in the other systems [20].

Figure 7.3. Time constants of the α and β -process in m-FAN as a function of reduced inverse temperature compared with those from some type B glass formers; cbz/dec stands for 44% chlorobenzene in cis-decaline. Toluene and polybutadiene data are from Kudlik [74], m-FAN data are from Blochowicz [20] and cbz/dec from Tschirwitz [125] and Vogel et al. [136].

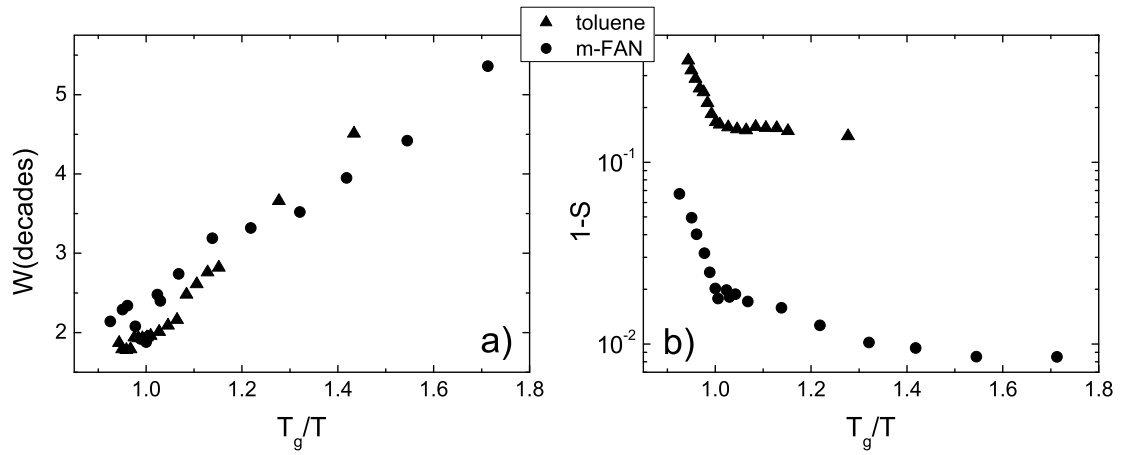
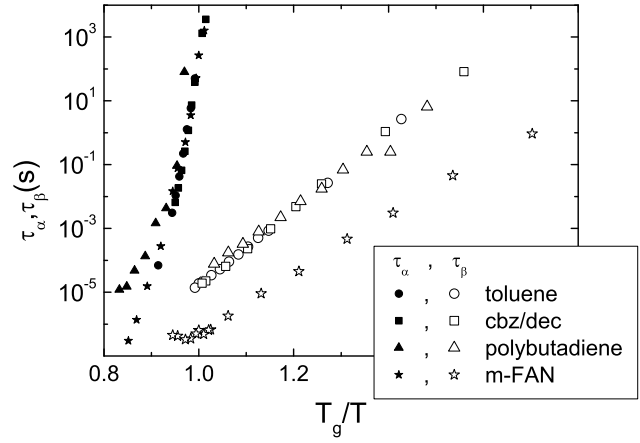


Figure 7.4. a) Width parameter W and b) the relative relaxation strength $(1 - S)$ for the β -process (from Benkhof [18]).

A log-Gauss function $\varepsilon''(\nu)$ proves appropriate to fit the β -peak [18, 74] and the fitted half width W at $1/e$ of the peak height for toluene and m-FAN is presented in Fig. 7.4 (a). One can see that the values are similar and they are strongly increasing

with decreasing temperature, typical for the β -process [74]. The fraction of the correlation that relaxes via the β -process, $(1 - S) = \Delta\varepsilon_\beta/\Delta\varepsilon$ is plotted in Fig. 7.4 (b). $(1 - S)$ decreases until T_g and remains roughly constant at lower temperatures. Moreover, the relaxation strength of m-FAN is by an order of magnitude smaller than that of toluene.

7.2. Experimental details

7.2.1. The deuterated sample

In the ^2H NMR experiments a m-FAN- d_3 sample was employed with the ^2H atoms belonging to the benzene ring (see Fig. 7.1) thus it is expected that their motion reflects the motion of the entire molecule.

A m-FAN- d_5 sample was kindly provided by C. Alba-Simionesco, Paris, Université de Paris-Sud. The two deuterons in the NH_2 group were exchanged by J. Gmeiner as follows: 0.7 ml m-FAN- d_5 was dissolved in 3.8 ml, 2*m* HCl (10% excess acid). The water was evaporated in vacuum at room temperature and a solid residue of m-fluoroaniline hydrochloride was obtained (m-FAN- $\text{d}_3\cdot\text{HCl}$). The hydrochloride was dissolved in a small amount of water and then 3.8 ml, 2*m* sodium hydroxide was added to set the m-FAN- d_3 free. The m-FAN- d_3 was extracted by washing three times with diethylether, drying over sodium sulfate and afterwards filtrating. After the evaporation of the ether, the sample was distilled in low vacuum (at 45°C), the result being a few drops of m-FAN- d_3 .

7.2.2. Measurement parameters

For the sample m-FAN- d_3 a Bruker CXP 300 spectrometer equipped with a TecMAG data acquisition system was used in connection with a super-conducting magnet with a magnetic field strength of 7.05 T corresponding to a ^2H Larmor frequency of 46.07 MHz. The sample was placed in a home built low-temperature probe inserted in an Oxford static cryostat CF 1200 providing a temperature stability better than 0.2 K.

The spectra were measured applying a solid echo pulse sequence preceded by a saturation sequence (five 90° pulses). A time period t_d between the saturation and the solid echo sequences was chosen such that more than 95% of the equilibrium magnetization was probed.

The spin-lattice relaxation function was measured by applying the saturation recovery sequence while the spin-spin relaxation time was obtained by measuring the echo height for different interpulse delays in the solid echo sequence.

Sin-sin and cos-cos decay curves were measured with a four pulse sequence with a minimum phase cycling of 16 scans to cancel double-quantum coherences [109]. Again a saturation sequence with five 90° pulses was preceding the measuring sequence. In all the cases we had a pulse length for the 90° pulse of about 2.5 μs .

7.3. Results

7.3.1. Spin-lattice and spin-spin relaxation

Spin-lattice and spin-spin relaxation phenomena are governed by the α -process at temperatures higher than T_g while at lower temperatures the β -process is the main factor that influences them. Hence an investigation in a wide temperature range would provide information about both the α and β -process.

We note that Kircher et al. [70] measured proton and fluorine spin-lattice relaxation times of m-FAN for temperatures higher than T_g in order to study the properties of the α -process.

Spin-lattice relaxation

The mean spin-lattice relaxation time $\langle T_1 \rangle$ for m-FAN-d₃ is plotted in Fig. 7.5 as a function of inverse reduced temperature T_g/T (for the definition of $\langle T_1 \rangle$ see the theory chapter, page 23). With lowering the temperature, $\langle T_1 \rangle$ increases sharply till around T_g below which it shows a weaker dependence on T_g/T .

In the following we will focus our attention on the temperature range $T < T_g$, where the spin-lattice relaxation is dominated by the β -process [59, 82]. One expects that the differences between the β -processes of m-FAN and toluene found by DS should be rediscovered in the spin-lattice relaxation features. Figure 7.5 shows data from m-FAN-d₃ along with the one from toluene-d₅ and one sees that $\langle T_1 \rangle$ is longer for the former glass at the same T_g/T . For, example, close to T_g the ratio of two $\langle T_1 \rangle$ s is almost two (1.96). Given the fact that, for a type A glass former (displaying no β peak in its DS spectrum), $\langle T_1 \rangle(T_g)$ is longer than the one for toluene by roughly an order of magnitude (compare, for example, Fig. 4.5 with Fig. 7.5 or cf. [82]), we can understand the similar trend of longer $\langle T_1 \rangle(T_g)$ for m-FAN-d₃. The relaxation strength of the β -process in m-FAN is much smaller with respect to toluene thus the DS spectrum of the previous glass former shows an intermediate shape between a type A glass former and toluene. Therefore one would expect that the value of $\langle T_1 \rangle(T_g)$ for m-FAN-d₃ is intermediate between the one from toluene-d₅ and those from type A glass formers and, indeed, this is our experimental finding.

We note another difference that is rather subtle between $\langle T_1 \rangle$ dependence on temperature of the two materials: in the range $1 < T_g/T < 1.75$ the data for toluene-d₅ can be interpolated by a straight line while those for m-FAN-d₃ cannot.

Regarding the stretching parameters of the spin-lattice relaxation function it is observed that for m-FAN-d₃ the functions are not exponential (cf. inset in Fig. 7.5); moreover, m-FAN-d₃ has a somewhat smaller β_{KWW} than toluene-d₅ at temperatures $T < T_g$, an indication that the spin-lattice relaxation functions are more stretched. We interpret this finding in the view of results reported by Hinze et al. [58]: at temperatures lower than T_g , the spin-lattice relaxation is strongly influenced by spin diffusion

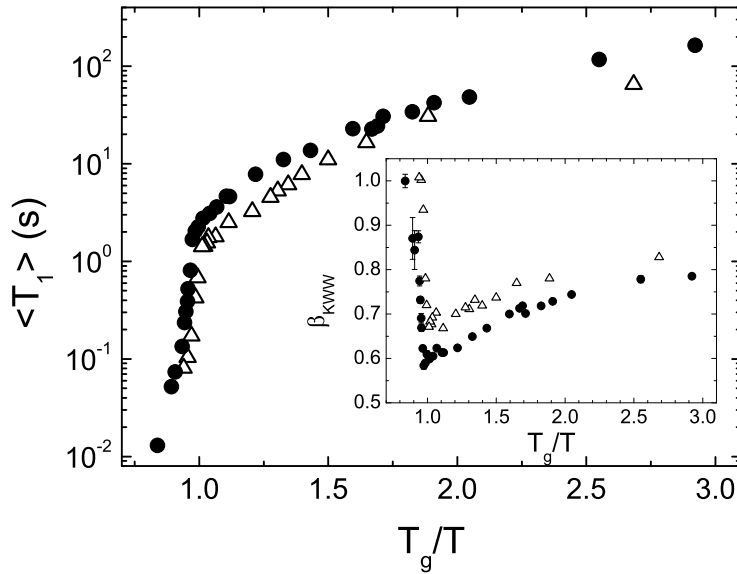


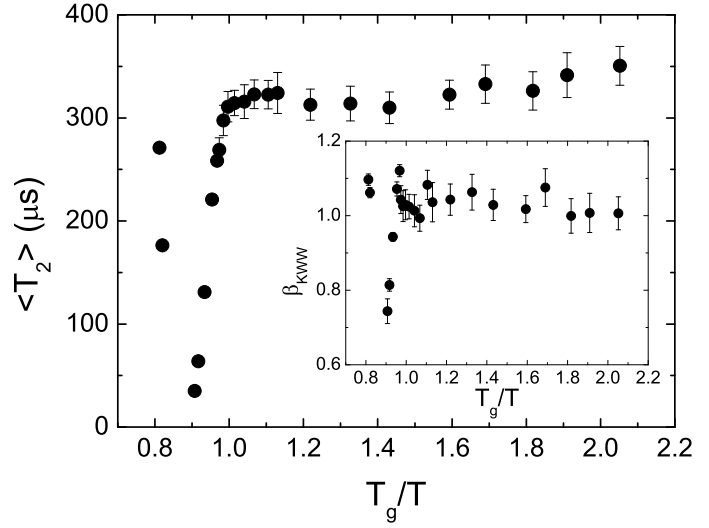
Figure 7.5. Full circles: the mean spin-lattice relaxation time for m-FAN-d₃; inset: corresponding stretching parameter β_{KWW} . Triangles: toluene-d₅ data are displayed for comparison (from Vogel [129]).

therefore the stretching β_{KWW} is mainly given by the spin density. Thus the smaller β_{KWW} in m-FAN-d₃ as compared to toluene-d₅ is a consequence of the smaller spin density in the previous compound.

Spin-spin relaxation

Figure 7.6 shows the mean spin-spin relaxation time of m-FAN-d₃ as a function of reduced inverse temperature T_g/T . The data display a deep minimum at $T > T_g$ where $\langle T_2 \rangle \rightarrow 0$ around $T_g/T = 0.9$ and they strongly increase at lower temperatures. In the range $T < T_g$, $\langle T_2 \rangle$ is only slightly dependent on temperature but still a local minimum is observed at $T_g/T \simeq 1.4$. Different from other glass formers, the spin-spin relaxation for m-FAN is virtually exponential below the glass transition temperature (see inset in Fig. 7.6).

Figure 7.6. The mean spin-spin relaxation time for m-FAN-d₃. Inset: corresponding stretching parameter β_{KWW} .



7.3.2. Solid echo spectra measured with a short interpulse delay

Figure 7.7 (a) shows the solid echo spectra of m-FAN-d₃ measured with a short interpulse delay $t_p = 20 \mu s$. One can observe that at the lowest temperatures the spectra are similar and, with increasing the temperature, they remain alike up to, say, $T = 185.4 K$. From dielectric spectroscopy it is expected that the line shape is influenced by the β -process in the temperature range $T \lesssim T_g$ and finding spectra that look identical at a first glance, proves that the angular amplitude of the β -process is very small (cf. 7.7 (a)). At temperatures larger than $190 K$, the spectra change their shape, finally collapsing to a central narrow line at $T \geq 206.6 K$. These line shape changes are the fingerprint of the isotropic α -process (isotropic in the sense that a unit vector associated with a fixed direction in the m-FAN molecule can jump to any orientation with respect to the external magnetic field during the specific time constant of the α -process).

A closer look at the spectrum measured with a short interpulse delay at $91 K$ (cf. Fig. 7.7 (b)) reveals that its shape is not that of a Pake spectrum but it displays an asymmetry parameter η slightly different from zero (for details on spectral shapes, see page 15). In the same figure a fit line is presented, interpolating very satisfactorily the experimental points. The fit provides: $\eta = 0.06$ and $\delta = 137 kHz$, values typical for a benzene ring derivate (for toluene-d₅ $\delta = 135 kHz$ [106]). (A dipolar broadening of $GB = 1.9 kHz$ was employed in the fitting procedure.)

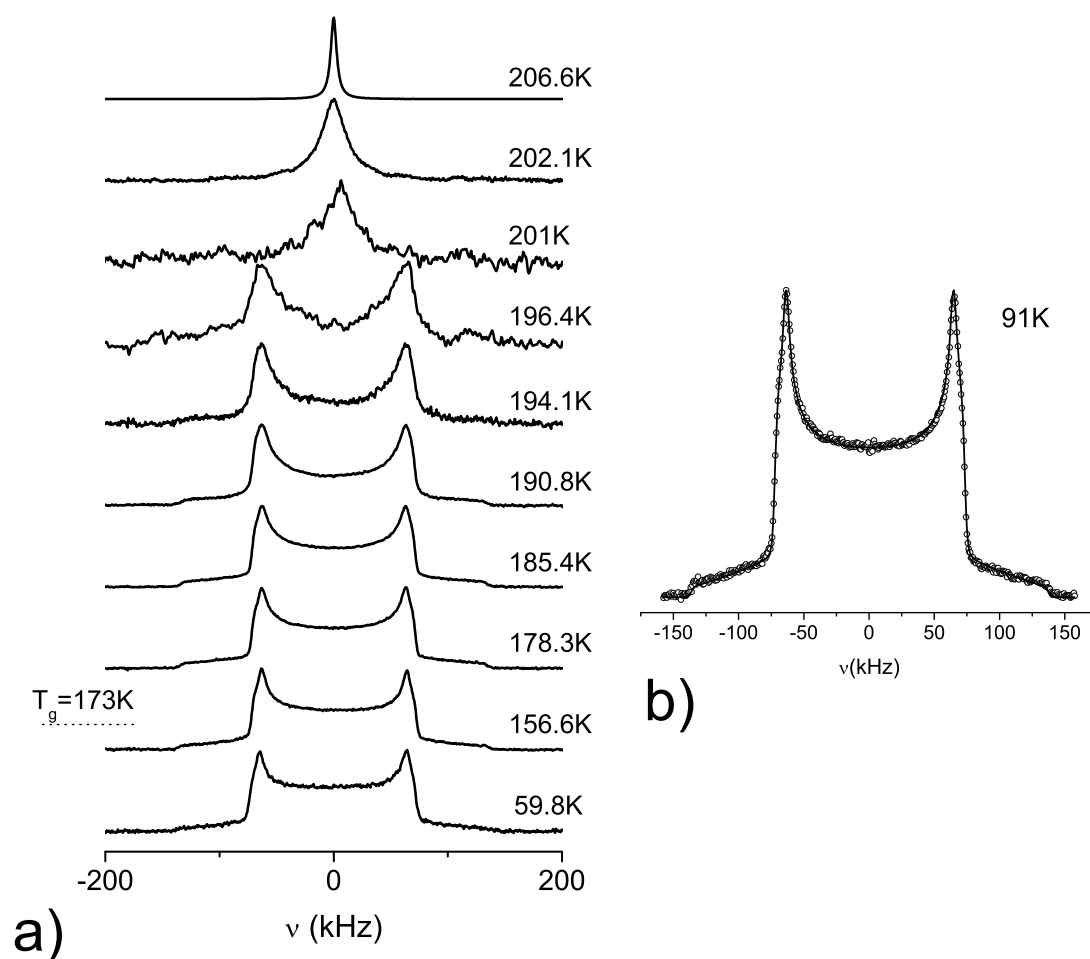


Figure 7.7. a) m-FAN- d_3 solid echo spectra for the interpulse delay $t_p = 20 \mu s$ at several temperatures. The glass transition temperature T_g is also indicated. b) Solid echo-spectra acquired with $t_p = 20 \mu s$; the points represent the experimental data; the solid line is a fit.

The apparent spectral width

Restricted molecular motion can have subtle effects on the shape of the spectra provided that it is not in the slow motion limit (cf. following paragraphs). One of the parameters that are affected by the motion is the apparent spectral width C (for the definition of C , see page 17). Therefore we measured $C(T)$ for the spectra acquired with a solid echo interpulse delay of $t_p = 20 \mu s$ and the results are shown in Fig. 7.8 (a). It is observed that the curve displays a step at temperatures well below T_g while at temperatures higher than T_g it is sharply increasing. We tentatively interpret the step as an effect of the slowing down of the β -process. That is, at temperatures higher than,

say, 110 K the mean time constant of the β -process is shorter than the characteristic time of the NMR experiment ($\langle\tau_\beta\rangle \ll 1/\delta \simeq 10 \mu\text{s}$: fast motion limit). Therefore the apparent spectral width is averaged (cf. Section 2.3.1). At $T < 70 \text{ K}$ the β -process is in the slow motion limit ($\langle\tau_\beta\rangle \gg 1/\delta$) and the observed spectral width is no longer influenced by molecular dynamics. Thus we believe that we measured the passage of the distribution of correlation times $G[\ln(\tau_\beta)]$ through the experimental window of the solid echo technique. From the ratio between the level of C for the slow motion, respectively fast motion regime, one can extract a mean angular amplitude for the β -process under reasonable assumptions (cf. Section 6.3.1). More details concerning our interpretation of the dependence on temperature of C will be given in this chapter in Section 7.4 where we also will present further arguments that support this interpretation. The increase of C above T_g is explained as an influence of the α -process that broadens the line before it collapses to a narrow central peak.

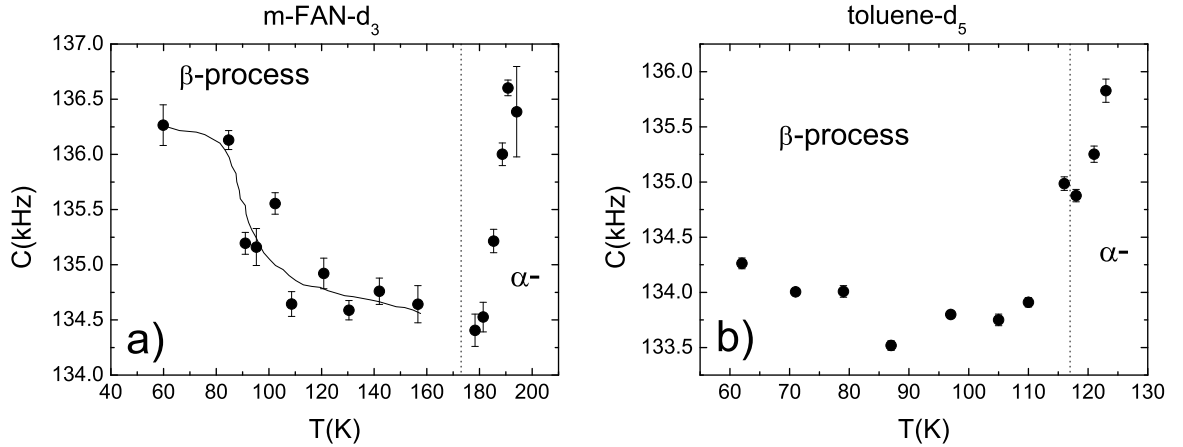


Figure 7.8. The apparent spectral width C vs. temperature T for a) m-FAN-d₃ (the solid line is guide for the eye) and b) for toluene-d₅ (data from the spectra acquired by Vogel [129]). In both cases the spectrum measured with the solid echo pulse delay $t_p = 20 \mu\text{s}$ was used; the dotted vertical lines indicate $T_g = 173 \text{ K}$ (m-FAN-d₃) and $T_g = 117 \text{ K}$ (toluene-d₅).

For comparison, Fig. 7.8 (b) presents the dependence on temperature of the apparent spectral width for toluene-d₅. It is seen that, with increasing the temperature, C shows a mild dependence on temperature below T_g and a step similar to the one found in m-FAN-d₃ cannot be observed. We explain this feature in the case of toluene-d₅ as being a proof that the fast motion limit of the β -process is not reached at temperatures smaller than T_g . Our interpretation is consistent with the fact that for toluene τ_β is longer than the one for m-FAN at the same reduced temperature T_g/T (cf. Fig. 7.3); thus at temperatures close to T_g , the β -process in the case of toluene is slower than the in the case of m-FAN and does not fulfill the fast motion condition $\langle\tau_\beta\rangle \ll 1/\delta \simeq 10 \mu\text{s}$.

7.3.3. Solid echo spectra measured with various interpulse delays

In order to get more informations about the β -process we measured the dependence of the solid echo spectra on the interpulse distance t_p and the results of such an experiment are displayed in Fig. 7.9 for several selected temperatures. It is observed that for the

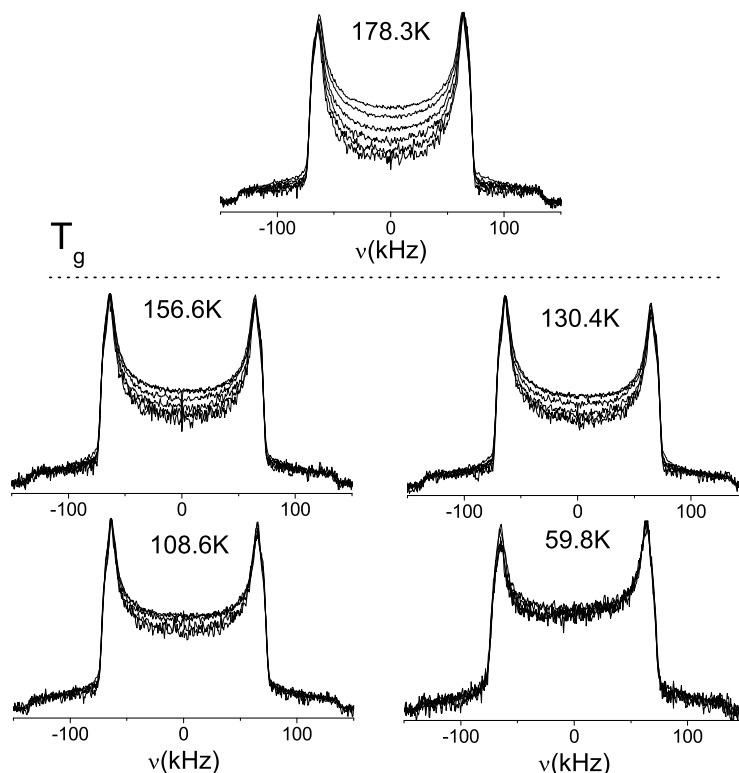


Figure 7.9. a) Normalized solid echo spectra of m-FAN-d₃ as a function of interpulse delay t_p at different temperatures. For the two lowest temperatures the t_p values are $t_p = 20, 50, 100, 150, 200 \mu s$; for the remaining temperatures the spectrum for $t_p = 250 \mu s$ is displayed, too. The larger the area of the spectrum, the smaller is t_p .

lowest measured temperature (59.8 K) the spectra for different t_p are similar. With increasing the temperature, the spectra change their shape for various t_p . Above T_g , at 178.3 K, the difference between spectra measured with distinct t_p becomes the largest in all the presented data. The spectra are typical of restricted small angle motion [132, 134, 135, 136] and we interpret these findings as follows: at very low temperatures (~ 60 K) the β -process has almost exited the time window of the ^2H NMR line shape experiment, and therefore no difference between spectra measured with various t_p is

seen. With increasing the temperature, the time constant of the β -process decreases, entering the time window of the experiment and affecting the spectra acquired with a long t_p . Close to and above T_g the line shape is additionally influenced by the α -process and thus the spectra display larger differences.

For selected t_p values the relative spectral intensity at zero frequency $R(t_p, T)$ is displayed in Fig. 7.10 (a). The R values are taken as a quantitative measure for the line shape changes caused by the β -process (for the definition of R , see page 17). One observes the features already discussed above: around 60 K the R values for different t_p are similar indicating that the β -process has exited the time window of the experiment. With increasing the temperature, the difference $[R(t_p = 20 \mu s, T) - R(t_p = 250 \mu s, T)]$ is increasing. A closer look to $R(t_p = 20 \mu s, T)$ reveals that the line exhibits a local minimum around $T = 120$ K. Above T_g , R is strongly decreasing and the temperature when R sharply drops seems to be slightly different for distinct t_p , i.e. it is higher, the smaller t_p is.

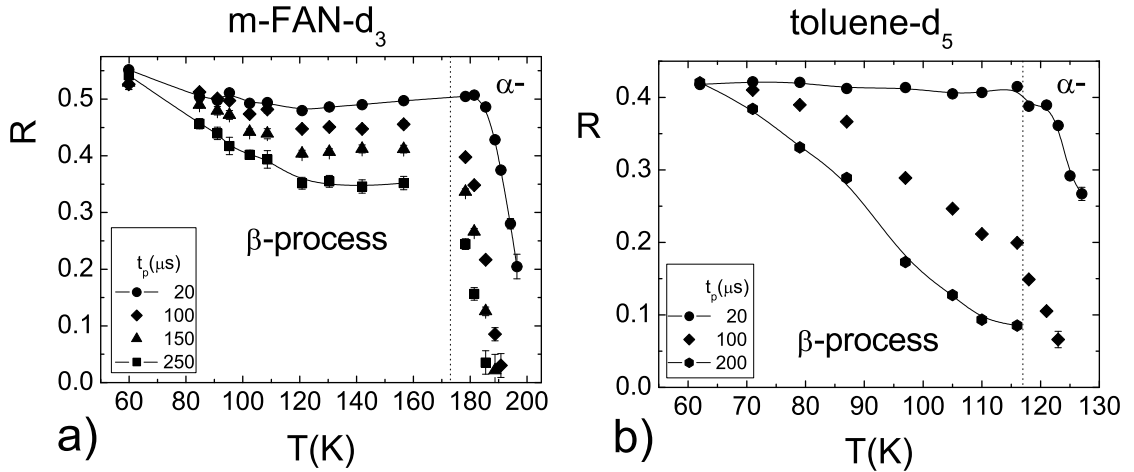


Figure 7.10. The relative spectral intensity at zero frequency R as a function of temperature for a) m-FAN-d₃ and b) toluene-d₅ (estimated from the spectra acquired by Vogel [129]). The solid line is a guide for the eye. The vertical dotted lines mark $T_g = 173$ K (m-FAN-d₃) and $T_g = 117$ K (toluene-d₅).

Figure 7.10 (b) shows the R values for toluene-d₅ so that a direct comparison between the two systems can be done. Note that the dependence on temperature of $R(t_p = 100 \mu s, T)$ and $R(t_p = 200 \mu s, T)$ is more accentuated than in the case of m-FAN-d₃, with the last R value decreasing from about 0.4 to roughly 0.08 at temperatures below the glass transition temperature. This clearly demonstrates that the β -process in the two systems shows different features from an ²H NMR point of view. Before any quantitative analysis we can say that the β -process in m-FAN-d₃ is definitely faster and probably displays a smaller mean angular amplitude as compared to toluene-d₅.

and in Section 7.4 we will discuss more on the figure above.

7.3.4. Stimulated echo experiments

Investigation of the α -process: the sin-sin correlation functions

By acquiring the sin-sin correlation function $\mathcal{F}^{\text{sin}}(t_1 \rightarrow 0, t_m)$ at temperatures higher than T_g one can extract information about the autocorrelation function f_2 associated with the α -process (cf. Section 2.3.2, page 20). Still it is not simple to measure the effect of the α -process on $\mathcal{F}^{\text{sin}}(t_1, t_m)$ because of several reasons: first, the time window of the technique is $10^{-5} < \tau_2 < T_1$ and above T_g the spin-spin relaxation becomes fast, thus restricting the interesting time window. In addition, m-FAN is one of the most fragile glass formers (cf. Section 7.1.1) and therefore the correlation times that affect $\mathcal{F}^{\text{sin}}(t_1, t_m)$ are in a relative narrow temperature range. Nevertheless we measured the functions for three temperatures, as shown in Fig. 7.11. The lines display two decays,

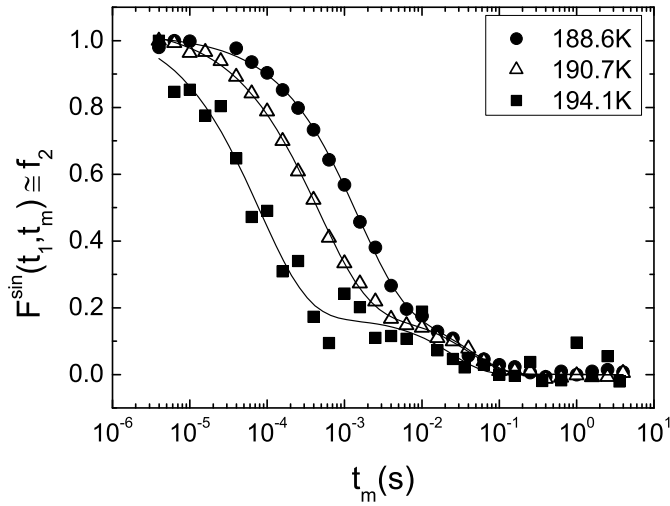
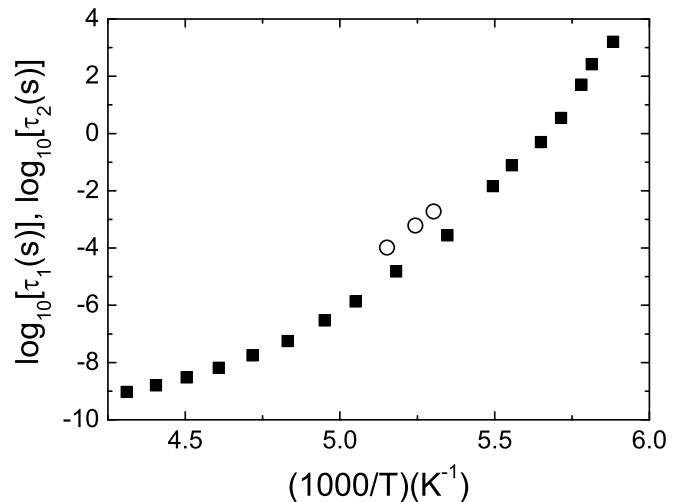


Figure 7.11. Sin-sin correlation functions of m-FAN-d₃ at two different temperatures and the evolution time $t_1 = 3 \mu\text{s}$. Solid line is fit with Eq. 2.42.

the first is the actual sin-sin correlation function \mathcal{F}^{sin} while the second is caused by the decay of the spin-alignment state (cf. Section 2.3.2, its characteristic time scale being described by T_{1Q}). With increasing the temperature the first decay becomes faster, shifting to shorter times. In the same figure it is seen that the experimental points are well fitted by Eq. 2.42 with the short time decay being a KWW function and the long time decay an exponential function. Because the evolution time is experimentally very short ($t_1 = 3 \mu\text{s}$) the obtained relaxation time for the sin-sin decay is an estimate for τ_2 , the correlation time of the rotational autocorrelation function of rank $\ell = 2$

(f_2). The so obtained τ_2 is displayed in Fig. 7.12 where it is compared with the time constant obtained from dielectric spectroscopy experiments (DS, $\ell = 1$). The data

Figure 7.12. Time constants for the α -process. Full squares: from dielectric spectroscopy - Blochowicz [20]; open circles: from the ^2H NMR sin-sin correlation functions.



points from NMR indicate a longer correlation time than the one obtained from DS at the same temperature. This is somewhat unusual and a large difference between the time constants delivered by the two techniques being not reported anywhere else to our knowledge. Deuteration renders the molecule heavier hence an increase in the rotational correlation time with respect to the protonated molecule is expected. However, the increase of the time constant looks more significant than being the sole effect of deuteration and the exact cause of it eludes us at the present moment.

As a speculation we offer the following interpretation: at high temperatures the α -process is given by a rotational molecular motion that is isotropic and random (in the sense that after a jump, the orientation of a molecule can change by any angle between 0° and 360°). Therefore one expects that $\tau_1 = \tau_2$. With lowering the temperature the mechanism of motion changes, the molecules reorient isotropic but with a fixed angular amplitude $\Delta\Omega$. Then one expects that the ratio τ_2/τ_1 is different from 1 as demonstrated by Anderson [10]:

$$\frac{\tau_2}{\tau_1} = \frac{2}{3[1 + \cos(\Delta\Omega)]}. \quad (7.1)$$

If this phenomenon is the only cause for the difference of τ_1 and τ_2 then we can estimate $\Delta\Omega = 110^\circ$ for the lowest investigated temperature. A somewhat similar scenario in which $\Delta\Omega$ has a bimodal distribution can be found in literature [29, 52, 57]. Still, as said in the Introduction, in the reported cases, the distribution contains a large percent

K_{small} of small angles, typically about $2^\circ - 3^\circ$ and a percent K_{large} of large angles in the range $30^\circ - 50^\circ$ [28]. The ratio K_{large}/K_{small} differs between glass formers, and it was argued that it is smaller when hydrogen bondings or other association effects are present [28] therefore our explanation which considers that the fraction of large angles is substantial seems improbable. Future experiments measuring the 2D spectrum as well as acquiring $\mathcal{F}^{sin}(t_1, t_m)$ for different values of t_1 will shed light on the α -process in m-FAN.

Investigation of the β -process: the cos-cos correlation functions

Vogel et al. [133, 134, 135] demonstrated that features of the β -process can also be investigated by measuring the cos-cos correlation functions for long values of the evolution time t_1 . Carrying out such experiments at $T < T_g$ allows one to study slow dynamics, with the time constants up to the spin-lattice relaxation time T_1 . In addition, highly restricted reorientation can be probed if long values of t_1 are employed.

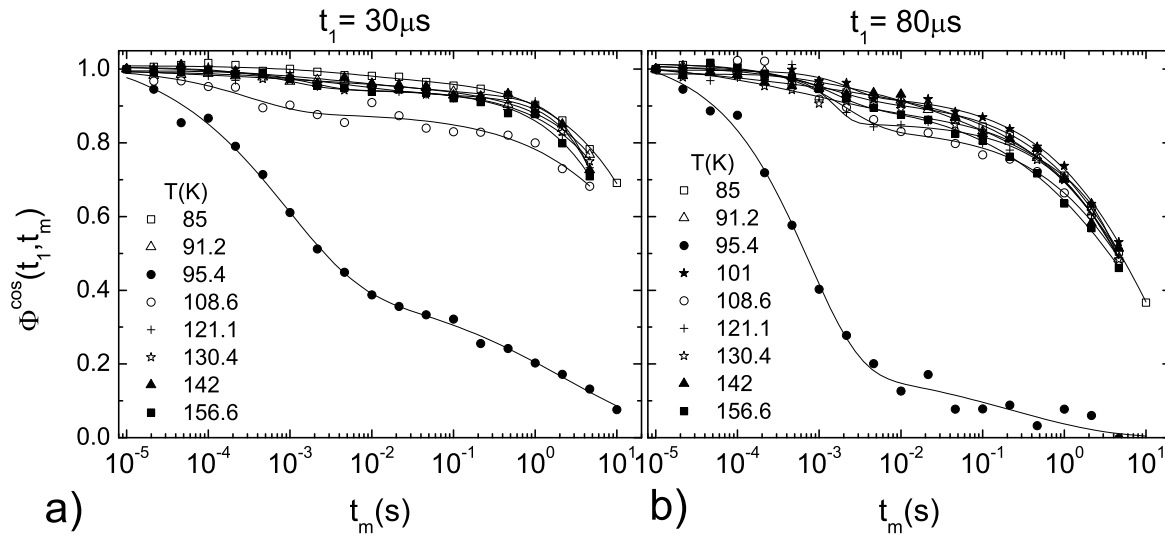


Figure 7.13. Cos-cos correlation functions $\Phi^{cos}(t_1, t_m)$ for different temperatures and two evolution times t_1 . The data were corrected against spin-lattice relaxation. Lines are fits with Eq. 2.50.

Therefore we acquired the cos-cos correlation functions for m-FAN- d_3 for two values of t_1 as shown in Fig. 7.13 where the points were corrected against spin-lattice relaxation (for the details regarding the measurement of cos-cos correlation functions, see page 19). The data for $t_1 = 30 \mu s$ (cf. Fig. 7.13 (a)) have such a shape that it is difficult to distinguish the expected two-step decay (cf. Eq. 2.50); only for $T = 95.4$ and 108.6 K the two-step decay is clearly seen. For the longer $t_1 = 80 \mu s$ (Fig. 7.13 (b)),

the bimodal function is easier to be recognized. While the curves corresponding to almost all temperatures are somewhat similar, the one for $T = 95.4\text{ K}$ has a very low plateau value S^{cos} .

Equation 2.50 was used to fit the experimental data points (cf. Fig. 7.13) and the resulting fit parameters are displayed in Fig. 7.14. The mean time constants for the two decays are temperature independent, in the limit of scattering. This behavior is similar

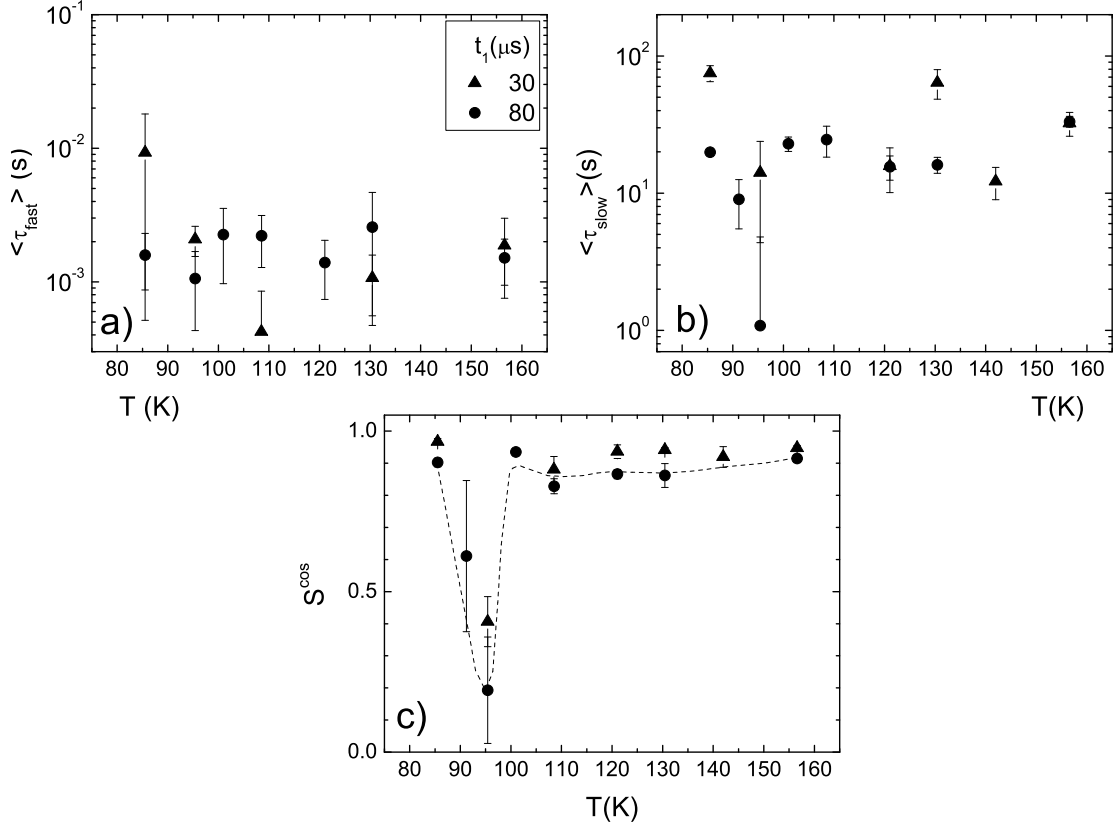


Figure 7.14. Parameters of the fits lines in Fig. 7.13; the symbols correspond to the same t_1 in all figures. The dashed line in c) is a guide for the eye corresponding to $t_1 = 80\text{ }\mu\text{s}$.

with what is found, for example, in 45% chlorobenzene/decaline or in toluene where both time constants present a weak temperature dependence [71, 129, 134]. It was demonstrated that the long time decay of $\Phi^{cos}(t_m)$ is due to spin diffusion, thus it can be disregarded when investigating the effects of molecular dynamics [129, 134]. Concerning the short time decay of the $\Phi^{cos}(t_m)$, if it is caused by a process that displays a broad distribution of correlation times with respect to the accessible experimental time window, then one expects that $\langle \tau_{fast} \rangle$ is virtually temperature independent. That happens because the observed $\langle \tau_{fast} \rangle$ is always determined by the width of the ex-

perimental time window [129, 134] and not by the mean value of the distribution of correlation times. In our case, the limits of this time window are set by the onset of spin diffusion towards long times (on the order of 1 s) and by the length of t_1 towards short times ($\sim 100 \mu s$).

The plateau value S^{cos} displays a minimum around 95 K and its temperature behavior is somewhat similar with the one found in typical glass formers [71, 115, 129] with the major difference that the minimum is low (less than 0.5) and sharp. It was proved that the temperature dependence of S^{cos} reflects the evolution of the distribution of correlation times for the β -process, more precise, it is proportional to the fraction of $G[\ln(\tau_\beta)]$ present in the time window of the experiment [71, 115, 129, 133, 134]:

$$(1 - S^{cos}) = p(t_1) \int_{\ln(\tau')}^{\ln(\tau'')} G[\ln(\tau_\beta)] d\ln(\tau_\beta), \quad (7.2)$$

where $p(t_1)$ is a temperature independent factor depending on the geometry of the molecular motion involved in the β -process. Therefore one can reproduce the function $S^{cos}(T)$ by using the above equation with the appropriate $G[\ln(\tau_\beta)]$ and limits of integration. Generally speaking, the minimum in S^{cos} vs. T will emerge at the temperature where the fraction of $G[\ln(\tau_\beta)]$ that is present in the experimental time window is maximum. Hence one may argue that, under the assumption that $G[\ln(\tau_\beta)]$ is a log-Gauss, S^{cos} shows a minimum at the temperature where the mean $\langle \ln(\tau_\beta) \rangle$ lies in the middle of the experimental time window. We used this simple approach and the resulting time constant is shown in the following section (cf. Fig. 7.16 (b) and Fig. 7.17).

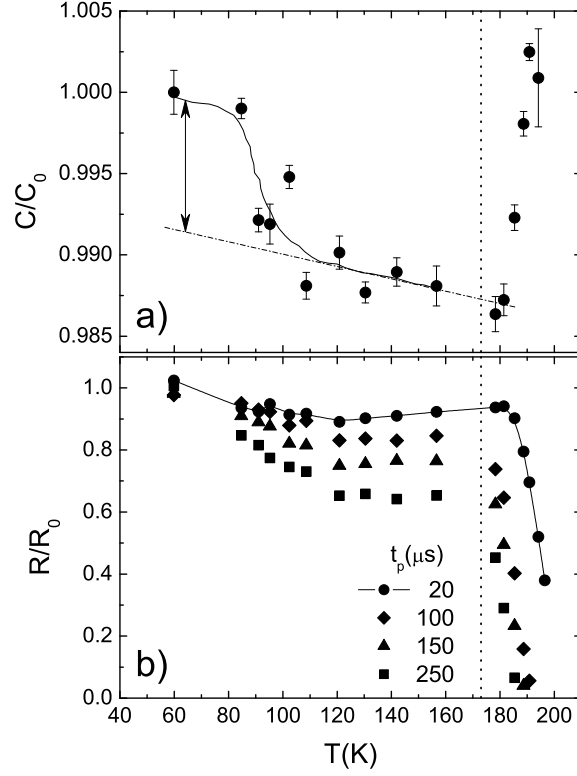
7.4. The β -process in m-FAN: discussion and conclusions

All the experimental results being presented, we will try to further analyze the 2H NMR measurements on m-FAN- d_3 referring to a large extend to the conclusions drawn in the simulation chapter (cf. Chapter 6). In addition, a comparison with the corresponding features in toluene will be provided.

Angular amplitude of the molecular motion

As shown in Fig. 7.15 (a), the normalized apparent spectral width C/C_0 of m-FAN- d_3 displays a step in its temperature dependence. It is interpreted as being a consequence of the passage of the time constant $\langle \ln(\tau_\beta) \rangle$ from the slow motion limit (at low temperatures) to the fast motion limit (at high temperatures). In the frame of the cone model, which assumes that the $C-^2H$ bond of a molecule moves *on* a cone of semiangle χ during the β -process, one can make an estimate of this angle. From the ratio $C_{fast}/C_0 \simeq 0.9918$, indicated by the double arrow in Fig. 7.15 (a) and applying

Figure 7.15. m-FAN-d₃: a) normalized apparent spectral width C/C_0 vs. temperature T and b) the normalized relative spectral intensity at zero frequency for several interpulse delays t_p . Solid lines are guides for the eye; the vertical dotted line marks T_g .



the equation $C_{fast}/C_0 = [3\cos^2(\chi) - 1]/2$, we calculate an angular amplitude of the β -process $\chi \simeq 4^\circ$. Of course, the use of this simple model provides an evaluation of the mean angular amplitude. If we assume that the $C-^2H$ bond moves *within* the cone of semiangle χ than the estimated mean angular amplitude is somewhat larger, $\chi \simeq 6^\circ$ (cf. equation $C_{fast}/C_0 = \cos(\chi)[1 + \cos(\chi)]/2$). We are aware that the value C_0 in the experimental results is given by only one point at the lowest measured temperature and one may argue that the estimated angular amplitude χ is questionable. Even without that point the result in Fig. 7.15 (a) provides a qualitative observation. It proves that the passage from the slow motion limit to the fast motion limit, seen as a drop in the trace of C/C_0 vs. T , can be measured in the case of m-FAN-d₃. This is different from toluene where the β -process is too slow and this passage is obscured by the line-shape changes due to the α -process (cf. Fig. 7.8). Therefore one expects that for faster β -processes, comparable with the one in m-FAN, it might be possible to directly estimate the angular amplitude of the molecular motion by measuring the temperature evolution of the apparent spectral width. This is indeed the case for ethanol-d₁ as shown in

Fig. 6.21 (a).

In order to check our evaluation of the angle χ against other experiments, we consider the approach of Döss et. al [42], that provides an estimate of the cone angle in a model in which the dipole moment of the molecule moves *on* a cone of semiangle χ . Then, from dielectric spectroscopy (DS) data: $\sin(\chi_{DS}) = (\Delta\varepsilon_\beta/\Delta\varepsilon_\alpha)^{1/2}$, where $\Delta\varepsilon$ represents the peak area and $\Delta\varepsilon_\beta/\Delta\varepsilon_\alpha \simeq (1 - S)$ (we assumed that $\Delta\varepsilon_\beta \ll \Delta\varepsilon_\alpha$). As $(1 - S)$ slightly decreases below T_g , the estimated angle also changes in the range $5^\circ \lesssim \chi_{DS} \lesssim 8^\circ$ that is compatible with the ^2H NMR result.

The finding of a small angular amplitude for the molecular motion associated with the β -process is not a surprise as already a previous study on toluene concluded that the secondary relaxation processes are characterized by a highly restricted motion (see, for example, [135]). Still, the outcome of the line-shape analysis for m-FAN is somewhat different from that of toluene because, in the case of the latter, it was concluded that a certain fraction of large cone angles ($\sim 15\%$, $\chi = 20 - 25^\circ$) is required in order to explain the experimental results (cf. Fig. 1.4 (a) and [135]). Unlike that, an angle χ of about 4° in the cone model is sufficient to account for the observed changes in the solid echo spectra of m-FAN. The assertion of distinct amplitudes in the two glasses is further supported by the well different dielectric relaxation strength $(1 - S)$. For toluene $(1 - S)$ is larger by roughly one order of magnitude and therefore a larger angular amplitude is to be expected (cf. Fig. 7.4 (b)).

Time scale of molecular motion

In the former ^2H NMR study on toluene, the observed experimental features were successfully reproduced by simulations in which the time scale and the distribution of correlation times were used as inputs provided by DS experiments [129, 132, 134, 135, 136]. In contrast, we tried to estimate time constants for the β -process in m-FAN directly from the ^2H NMR data. As proved by the simulations discussed in Chapter 6, the mean time constant of the β -process is $1/\delta$ at the temperature where the trace $[R(t_p = 20 \mu\text{s})/R_0]$ shows a minimum. In Fig. 7.15 (b) one can see that the points for $[R(t_p = 20 \mu\text{s})/R_0]$ clearly describe a minimum located at a temperature of roughly 120 K . In addition, the traces for $[R(t_p = 100 \mu\text{s})/R_0]$ and $[R(t_p = 50 \mu\text{s})/R_0]$ (the last one is not shown in the figure for reasons of clarity) display a minimum around the same temperature hence the above mentioned temperature is dependably determined. Thus the effect observed in the simulations is rediscovered in the real ^2H NMR experiment on m-FAN- d_3 . It follows that, assuming a symmetric distribution of $G[\ln(\tau_\beta)]$, we can estimate a time constant $\langle \ln(\tau_\beta) \rangle = 1/\delta$ at the temperature $T = 120 \pm 7 \text{ K}$ (shown in Fig. 7.17). It is seen that it is considerably smaller than the one obtained at the same temperature from DS. We emphasize that the temperature where $[R(t_p = 20 \mu\text{s})/R_0]$ displays a minimum is very similar with the one where $\langle T_2 \rangle$ has a local minimum below T_g (cf. Fig. 7.6). This finding is analogous with, for example, the result for

ethanol, and the correlation between the minima in the traces of $\langle T_2 \rangle$ and R vs. T is always to be expected because both experiments used to determine them share the same experimental time window [115].

In the simulation chapter it was demonstrated that the value of the minimum in the $[R(t_p = 20 \mu s)/R_0]$ trace depends on the angle χ and on the width σ of the distribution of the jump times (see page 96). If we consider that the angle for the cone model is reliably determined as presented above, $\chi \simeq 4^\circ$ then the value $\min[R(t_p = 20 \mu s)/R_0] \simeq 0.9$ is solely a function of σ . Fig. 6.17 (b) shows the trace of σ vs. $\min[R(t_p = 20 \mu s)/R_0]$ for a simulation angle of 5° . Assuming that in our case the same trace holds, one can say that the width of the distribution of correlation times $G[\ln(\tau_\beta)]$ is larger than 3.5 decades (provided that it has a ln-Gauss shape).

A further time constant $\langle \log(\tau_\beta) \rangle$ can be estimated quasi model-free if one analyzes the temperature dependence of the plateau value S^{cos} of the cos-cos correlation functions. First, we will try to prove that this method provides a reliable output, by discussing former experimental data. Fig. 7.16 (a) shows the function $(1 - S^{cos})$ for several type B glass formers. All data display a maximum below T_g but it is seen that only polybutadiene-d₆ and toluene-d₅ data are similar. Ethanol-d₁ presents

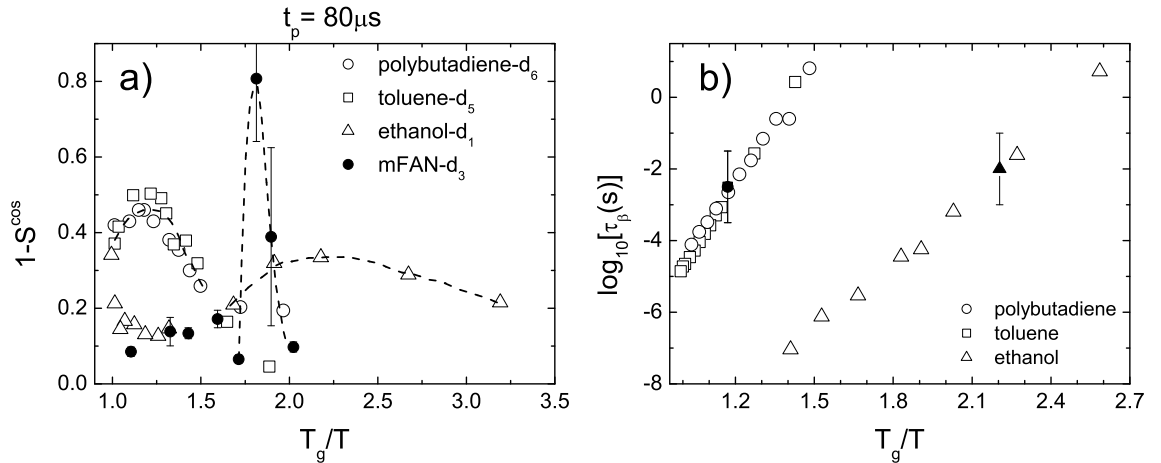


Figure 7.16. a) $1 - S^{cos}$ of the cos-cos correlation functions vs. inverse reduced temperature T_g/T for several type B glass formers; polybutadiene-d₆ and toluene-d₅ from Vogel [129, 134], ethanol-d₁ from Schneider [115]. The dashed lines are guides for the eye. b) Open symbols: time constants from dielectric spectroscopy; toluene and polybutadiene data are from Kudlik [74], ethanol from Benkhof [18]. The full symbols are time constants determined from cos-cos correlation functions.

a very broad maximum at a high value of T_g/T while m-FAN-d₃ has an atypically sharp maximum, with the largest value. As said before, the temperature dependence of S^{cos} reflects the evolution of the distribution of correlation times of the β -process

[71, 115, 129, 133, 134]. Using the arguments given on page 122 and following, at the temperature where $(1 - S^{cos})$ displays a maximum we estimated a time constant for the β -process. These temperatures are $T_{max,tol} = 100 \pm 8 K$, $T_{max,PB} = 147 \pm 4 K$, $T_{max,eth} = 44 \pm 6 K$ and $T_{max,m-FAN} = 95 \pm 5 K$. For the first two glass formers we evaluate a time constant of $\langle \log(\tau_\beta) \rangle = -2.5 \pm 1$ that is in the middle of the expected characteristic time window 10^{-4} - $10^{-1} s$ [71, 115, 129, 133, 134]. (We remind the reader that the short time limit of the time window is given by the values of the time t_1 employed in the cos-cos experiments while the long time limit is determined by the onset of the spin diffusion.) Because the long time decay of cos-cos correlation functions is longer in ethanol- d_1 [115] and in m-FAN- d_3 , the corresponding time window is 10^{-4} - $1 s$ and therefore, for these samples $\log(\tau_{cos}) = -2 \pm 1$. It is seen in Fig. 7.16 (b) that for polybutadiene, toluene and ethanol the so estimated time constants agree well with those reported from DS experiments, and moreover, for toluene and polybutadiene they are one on top of the other on the T_g/T scale. Hence this method of estimating time constants for the β -process looks trustworthy and it will be used in the case of m-FAN- d_3 , too.

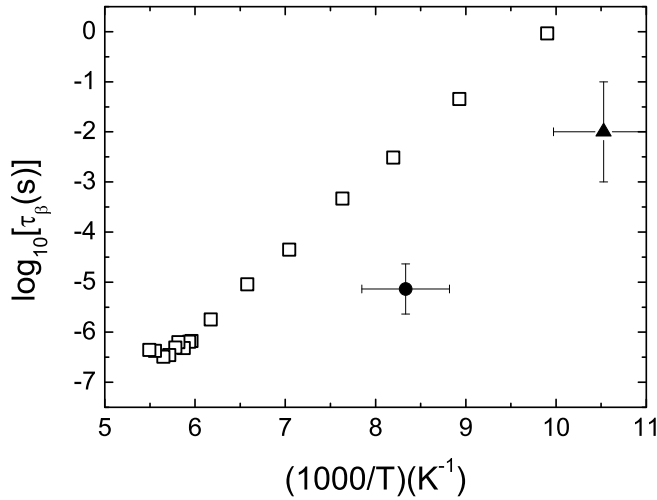


Figure 7.17. Time constants of the β -process; open squares: dielectric spectroscopy data from Blochowicz [20]; full circle: estimated from the R values; full triangle: estimated from cos-cos correlation functions.

Fig. 7.17 shows the time constants for m-FAN- d_3 obtained from 2H NMR in comparison with those from DS. One sees that the former are much shorter than those determined by DS although it seems that the temperature dependence is the same. This striking difference may be rationalized as follows: 2H NMR probes the motion of a single particle (thus the fastest time constant) while DS probably probes a collective motion. In a recent paper it was speculated that the hydrogen-bond-induced-clusters

of limited size in m-FAN display an own dipole moment and they could be responsible for the β -peak in the DS response [56].

The final conclusions regarding the β -process in m-FAN as compared to other glass formers are: it is similar in the sense that it comprises a highly restricted, small angle motion, fact demonstrated by the dependence of the solid echo line-shape on temperature and interpulse delay t_p . An angular amplitude of about 4° suffice to explain, within the cone model, the above mentioned evolution. Still, a slight difference with respect to toluene is remarked: all the observables can be understand assuming only small angular motions without any need for a small percent of large angles [129, 133, 134]. On the other hand, a prominent difference is the decoupling of the ^2H NMR and DS time scales, fact that might support the claim that m-FAN forms clusters of several molecules [88, 101].

8. Summary

In the present work molecular glass formers were investigated by means of multidimensional ^2H NMR (solid echo and 2D spectra, stimulated echo decays, spin-lattice and spin-spin relaxation). We focused our attention on glass forming liquids that were composed of simple, rigid molecules in order to study the properties of the secondary relaxation processes (β -processes) in the glassy state ($0.5T_g \lesssim T < T_g$). For several systems we also acquired NMR data at temperatures corresponding to the supercooled liquid state ($T > T_g$) providing information on the main relaxation process (α -process). In addition, extensive random walk simulations were performed to gain a deeper understanding of the experimental findings.

As the molecular motion involved in the β -process displays a highly restricted angular displacement, its effects on the line shape of the solid echo are subtle. The spectral changes due to molecular motion are quantified by the relative spectral intensity at zero ^2H NMR frequency $R(t_p, T)$ (t_p is the interpulse delay). Random walk simulations employing several simple models for the β -process were performed in order to estimate the evolution of $R(t_p, T)$. They proved that ^2H NMR can provide a time constant $\langle \ln(\tau_\beta) \rangle$ at a certain temperature. In addition, it was demonstrated that the $R(t_p, T)$ traces contain information about the angular amplitude and the distribution of correlation times $G[\ln(\tau_\beta)]$. The available data of ethanol- d_1 and ethanol- d_2 were successfully analyzed in the view of the simulation results, and the time constant of ethanol- d_1 agrees well with dielectric spectroscopy (DS) data.

We studied in detail m-fluoroaniline (m-FAN) by ^2H NMR as it is a glass former that displays a relatively peculiar β -process that is faster and shows a much smaller relative relaxation strength than most of the previously studied materials (e.g. toluene, polybutadiene). The geometry of molecular motion involved in the β -process in m-FAN was found to be similar with the one in toluene with the difference that in the case of m-FAN a smaller angular amplitude suffices to explain the experimental findings. However, a large discrepancy between the NMR and DS time scale of the β -process was found. The results support the claim of several authors that m-FAN forms hydrogen-bond-induced-clusters.

In the quest of further understanding the secondary relaxation processes, toluene and o-terphenyl (OTP) confined in a nanoporous SBA-15 matrix were investigated. The temperature dependence of spin-lattice relaxation time allows us to differentiate type A (without a secondary dielectric β -peak) from type B glass formers (with a β -peak). We find that the α -process in both OTP (type A) and toluene (type B) in

confinement is governed by a broad heterogeneous distribution of correlation times, not seen in the bulk. Additionally there is evidence that the β -process in toluene changes under confinement conditions, where it exhibits a distribution of spin-lattice relaxation times that is substantially broadened towards faster times. In contrast, the corresponding low temperature relaxation time for OTP is not altered in confinement ($T < T_g$).

Polybutadiene (PBD) is a widely investigated polymer without side groups. At low temperatures ($T < T_g$) we identified a further secondary process in addition to the β -process that was designated as the γ -process. In addition, a mixture of roughly 10% deuterated benzene in PBD was also measured by ^2H NMR. The results proved that the benzene molecules display features very similar to those of neat PBD, thus being sensitive to both β and γ -process of its host. In the end we established several constraints for any model to explain the γ -process ruling out a large angle reorientation of the $C-^2\text{H}$ bonds at low temperatures ($T < T_g$).

The supercooled plastically crystalline phase of cyanoadamantane was investigated in order to study the α -process ($T > T_g$). Although the orientationally disordered crystalline phase always coexisted with the orientationally ordered crystalline phase, we were able to single out the signal from the former by selective excitation and it was possible to carry out line shape measurements and 2D experiments. The latter directly reveal 6-fold reorientation of the molecular C_3 axis via 90° angles, thus reflecting the symmetry of the lattice. We can reproduce the line shape by random walk simulations properly taking into account the molecular motion. Both line shape and 2D experiments yield time constants which agree with those reported by other techniques. We did not find any indication of a small angle motion as usually found for the α -process in structural glasses. Thus, the motional process in the glassy crystal appears to be simple and quite different from that in the structural glasses.

Appendix.

A. Matrix representation of important spin operators

For $I = 1/2$ spin the essential spin matrices in a basis of \hat{I}_z eigenstates $|\frac{1}{2}\rangle, |-\frac{1}{2}\rangle$ are the so called Pauli spin matrices [112]:

$$\mathbf{I}_z = \frac{1}{2} \begin{bmatrix} 1 & 0 \\ 0 & -1 \end{bmatrix} \quad \mathbf{I}_x = \frac{1}{2} \begin{bmatrix} 0 & 1 \\ 1 & 0 \end{bmatrix} \quad \mathbf{I}_y = \frac{1}{2} \begin{bmatrix} 0 & -i \\ i & 0 \end{bmatrix} \quad (\text{A.1})$$

$$\mathbf{I}_x^2 = \mathbf{I}_y^2 = \mathbf{I}_z^2 = \frac{1}{4} \begin{bmatrix} 1 & 0 \\ 0 & 1 \end{bmatrix} = \frac{1}{4} \mathbf{1} \quad (\text{A.2})$$

For $I = 1$ the representation of spin operators in a basis of \hat{I}_z eigenstates $|1\rangle, |0\rangle$ and $|-1\rangle$ are:

$$\mathbf{I}_z = \begin{bmatrix} 1 & 0 & 0 \\ 0 & 0 & 0 \\ 0 & 0 & -1 \end{bmatrix} \quad \mathbf{I}_x = \sqrt{\frac{1}{2}} \begin{bmatrix} 0 & 1 & 0 \\ 1 & 0 & 1 \\ 0 & 1 & 0 \end{bmatrix} \quad \mathbf{I}_y = \sqrt{\frac{1}{2}} \begin{bmatrix} 0 & -i & 0 \\ i & 0 & -i \\ 0 & i & 0 \end{bmatrix} \quad (\text{A.3})$$

For a general spin I , the elements $(\mathbf{I}_\alpha)_{m',m} = \langle m' | \hat{I}_\alpha | m \rangle$ of the $(2I+1) \times (2I+1)$ matrices in the basis of \hat{I}_z eigenstates $|m\rangle$ can be derived from:

$$(\mathbf{I}_z)_{m',m} = \langle m' | \hat{I}_z | m \rangle = \langle m' | m | m \rangle = m \delta_{m',m} \quad (\text{A.4})$$

$$(\mathbf{I}_x)_{m',m} = (\pm i \mathbf{I}_y)_{m',m} = \frac{1}{2} \sqrt{I(I+1) - m(m \pm 1)} \delta_{m',m \pm 1}$$

The quadrupolar Hamiltonian matrix reads:

$$\mathbf{H}_Q = \frac{\omega_Q}{3} \begin{bmatrix} 1 & 0 & 0 \\ 0 & -2 & 0 \\ 0 & 0 & 1 \end{bmatrix} \quad (\text{A.5})$$

and the matrix \mathbf{r}_1 that is included in the time evolution of the spin density matrix for a spin $I = 1$ has the following form:

$$\mathbf{r}_1 = [\mathbf{H}_Q, \mathbf{I}_x] = \omega_Q \sqrt{\frac{1}{2}} \begin{bmatrix} 0 & 1 & 0 \\ -1 & 0 & -1 \\ 0 & 1 & 0 \end{bmatrix} \quad (\text{A.6})$$

B. Features of $\min(T_1)$ for a Cole-Davidson spectral density

The spin-lattice relaxation rate $1/T_1$ can be related to the spectral density of molecular reorientation $J(\omega_L)$ by [59]:

$$\frac{1}{T_1} = \frac{3}{8} \left(\frac{eQeq}{\hbar} \right)^2 [J(\omega_L) + 4J(2\omega_L)]. \quad (\text{B.1})$$

Assuming a Cole-Davidson distribution of correlation times τ_{CD} , the spectral density becomes [59]:

$$J(\omega_L) = \frac{1}{5} \frac{\sin[\beta_{CD} \arctan(\omega_L \tau_{CD})]}{\omega_L [1 + (\omega_L \tau_{CD})^2]^{\beta_{CD}/2}}. \quad (\text{B.2})$$

The mean correlation time τ_c is given by:

$$\tau_c = \beta_{CD} \tau_{CD}. \quad (\text{B.3})$$

When β_{CD} is set to a constant value than one can numerically find τ_{CDmax} where Eq. B.1 has a maximum (T_1 function will have a minimum). Consequently, a corresponding T_1 value can be calculated. If various values of β_{CD} are used, we obtain numerically the function $\beta_{CD}[\min(T_1)]$ that is displayed in Fig. B.1. The presented line can be used to estimate $\beta_{CD}[\min(T_1)]$ when the minimum value of T_1 is measured. We mention that the following equation holds, when δ is expressed in units of kHz :

$$\left(\frac{eQeq}{\hbar} \right) \frac{1}{2\pi} = \frac{4}{3} \delta. \quad (\text{B.4})$$

One can see that small variations in δ , related to different samples, do not influence much the shape of $\beta_{CD}[\min(T_1)]$ function (cf. Fig. B.1). In the inset of the same figure we plotted the corresponding correlation time τ_c and it is seen that it does not change much; one can safely to use $\tau_c \simeq 1.8 ns$ when comparing with correlation times from other techniques plotted on a logarithmic scale.

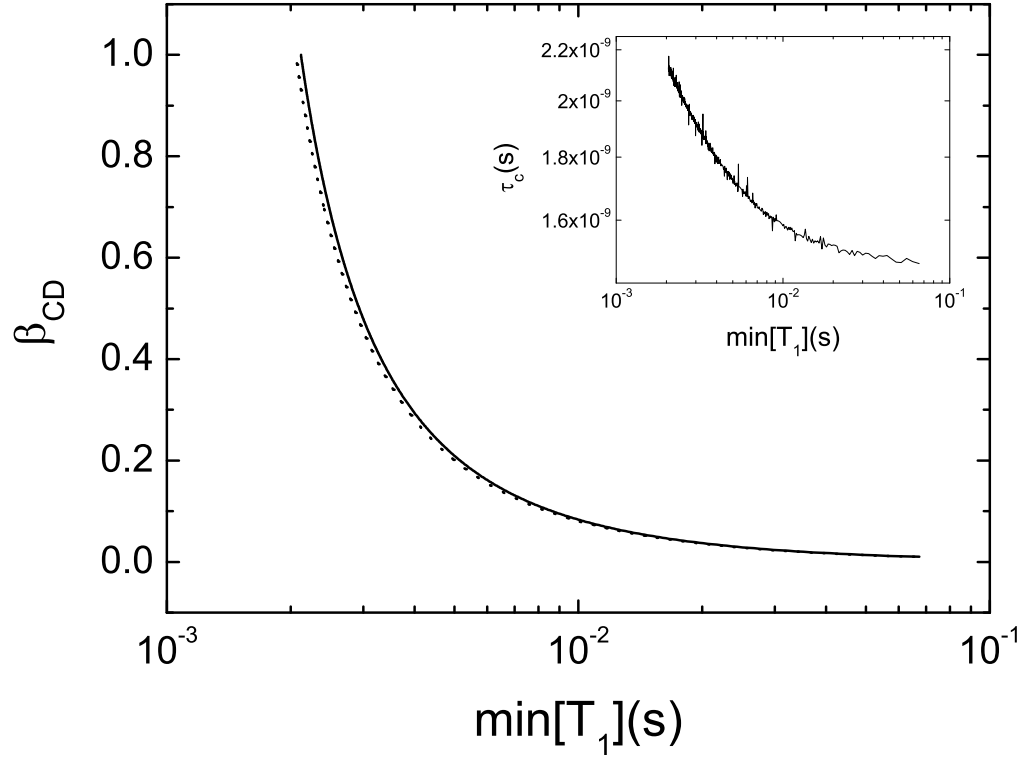


Figure B.1. Numerical estimation of β_{CD} vs. the value of the minimum T_1 . $\omega_L = 2\pi \times 46.07 \text{ MHz}$ and $\delta = 137 \text{ kHz}$ were used for the solid line; inset: the corresponding correlation time. Dotted line in the main figure: $\delta = 135 \text{ kHz}$.

C. Simulation details

For those interested in random walk simulations related to ^2H NMR and various applications, the following names might be useful: Hinze [57], Böhmer et al. [29], Vogel and Rössler [129, 133, 134, 135]. A comparison between different correlation times in the case of an isotropic motion might be found in Anderson [10]. For random number generators and hints about various random distributions see the book Numerical Recipes in C [99]. Several authors (Ponti [98], Bak et al. [14], Alderman et al. [5] and Cheng et al. [35]) discuss different numeric methods of generating powder distributions.

C.1. Solid echo spectra

To simulate the 1D spectra we created the trajectories of many molecules ($10^6 - 10^7$) over the experimental time, calculated the time signal generated by a solid echo pulse sequence for each trajectory and added it up. The final signal was Fourier transformed. For the trajectory of one molecule we used the random walk method and, as previously pointed out [57, 133], there are three steps to be accounted for:

1. The initial orientation of the C_3 axis is chosen randomly, ensuring an isotropic distribution of starting orientations, i.e. a powder sample.
2. Assuming Poisson distributed jump events, the waiting time t_w is randomly chosen from an exponential distribution of correlation times described by the jump correlation time τ_j [128]:

$$P(t_w) = \frac{1}{\tau_j} e^{-\frac{t_w}{\tau_j}}. \quad (\text{C.1})$$

3. After the waiting time, the axis instantaneously jumps into a new orientation; the new orientation is calculated taking into account the geometrical model of the motion.

When using a distribution of jump correlation times the same method as above was applied with the only exception that, at the beginning of the calculations for one molecule, a jump correlation time $\tau_j = \tau_j^i$ was chosen from the distribution. Different τ_j^i values were used, the number of trajectories calculated with a specific τ_j^i was proportional to $G[\ln(\tau_j^i)]$.

Cyanoadamantane case

For the jump model only six positions of the C_3 axis are possible. If we look at Eq. 2.9 (assuming $\eta = 0$) we can see that, by measuring one frequency ω for a molecule, we cannot distinguish between the position of a $C-^2\text{H}$ bond described by an angle θ and the one with an angle $(180^\circ - \theta)$ with respect to the external magnetic field.

Because of this our model can be simplified including only three sites on the positive axes of a Cartesian coordinate system and disregarding those on the negative axes. Therefore any molecule gives rise to a signal at only three frequencies ω_{s1} , ω_{s2} , ω_{s3} .

To account for the broadening of the line due to additional spin-couplings (dipole-dipole interaction) we multiplied the simulated time domain signal with a Gaussian damping ($\exp[-(\pi GBt)^2]$, with $GB = 1 \text{ kHz}$).

1D spectra for models used to simulate the β -process

In this case, after a jump the $C-^2H$ bond has a new orientation corresponding to the chosen geometrical model.

In addition to the Gaussian damping ($GB = 2.5 \text{ kHz}$), the spectra were corrected to account for distortions due to finite pulse lengths [26, 113]. That is, in the case of a solid echo pulse sequence with equal pulse lengths Δ_p , the simulated spectrum is multiplied with:

$$A(\omega) = \left[\omega_p \Delta_p \frac{\sin\left(\Delta_p \sqrt{\omega_p^2 + \frac{1}{2}\omega^2}\right)}{\Delta_p \sqrt{\omega_p^2 + \frac{1}{4}\omega^2}} \right]^3, \quad (\text{C.2})$$

where $\omega_p = \gamma B_1 = \pi/(2\Delta_p)$ and we used $\Delta_p = 2.5 \mu\text{s}$.

C.2. The 2D spectrum and F_∞^{sin} for cyanoadamantane

The 2D spectrum in the idealized case of no motion during evolution and detection time can be calculated analytically in such a simple geometrical model as described before [119]. We chose a different way: in a similar manner as in 1D simulation we followed the orientation of a large number of molecules prior to and after the mixing time. At the beginning of the experiment the C_3 axis has one orientation (and a corresponding ω_{start}), after the mixing time, assuming that 90° jumps have taken place, the molecule has a different orientation (and the frequency ω_{end}). A histogram of all the pairs $(\omega_{start}, \omega_{end})$ with $\omega_{start} \neq \omega_{end}$ is the off-diagonal spectrum S_{off} while a histogram of $(\omega_{start}, \omega_{start})$ is the diagonal spectrum S_d . The final spectrum is a weighted sum of these two. The diagonal part is present because for some of the molecules the orientation at the beginning of the experiment is the same as the one at ending of the experiment (and thus, $\omega_{start} = \omega_{end}$). We assumed that one third of the molecules are fulfilling the previous condition and this causes the weighting factors for the diagonal and off-diagonal spectra to be: $\left(\int S_{off} d\omega_{start} d\omega_{end}\right) / \left(\int S_d d\omega_{start} d\omega_{start}\right) = 2/1$. The final spectrum was convoluted with a Gaussian to account for experimental line-broadening.

Within the same geometrical model we calculated the dependence $F_\infty^{\text{sin}}(t_1)$, once again adding over a large number of molecules. A large group of molecules which

are in one site at the beginning of the experiment will be equally distributed between the three available sites at the end of the experiment. If we assume that the starting site has the frequency ω_{s1} , then the signal in F_{∞}^{sin} generated by such a group will be proportional to:

$$F_{\infty}^{\text{sin}}(t_1) \propto \sin(\omega_{s1}t_1) \sin(\omega_{s1}t_1) + \sin(\omega_{s1}t_1) \sin(\omega_{s2}t_1) + \sin(\omega_{s1}t_1) \sin(\omega_{s3}t_1), \quad (\text{C.3})$$

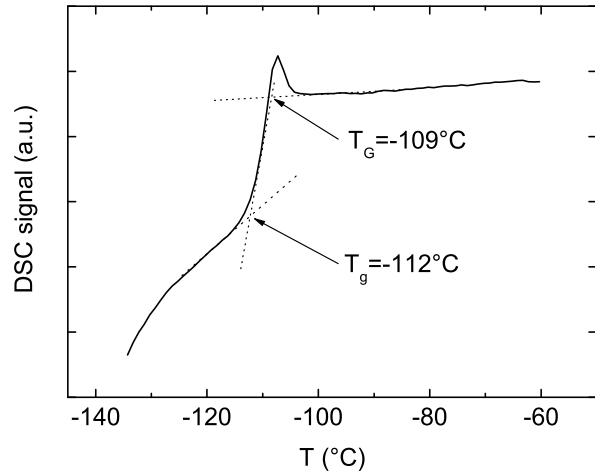
where t_1 is the evolution time chosen for measuring a certain value of F_{∞}^{sin} . Now if we choose a large number of groups so that they will have different starting sites, according to a isotropic distribution, it will be enough to add up the product in Eq. C.3 to get $F_{\infty}^{\text{sin}}(t_1)$.

D. Additional data: polybutadiene

DSC results

Figure D.1 shows the differential scanning calorimetry (DSC) result for the mixture of 9.4% weight percent benzene-d₆ in 1,4 polybutadiene with $M_w = 777 \text{ g/mol}$. In the case of mixtures the step in the DSC signal is extending on a wide temperature range and the glass transition temperature T_g is not well defined. In contrast the high temperature ‘end’ of the DSC step allows an unambiguous definition of a temperature T_G (as indicated in Fig. D.1). Hence, for mixtures it is custom to use the glass transition temperature T_G instead of T_g [21]. Actually, in the case of the mixture studied in this work, the difference between T_G and T_g is negligible, the only reason we used the former one is consistence with previous work [20].

Figure D.1. DSC trace for the sample benzene-d₆-PB777.



¹³C measurements

Looking for a possible explanation of the different manifestation of the γ -process we determined the chemical structure of the chosen PB polymers, in terms of the *cis*, *trans* and *vinyl* content. ¹³C spectra were measured and analyzed as proposed by Sato et al. [108]. A typical spectrum is presented in Fig. D.2 where the peaks are identified according to their chemical shift presented in Table III in Sato et al. [108]. Using the Equations 1 to 8 in the before mentioned reference and the integral of the numbered peaks, one can estimate the content of *cis*, *trans* and *vinyl* units. The results for our samples are displayed in Fig. 5.2. Clearly, a systematic change occurs with molecular

weight. However, interpreting ^{13}C spectra under ^1H decoupling condition some care has to be taken. Due to cross relaxation effects some of the NMR intensities may be distorted. However, since quite similar PB spectra were recorded it means that these effects are very similar for all spectra and do not change the conclusion concerning the molecular dependence.

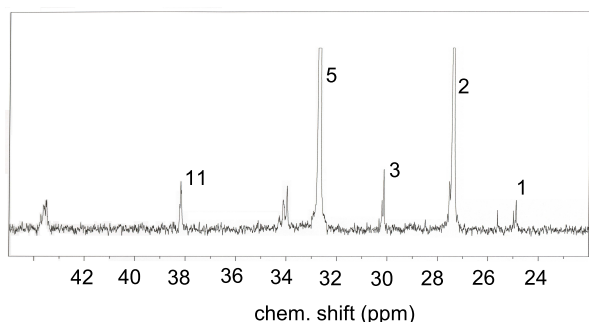


Figure D.2. ^{13}C spectrum for PBD-11500. The peaks are identified according to Sato et al. [108].

Additional dielectric spectroscopy data

In order to illustrate the presence of two groups of PB, data for a member of each group are presented in Fig. D.3. Clearly, the γ -process manifests at different temperatures. Moreover it is obvious that the γ -process is much broader than a Debye process.

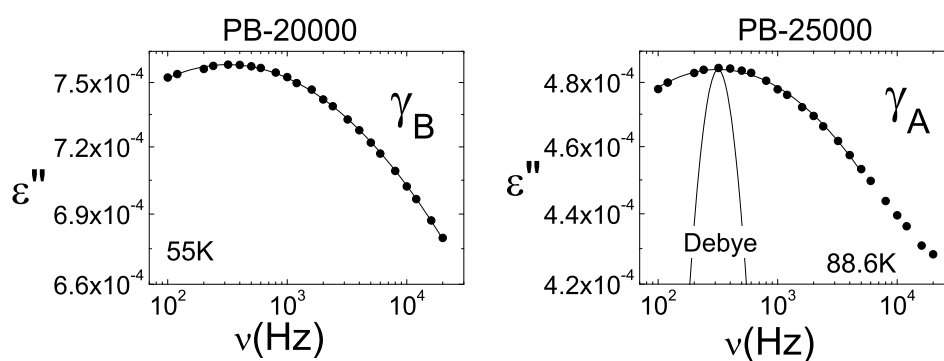


Figure D.3. Dielectric spectra (on linear scale) for two polybutadiene samples (PB-20000 and PB-25000). The maximum of the γ peak passes through the frequency window at different temperatures. Line is log Gauss fit. A Debye curve is displayed for comparison.

E. Additional data: ortho-terphenyl

Measurements details

We measured solid echo spectra for a sample of ortho-terphenyl-d₁₄ (OTP-d₁₄), 98.2% atom D, produced by CDN isotopes (product no. D-4165). For the NMR experiments a Bruker DSX 400 spectrometer (operating at a ²H Larmor frequency of 61.4 MHz) was used. The sample was inserted in a commercial probe (Bruker) and a heating device Bruker VT 2000; the temperature stability was better than 1 K. The 1D spectra were obtained with a solid-echo sequence preceded by a saturation sequence (five $\pi/2$ pulses) with the delay time between the end of the saturation sequence and the beginning of the solid-echo sequence chosen so that more than 95% of the equilibrium magnetization was probed. The pulse length of a $\pi/2$ pulse was around 2.8 μ s and the interpulse delay $t_p = 20 \mu$ s.

Results

The solid echo spectra of OTP-d₁₄ display at certain temperatures a central feature (see Figs. E.1, E.2). The weighting of this feature is enhanced in the partially relaxed spectrum, when only a part of the equilibrium magnetization is probed (cf. Fig. E.3). We interpret this feature as an indication that a certain fraction of the molecules display a phenyl flip phenomenon and the measured spectrum is a weighted sum of a powder spectrum and one of the spectra in Fig. E.5 (or one at an intermediate jump correlation time).

For the record, we show in Fig. E.4 the apparent spectral width of the solid echo spectra.

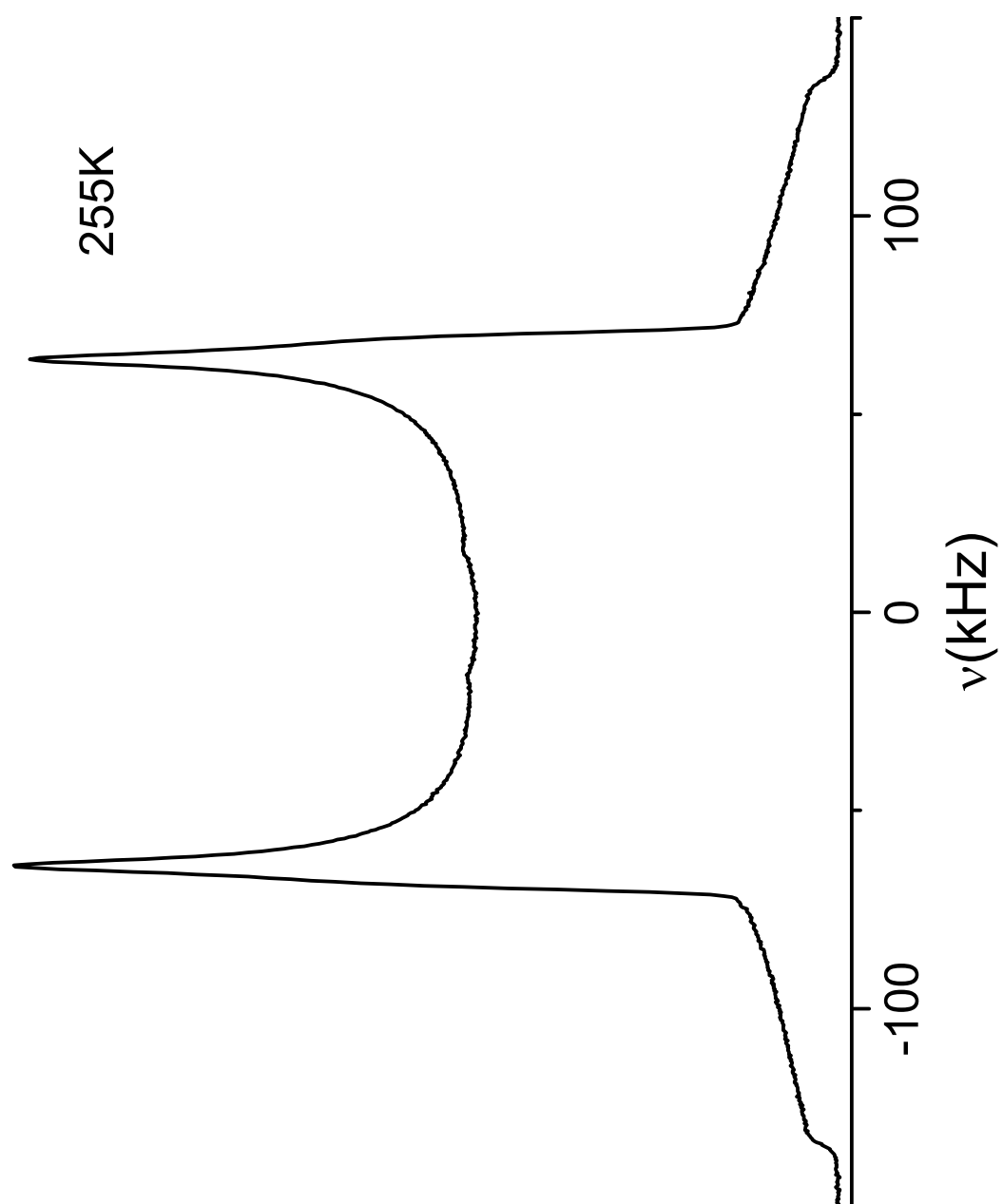


Figure E.1. Solid echo spectrum of OTP-d₁₄.

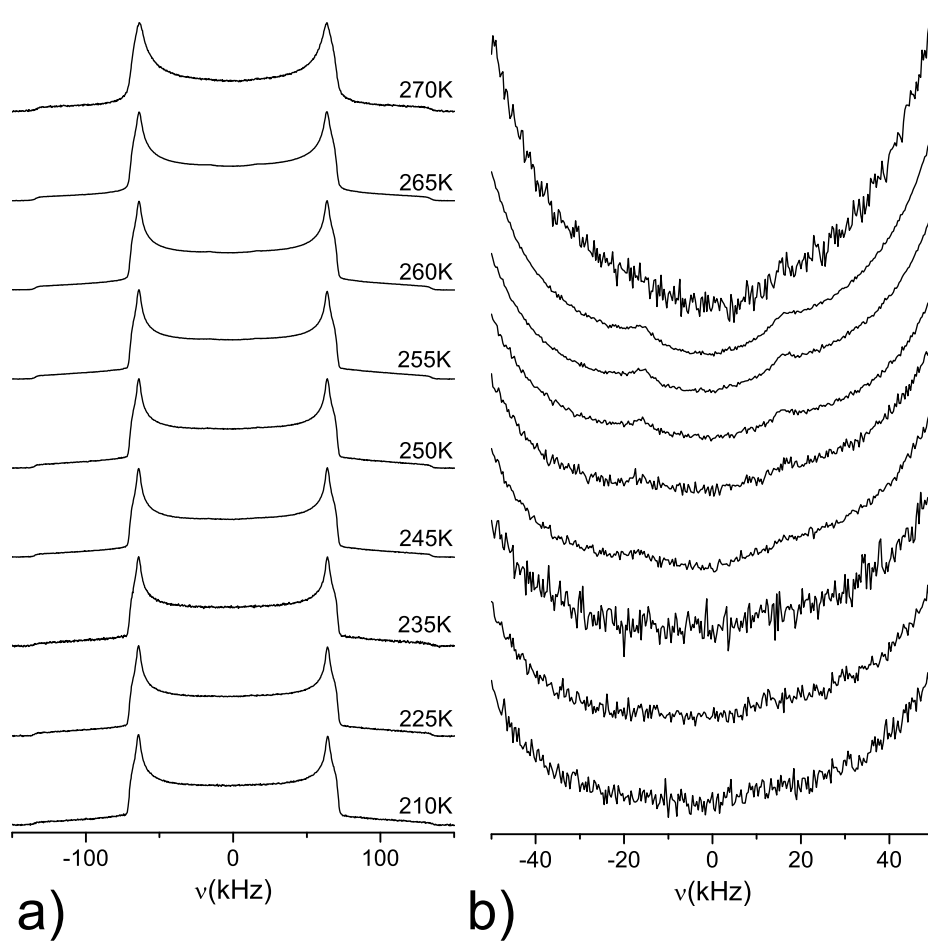


Figure E.2. a) Solid echo spectra of OTP-d₁₄ at various temperatures; b) the central part of the same spectra.

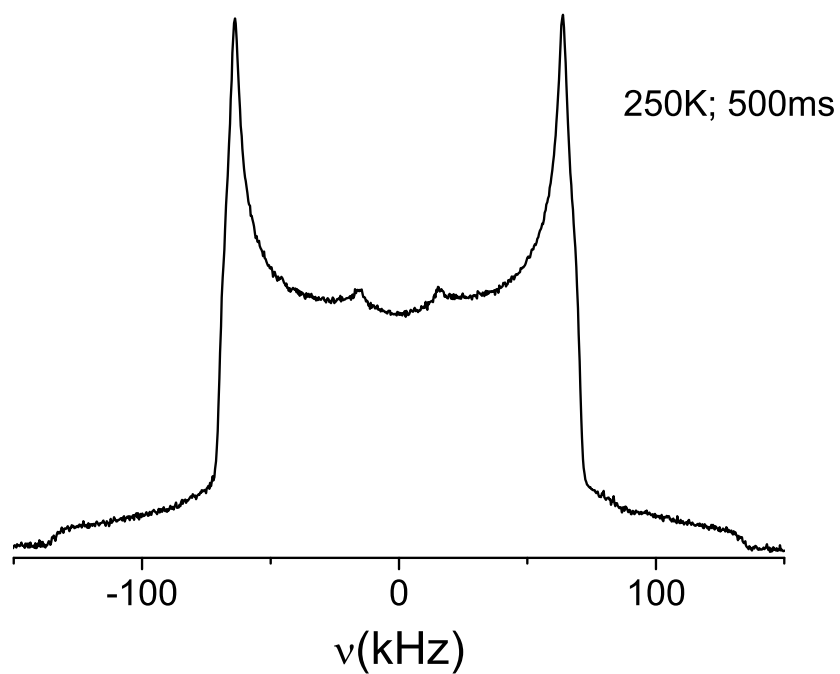


Figure E.3. Solid echo spectrum of OTP-d₁₄ measured with fast triggering (delay after the saturation sequence 500 ms; the equilibrium magnetization was not reached).

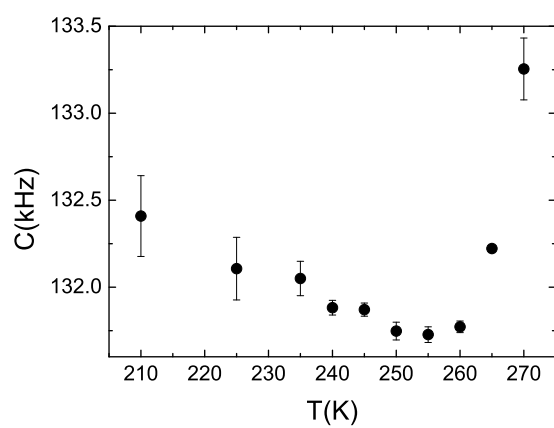


Figure E.4. The apparent spectral width for the spectra in Fig. E.2 (a).

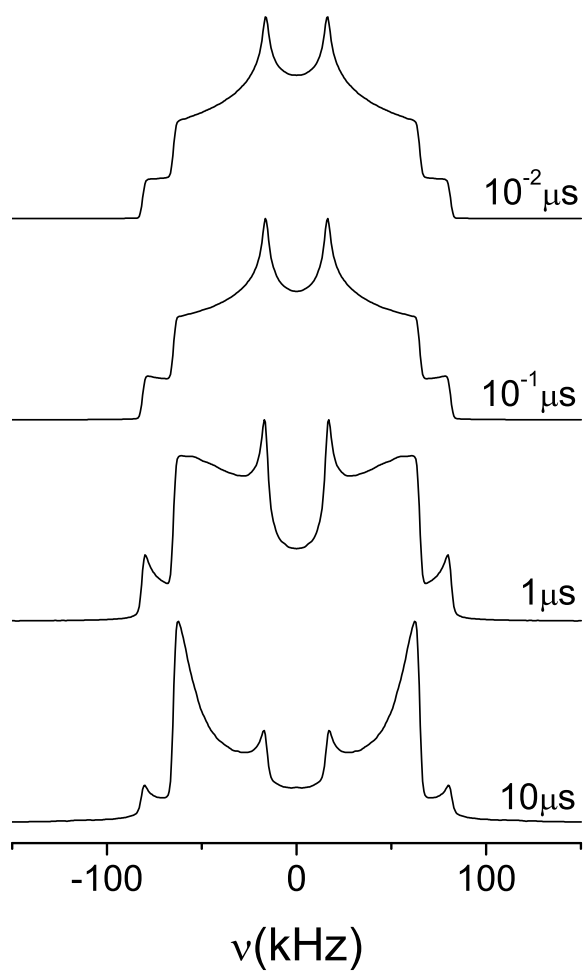


Figure E.5. Simulated solid echo spectra for a phenyl flip motion. The jump correlation time is indicated close to each spectrum.

F. Tables with the phase cycles for the used pulse sequences

This section presents the tables with the phase cycling employed for the pulse sequences used in this work (copied from Medick [85], a reference paper is the one by Schaefer et al. [109]).

	Solid echo		
#	P_1 90	P_2 90	Det.
1	+y	+x	+x
2	+y	-x	+x
3	-x	+y	+y
4	-x	-y	+y
5	-y	-x	-x
6	-y	+x	-x
7	+x	-y	-y
8	+x	+y	-y

Table F.1. Phase cycle for the solid echo sequence.

	Zeeman					Spin alignment					
#	P_1	P_2	P_3	P_4	Det.	P_1	P_2	P_3	P_4	Det.	
	90	90	90	90		90	45	45	90		
1	+x	+x	+x	+y	+y	+x	+y	+y	+y	-y	(a)
2	+x	-x	+x	+y	-y	+x	-y	+y	+y	+y	
3	-x	+x	+x	+y	-y	-x	+y	+y	+y	+y	
4	-x	-x	+x	+y	+y	-x	-y	+y	+y	-y	
5	+y	+y	+x	+y	+y	+y	-x	+y	+y	-y	
6	+y	-y	+x	+y	-y	+y	+x	+y	+y	+y	
7	-y	+y	+x	+y	-y	-y	-x	+y	+y	+y	
8	-y	-y	+x	+y	+y	-y	+x	+y	+y	-y	
9	+x	+x	+x	-y	+y	+x	+y	+y	-y	-y	
10	+x	-x	+x	-y	-y	+x	-y	+y	-y	+y	
11	-x	+x	+x	-y	-y	-x	+y	+y	-y	+y	
12	-x	-x	+x	-y	+y	-x	-y	+y	-y	-y	
13	+y	+y	+x	-y	+y	+y	-x	+y	-y	-y	
14	+y	-y	+x	-y	-y	+y	+x	+y	-y	+y	
15	-y	+y	+x	-y	-y	-y	-x	+y	-y	+y	
16	-y	-y	+x	-y	+y	-y	+x	+y	-y	-y	
17	y	y	y	-x	-x	y	-x	-x	-x	x	(b)
\vdots	\vdots	\vdots	\vdots	\vdots	\vdots	\vdots	\vdots	\vdots	\vdots	\vdots	

Table F.2. Phase cycle for a four pulse stimulated echo experiment. a) Minimum phase cycle; (b) all phases simultaneously shifted with $\pm 90^\circ$ and 180° . The full phase cycle contains 64 steps.

#	Zeeman						Alignment						
	P_1 90	P_2 90	P_3 54.7	P_4 54.7	P_5 90	Det.	P_1 90	P_2 90	P_3 54.7	P_4 54.7	P_5 90	Det.	
1	+x	+y	+x	+x	+y	+y	+x	+y	+y	+y	+y	-y	(a)
2	+x	+y	-x	+x	+y	-y	+x	+y	-y	+y	+y	+y	
3	-x	-y	+x	+x	+y	-y	-x	-y	+y	+y	+y	+y	
4	-x	-y	-x	+x	+y	+y	-x	-y	-y	+y	+y	-y	
5	+y	-x	+y	+x	+y	+y	+y	-x	-x	+y	+y	-y	
6	+y	-x	-y	+x	+y	-y	+y	-x	+x	+y	+y	+y	
7	-y	+x	+y	+x	+y	-y	-y	+x	-x	+y	+y	+y	
8	-y	+x	-y	+x	+y	+y	-y	+x	+x	+y	+y	-y	
9	+x	+y	+x	+x	-y	+y	+x	+y	+y	+y	-y	-y	
10	+x	+y	-x	+x	-y	-y	+x	+y	-y	+y	-y	+y	
11	-x	-y	+x	+x	-y	-y	-x	-y	+y	+y	-y	+y	
12	-x	-y	-x	+x	-y	+y	-x	-y	-y	+y	-y	-y	
13	+y	-x	+y	+x	-y	+y	+y	-x	-x	+y	-y	-y	
14	+y	-x	-y	+x	-y	-y	+y	-x	+x	+y	-y	+y	
15	-y	+x	+y	+x	-y	-y	-y	+x	-x	+y	-y	+y	
16	-y	+x	-y	+x	-y	+y	-y	+x	+x	+y	-y	-y	
17	+x	-y	+x	+x	+y	+y	+x	-y	+y	+y	+y	-y	
18	+x	-y	-x	+x	+y	-y	+x	-y	-y	+y	+y	+y	
19	-x	+y	+x	+x	+y	-y	-x	+y	+y	+y	+y	+y	
20	-x	+y	-x	+x	+y	+y	-x	+y	-y	+y	+y	-y	
21	+y	+x	+y	+x	+y	+y	+y	+x	-x	+y	+y	-y	
⋮	⋮	⋮	⋮	⋮	⋮	⋮	⋮	⋮	⋮	⋮	⋮	⋮	
32	-y	-x	-y	+x	-y	+y	-y	-x	+x	+y	-y	-y	
33	y	-x	y	y	-x	-x	y	-x	-x	-x	-x	x	(b)
⋮	⋮	⋮	⋮	⋮	⋮	⋮	⋮	⋮	⋮	⋮	⋮	⋮	

Table F.3. Phase cycle for acquiring a 2D spectrum. a) Minimum phase cycle; (b) all phases simultaneously shifted with $\pm 90^\circ$ and 180° . The full phase cycle contains 128 steps.

List of Publications

- S. A. Lusceac, I. Roggatz, P. Medick, J. Gmeiner and E. A. Rössler, *^2H nuclear magnetic resonance study of the molecular motion in cyanoadamantane. I. Supercooled plastically crystalline phase*, J. Chem. Phys., 121, 4770-4780, 2004.
- S. A. Lusceac, C. Koplin, P. Medick, M. Vogel, N. Brodie-Linder, C. LeQuelléc, C. Alba-Simionesco and E. A. Rössler, *Type A versus Type B glass formers: NMR relaxation in bulk and confining geometry*, J. Phys. Chem., 108, 16601-16605, 2004.
- S. A. Lusceac, C. Gainaru, M. Vogel, C. Koplin, P. Medick and E. A. Rössler, *Secondary relaxation processes in polybutadiene studied by ^2H nuclear magnetic resonance and high-precision dielectric spectroscopy*, Macromolecules, 38, 5625-5633, 2005.

Acknowledgments

Here I would like to thank to all who contributed to the making of this PhD thesis.

In the first place I thank to Mr. E. A. Rößler for giving me the opportunity to work in Bayreuth and for his way of supervising my work. I appreciated very much the freedom of thinking and action that he gracefully supports. The long discussions that we had concerning my experimental results were very useful and they are highly prized.

The help of Mr. P. Medick is greatly appreciated; both measurement and simulation-related problems were successfully surpassed using his advice. I thank to Mr. J. Gmeiner for his assistance in the preparation and characterization of several of my samples and also to Mr. J. Senker who helped me with the ^{13}C NMR measurements of the polybutadiene samples. Ms. C. LeQuellec, with her work and ideas, made possible the successful project of investigating glass formers in confinement and I am deeply indebted to her, many thanks!

My best regards to the ‘dielectric guys’ with whom I had fruitfully discussions: A. Rivera, V. Porokhonsky, S. Adichtchev (though the last one was actually a ‘light scattering guy’). Alberto, thank you for reading the manuscript of my thesis! Special thanks to Mr. C. Tschirwitz who, with his great social skills, made easy my first days in Bayreuth and the adaptation to the german life style. Also special considerations to my countryman (and ‘dielectric guy’) Mr. C. Gainaru with whom I spend many hours of endless discussions (some of which finally concluded to a scientific paper).

Many thanks to Mr. B. Micko who helped me with the german translation of the summary.

I want to thank to Reta for her kind support and gentle understanding, it kept me going.

Ms. N. Lupu read and corrected the english of one of my many versions of this thesis, thank you!

I also thank to my parents for all that they have done for me: ‘dragii mei, vă mulțumesc pentru tot ce ați facut pentru mine, fără voi nu aş fi ajuns aici!’

Bibliography

- [1] A. Abragam. *The Principles of Nuclear Magnetism*. Oxford University Press, 1961.
- [2] S. Adichtchev, T. Blochowicz, C. Gainaru, V. N. Novikov, E. A. Rössler, and C. Tschirwitz. *J. of Phys.: Condensed Matter*, 15:S835, 2003.
- [3] C. Alba-Simionesco, G. Dosseh, E. Dumont, B. Frick, B. Geil, D. Morineau, V. Teboul, and Y. Xia. *Eur. Phys. J. E.*, 12:19, 2003.
- [4] C. Alba-Simionesco, J. Fan, and C. A. Angell. *J. Chem. Phys.*, 110:5262, 1999.
- [5] D. W. Alderman, M. S. Solum, and D. M. Grant. *J. Chem. Phys.*, 84:371, 1986.
- [6] Y. Alm  ras, J.-L. Barrat, and L. Bocquet. *J. Phys. IV (France)*, 10:Pr7–27, 2000.
- [7] J. P. Amoureux, M. Castelain, M. Bee, B. Arnaud, and M. L. Shouteenten. *Mol. Phys.*, 42:119, 1981.
- [8] J. P. Amoureux, R. Decresian, M. Sahour, and E. Cochon. *J. Phys. II (France)*, 2:249, 1992.
- [9] J. P. Amoureux, G. Noyel, M. Foulon, M. Bee, and L. Jorat. *Mol. Phys.*, 52:161, 1984.
- [10] J. E. Anderson. *Faraday Symp. Chem. Soc.*, 3:82, 1972.
- [11] C. A. Angell, K. L. Ngai, G. B. McKenna, P. F. McMillan, and S. W. Martin. *J. Appl. Phys.*, 88:3113, 2000.
- [12] A. Aouadi, M. J. Lebon, C. Dreyfus, B. Strube, W. Steffen, A. Patkowski, and R. M. Pick. *J. Phys.: Condens. Matter*, 9:3803, 1997.
- [13] A. Arbe, D. Richter, J. Colmenero, and B. Farago. *Phys. Rev. E*, 54:3853, 1996.
- [14] M. Bak and N. C. Nielsen. *J. Magn. Reson.*, 125:132, 1997.

- [15] L. S. Batchelder, C. H. Niu, and D. A. Torchia. *J. Am. Chem. Soc.*, 105:2228, 1983.
- [16] M. Bee. *Quasielastic Neutron Scattering*. Adam Hilger-Bristol, 1988.
- [17] M. Beiner, S. Kahle, E. Hempel, K. Schröter, and E. Donth. *Macromolecules*, 31:8973, 1998.
- [18] S. Benkhof. *Dielektrische Relaxation zur Untersuchung der molekularen Dynamik in unterkühlten Flüssigkeiten und plastischen Kristallen*. PhD thesis, Universität Bayreuth, 1999.
- [19] R. Bergman, J. Mattsson, C. Svanberg, G. A. Schwartz, and J. Swenson. *Europhys. Lett.*, 64:675, 2003.
- [20] T. Blochowicz. *Broadband Dielectric Spectroscopy in Neat and Binary Molecular Glass Formers*. PhD thesis, Universität Bayreuth, 2003.
- [21] T. Blochowicz. *Broadband Dielectric Spectroscopy in Neat and Binary Molecular Glass Formers*. PhD thesis, Universität Bayreuth, 2003. pp. 90-91.
- [22] T. Blochowicz, A. Kudlik, S. Benkhof, J. Senker, and E. Rössler. *J. Chem. Phys.*, 88:2139, 1999.
- [23] T. Blochowicz, A. Kudlik, S. Benkhof, J. Senker, E. Rössler, and G. Hinze. *J. Chem. Phys.*, 110:12011, 1999.
- [24] T. Blochowicz and E. A. Rössler. *Phys. Rev. Lett.*, 92:225701, 2004.
- [25] T. Blochowicz, C. Tschirwitz, S. Benkhof, and E. A. Rössler. *J. Chem. Phys.*, 118:7544, 2003.
- [26] M. Bloom, J. H. Davis, and M. I. Valic. *Can. J. Phys.*, 58:1510, 1980.
- [27] R. Böhmer and C. A. Angell. *Phys. Rev. B*, 45:10091, 1992.
- [28] R. Böhmer, G. Diezemann, G. Hinze, and E. Rössler. *Prog. NMR Spectrosc.*, 39:191, 2001.
- [29] R. Böhmer and G. Hinze. *J. Chem. Phys.*, 109:241, 1998.
- [30] R. Böhmer, G. Hinze, T. Jörg, F. Qi, and H. Sillescu. *J. Phys.: Condens. Matter*, 12:A383, 2000.
- [31] E. Bonjour, R. Calemczuk, R. Lagnier, and B. Salce. *J. Phys. (France)*, C6:63, 1981.

- [32] C. I. F. Böttcher and P. Borderwijk. *Theory of Electric Polarization*. Elsevier - Amsterdam, 1978.
- [33] R. Brand, P. Lunkenheimer, and A. Loidl. *J. Chem. Phys.*, 116:10386, 2002.
- [34] R. Casalini, K. L. Ngai, C. G. Robertson, and C. M. Roland. *J. Polym. Sci. B: Polym. Phys.*, 38:1841, 2000.
- [35] V. B. Cheng, H. H. Suzukawa Jr., and M. Wolfsberg. *J. Chem. Phys.*, 59:3992, 1973.
- [36] M. Cutroni, A. Mandanici, and A. Piccolo. *J. Phys.: Condens. Matter*, 7:6781, 1995.
- [37] R. D. Deegan and S. R. Nagel. *Phys. Rev. B*, 52:5653, 1995.
- [38] G. Diezemann and H. Sillescu. *J. Chem. Phys.*, 103:6385, 1995.
- [39] Y. Ding, V. N. Novikov, and A. P. Sokolov. *J. Polym. Sci. B: Polym. Phys.*, 42:994, 2004.
- [40] P. K. Dixon, L. Wu, S. R. Nagel, B. D. Williams, and J. P. Carini. *Phys. Rev. Lett.*, 65:1108, 1990.
- [41] E. Donth. *The Glass Transition*. Springer - Verlag Berlin Heidelberg New York, 2001.
- [42] A. Döss, M. Paluch, H. Sillescu, and G. Hinze. *Phys. Rev. Lett.*, 88:095701, 2002.
- [43] G. Dosseh, G. Ehlers, Y. Xia, and C. Alba-Simionesco. 2005. To be submitted for publication.
- [44] T. Dries, F. Fujara, M. Kiebel, E. Rössler, and H. Sillescu. *J. Chem. Phys.*, 88:2139, 1988.
- [45] J. Dubochet, C. M. Alba, D. R. MacFarlane, Angell C. A., R. K. Kadiyala, M. Adrian, and J. Teixeira. *J. Phys. Chem.*, 88:6727, 1984.
- [46] M. D. Ediger, C. A. Angell, and S. R. Nagel. *J. Phys. Chem.*, 100:13200, 1996.
- [47] D. Fioretto, C. Masciovecchio, M. Mattarelli, G. Monaco, L. Palmieri, G. Ruocco, and F. Sette. *Philos. Mag. B*, 82:273, 2002.
- [48] M. Foulon, J. P. Amoureux, J. L. Sauvajol, J. P. Cavrot, and M. Muller. *J. Phys. C*, 17:4213, 1984.
- [49] F. Fujara, S. Wefing, and H. W. Spiess. *J. Chem. Phys.*, 84:4579, 1986.

- [50] C. Gainaru. *Dielectric spectroscopy on molecular glass formers*. PhD thesis, Universität Bayreuth, 2005. To be submitted.
- [51] E. Gedat, A. Schreiber, J. Albrecht, Th. Emmeler, I. Shenderovich, G. H. Findenegg, H.-H. Limbach, and G. Buntkowsky. *J. Phys. Chem. B*, 106:1977, 2002.
- [52] B. Geil, F. Fujara, and H. Sillescu. *J. Magn. Reson.*, 130:18, 1998.
- [53] B. Geil, O. Isofort, B. Boddenberg, D. E. Favre, B. F. Chmelka, and F. Fujara. *J. Chem. Phys.*, 116:5, 2002.
- [54] W. Götze and L. Sjögren. *Rep. Prog. Phys.*, 55:241, 1992.
- [55] C. Hansen and R. Richert. *R. Acta Polymer.*, 48:484, 1997.
- [56] S. Hensel-Bielowka, M. Paluch, and K. L. Ngai. *J. Chem. Phys.*, 123:014502, 2005.
- [57] G. Hinze. *Phys. Rev. E*, 57:2010, 1998.
- [58] G. Hinze, G. Diezemann, and H. Sillescu. *J. Chem. Phys.*, 104:430, 1996.
- [59] G. Hinze and H. Sillescu. *J. Chem. Phys.*, 104:314, 1996.
- [60] G. Hinze, H. Sillescu, and F. Fujara. *Chem. Phys. Lett.*, 232:154, 1995.
- [61] A. Hofmann, A. Alegria, J. Colmenero, L. Willner, E. Buscaglia, and N. Hadjichristidis. *Macromolecules*, 29:129, 1996.
- [62] E. N. Ivanov. *Sov. Phys. JETP*, 18:1041, 1964.
- [63] G. P. Johari. *J. Chem. Phys.*, 58:1766, 1973.
- [64] G. P. Johari. *N. Y. Acad. Sci.*, 279:117, 1976.
- [65] G. P. Johari. *J. Chim. Phys.*, 82:283, 1985.
- [66] G. P. Johari and M. Goldstein. *J. Chem. Phys.*, 53:2372, 1970.
- [67] T. Jörg, R. Böhmer, H. Sillescu, and H. Zimmermann. *Europhys. Lett.*, 49:748, 2000.
- [68] T. Kanaya, T. Kawaguchi, and K. Kaji. *Macromolecules*, 32:1672, 1999.
- [69] S. Kaufmann, S. Wefing, D. Schaefer, and H. W. Spiess. *J. Chem. Phys.*, 93:197, 1990.
- [70] O. Kircher, R. Böhmer, and C. Alba-Simionesco. *J. Mol. Struct.*, 479:195, 1999.

- [71] C. Koplin. *²H-NMR Untersuchungen zur Sekundärrelaxation binärer organischer Glasbildner*. Master's Thesis, Universität Bayreuth, 2001.
- [72] F. Kremer and A. Schönhals. *Broadband Dielectric Spectroscopy*. Springer, 2003.
- [73] A. Kudlick. *Ein Beitrag zur Linienform der dynamischen Suszeptibilität*. PhD thesis, Universität Bayreuth, 1997.
- [74] A. Kudlik, S. Benkhof, T. Blochowicz, C. Tschirwitz, and E. Rössler. *J. Mol. Struct.*, 479:201, 1999.
- [75] A. Kudlik, S. Benkhof, R. Lenk, and E. Rössler. *Europhys. Lett.*, 32:511, 1995.
- [76] A. Kudlik, S. Benkhof, R. Lenk, and E. Rössler. *Europhys. Lett.*, 36:475, 1996.
- [77] R. L. Leheny and S. R. Nagel. *Europhys. Lett.*, 39:447, 1997.
- [78] C. Leon and K. L. Ngai. *J. Phys. Chem. B*, 103:4045, 1999.
- [79] D. L. Leslie-Pelecky and N. O. Birge. *Phys. Rev. Lett.*, 72:1232, 1994.
- [80] M. H. Levitt. *Spin Dynamics*. John Wiley & Sons, England, 2001.
- [81] S. A. Lusceac, C. Gainaru, M. Vogel, C. Koplin, P. Medick, and E. A. Rössler. *Macromolecules*, 38:5625, 2005.
- [82] S. A. Lusceac, C. Koplin, P. Medick, M. Vogel, N. Brodie-Linder, C. LeQuelléc, C. Alba-Simionesco, and E. A. Rössler. *J. Phys. Chem. B*, 108:16601, 2004.
- [83] S. A. Lusceac, I. Roggatz, P. Medick, J. Gmeiner, and E. A. Rössler. *J. Chem. Phys.*, 121:4770, 2004.
- [84] N. G. McCrum, B. E. Read, and G. Williams. *Anaelastic and Dielectric Effects in Polymeric Solids*. Dover Publications - New York, 1991.
- [85] P. Medick. *Zweidimensionale NMR zur Untersuchung der Dynamik in einem binren Glasbildner*. Master's Thesis, Universität Bayreuth, 1998.
- [86] P. Medick, T. Blochowicz, M. Vogel, and E. Rössler. *J. Non-Cryst. Solids*, 307-310:565, 2002.
- [87] P. Medick, M. Vogel, and E. Rössler. *J. Magn. Reson.*, 159:126, 2002.
- [88] D. Morineau, C. Alba-Simionesco, M.-C. Bellissent-Funel, and M.-F. Lauthié. *Europhys. Lett.*, 43:195, 1998.
- [89] D. Morineau, Y. Xia, and C. Alba-Simionesco. *J. Chem. Phys.*, 117:8966, 2002.

- [90] K. L. Ngai. *J. of Non-Cryst. Solids*, 275:7, 2000.
- [91] K. L. Ngai and S. Capaccioli. *Phys. Rev. E*, 69:031501, 2004.
- [92] K. L. Ngai and M. Paluch. *J. Chem. Phys.*, 120:857, 2004.
- [93] N. B. Olsen. *J. Non-Cryst. Solids*, 235:399, 1998.
- [94] G. E. Pake. *J. Chem. Phys.*, 16:327, 1948.
- [95] M. Paluch, C. M. Roland, S. Pawlus, J. Ziolo, and K. L. Ngai. *Phys. Rev. Lett.*, 91:115701, 2003.
- [96] K. Pathmanathan and G. P. Johari. *J. Phys. C*, 18:6535, 1985.
- [97] A. Patkowski, T. Ruths, and E. W. Fischer. *Phys. Rev. E.*, 67:021501, 2003.
- [98] A. Ponti. *J. Magn. Reson.*, 138:288, 1999.
- [99] W. H. Press, S. A. Teukolsky, W. T. Vetterling, and B. P. Flannery. *Numerical Recipes in C*. Cambridge University Press, 1992.
- [100] M. A. Ramos, Q. W. Zou and S. Vieira, and F. J. Bermejo. *Czechoslovak J. Phys.*, 46:2235, 1996.
- [101] A. Reiser, G. Kasper, and S. Hunklinger. *Phys. Rev. Lett.*, 92:125701, 2004.
- [102] R. Richert and M. Yang. *J. Phys. Chem. B*, 107:895, 2003.
- [103] I. Roggatz. *NMR-Untersuchungen zur Sondenbeweglichkeit in ungeordneten Festkörper*. PhD thesis, Universität Bayreuth, 2000.
- [104] I. Roggatz, E. Rössler, M. Taupitz, and R. Richert. *J. Phys. Chem.*, 100:12193, 1996.
- [105] C. M. Roland, M. J. Schroeder, J. J. Fontanella, and K. L. Ngai. *Macromolecules*, 37:2630, 2004.
- [106] E. Rössler and H. Sillescu. *Chem. Phys. Lett*, 112:94, 1984.
- [107] E. Rössler, A. P. Sokolov, P. Eiermann, and U. Warschewske. *Physica A*, 201:237, 1993.
- [108] H. Sato, K. Takebayashi, and Y. Tanaka. *Macromolecules*, 20:2418, 1987.
- [109] D. Schaefer, J. Leisen, and H. W. Spiess. *J. Magn. Reson. A*, 115:60, 1995.
- [110] D. Schaefer and H. W. Spiess. *J. Chem. Phys.*, 97:7944, 1992.

- [111] P. Scheidler, W. Kob, and K. Binder. *Europhys. Lett.*, 52:277, 2000.
- [112] K. Schmidt-Rohr and H. W. Spiess. *Multidimensional Solid-State NMR and Polymers*. Academic Press - New York, 1994.
- [113] K. Schmidt-Rohr and H. W. Spiess. *Multidimensional Solid-State NMR and Polymers*. Academic Press - New York, 1994. p. 60.
- [114] W. Schnauss, F. Fujara, and H. Sillescu. *J. Chem. Phys.*, 97:1378, 1992.
- [115] G. Schneider. *^2H NMR-Untersuchung der Sekundärrelaxation in den ungeordneten Phasen von Ethanol*. Master's Thesis, Universität Bayreuth, 2001.
- [116] U. Schneider, R. Brand, P. Lunkenheimer, and A. Loidl. *Phys. Rev. Lett.*, 84:5560, 2000.
- [117] G. P. Singh, R. Vacher, and R. Calemczuk. *J. Phys. (France)*, C9:525, 1982.
- [118] H. W. Spiess. *J. Chem. Phys.*, 72:6755, 1980.
- [119] H. W. Spiess and H. Sillescu. *J. Magn. Reson.*, 42:381, 1981.
- [120] H. W. Spiess and H. Sillescu. *Chem. Phys. Macromol.*, page 313, 1991.
- [121] V. Teboul and C. Alba-Simionesco. *J. Phys.: Condens. Matter*, 14:5699, 2002.
- [122] A. Tölle, H. Schober, J. Wuttke, O. G. Randl, and F. Fujara. *Phys. Rev. Lett.*, 80:2374, 1998.
- [123] D. A. Torchia and A. Szabo. *J. Magn. Reson.*, 49:107, 1982.
- [124] U. Tracht, M. Wilhelm, A. Heuer, H. Feng, K. Schmidt-Rohr, and H. W. Spiess. *Phys. Rev. Lett.*, 81:2727, 1988.
- [125] C. Tschirwitz. Unpublished results.
- [126] C. Tschirwitz, S. Benkhof, T. Blochowicz, and E. Rössler. *J. Chem. Phys.*, 117:6281, 2002.
- [127] M. Tyagi and S. S. N. Murthy. *J. Chem. Phys.*, 114:3640, 2001.
- [128] N. G. van Kampen. *Stochastic Processes in Physics and Chemistry*. North Holland - Amsterdam, 1981.
- [129] M. Vogel. *^2H NMR-Untersuchung der Sekundärrelaxation in organischen Glasbildner*. PhD thesis, Universität Bayreuth, 2000.

- [130] M. Vogel. *²H NMR-Untersuchung der Sekundärrelaxation in organischen Glasbildner*. PhD thesis, Universität Bayreuth, 2000. Fig. 8.1, p. 178.
- [131] M. Vogel and E. Rössler. *J. Phys. Chem. A*, 102:2102, 1998.
- [132] M. Vogel and E. Rössler. *J. Phys. Chem. B*, 104:4285, 2000.
- [133] M. Vogel and E. Rössler. *J. Magn. Reson.*, 147:43, 2000.
- [134] M. Vogel and E. Rössler. *J. Chem. Phys.*, 114:5802, 2001.
- [135] M. Vogel and E. Rössler. *J. Chem. Phys.*, 115:10883, 2001.
- [136] M. Vogel, C. Tschirwitz, G. Schneider, C. Koplin, P. Medick, and E. Rössler. *J. of Non-Crys. Solids*, 307-310:326, 2002.
- [137] H. Wagner and R. Richert. *J. Non-Cryst. Solids*, 242:19, 1998.
- [138] H. Wagner and R. Richert. *J. Phys. Chem. B*, 103:4071, 1999.
- [139] S. Wefing, S. Kaufmann, and H. W. Spiess. *J. Chem. Phys.*, 89:1234, 1988.
- [140] S. Wefing and H. W. Spiess. *J. Chem. Phys.*, 89:1219, 1988.
- [141] J. F. Willart, M. Descamps, and J. C. van Miltenburg. *J. Chem. Phys.*, 112:10992, 2000.
- [142] G. Williams. *Adv. Polym. Sci.*, 33:59, 1979.
- [143] G. Williams and D. C. Watts. *Trans. Farad. Soc.*, 67:1971, 1971.
- [144] M. Winterlich, G. Diezemann, H. Zimmermann, and R. Böhmer. *Phys. Rev. Lett.*, 91:235504, 2003.
- [145] D. Zhao, J. Feng, Q. Huo, N. Melosh, G. H. Fredrickson, B. F. Chmelka, and G. D. Stucky. *Science*, 279:548, 1998. Triblock copolymer Pluronic P123 (EO₂₀PO₇₀EO₂₀) was used as surfactant and tetraethoxysilane (TEOS) as silica source. After reacted at 35 °C for 20 hours, then aged at given temperature for another 24 hours, the mixture was collected by filtration without washing, dried and calcined in air at 500 °C for 6 hours. Different pore sizes were obtained by changing the aging temperature from 35 °C to 100 °C.

Zusammenfassung

Die vorliegende Arbeit befasst sich mit der Untersuchung molekularer Glasbildner mittels multidimensionaler ^2H NMR. Um die Eigenschaften der intrinsischen Sekundärrelaxationsprozesse (β -Prozesse) im Glaszustand ($\frac{1}{2}T_g \lesssim T < T_g$) zu studieren, richteten wir unsere Aufmerksamkeit auf glasbildende Flüssigkeiten, welche aus einfachen, starren Molekülen aufgebaut sind. Für einige Systeme wurden NMR Daten bei Temperaturen erfasst, die dem unterkühlten flüssigen Zustand ($T > T_g$) entsprechen. Damit wurden Informationen zum Hauptrelaxationsprozess (α -Prozess) gewonnen. Ausführliche Random-Walk (RW)-Simulationen wurden durchgeführt, um ein tieferes Verständnis der experimentellen Daten zu erhalten.

Da die molekulare Bewegung, die dem β -Prozess zugrunde liegt, räumlich hoch eingeschränkt ist, sind die Auswirkungen auf das ^2H NMR Festkörperspektrum subtil. Quantifiziert wurden dieser Änderungen über die relative spektrale Intensität $R(t_p, T)$ bei der Frequenz Null, wobei t_p den Inter-Impulsabstand für das Solid-Echo bezeichnet. RW-Simulationen, die auf einfachen Modelle des β -Prozesses basierten, wurden durchgeführt um die Entwicklung von $R(t_p, T)$ abzuschätzen. Die Ergebnisse zeigen, dass im Gegensatz zu vorausgegangenen NMR-Untersuchungen modellunabhängig eine verlässliche Abschätzung der Zeitkonstanten für den β -Prozess möglich ist. Außerdem wurde dargelegt, dass der Verlauf von $R(t_p, T)$ Informationen über Winkelamplitude sowie Verteilung der Korrelationszeiten $G[\ln(\tau_\beta)]$ beinhaltet. Die Daten von Ethanol- d_1 und Ethanol- d_2 konnten damit erfolgreich analysiert werden. Die Zeitkonstanten von Ethanol- d_1 stimmen gut mit den Werten aus der dielektrischen Spektroskopie (DS) überein.

m-Fluoroanilin (m-FAN) wurde detailliert mittels ^2H NMR untersucht, da dieser Glasbildner einen besonders schnellen β -Prozess mit einer deutlich geringeren Relaxationsstärke aufweist als dies bei den meisten der bislang untersuchten Materialien der Fall ist. Unsere Ergebnisse zeigen, dass die Geometrie der molekularen Bewegung, die dem β -Prozess zugrunde liegt, ähnlich zu derjenigen in Toluol ist, mit dem Unterschied, dass bei m-FAN eine kleinere Winkelamplitude genügt, um die experimentellen Befunde zu erklären. Jedoch wurde eine große Abweichung zwischen der mittels NMR und jener mittels DS bestimmten Zeitskala gefunden. Dieses Resultat unterstützt die Behauptung mehrerer Autoren, dass m-FAN Wasserstoffbrücken-Cluster ausbildet und diese einen besonderen Sekundärprozess verursachen.

Um Auskunft über eine mögliche Existenz einer Korrelationslänge des β -Prozesses zu erhalten, wurden Toluol und zum Vergleich o-Terphenyl (OTP; kein dielektrischer β -Peak) eingebettet in eine nanoporöse Glasmatrix (SBA-15) untersucht. Anhand der Temperaturabhängigkeit der Spin-Gitter Relaxationszeit fanden sich Hinweise, dass

sich der β -Prozess in Toluol unter der Bedingung der einschränkenden Geometrie verändert. Es zeigte sich eine Verteilung der Relaxationszeiten, welche zu kürzeren Zeiten hin gegenüber jener des bulk-Glasbildners verbreitert ist. Dahingegen ändert sich die entsprechende Relaxationszeitenverteilung von OTP in SBA-15 nicht ($T < T_g$). Der α -Prozess sowohl von OTP als auch von Toluol wird durch eine breite, heterogene Verteilung der Korrelationszeiten charakterisiert.

Polybutadien (PBD), ein umfassend untersuchtes Polymer ohne Seitengruppen, zeigt in unseren ^2H NMR Untersuchungen bei niedrigen Temperaturen ($T < T_g$) zusätzlich zum β -Prozess einen weiteren Sekundärprozess, der als γ -Prozess bezeichnet wurde. ^2H NMR Untersuchungen an 10% deuteriertem Benzol in PBD belegen, dass die Benzolmoleküle Bewegungseigenschaften aufweisen, die denen des reinen PBD sehr ähnlich sind. Das Gastmolekül Benzol wird also sowohl in den β - als auch den γ -Prozess von Polybutadien ‘eingebaut’. Anhand der NMR-Ergebnisse konnten Randbedingungen für in der Literatur diskutierte Modelle, die den γ -Prozess beschreiben, geliefert werden; wiederum wurde eine Reorientierung um große Winkel ausgeschlossen ($T < T_g$).

Schließlich wurde der α -Prozess der unterkühlten plastisch-kristallinen Phase von Cyanoadamantan untersucht. Wir waren in der Lage, das Signal dieser Phase durch selektive Anregung von jenem gleichzeitig vorhandenen der geordneten kristallinen Phase abzutrennen. ^2H NMR Festkörperechos und 2D-Spektren wurde gemessen. Es zeigte sich, dass die Moleküle entsprechend der Symmetrie des Kristallgitters 90° -Sprünge vollführen. RW-Simulationen reproduzieren sehr gut die Messungen. Beide Methoden liefern Zeitkonstanten, welche mit jenen anderer Techniken übereinstimmen. Es gab keinen Hinweis für eine Kleinwinkelbewegung wie sie für den α -Prozess von strukturellen Gläsern typisch ist.

Erklärung

Hiermit erkläre ich, dass ich die vorliegende Arbeit selbständig verfasst und keine anderen als die angegebenen Quellen und Hilfsmittel verwendet habe. Ferner habe ich keine früheren Promotionsversuche unternommen.

Bayreuth, November 2005

